Quantitative photoacoustic tomography: experimental phantom studies

Martina Paula Bargeman Fonseca

PhD Thesis
submitted for the degree of Doctor of Philosophy

University College London
Department of Medical Physics & Biomedical Engineering
Biomedical Optics Research Laboratory

December 2017

Declaration

I, Martina Paula Bargeman Fonseca, confirm that the work presented in this thesis is my own. Where information has been derived from other sources, I confirm this has been indicated in the thesis.

Signed .....

Date .....

We are surrounded by curtains. We only perceive the world behind a curtain of semblance.

At the same time, an object needs to be covered in order to be recognized at all.

René Magritte

Abstract

Photoacoustic tomography (PAT) is a promising non-invasive imaging modality exhibiting high resolution, good contrast and specificity to light-absorbing molecules (chromophores). One of the outstanding challenges the technique faces is that PAT images, though dependent on optical absorption, are not its direct representation because they are coloured by the unknown light fluence. Theoretical studies have succeeded in quantifying optical absorption and chromophore concentration by employing model-based inversions (MBI) that can deal with the non-linearity of the problem and the fluence-related distortion. However, experimental translation has been scarce. The aim was to perform quantitative PAT (qPAT) in a rigorous experimental phantom study to show that highly-resolved 3D estimation of chromophore distributions can be achieved. The first consideration was finding a tissue-relevant and stable matrix material and chromophores. Thermoplastic PVCP was fully assessed. Its stability, intrinsic optical properties, thermoelastic efficiency and low-frequency acoustic properties were suitable. The limitation was the lack of photostability of embedded pigments. Separately, we fully characterised aqueous solutions of sulphate salts and found them to be suitable chromophores for qPAT and potential surrogates for oxy- and deoxyhemoglobin. For a phantom made of sub-mm tubes filled with sulphate solutions in an intralipid-rich background, 3D high resolution estimates of chromophore concentrations were obtained through an efficient diffusion approximation MBI. Uncertainties in optical inputs of the MBI were tackled by assessing *in silico* their effect on quantification accuracy and then mitigated in the designed experiment through careful measurements. A faithful representation of the multiwavelength photoacoustic tomography (PAT) images was sought by employing broadband, near-omnidirectional and high-sensitivity sensors and a detection configuration and reconstruction that overcame the limited view problem. Estimation of the chromophore ratio, analogous to the much sought-after blood oxygenation, gave a mean absolute error of 3.4 p.p., whilst normalised estimates of the two main chromophore distributions gave errors of 13.2% and 17.2%.

Impact Statement

Photoacoustics is an imaging technique that has the capability to obtain high-resolution, 3D images whose contrast relates to the absorption of light by molecules in the tissue such as blood, fat or water, or from engineered contrast agents. Being able to, from these absorption rich images, extract the individual distributions of the various molecules, has been a long-standing aim for the technique, albeit challenging to achieve. A body of simulation-based studies on quantitative photoacoustic tomography (qPAT) have been proposed, but despite this, full quantification has not been translated as a tool into the ever-growing number of pre-clinical studies or into clinical systems under development. In this project, we aimed to bridge the gap between simulation and experiment. One of the aspects involved reviewing and developing better tissue-mimicking materials (TMMs) that could be used for testing and optimising quantification methodologies in experiment in a controlled and characterised way. We performed comprehensive studies for a thermoplastic candidate and a pair of sulphate salts and showed their suitability for qPAT as well as the limitations. We also elucidated the more extensive and rich material criteria and characterisation stages needed for materials to be used in proper quantification studies, compared to TMMs developed for more standard or qualitative studies. Namely, it was clear that there was a lack of information on the thermodynamic behaviour and on the stability of molecules to light exposure. There is a large scope for future investigations into TMM materials given their crucial role for proof-of-concept and validation. Not only that, suitable TMMs would facilitate the creation of standards, regulations, quality control and maintenance routines that are a necessity in the implementation of any imaging technique into the clinical routine. Another of the aspects in this project involved performing a well-controlled experimental qPAT study where all aspects of the full problem were considered - sample, instrumentation, acquisition, image reconstruction and quantification algorithm. By doing so, we identified bottlenecks, limitations and areas of intervention that can be explored in future theoretical and experimental studies or that can be taken into account during commercial system design and development. One of the examples of future clinical application may be photoacoustic mammography for breast cancer detection, staging and monitoring, which is undergoing its translation process. Quantitative data could be powerful to inform on the oxygen levels in the microvasculature surrounding the tumour or give distribution maps of contrast agents with affinity to e.g. malignant cells, angiogenesis co-factors or with sensitivity to hypoxic or altered pH

regions. Quantification could also lend robustness to longitudinal or inter-subject studies. Another example of a prospective clinical application is the use of photoacoustics in minimally invasive procedures given its potential for miniaturisation and compatibility with other instrumentation. Photoacoustic data sensitive to different constituents can aid navigation during surgery, give on-the-fly diagnosis or narrow down areas for biopsy. These could reduce the number and length of procedures and reduce the recovery time and complications, with benefits to the patient, medical staff and healthcare systems.

Acknowledgements

First and foremost, I would like to thank my supervisor Ben Cox for his ever-present support, availability and guidance as well as for his unwavering positive and constructive outlook that were indispensable during this PhD journey. I could not have asked for a better supervisor. I would also like to thank my secondary supervisor Paul Beard for his availability, thoroughness and keen eye for both detail and the bigger picture.

The work in this thesis would not have been possible without the always present support and synergy of the Photoacoustic Imaging Group, whether through collaborative work, discussions, assistance with trouble-shooting or moral support over a cup of tea and biscuits. Special thanks to Adrien Desjardins, Brad Treeby, Edward Zhang, Jamie Guggenheim, Jo Brunker, Lu An, Ollie Ogunlade, Roman Hochuli, Thomas Allen and Thomas Stahl. I am especially indebted to Emma Malone, Rob Ellwood and Teedah Saratoon for providing crucial code, computations and technical support. At CMIC, I would also like to thank Simon Arridge and Felix Lucka for the invaluable contributions to discussions, idea generation and data analysis. At the National Physical Laboratory, I would like to thank my external supervisor Bajram Zeqiri for all the support in his area of expertise as well as Neelaksh Sadhoo and Srinath Rajagopal for technical support. I would also like to thank my PhD examiners Jem Hebden and Sarah Bohndiek for the discussion, suggestions and amendments.

The positive and friendly atmosphere in BORL and the department was also a great booster, whether through social committee events or the day-to-day tea breaks, lunches and outings. Thank you especially to mood-makers and fellow foodies Sara Reis, Michael Brown, Prash Ganeswaran, Laura Dempsey. And to Lu An particularly, thank you for being the best deskmate, QPAT co-brainstormer, food-buddy, plant baby-sitter and even counsellor throughout my excessive nagging.

I would also like to give a heartfelt thank you to all my friends that have accompanied and been by my side over the years, during the adventurous, the festive, the comfortable and even the stressful moments. My 'sister' Stephanie Shearing; my life-of-the-party high school friends Ana Margarida Silva, Sara Carvalho, Sónia Tomás, David Simavorian, João Serra, João Leal, Catarina Martins, António Carvalho and Pedro Alexis; my MEBiom08 undergraduate friends, especially Catarina Realista, Joana Lourenço, Márcia Santos, Pedro Aparício, Rita Leal, Tiago Malaquias; the eclectic Imperial MSc crew 11/12

(Adit, Antoine, Bill, Caroline, Claire, Erik, Florie, Gaëlle, Greg, Laetitia, Jonny, Lucia, Marie, Martin, Nathalie, Octave, Shirin, Vincent) and those who I met through more recent London incursions with PARSUK and Madanyu - especially Rita Pinho, Pedro Antas and Inja Radman.

Finally, the warmest of thanks to my family. To my sister Rita and nephews João and Maria for always irradiating joy and happiness, to my grandmother Cia, and to my parents Ria and Sérgio, who have always been there unconditionally for me: if I have been able to aim higher and roam freely, it is largely because they have always been there as both my trampoline and safety net.

Contents

List of Figures

List of Tables

Abbreviations

AO acousto-optic tomography

BFGS Broyden-Fletcher-Goldfarb-Shanno

CNC computer numerical control

DA diffusion approximation

DOT diffuse optical tomography

FEM finite element modelling

FOV field-of-view

FP Fabry-Perot

FPI Fabry-Perot interferometer

IAD inverse adding-doubling

ICA Independent component analysis

ITF interferometer transfer function

iTR iterative time-reversal

L-BFGS Limited-Memory Broyden-Fletcher-Goldfarb-Shanno

LDPE low density polyethylene

LU linear unmixing

MBI model based inversion

MC Monte Carlo

MIP maximum intensity projection

MSOT multispectral optoacoustic tomography

NEP noise-equivalent pressure

NIR near infra-red

NPL National Physical Laboratory

OA osteoarthritis

OPO optical parametric oscillator

RTV Room temperature vulcanising

PA photoacoustic

PAI photoacoustic imaging

PAT photoacoustic tomography

PAM photoacoustic microscopy

PAS photoacoustic spectroscopy

PCA Principal component analysis

PE polyethylene

PMMA poly(methyl methacrylate)

PRF pulse repetition frequency

PVA Polyvinyl alcohol

PVCP Polyvinyl chloride plastisol

PVDF polyvinylidene fluoride

qPAI quantitative photoacoustic imaging

qPAT quantitative photoacoustic tomography

ROI region of interest

RTE radiative transfer equation

RTV room temperature vulcanising

SEM scanning electron microscopy

SNR signal-to-noise ratio

US ultrasound

UV ultraviolet

Part I

Introduction and Background

Chapter 1

Introduction

1.1 The need for functional and quantitative imaging

Imaging techniques play an important role in the ability to see structures and processes that would otherwise not be noticeable to the naked eye. The anatomical and functional information obtained can prove essential to have a wider understanding of our body, both in health and disease. Imaging techniques range in depth and field-of-view, spatial resolution, temporal resolution and source of contrast. This need comes from the fact that structures in the human body and other living systems vary in scale, location, organisation and composition and that the underlying processes vary in function and in temporal and spatial range of action. Also, since manifestations first noticed at the system or organ levels are often underlined by changes at the tissue, cell, molecular or even genetic level, a multiscale and versatile suite of tools is needed to tackle many clinical problems.

One of the main features desired for functional imaging, whether for pre-clinical or clinical studies, is the ability to provide specific and selective contrast from molecules or agents of interest at high-resolution and with sufficient field-of-view. Another important aspect is the ability to derive quantitative information from this contrast - namely on the concentration and distribution of these molecules/agents and on related physiological metrics (e.g. perfusion, oxygen saturation, metabolic activity).

In day-to-day clinical practice, these functional and quantitative imaging tools can be used to better diagnose and stage the progress of disease, to monitor response to treatment and to plan or guide surgical procedures. In clinical studies (trials), they can inform on the effectiveness of new pharmaceuticals or techniques. They can also help find new relevant processes or molecules that can become targets for new pharmaceuticals or act as markers for earlier prevention or diagnosis. In biological and pre-clinical studies, where cell and animal models are used to study processes and alterations from normality in a more controlled, versatile and multi-scale manner, quantitative imaging can again play a crucial role.

1.2 Photoacoustic tomography

Photoacoustic tomograpy (PAT) is a prime candidate for structural and functional imaging studies, both in pre-clinical and clinical scenarios [1]. The technique relies on the photoacoustic effect - wherein a pulsed laser light generates the emission of acoustic waves from optically absorbing tissue within the body. Alexander Graham Bell first discovered the effect in 1880 when he noticed that exposing a thin disk to modulated sunlight led to the emission of sound [2, 3]. For imaging purposes, these waves can then be detected by broadband ultrasound transducers and used to form an image. The ultrasonic detection gives the technique its high spatial resolution and imaging depth - in tomography mode, sub-100μm resolution at a few cm depths can be achieved [4] whilst the optical excitation provides the high specificity and contrast characteristic of optical techniques. The photoacoustic signal encodes optical absorption, and since different chromophores (light-absorbing molecules/compounds) have unique spectral features, imaging at multiple wavelengths can yield functionally-relevant information. Chromophores of interest include endogenous chromophores (e.g oxy- and deoxyhemoglobin, lipid, water or melanin), genetically encoded reporters and exogenous chromophores (e.g. dyes and nanoparticles with the potential of being funcionalised to target a specific process and therefore act as a biomarker) [1]. Fig. 1.1 shows a typical PAT volumetric image rich in hemoglobin contrast.

Due to its perceived potential, photoacoustic imaging has flourished as a field, with extensive and active research being done in aspects such as instrumentation, contrast agent design and reconstruction and processing algorithms. These have led to substantial advancements in the use of PA in pre-clinical *in vivo* studies [4–6] and led to leaps towards its full implementation for clinical applications [7, 8]. PA tomography has been able to image a variety of locations and structures, e.g. the breast [9], the skin [10], finger [11, 12], sentinel lymph nodes [13] and the gastrointestinal tract for clinical purposes and the head/brain [14–16], ear [17], eye [18], liver [19], gastrointestinal tract [7], kidney [19, 20], spleen [20], sentinel lymph nodes [21], peripheral nerves [22] for pre-clinical (small animal imaging) purposes. The discernible objects can range from organelles to full human organs or even whole-body small animals [23]. Its domain of application extends from anatomical studies to functional studies, whether focussed on molecular, metabolical, hemodynamic or neuronal activity. There are a number of clinical disciplines where photoacoustic imaging (PAI) may be of interest, namely in oncology [8, 13] to dermatology [10, 24], opthalmology [18], neurology [14, 25], cardiology [26, 27] and gastroenterology [7].

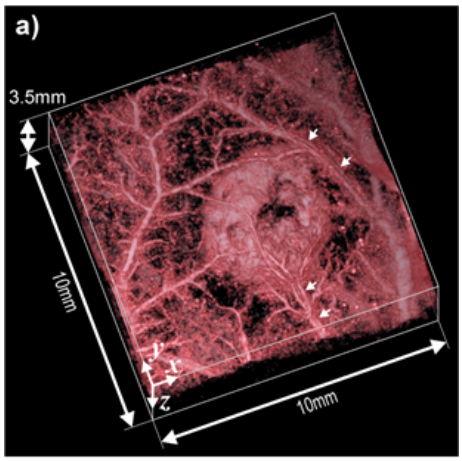

Figure 1.1: *Representative PAT volume rendering of a subcutaneous tumour and surrounding vasculature in a mouse. Image acquired at 600 nm and at 70µm resolution. Reprinted with permission from [28]. Copyright 2012 Society of Photo-Optical Instrumentation Engineers.*

1.3 PAT vs other modalities

	Technology parameters					Application parameters			
	Contrast	Sensitivity	Resolution	Cost of manufacture	Safety	Throughput capacity	Easiness of use	Equipment size	Penetration depth
MSOT	●	pmol (10^{-12})	~50µ	Low	●	High	●	Small	◑
X-ray	○	µmol (10^{-6})	~50µ	Medium	◔	High	●	Medium	●
XrayCT	◔	µmol (10^{-6})	~50µ	High	○	Low	◕	V large	●
MRI	●	nmol (10^{-9})	~50µ	V high	●	Low	◑	V large	●
US	○	nmol (10^{-8})	~50µ	Low	●	Medium	●	Small	◑
PET	●	fmol (10^{-15})	1-2mm	V high	◔	Low	◔	V large	●
SPECT	●	fmol (10^{-14})	1-2mm	High	◔	Low	◔	V large	●
Optical	◕	pmol (10^{-12})	1-2mm	Low	●	Medium	●	Small	○

Best in category Worst in category ● EXCELLENT ◑ AVERAGE ○ POOR

Figure 1.2: *PAT (here named MSOT) performance in comparison to other imaging modalities, both in terms of technical and application parameters. As can be seen, PAT excels for most parameters, except for penetration depth. MSOT - Multispectral Optical Tomography; MRI - Magnetic Resonance Imaging; US - Ultrasound; PET - Positron Emission Tomography; SPECT - Single Photon Emission Computed Tomography. Reprinted with permission from [6]. Copyright 2010 American Chemical Society.*

PA can provide several advantages over other imaging modalities. For instance, unlike techniques such as X-ray, computed tomography, PET and SPECT, it is non-ionising. MRI techniques provide large field-of-view, penetration depth and resolution, but can suffer from low sensitivity and involve high equipment cost. Also, though metrics of perfusion (with arterial spin labelling and dynamic susceptibility contrast) and deoxyhemoglobin-weighted images (BOLD-MRI) can be obtained, absolute concentrations or oxygenation are not available. PET and SPECT also enable whole-body imaging whose contrast encodes for metabolism, but at low resolution and high cost. PAT fares well in terms of various technical and application parameters, as summarised in Figure 1.2. Some

Feature	PA	Other Optical
Penetration depth	sub-mm to cm	Depends on technique [29]; Ballistic optical microscopy, Two-photon microscopy: ~ 0.5 mm; Optical Coherence Tomography: ~ 1 mm; Diffuse Optical Tomography: several cm
Scattering	Acoustic scattering in tissue about 3 orders of magnitude less than optical scattering in tissue per unit path length	High
Light leakage	No. Though PA waves can be generated in the transducer due to light absorption	Yes. Leakage of excitation photons into detectors [5]
Speckle	Speckle-free as long as the detectors are sufficiently broadband	Yes
Applicability	Broad, since all molecules are optically absorbing at some wavelengths	Fluorescence microscopy: few molecules are fluorescent
Intermodality	Yes - PA and optical methods can be combined (e.g. endoscopic probes)	
Blood flow measurement	Yes (PA Doppler flowmetry [30, 31])	Laser Doppler flowmetry
Temperature sensing	Yes (PA generation process) [32]	No

Table 1.1: *Comparison between PA and other optical modalities.*

summary lines should be considered more critically though. For instance, though cost of manufacture of PAT systems may not be exorbitant, the constituent components (such as the high energy ns-pulsed laser) are often very costly. Optical techniques (optical coherence tomography, fluorescence microscopy, standard microscopy, Raman scattering, two-photon microscopy, light sheet microscopy and so on) have been summarised into one line, when in fact a wide range of trade-offs and nuances exist between them . The table also shows PAT and optical techniques as having similar sensitivity, given as a single number - this is in fact hard to boil down into such a simplified metric when sources of contrast can be so diverse in nature (absorption weighted, refractive index change weighted, fluorescence weighted) and when we do not have a comparison of this sensitivity in a spatially resolved manner (depth-wise, resolution-wise).

Feature	PA	US
US origin	Optical excitation ⇒ Non-radiative decay ⇒ Heat ⇒ Pressure	Piezoelectric effect
Amplitude	Less than 10 kPa [4]	In excess of 1 MPa
Bandwidth	Broadband; Tens of MHz [4]	Defined by transmit transducer and typically centred around one frequency; Centre frequency can go to some tens of MHz. Relatively narrow fractional bandwidth
Contrast	Initial pressure distribution, which depends strongly on optical absorption; Better contrast than US	Acoustic impedance changes, which depend on mechanical & elastic properties
Selective contrast	Spectral dependence of optical properties ⇒ differentiation ⇒ quantification	No. Potentially through injection of targeted microbubbles.
Penetration depth	sub-mm to a few cm [33]	>∼ 10 cm
Resolution	lateral: sub-micron to sub-mm; axial: tens of micron to sub-mm [33]	lateral: depends on pulse duration; axial: depends on focal width
Focus	On receive; On transmit only if $d < 1$ mm	On transmit and receive
Nonlinear propagation	No	Yes ⇒ US tissue harmonic imaging
Speckle	Speckle-free as long as the detectors are sufficiently broadband	Yes
US exposure hazards	No	Yes - but not considered an issue for diagnostic US
Intermodality	PA-US systems have been developed.	

Table 1.2: *Comparison between ultrasound (US) and photoacoustic (PA) modalities. ΔZ - impedance mismatch, H - absorbed energy density, d - distance from surface.*

To elaborate, when compared to most available purely optical modalities, PA contrast is considerably more dependent on optical absorption than optical scattering, yielding a strong optical absorption-rich contrast. More so, PA is able to provide this rich optical contrast beyond the typical optical imaging depth limit without compromising high-resolution. For most 3D optical techniques (optical coherence tomography, confocal and two-photon microscopy), ~1 mm is the maximum achievable imaging depth in scattering media, since they rely on ballistic or quasi-ballistic photons. Beyond that, light becomes diffuse and too complex to interpret in a spatially meaningful way [3, 5]. Diffuse optical tomography does allow imaging in the range of centimetres, but at the cost of very poor spatial resolution and insufficient specificity to absorption over scatter [5]. For PA, the maximum achievable depth is mainly limited by signal-to-noise ratio (SNR), itself dictated by restrictions on maximum permissible exposure of the excitation light on the tissue surface and on the background optical attenuation levels; the spatial resolution with depth is mainly limited by frequency-dependent acoustic attenuation. Table 1.1 provides an overview of the main differences between PA and other optical modalities.

Finally, when comparing PA and ultrasound (US), both share core advantages in spatial resolution and depth of penetration due to the nature of acoustic propagation. Compared to ultrasound though, where contrast comes from changes in acoustic impedance, PA has a far richer set of possible contrast sources due to the optical nature of the excitation and a greater specificity due to wavelength tuning. The differences in optical absorption between different tissues also significantly exceed those in acoustic impedance [4]. Table 1.2 provides a comparative view of PA and US.

1.4 Quantification in PAT

Photoacoustic tomography, through the use of appropriate acoustic reconstruction algorithms, can yield high-resolution, depth-rich, 3D images of initial pressure distribution that also encode for optical absorption. If retrieving this optical absorption were straightforward and multiple wavelength acquisitions were made, it would be easy to retrieve chromophore concentrations. However, isolating the optical absorption term is not trivial because photoacoustic tomography (PAT) images are actually proportional to the product of the optical absorption and the light fluence distribution, which itself depends on the overall behaviour of optical absorption. This means not only that the problem is non-linear, but also that the image is somehow corrupted by the fluence - there will be spectral colouring at each spatial point due to the paths the light will have travelled, spatial distortion caused by the light decay and overall non-uniqueness due to the also unknown light scattering characteristics.

A large body of theoretical and simulation studies has in recent years tried to tackle these problems and retrieve optical absorption (and concentration) data from PA images. The most effective and accurate are based on model-based minimisation frameworks,

which find the relevant information by iteratively minimising the difference between the measured data and a given model that accounts for light propagation [34]. Besides coping with non-linearity, spectral colouring and spatial distortion, adaptations have also been shown to be able to deal to various extents with the ill-posedness caused by the unknown scattering behaviour - through regularisation, information of spectral behaviour of scattering or measurements at additional source locations.

Despite the growth in successful theoretical-based quantification approaches, these have not been yet successfully transitioned into routine pre-clinical and clinical studies. This can be attributed to a range of factors. First off, early model-based algorithms suggested were not efficient enough (time- and memory-wise) to deal with the high dimensionality of the PA data, making heuristic data decomposition strategies more appealing to experimentalists. Most of the implementation issues are however related to the expectations placed on simulated data compared to actual experimental data, which if different and not properly accounted for may complicate implementation or upset the quantification. Namely, theoretical quantitative photoacoustic tomography (qPAT) algorithms often assume that the experimentally acquired pressure time-series data are noise-free and complete, i.e. that they have been acquired on a system with high sensitivity, infinite sensor bandwidth, perfect omnidirectional response and a full view of the acoustic field. Also, they go on to assume that the acoustic reconstruction will yield a faithful reconstruction of the initial pressure distribution, without artefacts, noise or unphysical features like negative values. More specifically for model-based inversions, these will also typically assume that there is no uncertainty in the input parameters (e.g. chromophore absorption spectra, beam profile and location, data scaling) and that the model represents the underlying physics well enough, which may not always be the case. Another hurdle in the pre-clinical/clinical translation process relates to the validation and optimisation process itself of these frameworks. Simulations can assess and address some issues, but in a limited way. On the other hand, whilst using *in vivo* subjects would be closest to the potential end-applications of qPAT, these often do not give access to the much-needed ground-truth, and they do not give the necessary stability and control to vary individual aspects. Extensive *in vitro* or phantom studies would be a necessary and crucial step to properly bridge between simulation and actual pre-clinical or clinical implementation, but there is a lack of suitable candidate materials for phantoms and chromophores (stable, tissue-mimicking in optical thermal and acoustic properties, reproducible).

Due to these challenges, only very few studies have actually rigorously and meticulously explored the degree of accuracy that can be obtained experimentally in qPAT, and tried to address some of the issues that pure simulation studies did not traditionally consider [35–37]. These have mainly used model-based minimisation schemes of reduced dimensionality, by either applying a 2D model and/or by segmenting the domain into a finite set of regions of interest with constant optical properties. This helped reduce

the number of unknowns considerably and hence the computational load of the inverse scheme. It also increased robustness to noise and to the uncertainties mentioned, by imposing some *a priori* knowledge. Despite its advantages, reducing the number of spatial dimensions through slice-based inversion compromises the accuracy of the estimation in the full volume, whilst imposing piece-wise constancy sacrifices the level of spatial detail. This is ultimately not desirable for PAT as a functional imaging tool, since it undermines exactly some of its main qualities that we were aiming to explore - its volumetric and depth-rich nature and its high resolution.

Fortunately, recent advances in computing power as well as more efficient minimisation algorithms have allowed, at least in simulation, estimations that can cope with high-dimensional data memory-wise and time-wise. These can therefore yield the much-desired volumetric, highly-resolved images of absorption and of chromophore concentrations [34, 38–42] but have yet to be used in experiment. Applying these methods experimentally will probably mean that an even greater attention needs to be given to the various experimental factors and uncertainties, as they will be more sensitive to any model-experiment discrepancies compared to other schemes where spatial constraints or strict regularisation are imposed.

1.5 Aims of the project

In this study, the aim is to explore the feasibility of achieving fully-resolved (voxel-by-voxel), volumetric chromophore distribution estimation experimentally, through highly controlled virtual and physical phantom experiments. This involves:

- Identifying the main bottlenecks towards pre-clinical and clinical translation of qPAT;
- Finding suitable and well-characterised phantoms for well-controlled qPAT studies;
- Finding suitable and well-characterised sets of chromophores for well-controlled qPAT studies;
- Performing simulation studies that inform on the severity of experimental sources of uncertainty and error;
- Performing a well-controlled and illustrative qPAT experiment, that can yield high-resolution and volumetric estimates of chromophore distribution, and assess its accuracy and robustness;
- Identifying and developing adaptations to data acquisition and qPAT strategies that will maximise the accuracy and robustness of the measurements;

1.6 Thesis structure

The Thesis is divided into four parts.

Part I provides the context and state-of-the-art. Chapter 2 provides an overview of the photoacoustic effect and of forward models for light and sound propagation. Chapter 3 gives an overview of qPAT and the full inverse problem in photoacoustics - the acoustic inversion to retrieve a PA image and the optical inversion to retrieve distributions of optical properties and related quantities. Chapter 4 provides a literature review and state-of-the-art of qPAT approaches, both theoretical and experimental.

Part II focuses on the phantoms needed for experimental validation of multiwavelength qPAT strategies. Chapter 5 reviews phantom materials and characterisation methodologies available, and defines the specific criteria and characterisations needed for qPAT. Chapter 6 provides a full characterisation and discussion of a thermoplastic, PVCP, as a potential tissue-mimicking material for multiwavelength qPAT. Chapter 7 assesses and characterises aqueous solutions of sulphate salts as appropriate chromophores and potential oxy- and deoxyhemoglobin surrogates.

Part III focuses on the experimental implementation of qPAT - aiming to obtain high-resolution, volumetric and absolute quantification of chromophore distributions. Chapter 8 presents a simulation study looking at the effect of various sources of experimental uncertainty on the quantification. Chapter 9 provides the experimental methodology adopted and Chapter 10 shows the experimental results of the main quantification, tests some algorithm formulation and initialisation adaptations and makes considerations on sources of error and areas for improvement.

Part IV concludes the Thesis.

Chapter 2

Photoacoustic signal generation

The process behind the PA effect is described in broad terms in Figure 2.1. As a starting point, a nanosecond pulsed laser is shone onto tissue. This light is then propagated throughout tissue, undergoing scattering and absorption. Once a photon is absorbed by a given light absorbing molecule, heat conversion follows as vibrational and collisional relaxation occurs. This causes a local rise in temperature T' and an increase in pressure p' - thermoelastic expansion. This initial acoustic pressure p_0 propagates through the elastic medium and is eventually detected and converted into a time-resolved electric signal $p(t)$ by an acoustic detector at the surface of the entity being scanned. By applying an appropriate image reconstruction algorithm to the temporally resolved acoustic signals, an image of the initial pressure distribution can be retrieved, p_0^{recon} [34]. This estimate is typically called the PAT image. In this Chapter we will discuss the forward problem and in Chapter 3 we will describe the inverse problem, which is necessary to form the PAT image and also to retrieve optical properties of interest.

2.1 Overview of the PA signal generation process

The forward PA problem, from absorber to measured PA signal, can be divided into two main problems: the optical propagation leading to a fluence distribution Φ and an absorbed energy density H and the acoustic propagation leading to the ultimate detection of PA acoustic waves $p(t)$. These two problems are coupled by the thermalisation of the light energy (conversion of absorbed energy to heat) and thermoelastic coupling (conversion of heat to a pressure rise).

The absorbed energy density can be described as:

$$H(\mathbf{x}) = \mu_a(\mathbf{x})\Phi(\mathbf{x}; \mu_a, \mu_s, g), \tag{2.1}$$

where $\Phi(\mathbf{x}; \mu_a, \mu_s, g)$ [J/m^{-2}] is the fluence term, describing light propagation, itself dependent on the optical absorption μ_a [mm^{-1}] and scattering properties (scattering coefficient

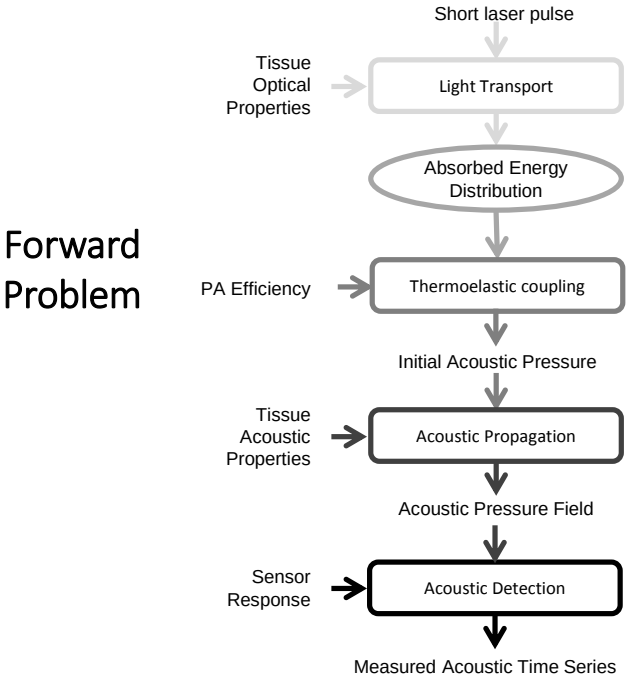

Figure 2.1: *Forward model diagram describing the successive phases of light excitation and propagation, optical absorption, thermoelastic coupling, acoustic propagation and detection.*

μ_s [mm^{-1}] and the anisotropy factor g) of the medium. Section 2.2 describes the typical tissue optical properties that dictate the propagation and absorption of light. Section 2.3 then gives an overview of light propagation in tissue and how it can be modelled. This absorbed energy density will then be converted to heat, assuming that the decay is done non-radiatively. This is discussed in Section 2.4. This will lead to a rise in temperature accompanied by a rise in pressure. The efficiency of the conversion of heat to pressure (thermoelastic efficiency) will depend on the characteristics of the local environment and can be represented and accounted for through the dimensionless Grüneisen parameter Γ, such that the local pressure rise is given by:

$$p_0(\mathbf{x}) = \Gamma(\mathbf{x})H(\mathbf{x}) = \Gamma(\mathbf{x})\mu_a(\mathbf{x})\Phi(\mathbf{x}; \mu_a, \mu_s, g). \tag{2.2}$$

Given that the time-length of the laser pulse is much shorter than the time for volume expansion or thermal diffusion, the laser pulse and subsequent heating and pressure rise can be considered instantaneous. The pressure rise is therefore commonly referred to as initial pressure distribution. Due to the elastic nature of the medium, this local pressure will propagate through the medium as an acoustic wave. These waves can then be detected at the tissue surface with appropriate acoustic detectors. The initial pressure rise and acoustic wave propagation are discussed in Section 2.5 whilst detection is approached in Section 2.6.

2.2 Tissue optical properties

2.2.1 Tissue optical absorption

Light absorption has as overall effect the loss of light intensity as it travels on through the medium. The light is absorbed by molecules, causing electronic excitation (or vibrational in some near infra-red (NIR) cases). The absorption coefficient μ_a of a specific medium denotes the rate at which photons are absorbed per unit length, and will depend on the density of the absorbing molecules (chromophores) present in the medium, ρ [$units\,\mathrm{mm}^{-3}$] and on the absorption cross-section of those molecules σ_a [$\mathrm{mm}^{-2}\,unit^{-1}$]. If the medium contains only this chromophore, the absorption coefficient can be given by $\mu_a = \rho\sigma_a$. The expression can also be re-written as a function of chromophore concentration c [$Molar$], where $\mu_a = c\alpha$ and α [$Molar^{-1}\,\mathrm{mm}^{-1}$] is the specific absorption coefficient. If the medium contains K absorbing chromophores, the absorption coefficient can be re-written as a linear combination, such that:

$$\mu_a(\lambda) = \sum_{k=1}^{K} c_k \alpha_k(\lambda), \tag{2.3}$$

where c_k and α_k are the concentration and specific absorption coefficient respectively, of the k^{th} chromophore. This dependence of optical absorption on chromophore concentration and the distinct spectral signatures of different chromophores, meaning that contrast can be tuned and that c can be retrieved directly from $\mu_a(\lambda)$, are some of the reasons why the optical absorption-rich nature of the contrast of PA images is so appealing.

A range of molecules and compounds provide optical absorption. Depending on the way they convert the absorbed energy during decay, they will be referred to as chromophores (predominant non-radiative relaxation through vibrational and rotational collisions, generating heat) or fluorophores (significant radiative relaxation through fluorescence). The former will be the focus of interest for PA. Chromophores can be either endogenous - i.e. typical tissue constituents - or exogenous.

The main endogenous chromophores are melanin [43, 44], lipid [45], water [46], DNA/RNA [47] and oxy- (HbO_2) and deoxyhemoglobin (HHb) [28, 44, 48, 49]. The latter two can be used to define other physiologically relevant entities such as oxygen saturation $SO_2 = \frac{[HbO_2]}{[HbO_2]+[HHb]} \times 100$ and total hemoglobin $[HbT] = [HbO_2] + [HHb]$. These are crucial to identify vasculature networks and their degree of oxygenation, both important hallmarks for cancer (angiogenesis and hypoxic state are characteristic of tumours) [28], brain activity [14, 25], tissue damage and inflammatory processes (by analysing the microvasculature). The absorption of lipids and water in the near-infra-red region can allow the detection of atherosclerotic plaque [27, 50], injury [46] or the staging of carcinoma [45] whilst melanin absorption can be used for imaging melanomas [10, 44]. Contrast from DNA/RNA in the ultraviolet can be used for cell nuclear imaging [47]. Table 2.1

(summarised information mainly from [4, 5]) gives further information on endogenous chromophores. Exogenous contrast agents can also be used to highlight certain entities of interest, either through localised expression, deposition or specific affinity. They can be engineered to absorb in certain wavelength ranges, to have higher specific absorption coefficient for improved SNR, to bind specifically to certain molecules or to display other phenomena such as being photosensitizing, activable or switchable. Exogenous agents are of special importance in pre-clinical studies, mainly those based on mouse models, since they allow obtaining information on various anatomical, physiological, molecular and genetic characteristics [4]. Examples of exogenous contrast agents include nanoparticles (gold [24, 51, 52], carbon-based [53] and organic polymer constructs), reporter gene products [54, 55] (encoding for absorbing proteins or substrates) and organic [11, 46] and inorganic dyes [56]. Table 2.2 summarises information on some exogenous absorbers. More detailed listings can be found elsewhere [1, 7, 57, 58].

The spectral characteristics of some of these absorbers are given in Fig. 2.2. It can be seen that all chromophores have their own spectral signatures, which can be taken advantage of. Tuning the laser interrogation to a wavelength where absorption of a particular chromophore is particularly strong can give rich image contrast for that chromophore (although not directly proportional to its concentration or spatial distribution due to fluence corruption and due to contributions of other chromophores in the p_0 mapping). Extending the acquisition to multiwavelength will yield datasets that encode information on the behaviour of multiple chromophores. When choosing wavelengths, it should however be noted that, since the PA signal is proportional to the fluence, which decays as a function of absorption (and scattering), choosing wavelengths where there is high optical absorption for typical background tissue constituents (namely blood and water) will exacerbate light attenuation and limit the depth of penetration of the light. The area where this absorption is weaker (i.e. where tissue is more 'transparent'), between 650 and 1100 nm, is commonly referred to as the NIR window and is typically explored to achieve depth-rich images.

Endogenous chromophore	Characteristic features
DNA and RNA	• Strong ultraviolet (UV) absorption; • OR-PAM can be used for imaging of individual cell nuclei [47]; • Clinical metrics of interest: cell nuclear density; • In PAT, contrast and related metrics may aid tumor demarcation
Hemoglobin	• Predominant optical absorption in the visible range; • $\lambda_p < 1000$ nm [4]; • More than ten-fold higher absorption than other chromophores; • Clearly distinct spectral signature between different variants - oxy-hemoglobin, deoxy-hemoglobin, methemoglobin; • Clinical metrics of interest: blood vessel diameter and shape, blood flow, oxygen saturation and concentration, metabolic rate of oxygen; • Its contrast in PAT and related metrics can be used to study the vasculature, for anatomical, physiology and pathology purposes (e.g. stroke, diabetes, atherosclerosis) [49]. • Its contrast in PAT and related metrics can be used in neurology since hemodynamic changes are closely related to neural activity (e.g. epilepsy, response to stimulation and resting state functional connectivity)
Water	• Strong absorption in the NIR; • $\lambda_p \sim 975$ nm [4]. • Its contrast in PAT can be used to study edema [46];
Lipid	• Strong absorption in the NIR ; • $\lambda_p > 1100$ nm, lipids dominate [4] $\lambda_{max} = 1210$ nm; • Its contrast in PAT can be important disease indicator e.g. atherosclerotic plaque, injury, carcinoma staging [45] . Considerable depths *in vivo* can be achieved in the NIR.
Melanin	• Broadband optical absorption (ultraviolet to the NIR) [5]; • Absorbs at any wavelength, but spatially localised and scarce; • When PAT highlights melanin structure together with vascular information, it can be a powerful tool to characterise melanoma, or interactions between other tumours and their microenvironment [5, 10, 44]. • Clinical metrics of interest: depth of melanoma, growth, metastatic rate;

Table 2.1: *The characteristic features of endogenous chromophores for use in photoacoustic imaging. λ_p refers to the wavelengths of prominent absorption peaks/ranges.*

Exogenous contrast agent	**Characteristic features**
Gold Nanoparticles e.g. nanostars, nanospheres, nanorods;	• av: High specific absorption within the optical window; • av: High thermoelastic efficiency; • av: Bioinertness; • av: Enhanced permeability and retention effect; • av: Bioconjugation and functionalisation capability; • av: Received FDA approval for various phase-I clinical trials as therapeutic agents or drug carriers [24]; • dv: Expensive; • dv: Thermoelastic behaviour complex to characterise and model [52]; • dv: Further long-term toxicity studies needed.
Single-walled carbon nanotubes	• av: Can exhibit multiple absorption peaks; • av: Optical properties can be tuned with changes in tube structure; • av: High photostability; • av: Provides a variety of routes for functionalisation; • dv: Usually with very broadband and low specific absorption coefficient; • dv: Photophysics is not well understood enough; • dv: Toxicity [24], but could be reduced with functionalisation; • Has been demonstrated as contrast agent for PAT [59].
Reporter gene products e.g. direct: eGFP, mCherry [60], phytochromes [61] substrates: LacZ [62], tyrosinase [55]	• av: Biological processes can be detected at the genetic level; • av: Some proteins can be made photoswitchable or photoactivable in response to certain processes [61]; • dv: Proteins may have low PA yield [54]; • dv: Proteins may have low transient and permanent photostability [54]; • dv: Fluorescent proteins geared for the NIR window are not that common; • Fluorescent proteins from reporter genes have been imaged *in vivo* by PAT [54].
Organic dyes e.g. indocyanine green, methylene blue [13], evans blue	• av: Clear easily from the body thanks to their small molecular size [5, 24]; • av: Some can penetrate the blood-brain barrier [5]; • dv: Have relatively small optical absorption cross-sections; • dv: Low photostability; • dv: Specific absorption spectra may depend on concentration and environment [56]; • Methylene blue has been used to identify sentinel lymph nodes [13]

Table 2.2: *The characteristic features of exogenous chromophores for use in photoacoustic imaging. Advantages ("av"), disadvantages("dv") and application are mentioned where appropriate.*

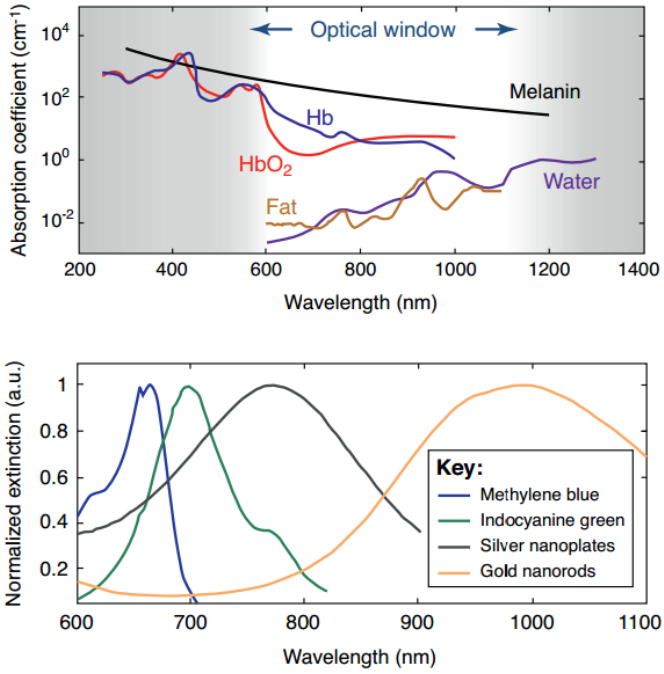

Figure 2.2: *Absorption spectra for a selection of endogenous (top) and exogenous absorbers (bottom). As can be seen, melanin provides a rather flat response. The region in which water and hemoglobin is low-absorbing is called the optical window. Differences in the spectrum of Hb and HbO_2, especially in the 600-1000 nm region, explain why their differentiation is possible. Exogenous absorbers can be manufactured to have well-defined and characterised peaks. Reprinted from [8], Copyright 2011, with permission from Elsevier.*

2.2.2 Tissue optical scattering

Despite the strong local absorption-based contrast, the PA signal is also sensitive to changes in optical scattering, through the fluence term. Tissue is known to be highly scattering (turbid), which promotes the diffuse propagation of light through the medium for broader spatial excitation but also adds intricacy to the contrast information.

Mie scattering occurs when light hits a particle whose refractive index differs from its background, causing refraction. Scattering also occurs when light propagates through a medium with continuous but varying refractive index [63]. The scattering coefficient μ_s describes the probability of light being scattered per unit length. The angle at which light will be diverted will depend on characteristics such as the size and shape of the particle. This scattering angular dependence is usually modelled through the scattering phase function, $\Theta(\hat{\mathbf{s}}, \hat{\mathbf{s}}')$, which describes the probability that a photon travelling in direction $\hat{\mathbf{s}}$ will be scattered into direction $\hat{\mathbf{s}}'$. A common phase function used for biological tissues is the Henyey-Greenstein phase function, where:

$$\Theta_{HG}(\hat{\mathbf{s}}, \hat{\mathbf{s}}') = \frac{1}{4\pi} \frac{1 - g^2}{(1 + g^2 - 2g(\hat{\mathbf{s}} \cdot \hat{\mathbf{s}}'))^{3/2}}, \tag{2.4}$$

where g is known as the anisotropy factor.

In cases where multiple scattering events occur, the anisotropy of scatter is usually considered a good simplified behaviour descriptor, defined as the mean cosine of the

scattering angle:

$$g = \int_{-1}^{1} (\hat{\mathbf{s}} \cdot \hat{\mathbf{s}}')\Theta(\hat{\mathbf{s}}, \hat{\mathbf{s}}')d(\hat{\mathbf{s}} \cdot \hat{\mathbf{s}}'). \tag{2.5}$$

Anisotropy is a property that defines the directional dependence of the scattering behaviour. g can take values between -1 and 1, where $g < 0$ means light is preferentially backward scattered, $g > 0$ means light is preferentially forward scattered and $g = 0$ means light has no preferential direction and scatters equally in all directions, i.e. is isotropic. The reduced scattering coefficient is defined by $\mu_s' = \mu_s(1 - g)$.

For biological tissues, characterisation of scattering properties is not trivial and will vary widely among tissues and even within different samples or areas of a same tissue. Reviews that summarise measurements of μ_s, g and/or μ_s' do exist in the literature [63, 64]. In terms of the anisotropy factor, in biological tissues light scatters preferentially in the forward direction, most often assuming values $g > 0.7$ [63]. Reduced scattering has been found to usually be well described by a function of the sort:

$$\mu_s' = a\left(\frac{\lambda}{500(nm)}\right)^{-b}, \tag{2.6}$$

where b is a fitted power law parameter known as the *scattering power* and a is a scaling term that corresponds to the reduced scattering at 500 nm, $\mu_s'(500nm) = a$. This behaviour follows the predicted behaviour for Mie scattering (scattering by spherical particles comparable to or larger in size than the wavelength of light). Some typical, averaged, values for a [mm^{-1}] are: 4.6 for skin, 2.42 for brain and 1.68 for breast. For the scattering power b, 1.421 for skin, 1.611 for brain and 1.055 for breast [63].

2.3 Light propagation in tissue

A model describing light propagation through biological media can be formulated in several ways. For instance, it can be defined through the movement of an electromagnetic wave in a medium - in which case it is described analytically through Maxwell's equations. These equations are however difficult to implement and solve and require knowledge of the refractive indices throughout the medium. Alternatively, light propagation can be thought in terms of a concentration of optical energy that propagates down a gradient according to a probability density function for scattering - this approach, known as transport theory, can also be derived from Maxwell's equations by ignoring coherent (phase) effects and is underpinned by Boltzmann's transport equation. Phenomena such as interference or diffraction are neglected. For the specific case of low-energy photons, the theory is further known as radiative transfer and described analytically by the radiative transfer equation (RTE). Solving the RTE analytically is only possible in simplified scenarios (e.g. homogeneous medium or non-scattering medium) with most cases usually involving the use of a numerical approach such as finite-elements, finite-differences or boundary-elements. In a third, purely numerical, way of formulating light transport, the

intensity distribution is built by thinking of the movement of packets of ballistic photons, where each individual photon packet follows a path defined by a random walk model - at each point its direction of travel will depend on the single-scattering event characteristics of the medium (Monte-Carlo simulations).

2.3.1 Transport theory

The RTE models light propagation by considering phase-less packets of optical energy, and is applicable to low energy, monochromatic photons. The main quantity of interest in transport theory is the light radiance $\phi(\mathbf{x}, \hat{\mathbf{s}}, t)$, representing the rate of energy flow per unit area per unit solid angle in direction $\hat{\mathbf{s}}$ at position $\mathbf{x}$ at time t. The following equation defines the RTE through the conservation of energy (neglecting e.g. inelastic scattering, fluorescence):

$$\frac{1}{c}\frac{\partial \phi}{\partial t}(\mathbf{x}, \hat{\mathbf{s}}, t) = q(\mathbf{x}, \hat{\mathbf{s}}, t) - \left[\hat{\mathbf{s}}.\nabla + \mu_a(\mathbf{x}) + \mu_s(\mathbf{x})\right]\phi(\mathbf{x}, \hat{\mathbf{s}}, t) + \mu_s \int \Theta(\hat{\mathbf{s}}, \hat{\mathbf{s}}')\phi(\mathbf{x}, \hat{\mathbf{s}}', t)d\hat{\mathbf{s}}', \quad (2.7)$$

where $q(\mathbf{x}, \hat{\mathbf{s}}, t)$ is the light source, c is the speed of light and $\Theta(\hat{\mathbf{s}}, \hat{\mathbf{s}}')$ the scattering phase function yielding the probability that a photon following direction $\hat{\mathbf{s}}$ will be scattered in direction $\hat{\mathbf{s}}'$. In PA, since the timescale for heat deposition is substantially smaller than that for acoustic propagation, we are interested in the time integral, $\int_0^\infty$ (2.7) dt:

$$0 = q(\mathbf{x}, \hat{\mathbf{s}}) - \left[\hat{\mathbf{s}}.\nabla + \mu_a(\mathbf{x}) + \mu_s(\mathbf{x})\right]\phi(\mathbf{x}, \hat{\mathbf{s}}) + \mu_s \int \Theta(\hat{\mathbf{s}}, \hat{\mathbf{s}}')\phi(\mathbf{x}, \hat{\mathbf{s}}')d\hat{\mathbf{s}}', \quad (2.8)$$

where ϕ is now re-defined as the time-integrated radiance and q the time-integrated source term. For most non-time-resolved biomedical optics applications, the fluence Φ will be the entity of interest to recover/model, defined as the integration of the time-integrated radiance over all angles, $\Phi(\mathbf{x}) = \int \phi(\mathbf{x}, \hat{\mathbf{s}})d\hat{\mathbf{s}}$.

Solving ϕ (and Φ) from Eq. (2.8) has no general analytical solution, making numerical implementations such as finite element modelling (FEM) necessary. Implementing RTE-FEM is however computationally challenging, especially in 3D. In certain specific cases, the RTE can be solved analytically - namely for cases where the medium is homogeneous or layered. The well known Beer-Lambert law is an example of an exact solution for simplified scenarios where there is absence of scattering ($\mu_s = 0$). The RTE simplifies to $0 = q(\mathbf{x}) - \left[\hat{\mathbf{s}}.\nabla + \mu_a(\mathbf{x})\right]\phi(\mathbf{x}, \hat{\mathbf{s}})$ and the radiance can now be represented as fluence since $\hat{\mathbf{s}'} = \hat{\mathbf{s}} = \mathbf{z}$, such that $\frac{\partial \Phi}{\partial z} = -\mu_a \Phi$ if the sources q are ignored. Considering a depth-dependent $\mu_a(z)$ and a surface incident fluence Φ_0, the solved equation yields the well known expression [65]:

$$\Phi(z) = \Phi_0 e^{-\int_0^z \mu_a(\xi)d\xi}. \quad (2.9)$$

2.3.2 Diffusion approximation

When the computational demand of RTE-FEM is deemed too high and the case of interest does not have an analytical solution, other more wide-ranging simplifications to the RTE

can be made. For instance, the angular dependence of the radiance can be represented as a sum of spherical harmonics truncated after n terms, known as the P^n-approximation. The level of truncation will dictate the level of simplification. For instance, when the directional dependence of the radiance is weak, truncating to the first term is sufficient (known as the P^1 approximation), giving:

$$\mu_a \mathbf{\Phi} + \nabla . \mathbf{F} = q_0 \tag{2.10}$$

$$\frac{\mathbf{F}}{D} + \nabla \mathbf{\Phi} = 3\mathbf{q}_1, \tag{2.11}$$

where $F(\mathbf{x}) = \int \phi(\mathbf{x}, \hat{\mathbf{s}}')\hat{\mathbf{s}}' d\hat{\mathbf{s}}'$ is the flux vector, $D = [3(\mu_a + \mu_s')]^{-1}$ is the optical diffusion coefficient, $\mu_s' = (1-g)\mu_s$ the reduced scattering coefficient, g the anisotropy factor, q_0 the isotropic source term and $\mathbf{q_1}$ a first order (and thus mildly) directional term.

The most well-known case is the diffusion approximation to light transport, which assumes that light is isotropic, i.e. has no preferential direction of travel, $\mathbf{q_1} = 0$. Relation $\frac{\mathbf{F}}{D} + \nabla \mathbf{\Phi} = 0$ yields, together with equation 2.10, the well-known diffusion theory expression [66–68]:

$$\mu_a \mathbf{\Phi} - \nabla . (D \nabla) \mathbf{\Phi} = q_0. \tag{2.12}$$

Diffusion theory is useful for many tissue-realistic scenarios, besides being simple and quick to implement, but caution must be taken before employing it. As defined above, diffusion assumes that there is no preferential direction of travel. This means that, for instance, it does not apply to photons that have just been delivered into a medium by a collimated beam, as these will have a clear direction of travel [67, 69]. Successive scatter interactions with the tissue medium of interest may however cause these photons to lose their directionality and become isotropic, and therefore respect the diffusion regime. As a general rule for the case of a collimated beam incident on a light-absorbing and light-scattering medium, diffusion theory is considered reasonably accurate after a distance $MFP' = \frac{1}{\mu_t'} = \frac{1}{\mu_a + \mu_s'}$ from the source, named the transport mean free path [67]. Caution should also be taken in places near strongly absorbing objects or boundaries with drastic changes in optical properties. Diffusion theory also assumes that the photons take part in a random walk, i.e. that they are able to go through various scattering events before undergoing absorption ($\mu_s' >> \mu_a$) since this will make the mean photon propagation dependent on μ_s' rather than on μ_s and g separately. As a rule of thumb, $\mu_s' > 10\,\mu_a$ is usually considered sufficient. For the one-dimensional case, the solution is given by the following:

$$\mathbf{\Phi}(z) \sim k \mathbf{\Phi_0} e^{-\mu_{\text{eff}} z} \; for \; z >> \frac{1}{\mu_t} \tag{2.13}$$

$$\mu_{\text{eff}} = \sqrt{3\mu_a(\mu_a + \mu_s(1-g))}, \tag{2.14}$$

where $\mu_t = \mu_a + \mu_s$ is the total attenuation coefficient, valid close to the source, μ_{eff} is the effective attenuation coefficient, valid once the light regime can be considered diffuse, and k is actually an additional empirical constant added due to the fact that the maximum fluence now occurs not at the surface but rather somewhat further due

to the contribution of backscatter. Further analytical solutions only exist for scenarios that do not involve inhomogenous parameter distributions or complex boundaries. For most practical scenarios, a numerical model will need to be employed - most commonly finite-elements (the Galerkin method).

The diffuse approximation can be solved numerically through a finite-element approach [66, 68], by expressing it in its weak formulation and by constructing the domain from piecewise linear basis functions $u_i(\mathbf{x})$ such that:

$$\Phi(\mathbf{x}) \approx \sum_i \Phi_i u_i(\mathbf{x}) \tag{2.15}$$

$$\mu_a(\mathbf{x}) \approx \mu_{a_i} u_i(\mathbf{x}) \tag{2.16}$$

$$\mu_s'(\mathbf{x}) \approx \mu_{s_i}' u_i(\mathbf{x}), \tag{2.17}$$

where Φ_i, μ_{a_i} and μ_{s_i}' are nodal coefficients and $i = 1, ..., Nh$ where Nh is the total number of nodes. It can be shown that the diffusion approximation (DA) equation can now be described in matrix form as:

$$A\Phi = q, \tag{2.18}$$

where $\mathbf{A}$ is the system matrix. For $j = 1, ..., Nh$ and $k = 1, ..., Nh$, its entries are defined as:

$$A_{jk} = \sum_i \mu_{a,i} \int_\Omega u_i u_j u_k d\Omega + \sum_i D_i \int_\Omega u_i \nabla u_j \cdot \nabla u_k d\Omega \tag{2.19}$$

and

$$q_j = \sum_i q_i \int_\Omega u_i u_j d\Omega. \tag{2.20}$$

Having assembled A and q, it is then straightforward to solve the DA using linear algebra techniques as:

$$\Phi = A^{-1} q. \tag{2.21}$$

If it becomes important to model the light propagation close to a collimated source, in the sub-diffusive regime, a higher-order (less truncated) approximation to the RTE known as the δ-Eddington (or P^3) approximation can be implemented, also through a FEM implementation. This will improve the accuracy of the fluence distribution in the superficial region [70].

2.3.3 Monte Carlo model of light transport

As an alternative to all the previous approaches, purely numerical methods can be employed to solve the full RTE, such as Monte Carlo [71] - these are still computationally costly but generally more feasible than RTE-FEM for complex, 3D scenarios. Monte Carlo refers to the set of computational methods that estimate a physical quantity through random sampling, i.e. stochastically. In the case of light transport, it simulates and tracks the trajectories of photon packets with a given initial assigned weight as each of them

undergoes a random walk due to successive single scattering events. These events are modelled in steps of varying lengths and varying directions, as sampled from assigned probability distributions. Each step will also usually be accompanied by a decrease in packet weight, in conformity with the probability of optical absorption. The cumulative distribution of all photon packet paths will give the absorbed energy/power density. Its accuracy can be as high as desired (influenced by the number of packets launched) and should converge to what could have been obtained from the RTE-derived radiance. Monte-Carlo is also quick to implement for a wide range of scenarios due to its flexibility. It is therefore viewed as the gold-standard method for light modelling, being often used to validate other more simplified, efficient methods, such as the DA. Despite the fact that its computational load and running time have often precluded its direct use for large-scale forward simulations, or for inverse problem formulations that involve several successive runs of the forward model, advances in computational speed and parallelisation have meant that Monte Carlo (MC) is starting to be explored more widely for biomedical optics applications beyond model validation [72–74].

2.4 Absorbed energy and thermalisation

The photon energy propagated into the domain will be absorbed by tissues and lead to subsequent heating. The rate of energy absorbed by tissue can be given by the absorbed power density $Q(\mathbf{x}, t) = \mu_a(\mathbf{x})\Psi(\mathbf{x})f(t)$ [W m^{-3}] where $\mu_a(\mathbf{x})$ is the optical absorption coefficient, $\Psi(\mathbf{x})$ is the irradiance (or fluence rate) [W m^{-2}] and $f(t)$ is the unitary area temporal profile of the incident laser pulse. This energy will then be either converted into further radiation (fluorescence, phosphorescence) through radiative decay, or converted into heat and cause a temperature rise, as a result of relaxation through vibrational/rotational collisions. PA depends on the latter. It can be considered that the rate at which heat is deposited onto the tissue (also known as the heating function) is given by $Q(\mathbf{x}, t) = \eta_{th}\mu_a(\mathbf{x})\Psi(\mathbf{x})f(t)$ [W m^{-3}], where η_{th} defines the thermalisation efficiency, i.e. the percentage of energy converted into heat. The usual entity of interest for photoacoustics is the total energy delivered during the excitation pulse, known as the absorbed energy density H:

$$H(\mathbf{x}) = \int Q(\mathbf{x}, t)dt = \mu_a(\mathbf{x})\Phi(\mathbf{x}), \tag{2.22}$$

where $\Phi(\mathbf{x})$ is the fluence, obtained by temporally integrating the irradiance and where thermalisation has been set to unity, $\eta_{th} = 1$ since it will be a true first-order approximation for many compounds of interest.

2.5 Acoustic propagation in tissue

The general photoacoustic wave equation describes the acoustic propagation in an elastic, homogeneous and non-absorbing medium as [29, 69]:

$$\nabla^2 p(\mathbf{x}, t) - \frac{1}{c_s^2}\frac{\partial^2}{\partial t^2} p(\mathbf{x}, t) = -\frac{\beta}{\kappa c_s^2}\frac{\partial^2 T(\mathbf{x}, t)}{\partial t^2}, \tag{2.23}$$

where $p(\mathbf{x}, t)$ represents the acoustic pressure at location $\mathbf{x}$ at a timepoint t, κ is the isothermal compressibility, β is the volume thermal expansivity and c_s is the speed of sound.

The heat equation can in turn be written as:

$$\frac{\partial T(\mathbf{x}, t)}{\partial t} - \nabla \cdot (D \nabla T) = \frac{Q(\mathbf{x}, t)}{\rho C_V}, \tag{2.24}$$

where C_V is the specific heat capacity at constant volume, ρ is the mass density and $T(\mathbf{x}, t)$ is the rise in temperature from the baseline.

2.5.1 Initial pressure rise - thermal and stress confinement

The typical timescale of the optical pulse τ, of absorption and of thermalisation is much shorter than the timescale of thermal diffusion τ_{th} - a condition known as thermal confinement. Furthermore, since τ is also much shorter than the time needed for the acoustic wave to travel across the heated region τ_{st}, any expansion (density change) of the absorber/source during the illumination period can be neglected - a condition known as stress confinement. These conditions ($\tau < \tau_{st} << \tau_{th}$) mean that the optical pulse can be treated as a delta function (impulse) and that the heating function can be described as:

$$Q(\mathbf{x}, t) = H(\mathbf{x})\delta(t). \tag{2.25}$$

Also, under the assumption of null thermal diffusion due to thermal confinement, the increase in temperature T can be related to the absorbed energy density H through the simplified heat equation where the thermal diffusion term ($\nabla \cdot (D \nabla T)$) is neglected:

$$\rho C_V \frac{\partial T(\mathbf{x}, t)}{\partial t} = Q(\mathbf{x}, t). \tag{2.26}$$

The instantaneous local temperature rise T′ therefore relates to the instantaneous absorbed energy density H through:

$$T' = \frac{H}{\rho C_V}. \tag{2.27}$$

The thermodynamic relation $\rho' = \rho\kappa p' - \beta\rho T'$ establishes the relation between small changes in density ρ', pressure p' and temperature T', assuming constant isothermal compressibility κ and volume thermal expansivity β. Since the isochoric condition is

respected ($\rho' = 0$), the instantaneous rise in pressure can be related to that of temperature through the following:

$$p' = \frac{\beta T'}{\kappa}. \tag{2.28}$$

Based on equations 2.28 and 2.27, this means that the increase in pressure p' due to laser absorption by tissue and subsequent heating, which we will more commonly refer to as the initial pressure p_0, can be given by:

$$p_0 = \frac{\beta H}{\rho C_V \kappa} = \Gamma H, \tag{2.29}$$

where $\Gamma = \frac{\beta}{\kappa \rho C_V} = \beta c_s^2 / C_p$ is the Grüneisen parameter, a dimensionless thermodynamic constant that reflects the efficiency of the conversion from heat to pressure and where κ respects the following relation:

$$\kappa = \frac{C_P}{\rho c_s^2 C_V}, \tag{2.30}$$

where C_p is specific heat capacity at constant pressure.

This rise in pressure p_0 will become an acoustic wave that will propagate through tissue due to its elastic nature.

2.5.2 Photoacoustic wave equation

Since thermal confinement is respected, we can use Eq. (2.26) and the relation Eq. (2.30) to re-write the wave equation for an elastic, homogeneous and non-absorbing medium (Eq. (2.23)) as [75]:

$$\left(\nabla^2 - \frac{1}{c_s^2}\frac{\partial^2}{\partial t^2}\right) p(\mathbf{x}, t) = -\frac{\beta}{C_p}\frac{\partial Q(\mathbf{x}, t)}{\partial t}. \tag{2.31}$$

With the heating function given by the impulsive response in Eq. (2.25) and assuming constant speed of sound c_s and free-space propagation (no boundaries), Eq. (2.31) can be solved by applying the Green's function approach, yielding the pressure at time t [75]:

$$p(\mathbf{x}, t) = \frac{\beta}{C_p} \int_V H(\mathbf{x}') \frac{\partial G}{\partial t}(\mathbf{x}, t; \mathbf{x}', t') d\mathbf{x}', \tag{2.32}$$

or, written as a function of initial pressure p_0 (Eq. (2.29)):

$$p(\mathbf{x}, t) = \frac{1}{c_s^2} \int_V p_0(\mathbf{x}') \frac{\partial G}{\partial t}(\mathbf{x}, t; \mathbf{x}', t') d\mathbf{x}', \tag{2.33}$$

where the Green's function is given by:

$$G(\mathbf{x}, t, \mathbf{x}', t') = \frac{\delta(|\mathbf{x} - \mathbf{x}'| - c_s |t - t'|)}{4\pi |\mathbf{x} - \mathbf{x}'|}. \tag{2.34}$$

In the previous case the acoustic propagation problem was solved with heating being considered as a source term in the differential equation. Since we are in the presence of instantaneous heating, where the pulse can be considered as a delta function, a more

convenient way to solve the problem is to recast it as an initial value problem with no explicit source term, and where the initial, instantaneous, pressure is given by p_0. The initial value problem then involves solving a homogeneous differential equation with two initial conditions:

$$\left(\frac{\partial^2}{\partial t^2} - c_s^2 \nabla^2\right) p(\mathbf{x}, t) = 0, \tag{2.35}$$

with $p(\mathbf{x}, t)|_{t=0} = p_0$ and $\frac{\partial p}{\partial t}|_{t=0} = 0$.

2.5.3 Numerical models of acoustic propagation

Most commonly, solving partial differential equations is done through finite-difference, finite-element or boundary-element approaches. This can however be slow and computationally intensive for large domains with broadband, high frequency waves. Reasonable stability and accuracy requires small time-steps and sufficient (at least ten) grid points per acoustic wavelength. Pseudo-spectral methods can reduce the computational load in the calculation of the spatial gradients by fitting a Fourier series to all the data (i.e. fitting globally). Improvements come from the fact that only two grid points are needed per wavelength (three- to five-fold less than other numerical methods) and from the efficiency of the FFT [76]. The toolbox k-Wave adopts such a strategy. It also formulates the problem through a system of coupled first-order equations of motion and continuity, and an equation of state rather than through a single second-order photoacoustic equation, as this facilitates the eventual inclusion of acoustic attenuation, non-linear phenomena and a perfectly-matched-layer at the domain boundaries:

$$\frac{\partial \mathbf{u}}{\partial t} = -\frac{1}{\rho_0} \nabla p \tag{2.36}$$

$$\frac{\partial \rho}{\partial t} = -\rho_0 \nabla \cdot \mathbf{u} \tag{2.37}$$

$$p = c_s^2 \rho, \tag{2.38}$$

with initial conditions:

$$\begin{aligned} p|_{t=0} &= p_0 = \Gamma \mu_a \Phi \\ \mathbf{u}|_{t=0} &= 0, \end{aligned} \tag{2.39}$$

where ρ is the acoustic density, ρ_0 the ambient density and $\mathbf{u}$ is the particle velocity.

2.6 Imaging systems (acoustic detection)

Once the pressure waves propagate through the medium, they can be detected at its surface with an appropriate detector or array of detectors. For imaging, different modalities of acquisition are available. The modality and the transducer characteristics and configurations of the arrays used will dictate the quality, resolution, field-of-view and depth of penetration achievable.

2.6.1 PA modalities

PA imaging modalities can be divided into two main variants. These are photoacoustic microscopy (PAM) and PAT [4, 5]. The differences are mainly related with the system implementation, instrumentation and acquisition routines.

PAT is the least restrictive and most flexible approach since its practical implementation poses less limitations on imaging performance. Full field illumination is used to illuminate a sample. At typical NIR wavelengths in a typical tissue, light will be able achieve large penetration depths and will be scattered through the turbid medium, leading to a large volume of the sample being exposed to the diffuse light. Depths considerably larger than the transport mean free path can be probed. Arrays of transducers or a mechanically scanned transducer at the surface are then used to detect the broadband acoustic waves generated by the photoacoustic events. These time-resolved signals can be spatially resolved with knowledge of the speed of sound, and appropriate acoustic reconstruction algorithms can then be used to reconstruct the 3D PA image.

PAM is used to allude to the approaches that involve mechanical scanning of either a focussed laser source (OR-PAM) or a focussed ultrasound detector (AR-PAM). Unlike PAT, where the point-by-point distribution of initial pressure has to be obtained through reconstruction methods, in PAM the location is usually directly and inherently given by the focussing. In acoustic resolution PAM (AR-PAM), the acoustic propagation and detection dictates the lateral and axial resolution constraints. In optical resolution PAM (OR-PAM), the lateral resolution is dictated by the tightness of the laser beam focus, which itself depends on the wavelength and the numerical aperture of the optical focusing lens [5]. Some PAM studies will be mentioned, but quantification in PAT will be the main emphasis in this work.

2.6.2 Detection geometries in PAT

The detection geometry can vary, though it will most commonly follow a planar, cylindrical or spherical configuration [4]. Various instrumentation implementations exist for each [77]. Acoustic reconstruction will always be necessary but the preferred methods will vary with the chosen geometry. Adopting a cylindrical or spherical configuration will allow collecting the acoustic wavefront in its entirety (or almost), but getting access to all these locations around the sample may not always be feasible - they are in many cases limited to applications such as the breast (semi-spherical configuration) or for small-animal imaging. Planar detection geometries will be easier to adopt in terms of the feasibility of surface access to most anatomical structures of interest but will lack wavefront information.

2.6.3 Transducer characteristics

There is a range of transducer characteristics to be mindful of. One important specification is the frequency response of the transducer - both its centre frequency and its frequency bandwidth. PA signals extend from low to several tens of MHz in frequency [4], so broadband transducers are desired. Another important characteristic is the minimum achievable element size - small element sizes help achieve a near-omnidirectional response, i.e. similar sensitivity to wavefronts travelling at any angle relative to the detector. Another crucial characteristic is the sensitivity of the transducer, usually presented through the peak noise-equivalent pressure (NEP) parameter, which is defined as the minimum resolvable peak pressure when in the presence of noise. This parameter will vary with frequency and detection angle.

Broadband piezoelectric acoustic receivers are very popular. They can be made to have very good sensitivity, even at high central-frequencies (tens of MHz). Sensor arrays with piezoelectric elements can be built in a variety of arrangements (single element, linear, spherical) which accelerates acquisition, with mechanical scanning also available as an option to complement coverage where necessary. As main disadvantages, it is very challenging to achieve small enough detector element sizes (in the tens of μm is desired) in fabrication whilst keeping sufficient levels of sensitivity [4]. Also, despite the high central-frequencies, they do not have a large bandwidth, leading to bandlimiting of the signals. Detection based on Fabry-Pérot sensors on the other hand, which rely on light interferometry for pressure transduction (further discussed and explained in Section 6.6.2), have high sensitivities that, as a rough approximation, do not depend on the element size. The size of the element itself is dictated by the size of the used laser beam spot size and can therefore be made quite small (in the order of tens of μm), achieving near omni-directionality and fine spatial sampling at high sensitivity. The frequency response also extends from near-DC to tens of MHz [78], outperforming piezoelectric elements. In terms of detection geometry, because of the constraints of the fabrication process, these sensors are usually restricted to a planar sensor geometry. Also, since the technique relies on raster scanning of the interrogation beam point-by-point on the sensor surface, frame rate is mainly limited by the pulse repetition frequency of the PA excitation laser.

Chapter 3

Photoacoustic image reconstruction and quantification (inverse problem)

Whilst the photoacoustic forward problem takes us from the tissue optical property mappings to the measured PA pressure time series, the full PA inverse problem can be described as mapping the PA time series back into the domain to eventually regenerate distributions of the optical tissue properties that were in the origin of the signal (Fig. 3.1).

Generally speaking, the photoacoustic inverse problem can be decoupled into 3 main inverse problems: the acoustic inverse problem, where the initial acoustic pressure $p_0(\mathbf{x})$ should be estimated from the measured PA data; the thermoelastic coupling problem, where the absorbed energy distribution $H(\mathbf{x})$ should be retrieved from $p_0(\mathbf{x})$ and finally the optical inverse problem, where the main quantity of interest - usually $\mu_a(\mathbf{x})$, should be retrieved from $H(\mathbf{x})$.

For the multiwavelength case, one further step can be considered. Absorption is typically given by $\mu_a(\lambda) = \sum_C \alpha_i(\lambda) c_i$ ($\boldsymbol{\mu_a} = [\boldsymbol{\alpha}]\,\mathbf{C}$ in matrix form), based on the Beer-Lambert formulation for multiple chromophores. If multiwavelength absorption coefficient distributions $\mu_a(\mathbf{x}, \lambda)$ were readily available from PA data, this information together with the specific absorption spectra $\alpha_i(\lambda)$ of the chromophores of interest would also allow extracting maps of chromophore concentration c_i straightforwardly (assuming sufficient wavelengths were used) through the simple linear inversion procedure:

$$\mathbf{C} = \left[\boldsymbol{\alpha}^T \boldsymbol{\alpha}\right]^{-1} \boldsymbol{\alpha}^T \boldsymbol{\mu_a}. \tag{3.1}$$

The first stage of the PA inverse problem, the acoustic inversion, is necessary in any PAT study to spatially resolve the PA time-series information and reconstruct an accurate volumetric representation of the initial pressure distribution (commonly referred to as PA image). Section 3.1 will describe the acoustic inverse problem, including some of the algorithms available and outstanding challenges for accurate initial pressure distribution estimation. Solving the PA inverse problem further, to obtain accurate identification,

differentiation and/or quantification of optical properties, chromophore distributions or related quantities is commonly referred to as the Quantitative PAT problem and is of great interest for pre-clinical and clinical applications. Section 3.2 will describe qPAT and especially the optical inverse problem. The challenges towards achieving quantification from photoacoustic data will also be emphasised.

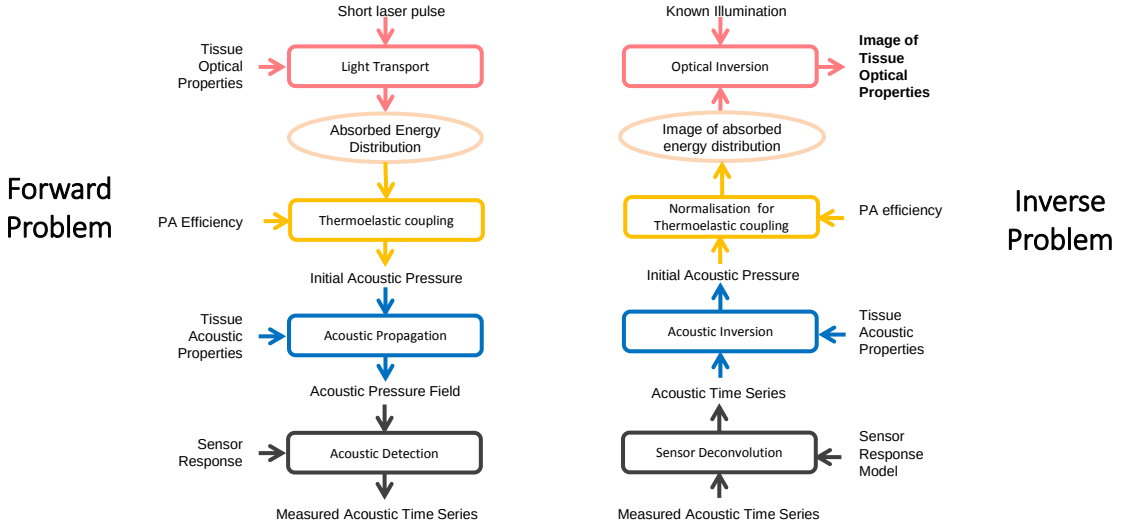

Figure 3.1: *Schematic diagram of photoacoustic forward and inverse problems. By solving the stages of the forward model in inverse order, it should be possible to retrieve information on the optical properties of tissues, and possibly use this information to differentiate them or characterise their composition.*

3.1 Acoustic inversion

Acoustic inversion, also known as reconstruction, is necessary in PAT type methodologies [4, 79]. It is an inverse initial value problem that aims to recover the initial pressure distribution, $p_0(\mathbf{x})$ from a set of detected temporal signals $p_0(\mathbf{x}', t)$. This can be done through a variety of acoustic reconstruction algorithms. In a primary instance the algorithm can be chosen based on whether, under ideal conditions and with sufficient data (i.e. all algorithm assumptions met), it can yield an exact reconstruction for the desired geometry. In practice, the choice of preference will depend heavily on the application of interest, where different assumptions will be met. The choice of algorithm may depend on how accuracy is affected when considering non-ideal acquisition geometries, how it deals with relevant acoustic properties (presence of acoustic attenuation or of inhomogeneities in speed of sound, unknown speed of sound, reflections induced by impedance mismatch) or how it deals with some typical PA data limitations - noise, directionality, bandwidth of the sensors or limited-view detection. Some decisions in favour of computational speed and load may also involve sacrificing some degree of accuracy (e.g. employing stacked 2D reconstructions vs a full 3D reconstruction, or employing some efficient methods that hinder accounting for speed of sound variation and modifications in geometry). For qPAT, it is particularly crucial to obtain an estimate of $p_0(x)$ with minimal noise and artefacts and

with quantitatively accurate pressure values.

3.1.1 Image reconstruction algorithms

Ad-hoc back-projection is one of the most used reconstruction methods, whereby each PA waveform is backprojected into the plane as a spherical wave, based on knowledge that the pressure measured at a given detector position at time t will have originated from sources over a $x = c_s\, t$ radius from the detection point (c_s is the speed of sound). Summation of all the spherical waves yields a reconstructed version of the pressure field. Simple back-projection is however not ideal from the point of view of accuracy and computational load and requires a homogeneous medium [4].

Filtered (or modified) back-projection is an improvement to conventional back-projection which applies a filtering stage preceding or following the back-projection step [80, 81]. Many of these strategies exist, and they can be exact for a certain set of geometries - planar [80], cylindrical [80], spherical [80, 82, 83] - when given full-view and noise-free data that have propagated though a non-attenuating, homogeneous acoustic medium.

A more efficient and less computationally-intensive alternative to the previous time-domain reconstructions involves employing series-summation-based methods. These approximate time-domain algorithms, based on mathematical methods from ultrasonic reflectivity imaging, employ temporal and spatial spectral decomposition of PA signals followed by spatial frequency component mapping to retrieve $p_0(\mathbf{x})$ [84]. Exact reconstruction formulations have been derived for a specific set of pre-determined geometries, for instance planar [85, 86], cylindrical [87], spherical [88, 89] and cubical [90]. The planar case can be run especially fast, as FFTs can be used for implementation [85].

All the methods above still pose stringent conditions on the geometry and distribution of the detection and on the characteristics of the medium (acoustically non-attenuating and homogeneous). Time-reversal methods have been recognised as one of the most flexible, least restrictive approaches [4, 33]. They are very general and rely on few assumptions, being able to deal with any closed geometry and with acoustic heterogeneities and attenuation (so long as these do not prevent the data from reaching the detectors). The working principle involves re-propagating the detected waveform from each detector into the domain in reverse order. This is implemented by backwards-running a numerical acoustic forward propagation model [76, 91, 92]. The full computation time of these is considerable, especially if using time-domain finite-difference techniques. An efficient pseudo-spectral k-space propagation model has been suggested to accelerate the approach [76, 93]. GPU implementations currently in development can also accelerate the computations considerably.

Finally, model based inversion strategies are becoming increasingly popular and are the least restrictive. They rely on a suitable numerical forward model estimating PA sig-

nals from an initial p_0 formulation [4], where the solution of the inverse problem is found by minimising the difference between estimated and measured PA signals throughout several iterations. These strategies are very versatile, general and well-suited to deal with noise, artefacts and other data limitations. They can include prior knowledge and other regularisers, deal with acoustic heterogeneities and attenuation and even invert for some of these parameters if necessary. Though they are as a general rule more computationally intensive than most other approaches, gradient-based minimisation schemes and efficient computation of functional gradients with the adjoint operator have increased considerably their efficiency [94, 95]. Some examples of model-based inversion strategies and implementations can be found in refs. [94–97].

3.1.2 Challenges in acoustic reconstruction

Despite the variety and quality of acoustic reconstruction algorithms, there are still issues that can affect the retrieval of a faithful image of the initial pressure distribution p_0.

Effect of uncertainty on inputs An acoustic reconstruction will need as input not only the PA data but also information on material properties of the acoustic field and characteristics of the detection geometry. In a real-life experiment, there will be uncertainty on these. Namely, speed of sound will generally not be fully known despite being an essential input in any acoustic reconstruction. In some cases acoustic attenuation or acoustic impedance (the product of speed of sound and tissue density) mismatch will also need to be known to explain, respectively, decays in amplitude and reflection phenomena. There is a rich body of literature on acoustic properties of tissues [98] and this information will many times suffice for a reasonable reconstruction. Alternatively, complementary experimental techniques such as ultrasound computed tomography or even x-ray images in Hounsfield units may help inform maps of speed of sound distribution for the object of interest. Estimation could also be done in post-processing, for instance by choosing the speed of sound that promotes image sharpening [99] or by incorporating speed of sound as an additional unknown in the inversion [100]. Uncertainty in inputs related to the detection geometry may also affect inversion - namely sensor positioning and system calibration.

Effect of incomplete visibility Non-iterative algorithms that are exact in the limit of complete and noise-free data will expect PA data as input where there is full-view of the acoustic field - i.e. where it has been possible to collect full wavefront information. For a spherical detection geometry, this means the surface should be closed (4π steradian view), whilst for cylindrical and planar geometries it means that the surface should have infinite length. In practice though, this will rarely be possible - the measurement surface will usually be finite or open to some extent, hindering the collection of the full wavefront

information. This may arise due to constraints of the system design, characteristics of the sample (many areas of interest only accommodate partial access and view) or a compromise in favour of other characteristics (e.g. Fabry-Perot sensors are chosen because they excel in bandwidth, sensitivity and directionality but are typically only available as a planar array due to ease of manufacture and interrogation). The discrete sampling by a finite number of detectors as opposed to a fully continuous mapping by infinite point detectors over the detection surface will also affect the mapped field. This incomplete data issue is commonly referred to as the limited-view or limited-aperture problem. Unless otherwise enforced, non-iterative reconstruction algorithms will by default assume that unmeasured data equates to zero-valued datapoints. The practical implications of this issue are that the reconstructed image will lack information and suffer from artefacts, distortion, blurring and an overall inaccurate pressure amplitude estimation. To better understand this issue, it may be useful to define the *visible region* of a given detector geometry.

The *visible/detection region* is the region where all location points have sufficient detection views, i.e objects that fall inside this region will not suffer from the limited-view problem when reconstructed with an appropriate iterative algorithm. Objects falling outside the detection region will suffer from limited-view, with some boundaries being correctly recovered (those whose normal passes through a detector position) whilst other boundaries will inevitably blur away. In 2D, the region can be found through the following rule: the fully visible domain is formed by all lines connecting detection points. Fig. 3.2 provides an illustrative example of the limited view problem and of the *visible region*.

Planar detectors have no way of having objects immersed in a *detection region*. General strategies to cope with this include weighting time-series based on their view-angle, interpolating data onto virtual surfaces based on measured data, employing acoustic reflectors that back-propagate the data onto a detection region [101] or regularisation [102]. A more straightforward approach would be to combine measurements of multiple planes, for instance by including a second orthogonal detection plane - forming a V-shaped scanner. Fig. 3.3 exemplifies these scenarios.

Effect of transducer response Due to typical transducer characteristics (Section 2.6.3), acquired PA time-series will never perfectly capture the PA pressure wave behaviour. On one hand, data will only be acquired over a certain finite range of frequencies due to detector bandwidth. Also, due to sensor directionality, there will be a weighted sensitivity to waves travelling at different angles relative to the active element plane. There will also be noise incorporated and signal contributions that fall below the noise-equivalent pressure (NEP), therefore going undetected. All these sensor limitations will have an effect on the reconstructed p_0 distribution.

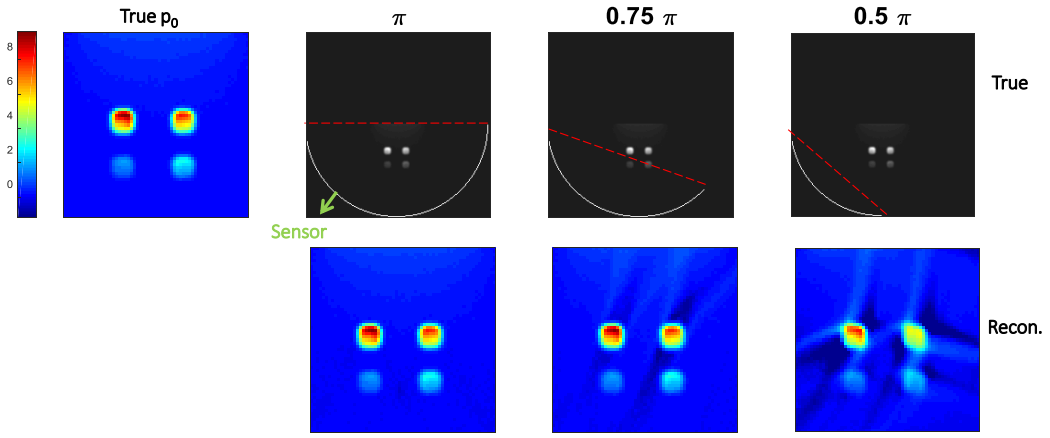

Figure 3.2: *Outcomes of applying acoustic reconstruction to data acquired with various apertures in a partial circular arrangement. The acquisition geometry is shown by the gray lines in the top row figures. The red dashed line indicates the top edge of the visible region. All initial pressure distribution images are colour-coded for the same range.*

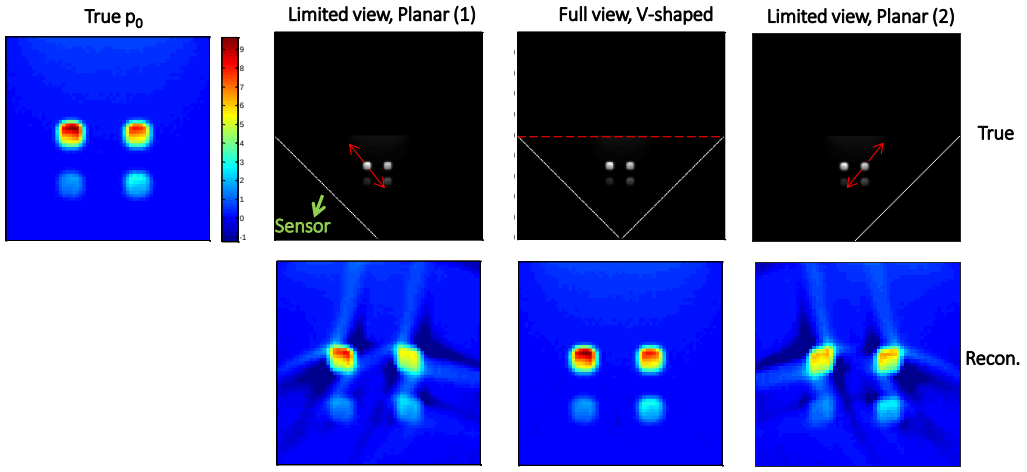

Figure 3.3: *Outcomes of applying acoustic reconstruction to data acquired with a single planar detection on either side or with an orthogonal (V-shaped) arrangement. The acquisition geometry is shown by the gray lines in the top row figures. The red dashed line indicates the top edge of the visibility region. The red arrows indicate how waves generated from feature edges orthogonal to the detector, and therefore travelling parallel to the sensor, will never be detected regardless of the spatial location of the feature. All initial pressure distribution images are colour-coded for the same range.*

3.2 The quantification problem (optical inversion)

After solving the acoustic part of the problem to obtain a PA image of initial pressure distribution, an optical inversion scheme can be employed to retrieve further encoded information. In its simplest formulation, the aim of quantitative photoacoustic tomography (qPAT) could be to simply detect the presence of a given chromophore [103]. Even this is challenging, due to the potentially low concentrations involved or due to confounding factors such as cross-talk from other chromophores or contribution of the fluence term. At a somewhat higher complexity, the ability to extract and uncouple contributions of an exogenous contrast agent from endogenous tissue contrast could be pursued to obtain meaningful spatial or temporal mappings of distribution, indicating regions or intervals of increased uptake (in the case of a targeted contrast agent) or upregulation (in the case of genetic reporters). The ultimate and most challenging aim of qPAT is to obtain high-resolution, three-dimensional imaging and absolute estimates of individual chromophore concentrations or related metrics such as oxygen saturation.

In summary, the following quantities are of interest in the Quantitative PAT problem:

- chromophore concentrations (e.g. endogenous and exogenous chromophore distributions) [104];
- ratios of chromophore concentrations (e.g. oxygen saturation) [104];
- optical parameters (e.g. scattering coefficient, anisotropy factor) [105, 106];
- chromophore based segmented regions (e.g. delimiting vasculature, atherosclerotic plaque, melanoma) [107];
- relative spatial variation of chromophore concentration (e.g. upregulation of gene reporters, differential uptake or affinity to a contrast agent) [108];
- relative temporal variation of chromophore concentration (e.g. hemodynamic or other biomarker changes in response to a stimulus, growth, disease development or treatment) [108].

Ideally, the estimations will preserve the inherently high-resolution and three-dimensional characteristics of PAI.

Solving the optical inverse problem is far from trivial. Section 3.2.1 will explain the inherent challenges. Section 3.2.2 will then give a quick overview of the types of algorithms proposed to tackle these (these will be explained in more depth in Chapter 4). Finally, Section 3.2.3 will explain why, despite advances in tackling the optical inverse problem and accurate results in simulation, there is still a lag in the experimental implementation and clinical translation of qPAT approaches.

3.2.1 Inherent challenges

Although the PA image is representative of the optical absorption in the tissue, it does not provide a direct proportionality to the optical absorption coefficient but rather to the optically absorbed energy density H (Eq. (2.2)). In turn, H is given by the product of the local optical absorption and the fluence. We will now explain the series of intertwined and equally crucial inherent challenges that arise from this.

Non-linearity Extracting μ_a from H is an intrinsically non-linear problem, since H is given by the product of the local optical absorption and the fluence, which itself is a function of the optical absorption throughout the domain, $H = \mu_a \Phi(\mu_a)$. Solving this non-linear problem for μ_a is non-trivial and the majority of relevant cases do not have a closed-form analytical solution.

Spectral colouring and spatial distortion Re-writing the expression for the initial pressure distribution for the multiwavelength case, i.e. considering that both optical absorption μ_a and scattering properties g and μ_s will have a wavelength dependence λ and spatial dependence $\mathbf{x}$:

$$p_0(\mathbf{x}, \lambda) = \Gamma(\mathbf{x})\, \mu_a(\mathbf{x}, \lambda)\, \Phi(\mathbf{x}, \lambda; \mu_a(\mathbf{x}, \lambda), \mu_s(\mathbf{x}, \lambda), g(\mathbf{x}, \lambda)). \tag{3.2}$$

The fluence at any given point $\mathbf{x_0}$ in the domain is a function of the optical absorption and scattering properties of tissue along the set of convoluted paths the light has taken to reach that point. This means that the spectral signature of $p_0(\mathbf{x_0}, \lambda)$ is not just given by the spectral absorption behaviour at that point, $\mu_a(\mathbf{x_0}, \lambda)$, but is weighted intricately by the spectral characteristics of structures along the light path. This phenomenon is known as spectroscopic cross-talk or spectral colouring. Linear unmixing strategies cannot therefore be applied straightforwardly to decompose/decouple individual chromophore contributions from $p_0(\mathbf{x}, \lambda)$. Also, since the fluence also has a spatial dependence $\mathbf{x}$, spatial distortion will also occur.

Scattering ill-posedness Another common complicating factor in the inversion relates to the fact that the fluence does not solely depend on μ_a but also on μ_s' (or μ_s and g). Both entities are usually unknown from the start and should therefore be estimated simultaneously. However, estimating both parameters poses additional complications related to an increase in the ill-posedness of the problem.

The first issue is non-uniqueness. For the single-wavelength scenario, it is possible that different combinations of optical absorption and scattering distributions yield the same absorbed energy, making the problem non-unique unless additional information is incorporated. The most common approach in the mathematical literature is to obtain data from

more than one source position [109], $H_1 = \mu_a \Phi_1(\mu_a, \mu_s)$ and $H_2 = \mu_a \Phi_2(\mu_a, \mu_s)$ or alternatively to obtain data from multiple wavelengths, assuming the spectral characteristics of both absorption and scattering are known [38].

Even if the problem is defined to have a unique solution, it can still be ill-posed due to the diffusive nature of light transport. Thinking about the absorbed energy at a given position, it will only have a weak and spatially-integrated dependence on optical scattering (through the fluence term), contrary to the strong and primarily local dependence on optical absorption. Due to this low sensitivity of H to changes in scattering, inverting for scattering can be especially problematic, particularly at increasing distances from the source. The ill-posedness can be reduced by including a greater number of sources - ideally spaced at different locations along the boundaries - or by incorporating further *a priori* knowledge related to spatial characteristics (e.g. piece-wise constancy, smoothness, segmented regions). A combination of multi-source, multi-wavelength and spatial information can yield promising outcomes, but the added practical requirements of acquisition time, complexity and access to prior information should be considered carefully.

3.2.2 QPAT strategies

A series of strategies have been developed over the years to tackle the quantitative problem, with a focus on the inherent challenges mentioned above. Typically, these studies assumed that the acoustic inversion and thermoelastic normalisation steps were relatively straightforward to tackle compared to the optical inversion. As such, many qPAT studies actually chose to address the optical inversion as the sole outstanding challenge, by assuming as a starting-point a perfect representation of p_0 and known Grüneisen parameter behaviour.

Linear spectroscopic unmixing is the simplest and fastest strategy but it disregards the fluence contribution and therefore its validity is limited. A way of solving the problem would be to have access to an independent estimate of the fluence. Incorporating diffuse optical tomography (DOT) or acousto-optic tomography (AO) information has been suggested. However, these strategies provide coarser resolution, and applying hybrid techniques entails increases in system and acquisition complexity and cost. Contrast agents and discrete internal fluence measurements are also possible but not desirable due to their invasiveness and sparseness of information. Other types of linear unmixing have been proposed that rely on certain heuristics to decompose the data in ways that may better cope with the fluence than those that rely simply on chromophore absorption spectra. Ultimately, the best ways to tackle the problem have been those that fully acknowledge the non-linear nature of the problem and the effect of the fluence in the inversion itself. In some cases, this inversion can be done analytically. In most cases, an iterative method will be needed that relies on repeated computations involving the forward model. The most common frameworks used are based on model based minimisation, where the true

solution is found by iteratively minimising the difference between the measured data and the modelled data. These strategies have been shown to be able to deal with the various inherent problems - non-linearity, spectral colouring, spatial distortion and, given appropriate data, even absorption-scattering non-uniqueness. All these strategies will be addressed in more detail in Chapter 4.

3.2.3 Further challenges in qPAT

Despite the growth in algorithms available that can deal with the inherent, cornerstone, challenges of the qPAT problem, these have not yet been been adopted in regular pre-clinical or clinical studies. Even simpler and more controlled experimental studies, such as those relying on *in vitro* samples or tissue-mimicking phantoms, have only been done for a small number of cases. The following paragraphs outline the other types of challenges for qPAT that may need to be addressed for experimental implementation to be successful and that partially explain the lag in and limited success of experimental translation. Of these, dealing with thermoelastic efficiency, obtaining faithful initial pressure maps and devising optimal validation paradigms and phantoms are arguably the most limiting facets.

Optical model mismatch Besides the inherent challenges affecting the optical inversion stage, mismatch between the true physical behaviour of light in the medium and the model used to describe it can also be a practical concern. Namely, the chosen model of light transport may make assumptions not met by the case under study (Section 2.3), which will directly affect accuracy. It has further been shown that an inadequate fluence model can affect the posedness of the problem (e.g. seen when DA was used for inverse computations for a sample in non-diffusive transport regime [40]). Also, it is usually assumed that there is no uncertainty in the inputs of the model when in practice that is never the case. There may be uncertainty on the specific absorption spectra of the chromophores, the profile and positioning of the light source or on any other optical properties that are set *a priori* - e.g. reduced scattering, anisotropy factor. Further assumptions on the *nature* of the behaviour of certain optical and setup properties used as inputs or outputs can also affect the agreement (e.g. assuming homogeneity, dynamic behaviour, piecewise-constancy of parameters such as μ_a, μ_s', g) [110, 111].

Dealing with thermoelastic efficiency and overall calibration An important step of the qPAT problem, often disregarded, is dealing with the thermoelastic efficiency. If its characteristics were fully known, dealing with it would be straightforward to achieve through a simple point-wise division:

$$H(\mathbf{x}) = \frac{p_0(\mathbf{x})}{\Gamma(\mathbf{x})}. \tag{3.3}$$

Often, in simulation studies, the Grüneisen parameter is set as constant and unitary, as it is not considered the main focus. Nevertheless, in practice having access to $\Gamma(\mathbf{x})$ is non-trivial, and the values it can take will vary considerably among tissues and even within similar tissues with different relative levels of constituents. Only some literature values are available but these are enough to show that we will typically be dealing with large intra-tissue, inter-tissue, inter-subject and temperature-pegged variations (e.g. blood can take values between 0.15-0.23 whilst fat varies between 0.7-0.9) [112, 113]. Some strategies have considered incorporating Γ fully as an additional unknown in the inversion - either as an independent unknown [114] or as a function of other unknowns based on empirical formulae [36]. Others have suggested re-formulations of the problem in which Γ cancels out [109, 111].

Additionally, though it is often assumed in theoretical qPAT studies that the obtained absorbed energy data are in absolute physical units, it will most commonly be scaled by at best a scalar factor due to the mechano-electrical transduction mechanism of the detectors. This can eventually be dealt with either by calibrating the sensor response with a calibrated transducer, by applying a normalisation to both modelled and experimental data [37] or by re-formulating the problem in such a way that it depends only on ratios of measurements [109].

Quality of the initial pressure estimation In typical qPAT studies, it is commonly assumed that a perfect representation of the initial pressure distribution p_0 can be straightforwardly obtained. This relies on assumptions that the measured acoustic field $p(t)$ is complete (omni-directional, broadband and full-aperture) and noise-free, that the model chosen accurately captures the physics of the problem and encapsulates correctly the nature of the behaviour of relevant acoustic properties, that the inputs themselves given are accurate (whether acoustic properties of the domain or sensor characteristics) and that, all other assumptions met, the algorithm will provide an exact reconstruction. This will in reality not be the case, as was discussed in Section 3.1.1 and 3.1.2.

Dimensionality The ability of PAT to provide highly-resolved (tens of micron) volumetric images of considerable-sized regions (tens of mm) - yielding a large ratio of image size to resolution -, coupled to the possibility of acquiring data at various wavelengths, create data of high dimensionality that can become a challenge during processing and modelling. If we consider a reasonable 10×10×10 mm^3 reconstructed domain at 100 μm resolution, acquired at 2 wavelengths, this yields a total of $2{\times}10^6$ data voxels. Supposing also that we want to estimate the distribution of two chromophores without compromising spatial specifications, this leads to $2{\times}10^6$ unknowns. Any n-fold increase in wavelengths will increase the available data voxels by n-fold, whilst an n-fold increase in domain size or n-fold improvement in resolution in all 3 directions will increase the data voxels by n^3-fold. For purposes of data modelling and especially inversion procedures, this can

quickly become unmanageable and impractical. Algorithms are therefore required to be more efficient and less computationally-intensive. The level to which this is necessary will also depend on whether the qPAT processing can be done offline or is needed in real-time.

Simple unmixing schemes or pre-learned machine-learning frameworks might be more likely to comply with the speed requirements, though a large range of factors needs to be considered in terms of accuracy, robustness and range of validity. Model-based inversion strategies are worth prioritising as they will provide the most accurate outcomes in theory, though they have traditionally posed challenges in terms of speed and computing resources. Model-based inversion strategies are usually solved in an iterative manner, meaning that several runs of the forward model are necessary, becoming time-consuming. In their most classic formulation, informing direction of descent at each iteration will also involve computing, storing, inverting and applying a matrix of second derivatives - the Hessian - which has dimensions of N^2, where N is the number of unknowns, which may further increase time-consumption or not be feasible at all memory-wise. Nevertheless, continuing improvements in computing memory, processing power and the appearance of efficient minimisation strategies that can circumvent Hessian matrix calculations and parallelise relevant computations are being made and are the subject of ongoing study.

Validation All proposed qPAT strategies need testing and validation in terms of accuracy, robustness and range of validity. Successful translation to pre-clinical and clinical scenarios depends on how proposed algorithms deal with all stages of the PA inverse problem (optical propagation, thermalisation, acoustic propagation) and also how they cope with practical challenges related to instrumentation and acquisition and characteristics of the sample or subject.

Theoretical formulations and related simulations focus primarily on solving the inherent problems of the optical inverse problem. They attempt to solve the algorithm under assumed near-perfect experimental conditions. Sensitivity studies in simulation give initial insights, for instance by assessing how disturbing one parameter or characteristic in isolation affects outcomes. Ideally though, validation should be done *in vivo*, in situations similar to those of interest. However, the necessary ground-truth information is often not accessible and it is difficult to avoid or trace dynamic changes mid-acquisition. There is also no possibility of fully reproducing conditions over several experimental runs - this lack of a baseline will preclude properly testing various acquisition or instrumentation variations. *In vitro* and phantom-based assessments provide the necessary bridging scenario between simulation and (pre-)clinical implementation, as experimental data are acquired on a sample where the ground-truth is known *a priori*, is stable and can be tuned. Finding suitable PA phantoms and chromophores is necessary, though not straightforward, since they need to meet a series of criteria - to be tissue-realistic, stable, tunable and repeatable in their acoustic, optical and thermoelastic properties.

Chapter 4

Review of qPAT strategies

The measured data, after an optimal acoustic reconstruction, can be defined as $p_{0,meas}(\lambda) = K\mu_a(\lambda)\Phi(\lambda)$, or in matrix form for each given voxel as:

$$\begin{bmatrix} p_0(\lambda_1) \\ p_0(\lambda_2) \\ \vdots \\ p_0(\lambda_L) \end{bmatrix} = K \begin{bmatrix} \Phi(\lambda_1) & 0 & \dots & 0 \\ 0 & \Phi(\lambda_2) & \dots & 0 \\ \vdots & & \ddots & \vdots \\ 0 & 0 & \dots & \Phi(\lambda_L) \end{bmatrix} \begin{bmatrix} \alpha_{c_1}(\lambda_1) & \alpha_{c_2}(\lambda_1) & \dots & \alpha_{c_N}(\lambda_1) \\ \alpha_{c_1}(\lambda_2) & \alpha_{c_2}(\lambda_2) & \dots & \alpha_{c_N}(\lambda_2) \\ \vdots & & \ddots & \vdots \\ \alpha_{c_1}(\lambda_L) & \alpha_{c_2}(\lambda_L) & \dots & \alpha_{c_N}(\lambda_L) \end{bmatrix} \begin{bmatrix} c_1 \\ c_2 \\ \vdots \\ c_N \end{bmatrix} \tag{4.1}$$

where $\Phi(\lambda_l)$ is the fluence at wavelength l, $\alpha_{c_m}(\lambda_l)$ is the reference absorption spectrum for chromophore m at wavelength λ_l, N is the total number of chromophores and K is a spatially-constant factor that encompasses thermoelastic efficiency Γ and acoustic sensor response. It has been shown in Chapter 3 that isolating optical absorption (and therefore concentration)-based quantities from $p_{0,meas}(\lambda)$ is not trivial. In this Chapter an overview is given of strategies that have been employed to recover quantitative information from PAT data. Emphasis is given to studies including experimental considerations or even experimental data. First, standard linear spectroscopic unmixing is introduced and discussed (Section 4.1), including considerations on its validity (Subsection 4.1.1). Afterwards, in Subsection 4.2 strategies are discussed that try to account for the fluence by dividing it out, where the estimate is based on a simplified fluence formulation informed by either invasive probings (Subsection 4.2.1), complementary modalities (Subsection 4.2.3) or contrast agents (Subsection 4.2.2). This is followed by an overview of other linear unmixing methods relying on different statistics, in Section 4.3. In Section 4.4 non-linear strategies are discussed that try to account for the fluence through the use of an appropriate light model (model-based inversions) whilst Section 4.5 reviews in more depth non-linear strategies implemented experimentally. Section 4.6 addresses the emergence of machine-learning aided approaches.

4.1 Standard linear unmixing

Linear unmixing strategies are popular for *in vivo* applications due to their efficiency, speed and ease of implementation. Standard linear unmixing, as used in conventional linear spectroscopy (which we will from now on refer to loosely as *linear unmixing*), assumes that, for each and every given point in space, the fluence is a fixed constant. It disregards spectral corruption from the fluence term (no wavelength dependence of the fluence at each spatial point), such that:

$$\begin{bmatrix} p_0(\lambda_1) \\ p_0(\lambda_2) \\ \vdots \\ p_0(\lambda_L) \end{bmatrix} = K\gamma \begin{bmatrix} \alpha_{c_1}(\lambda_1) & \alpha_{c_2}(\lambda_1) & \dots & \alpha_{c_N}(\lambda_1) \\ \alpha_{c_1}(\lambda_2) & \alpha_{c_2}(\lambda_2) & \dots & \alpha_{c_N}(\lambda_2) \\ \vdots & & \ddots & \vdots \\ \alpha_{c_1}(\lambda_L) & \alpha_{c_2}(\lambda_L) & \dots & \alpha_{c_N}(\lambda_L) \end{bmatrix} \begin{bmatrix} c_1 \\ c_2 \\ \vdots \\ c_N \end{bmatrix} \tag{4.2}$$

where $\Phi(\lambda_l) = \Phi(\lambda_j) = \gamma$, *constant*. This simplification conveniently makes the inversion for μ_a linear ($p_0(\lambda) \propto \mu_a(\lambda)$) and local (by ignoring the dependence of local fluence on overall absorption) [107, 115]. As such, under this assumption the estimation of chromophore concentrations can be done independently for each given position/pixel of the domain and also straightforwardly, through linear inversion:

$$\begin{bmatrix} K\gamma\, c_1 \\ K\gamma\, c_2 \\ \vdots \\ K\gamma\, c_N \end{bmatrix} \approx \begin{bmatrix} \alpha_{c_1}(\lambda_1) & \alpha_{c_2}(\lambda_1) & \dots & \alpha_{c_N}(\lambda_1) \\ \alpha_{c_1}(\lambda_2) & \alpha_{c_2}(\lambda_2) & \dots & \alpha_{c_N}(\lambda_2) \\ \vdots & & \ddots & \vdots \\ \alpha_{c_1}(\lambda_L) & \alpha_{c_2}(\lambda_L) & \dots & \alpha_{c_N}(\lambda_L) \end{bmatrix}^{\dagger} \begin{bmatrix} p_0(\lambda_1) \\ p_0(\lambda_2) \\ \vdots \\ p_0(\lambda_L) \end{bmatrix} \tag{4.3}$$

where † denotes the pseudo-inverse ($A^{\dagger} = \left[A^T A\right]^{-1} A^T$, where A is a matrix).

It is sometimes claimed that estimates obtained after linear unmixing correspond to information on chromophore distributions except for a multiplicative factor K'. This makes a further underlying assumption - that the fluence γ is spatially as well as spectrally constant. This not being true, since fluence spatial distortion is present, estimation will fare poorly. This will not be as severe for ratios of chromophore concentrations, since issues related to spatial distortion and even overall calibration can be dealt with partially as the calibration factor K and fluence-related γ at each position will cancel out:

$$R = \frac{K\gamma\, c_2}{K\gamma\, c_1 + K\gamma\, c_2} = \frac{c_2}{c_1 + c_2} \tag{4.4}$$

Even so, any linear unmixing estimation, even ratiometric, still relies on the two initial assumptions made by linear unmixing which do not agree with the formulation of the

optical inverse problem - 1) linearity between p_0 and μ_a; 2) neglect of spectral colouring - meaning that c_1 and c_2 estimations will be wrong to start with.

Some publications and technology from commercial vendors still use or present PAT to clinicians or pre-clinical researchers as a modality where SO_2 and hemoglobin estimates can be directly extracted [15, 45, 116, 117], but this should be avoided in the future, or at least be proven to be adequate in the used conditions through proper validation.

In some instances spectral colouring and non-linearity may be weak enough to make linear inversion an attractive estimation procedure.

4.1.1 Validity of linear unmixing

Linear unmixing has been shown to work satisfactorily in simple 1D cuvette-based measurements of an homogeneous medium, when peak-to-peak amplitudes of PA signals are taken, $S_{p-p}(\lambda)$. Since the peak-to-peak feature occurs close to the illuminated surface, little spectral colouring and attenuation will have ocurred. Measurements in saline suspensions of red blood cells showed an accuracy of better than 4% SO_2 and resolution of ±1% [104].

For imaging of structures with some detail rather than plain cuvette measurement spectroscopy, it has been shown that validity may hold for shallow depths (e.g. superficial blood vessels) [35, 115]. Even so, this validity may be compromised if for instance the superficial layer is highly absorbing (e.g. due to melanin in skin or hemoglobin from dense superficial microvasculature) [108]. On the other hand, it may be possible to extend validity to greater depths if the surroundings have either a uniform spectral response or are weakly absorbing. Wang *et al* (2006) [16] showed validity experimentally for a simple case - a feature of interest in a medium of negligible absorption and scattering. A tube filled with either a mixture of inks or fresh blood was immersed in a water tank: the peak-to-peak amplitude of the single PA signal trace (encoding the signal of the tube at depth) was used for linear unmixing and the resultant SO_2 showed good agreement with the ground-truth. Early imaging studies in PAT [16] and AR-PAM [118] estimated SO_2 through linear inversion and considered the approach validated after showing agreement *in vitro* in this type of phantom. However, it is now widely agreed that this phantom scenario - non-absorbing, non-scattering, homogeneous, will not reflect at all the typical challenges in quantification of tissue-realistic cases, especially at the depths light will have traversed in AR-PAM and PAT [115]. These challenges have been demonstrated experimentally (*in vitro*), when the depth or size of the feature of interest are increased and when the levels of absorption and scattering of the background are increased. Regarding feature size, Maslov *et al* (2007) [108] suggested that linear unmixing was valid for superficial vessels in a residually absorbing medium only if $\mu_a a << 1$, where a is the vessel radius and μ_a the absorption coefficient of blood, i.e. when there is negligible decay of the fluence through the vessel. This heuristic was tested in phantoms similar to the previous,

yielding systematic errors of ~ 1%, and a resolution of less than 1%. Despite its acceptable accuracy and uncertainty in phantoms and *in vitro*, they did report in the same study that this method yielded physiologically unrealistic and biased blood saturation values when applied to the segmented arteries of *in vivo* data of mice. This was attributed mainly to the presence of skin and microvasculature affecting the assumption of no spectral colouring. Laufer *et al* (2007) studied the bounds of validity more extensively *in vitro*. Blood-filled tubes were placed at different depths and various scenarios were tested - namely changing the oxygen saturation in the tubes and changing the absorption of the scattering background medium from residually-absorbing (water+Intralipid) to increasingly absorbing (addition of blood or near-infrared dye). 1D PA traces were acquired and peak amplitudes for each tube location taken. Highly unsatisfactory results were obtained, especially at increasing depths. Only the most superficial blood tube, for the case with a scattering background medium devoid of blood, yielded reasonable results for tube saturation levels of 50 to 80%. Absolute recovery of HHb and HbO_2 always led to very inaccurate results.

The unsuitability of linear inversion for most scenarios involving AR-PAM and PAT was further confirmed in a Monte Carlo simulation-based study with a virtual mouse brain phantom with realistic parameters [115] where PAT and AR-PAM data were emulated. For PAT, though acceptable estimates (within 10%) were possible for spectrally invariant backgrounds up to 6 mm deep, performance was poor for more typical blood-filled background scenarios (spectrally variant background). Once in the diffusive region, SO_2 estimation also clearly worsened with depth. For AR-PAM, estimations were extremely poor for all cases except at shallow, sub-diffusive depths. Broadly speaking, OR-PAM covers the majority of scenarios where linear unmixing can be used for SO_2 recovery, since depth is not expected to exceed 1 mm.

There may be some additional scenarios where meaningful quantities apart from absolute SO_2 can be obtained. Maslov *et al* (2007) [108] showed that the difference in SO_2 between neighbouring vessels (Δ SO_2) is still well preserved with linear unmixing, even for high blood and epidermal absorption cases where absolute SO_2 estimation was not possible. This was first shown in simulation, for a double layer diffuse approximation model for the dermis, epidermis and vessels, where 'neighbouring' was defined as two vessels being apart by less than an optical penetration depth. Tests were also done *in vivo*, with rats, for 3 oxygenation conditions. Linear unmixing with and without fluence compensation was performed and for each case Δ SO_2 (difference in saturation between neighbouring vein and artery) was computed. For all oxygenation states, there was an overlap in the estimates (difference of about 2.42% ± 0.58%), showing that a reliable and plausible variation in Δ SO_2 can be obtained even without spectral compensation.

Hochuli *et al* (2014) [115] also showed in theory and simulation that it should be possible to obtain accurate estimations of dynamic oxygenation changes in a vessel of interest, Δ_t SO_2, through consecutive measurements at a single wavelength, as long as it

is reasonable to assume that the background characteristics have not changed in the time-lapse of interest δt between states. Recently, Tomaszewski *et al* (2017) [119] computed a metric of bulk tumour oxygenation based on linear unmixing for analysis of *in vivo* PAT mice studies (SO_2^{MSOT}) and showed that the dynamic/differential response to an oxygen challenge ($\Delta_t\ SO_2^{bulk}$) correlated strongly with *ex vivo* histology assessment for vascular density and function. The correlation found does not prove that $\Delta_t\ SO_2^{bulk}$ is an accurate estimate of the true variation of bulk tumour oxygen saturation $\Delta_t\ SO_2$, but it does show that some meaningful physiological information is retained, which for some applications may be sufficient.

A final factor to be emphasised within the context of linear unmixing is the importance of appropriate wavelength selection. Luke *et al* (2014) [120] used *in vivo* studies to compare equally-spaced wavelength selection with two methods selecting wavelengths based on the spectral features of the chromophores (the highest condition number or the highest minimum single value in the specific absorption spectrum matrix), and showed that the latter two performed better. Hochuli *et al* (2015) [121] also performed data intensive studies on the performance of linear inversion in the same virtual mouse brain phantom as [115]. The issue with wavelength selection is that it will usually be very case specific, especially if different sets of chromophores are involved. Even for cases with known sets of chromophores, finding the ideal set of wavelengths will depend on chromophore distribution and concentration in the medium, which is exactly what we do not know. A feature shown to be helpful is choosing areas where there is spectral flatness, though the effectiveness of this will likely be limited by SNR [121].

4.2 Linear unmixing preceded by approximate fluence correction

For most cases, it seems evident and widely accepted that to obtain accurate estimates the spectral colouring and spatial distortion need to be accounted for [115]. The most straightforward and quick way of doing so is to directly divide out the fluence contribution from the PA signal, $H/\hat{\Phi}$. Nevertheless, obtaining an estimate of the wavelength-dependent fluence contribution $\hat{\Phi}(\lambda, \mathbf{r})$ is not straightforward, not only because of the complexity of properly modelling it but also because the input parameters of absorption needed to generate it will never be exactly known (since they are after all what we want to estimate in qPAT!). The following strategies obtain first-order estimates of $\hat{\Phi}$ from the PA data itself, either by exponentially fitting background decay or assessing superficial PA amplitude.

The simplest approximation to the fluence may be to assume that light decays diffusely and uni-dimensionally with a fixed background attenuation level ($\hat{\Phi}(y) = e^{-\mu_{fit}(y_Q - y)}\ \forall\ x$), where $(y_Q - y)$ is the distance from the source depth-wise, and where the value μ_{fit} can be obtained based on literature estimates [55, 78] or eventually directly from the data in question through an exponential fit to the laterally integrated background signal decay [115]. Applying linear inversion after this correction can lead to some degree of

improvement [115].

A similar approach was applied *in vivo* by Razansky *et al* (2007,2009) [60, 122] for studies aimed at detecting fluorescent proteins expressed in adult zebrafish. The fluence was defined by the 3D analytical solution of the DA (equation 2.12) for a cylindrical illumination configuration and a fully homogeneous medium: $\hat{\Phi} = I_0(|k_D|r)$ where I_0 is the modified Bessel function of first kind, zero order, $k_D = \sqrt{3\mu_A(\mu_A + \mu_S')}$ the diffusion wave number and r the distance from the phantom centre in the axial plane. The μ_A used within this fluence model was found by comparing the amplitude of the surface PA signal in the object of interest to the surface amplitude obtained in a calibration phantom with well-characterised optical properties. The spatially-variant μ_a was then once more found as $H/\hat{\Phi}$. Successful spectrally unmixed images of the protein of interest and the background were then obtained. It should be noted that given the small size and transparency of the specimen, the level of spectral corruption was probably lower than in cases where scattering dominates.

4.2.1 Fluence correction through invasive fluence measurement

Having shown that linear unmixing failed to recover SO_2 and HbT for PAT transcranial imaging of a rat brain, mainly due to the capillary network in the skin affecting the spectral signature, Wang *et al* (2006) [16] tried to account for the *in vivo* fluence spectral signature by performing measurements of light transmittance through excised tissue of subjects from the same group as the imaged ones, a clearly invasive approach. Transmittance was measured for the skin and skull at wavelengths λ_1 and λ_2, yielding the relation $\frac{\Phi^{\lambda_2}(\mathbf{r})}{\Phi^{\lambda_1}(\mathbf{r})}$ for the relative fluence difference beyond skin and skull, which was then used to improve estimates of HbT (arbitrary-scaling) and absolute SO_2. Three statuses were studied: hyperoxia, normoxia and hypoxia, and consistent functional and physiological trends were detected among them, in terms of changes in SO_2. This same methodology has been applied for another *in vivo* case with an exogenous contrast as additional unknown [123]. Nevertheless, in general this method is limited not only because of its invasiveness, but also because it assumes that the skin and skull covering the mouse brain are optically homogeneous and therefore that in the horizontal plane the light fluence in the cerebral cortex will also be homogeneously distributed. It also assumes transmission characteristics are constant among subjects and even within a same subject for different temporal timepoints and physiological states. This is unlikely because, for instance, a different overall oxygenation state will likely affect background oxygenation and blood supply, and consequently the spectral signature imprinted. Note that ideally uncertainties not exceeding 1-2 percentage points would be desired for SO_2, since the dynamic range between severe hypoxia and normoxia in a given vascular location is narrow (15-20 p.p.).

To deal with these issues of inter-subject and also temporal/physiological variability,

another possible approach consists of embedding a well-characterised reference absorber in the subject of interest. The same group did so by placing a black polyethylene film under the rat skin during PA measurements (in this case for PAM) [108, 124] to account for skin attenuation. The absorption coefficient of the film did not vary significantly with wavelength, so the wavelength-dependence of the measured PA signal from the film should match the wavelength-dependence of the local fluence at that depth z. In the first study [124], the authors used the following 1D simplified model for the PA signal at the film to estimate bulk saturation SO_2 and hemoglobin per unit area $[HbT].z$, through least-squares fitting:

$$H(\lambda) \propto \Phi(\lambda) = \Phi_0 e^{-z.[HbT].\varepsilon(\lambda, SO_2)} \tag{4.5}$$

where Φ_0 and $\varepsilon(\lambda)$ dependence on SO_2 were known *a priori*. For a given segmented vessel at a depth of interest in the same image, the wavelength-dependent fluence could be corrected from the signal based on the model above and the estimated physiological parameters. A subsequent paper [108] used a similar approach but improved on the 1D simplified model for skin attenuation by considering two layers - dermis and epidermis - and also accounted for the reduced scattering contribution in each layer, from literature values. In further *in vivo* AR-PAM studies of oxygenation states in the subcutaneous arteries of a mouse [48], reasonable trends between normoxia, hypoxia and hyperoxia were obtained with SO_2 [44, 118]. Plausible absolute values for SO_2 in normoxia were also reported [44], 0.97±0.02 for arterial blood and 0.77±0.04 for venous blood.

The main drawback of these approaches is their invasiveness and lack of practical feasibility. Validation of the methods was also conducted *in vivo* through pulse oximetry measurements of global oxygenation, which is indicative but does not fully inform how well the spatially resolved estimation performed in most cases (may however be more indicative for e.g. finger imaging). Some *in vitro* tests were performed, but they were highly simplified compared to realistic situations (point-measurements of blood-filled tubes in a non-scattering, non-absorbing, homogeneous medium). The accuracy and robustness of these techniques is therefore debatable.

4.2.2 Fluence correction using contrast agents

Another way of disentangling the unknown local light fluence contribution from the PA signal involves injecting a well-defined chromophore that can act as a reference for fluence retrieval - somewhat similar in principle to the black absorber film, but potentially less invasive.

Rajian *et al* (2009) [125] suggested a method where PA measurements with and without a well-characterised contrast agent were made. The specific blood absorption spectrum $\varepsilon(\lambda)$ of the sample could be obtained through:

$$\varepsilon(\lambda) = \frac{S_1(\lambda)\varepsilon_{dye}(\lambda)C_{dye}}{C_T[S_2(\lambda) - S_1(\lambda)]} \tag{4.6}$$

where $S_1(\lambda)$ and $S_2(\lambda)$ are the PA signal without and with injection of the agent respectively; ε_{dye} is the molar extinction coefficient of the dye and C_{dye} and C_T are the molar concentration of the dye and the total hemoglobin respectively. The oxygen saturation could then also be easily recovered. 1D spectroscopic PA experiments were made with fresh canine blood flowing through microflow vessels, with the ground-truth oxygenation level being monitored by a gas analyser. Three media were assessed: non-scattering (water), highly scattering (milk based) and fresh tissue (chicken breast). Whilst the fluence correction was not essential in the first case, in the two latter cases the correction improved substantially not only the goodness of fit of the PA spectrum to the expected blood absorption spectrum $\varepsilon(\lambda)$ at a given saturation level but also the calculated oxygen saturation SO_2. A limitation is that C_{dye} had to be known to compute $\varepsilon(\lambda)$ (although not required for SO_2): whilst C_{dye} is easy to stipulate *in vitro*, the same is not true *in vivo* since the circulatory system will spread the agent systemically and differentially, whilst the liver and spleen will work towards clearing it. There are also other constraints: the agent must not affect the local fluence (concentration should be kept low and the insert of interest should be smaller than the light travel path); the chromophores of interest should not interact chemically or physically with the agent; and the injection should not lead to alteration of hemoglobin concentration or thermalisation properties (achieved as long as amount injected is low).

Cox *et al* (2010) [126] suggested that the behaviour of fluence dependent chromophores (e.g. gold nanorods) could be explored. Computational simulations were used to show that for an idealised chromophore that stopped absorbing abruptly after a critical fluence threshold, photoacoustic images at increasing illumination strengths could be used to estimate its concentration. It was discussed that other fluence behavioural phenomena could in theory be explored as well. The field of photoswitchable chromophores has since shown great promise [61]. Dean-Ben *et al* (2015) [127] suggested exploiting the fluence-dependent kinetics of reversibly switchable fluorescent proteins, in tandem with time-resolved PAT acquisitions, to correct for the light fluence. The photoswitchable probe in question in this study, when illuminated with blue light, led to fluorescence excitation and also, with consecutive and long-lasting pulses, to an eventual switch of the probe from a fluorescent state to a non-fluorescent dark state due to structural changes at the molecular level. Subsequent illumination with violet light could then restore the fluorescent state of the protein (therefore being reversibly switchable). The number of active molecules N at a given time-point t could be expressed through the stochastic process $N(t) = N_0\, e^{-\alpha t}$, where N_0 is the initial number of active molecules and α is the photoswitching rate, which had been shown to be related to the light fluence, $\alpha = k_p\Phi$, where k_p is a scalar that will depend on wavelength and the characteristic photoswitching kinetics of the substance. This meant that a time-resolved PAT measurement would have local fluence temporally encoded as $p(t) = p_0 e^{-k_p\Phi t}$. Retrieving this through curve-fitting up to a multiplicative factor could then be used to divide out the fluence contribution from the initial, non-switched, image. Some aspects to be wary of are that this latter

method will only be able to estimate fluence decay where the protein is present. On the other hand, if the protein happens to be largely present throughout the domain, it might become important to consider that the local fluence will vary with time as a consequence of the photoswitching itself (as chromophores turn off, absorption decreases and hence fluence will increase, making the decay-rate α non-linear). Overall, strategies involving photoswitching proteins are promising but to best make use of their properties more studies are needed to accurately understand the kinetics and interplay between reversible and irreversible changes.

4.2.3 Fluence correction using separately measured fluence

A neater, non-invasive, way of obtaining an independent estimate of $\hat{\Phi}$ is to use a complementary optical imaging or sensing technique. Once such an estimate is obtained, it can then be used to predict μ_a through the linear relationship $\mu_a \approx \frac{H}{\hat{\Phi}}$ [128]. Yin *et al* (2007) [129] used discrete diffusing light measurements to estimate the full-field fluence distribution. The DA was assumed valid and a least-squares minimisation between discretely measured boundary fluence values $\Phi_i^{(m)}$ and DA computed ones $\Phi_i^{(c)}$ was used to find the optimal homogeneous absorption coefficient μ_A, reduced scattering coefficient μ_s' and excitation source S. Successful phantom studies were carried out. Ranasinghesagara & Zemp (2010) [130] performed a similar study, but obtained estimates of bulk optical properties μ_A and μ_s' from an oblique-incidence diffuse reflectance system. These parameters were then fed into a RTE Monte-Carlo model to obtain $\hat{\Phi}$. Results with phantoms showed that dividing the PA signal by the fluence successfully yielded the expected mathematical linear relationship with μ_a.

The main downfall of these studies is that assuming homogeneous/constant absorption coefficient μ_A for fluence computation enters in direct contradiction with the next step of the method, where this homogeneous-μ_A-generated field fluence is used as input to obtain spatially resolved $\mu_a(\mathbf{x})$ values from PA data. While this homogeneous fluence estimation may not be compromising for samples with small inserts or residual heterogeneities, for most real cases this will be an issue. DOT, which probes optical absorption and scattering at low spatial resolution, has therefore been suggested as a better approach by Bauer *et al* (2011) [131] and Li *et al* (2011) [132]. In both cases, DOT information was used within a finite difference DA model to obtain the continuous fluence Φ. In these studies, DOT and PA were not performed at the same wavelength, although this problem could be easily averted in future setups. The excitation source profile also needed to be known. In general, though applying two techniques improves versatility, it does also largely increase cost and complexity of the imaging procedure both from a computational and practical point-of-view. Acousto-optics is another technique that has been suggested to obtain a spatial representation of $\hat{\Phi}$ [133, 134].

4.3 Other linear decomposition approaches

Strategies to detect or classify certain tissue components, or to fully quantify optical absorption coefficients and concentrations from PA images, can also involve other more complex forms of linear signal decomposition besides standard spectroscopic unmixing, in an attempt to better deal with fluence corruption and avoid some of its erroneous assumptions. These statistical methods are usually based on certain heuristics or prior knowledge on the expected behaviour of the data.

4.3.1 Blind spectral unmixing of multiwavelength data

Spectral unmixing schemes assume that, for a given multiwavelength image, the multiwavelength pixel intensity at each point can be explained as a linear combination (weighted sum) of a fixed set of basis vectors. The aim of the schemes is thus to linearly factor the data by decomposing the contributions from each of the basis vectors and retrieving their relative weightings. This is done for all points in the image, resulting in a series of component images, one for each basis vector, indicating at each spatial location the expected weight of that component. When applying spectral unmixing schemes to multiwavelength photoacoustic tomography data, the aim is usually to decompose the data into a set of images representing separate distributions of particular chromophores of interest - either for classification or full quantification. Supervised spectral unmixing methods start from a known and fixed set of basis vectors. Conventional spectroscopic unmixing (Section 4.1) is an example of this, where the set of specific absorption spectra of the chromophores deemed to be present in the image act as the set of basis vectors. Other approaches generate different basis vectors in an unsupervised (blind) manner, based on characteristics of the data itself - these problems are usually underdetermined, contrary to supervised ones, which can often be made well-posed. Namely, Principal component analysis (PCA) decomposes data into statistically uncorrelated components by defining new basis vectors that maximise variance. Independent component analysis (ICA) defines new basis vectors by searching for directions that maximise non-gaussianity, under the assumption that this correlates to information maximisation under the central limit theorem. ICA can be refined by implementing PCA as a pre-processing step to ICA, since ICA alone cannot measure the significance and uncertainty in the extracted components. It should be noted that each of these decompositions should be applied with care, by confirming if the underlying assumptions are met. For instance, for ICA to successfully decompose distinct chromophore contributions, they need to be independent of each other - i.e. the knowledge of the probability of one chromophore being at a given location should not in any way decrease the uncertainty of the probability of the other chromophore being at that same location. This means that ICA will therefore never work for separating oxy- and deoxyhemoglobin contributions, because the probability of finding oxyhemoglobin in a given voxel will clearly also inform at least partially on the

probability of finding deoxyhemoglobin there [135]. Another limit with blind unmixing strategies is that they will at most be able to give estimates to within a multiplicative factor - where this factor will not be the same for each of the extracted components, meaning absolute concentrations and ratios of different chromophore concentrations are not easily retrievable.

Morscher *et al* (2011) [103] and Glatz *et al* (2011) [107] first suggested using these spectral unmixing strategies as schemes more robust to spectral colouring. Multiwavelength PAT studies were carried out on corpses of adult CD1 mice with implanted insertions and a reference fluorescing straw in the esophagus. Linear unmixing was unsuccessful. Among the PCA generated component images, a few successfully contained the inclusion but the contrast was rather low since only few components actually carried recognisable structural information. Both linear unmixing and PCA yielded a considerable amount of cross-talk. ICA rendered the best results both visually and in terms of signal-to-background ratio for the inclusions. ICA preceded by PCA did not improve on ICA alone. A subsequent simulation study [135] further assessed the accuracy and range of applicability of ICA (preceded by a simple background fluence correction) and showed that it performed better than linear unmixing (LU) in identifying chromophore components as long as absorption coefficients were lower than certain thresholds (sometimes physiological), after which error could increase drastically. Heterogeneous backgrounds also affected more considerably the successful decomposition.

Other spectral unmixing strategies have been suggested, namely vertex component analysis [136], blind logarithmic unmixing [137] and sub-pixel target detection methods [138]. Despite their promising outcomes in simulation and phantoms, the black-box nature of these makes it rather unclear how factors such as sensor response, acoustic properties or thermalisation are dealt with by these decomposition strategies or how generalisable their applicability is. More validation studies are warranted.

4.3.2 Exploiting sparsity

A conceptually neat way of dealing with and decoupling spectral corruption involves trying to decompose each single-wavelength PA map based on *a priori* expectations of the overall spatial behaviour of the optical absorption distribution $\mu_a(x, y)$ and the fluence propagation $\Phi(x, y)$, since the former is usually expected to vary locally and drastically at tissue boundaries and vasculature whilst the latter is expected to vary globally and smoothly due to the characteristics of light transport. Such an approach does not need a parameter-based physical model for the fluence or knowledge of parameters such as the illumination geometry or certain optical properties. Rosenthal *et al* (2009) [139] devised such a strategy. They considered a sparse signal representation of the absorbed energy distribution $H(x, y) = \mu_a(x, y)\Phi(x, y)$ and two libraries $\left\{\phi_n\right\}_n$ and $\{\psi_m\}_m$, that could sparsely represent $\mu_a(x, y)$ and $\Phi(x, y)$ respectively, but not the other way around. The smooth and

decay-like behaviour of the fluence led to the choice of the 2D set of discrete Fourier basis to represent $log\,[\Phi(x,y)]$. The 2D discrete Haar-wavelet basis, composed of local, piecewise constant basis functions, was chosen to define $log\,[\mu_a(x,y)]$. The aim was therefore to explain $log\,[H(x,y)]$ by making the assumption that:

$$log\,[H(x,y)] = \sum_{n=1}^{N} c_n \phi_n(x,y) + \sum_{m=1}^{M} d_m \phi_m(x,y) \tag{4.7}$$

where c_n and d_m are a set of unknown coefficients. The decomposition problem was formulated as a minimisation approach: finding the minimum number of coefficients c_n and d_m that fulfil an imposed data-*vs*-model fidelity criterion. It was solved through an orthogonal matching pursuit approach, to overcome issues of non-convexity and high resolution complexity. The retrieved μ_a should, in a best case scenario, be a constant-scaled outcome of the true absorption coefficient, after which calibration would still be necessary for absolute quantification. A numerical example with an abstract phantom yielded average errors of 6%. When Gaussian noise was added, yielding *SNR* values ranging from 2 to 100, average error across the insertion increased to 12%. Experimentally, a cylindrical solid-tissue mimicking phantom with added background absorption and scattering and two absorbing insertions embedded was scanned. The insertions, unclear in the PA image, became apparent after $\mu_a(x,y)$ computation. After the image was scaled to fix background μ_a at its ground-truth value, reasonable average recovered values for the insertions were obtained. Some of the main drawbacks of this approach are its relatively high sensitivity to noise and the need for calibration. It is also rather sensitive to the choice of the bases. An optimised choice is not always feasible, especially since the sparsity conditions for μ_a and Φ need to be met.

4.4 Non-linear inversion - fluence model incorporation

In this section, contrary to previous approaches, methods are presented that invert for μ_a (or chromophore concentrations) by fully acknowledging in the inversion scheme the non-linearity and spectral corruption brought by the fluence. To achieve this, an explicit light transport mathematical model that depends on the unknown μ_a will be incorporated. These strategies are known as model-based inversion and can, if given sufficient data and a low enough noise level, arrive to the correct solution. However, these inversions are not straightforward. If the fluence model used is analytical it may be possible to find an analytical closed form solution for μ_a - though in practice this will only be possible for very simple cases. Even in their forward mode, most fluence models that are analytically formulated will still need to be solved numerically, so it comes as no surprise that their inversion will not be straightforward analytically either.

4.4.1 Analytical solutions

Ideally, analytical closed form solutions would exist to directly estimate the unknowns (e.g. μ_a) as a function of the output (H). This would allow quick, repeatable and sound inversion without the need to apply computationally intensive minimisation schemes or matrix inversions. Nevertheless, no general, all-encompassing, closed-form solution exists and there is also no systematic way of finding closed-form solutions for specific sub-problems. Even when formulations are found, these will need to be stable and robust.

When certain assumptions and acquisition restraints are in place, it might be possible to perform direct non-linear inversion to certain analytically defined light models. The most simple example is the Beer-Lambert law with homogeneous μ_a, which is valid in a 1D context, for a homogeneous, absorbing and non-scattering medium exposed to wide illumination. For a known Φ, μ_a can be retrieved directly as $\mu_a = -ln\left[\Phi(z)/\Phi_0\right]$. For PA, what will be measured will be for instance the backward mode PA signal:

$$p(t) = \frac{1}{2}\Gamma\Phi_0\mu_a e^{-\mu_a c_s t},\ t \geq 0 \tag{4.8}$$

Here, parameter μ_a can be retrieved in two ways [140]: one involves taking the maximum amplitude of the PA signal, and normalising by Γ and Φ_0 (assuming they are known). The other involves performing curve-fitting to the decaying exponential, in which case c_s and the time resolution need to be known beforehand. These approaches are widely used for PA spectroscopy to characterise non-turbid solutions in cuvettes. This is discussed further in Chapter 5, Section 5.4.1.

If the previous medium is multi-layered rather than homogeneous (i.e. the absorption coefficient is depth-dependent), then the PA signal can rather be defined as (equations 2.2+2.9):

$$p(t) = \Gamma\mu_a(z)\Phi_0 e^{-\int_0^{c_0 t}\mu_a(\xi)d\xi} \tag{4.9}$$

and its inverse can be expressed as [141]:

$$\mu_a(z) = \frac{p(z/c_0)}{c_0\int_{z/c_0}^{\infty} p(t)dt},\ z \geq 0 \tag{4.10}$$

The feasibility of this formulation was experimentally validated.

Another scenario that can be described and solved analytically is the case of a homogeneous medium that is both absorbing and scattering (ie. turbid). If a plane wave illuminaion is used, the fluence will decay approximately as $e^{-\mu_t z}$ near the surface and as $e^{-\mu_{\text{eff}} z}$ at deeper depths (above a mean free path) since the light becomes diffuse (see Equation 2.13). The 1D diffusion approximation has therefore been employed [142], where the backscatter correction parameter k present in Equation 2.13 was derived from superficial diffuse reflectance measurements. Petrov *et al* (2004) [143] also used such an approach in multiwavelength PA cuvette measurements of ovine (sheep) blood to retrieve effective attenuation spectra at various saturation levels. These data were later used as calibration

data for subsequent studies by the same group [144, 145] where 1D PA measurements on the sheep skull were performed.

4.4.2 Fixed point iteration

When a direct analytical expression cannot be found for the inverse problem, iterative strategies can be adopted.

Fixed-point algorithms can sometimes be applied when the model expression can be rearranged such that the unknown parameter can be equalled to a known function of itself. The advantage of these is that, if they do converge, they will converge faster than any other iterative algorithm. For the case of single-wavelength PA data where the aim is to retrieve a map of μ_a, Cox *et al* (2006) [70] suggested the following rearrangement from equation 2.1:

$$\mu_a^i(\mathbf{x}) = \frac{H(\mathbf{x})}{\Phi_i(\mathbf{x}; \mu_a^{i-1}(\mathbf{x})) + \sigma} \tag{4.11}$$

to be calculated for each iteration i, where σ is a regularisation parameter and Φ_i is the fluence calculated by a given model with absorption information from the $(i-1)^{th}$ iteration. Experimental implementation of the DA-based fixed point strategy was done in 3D PAT phantom studies [146, 147]. The same group then improved the approach by employing the RTE (equation 2.8) [148]. As expected, phantom studies showed that the RTE-FEM implementation outperformed the DA-FEM one, especially when the $\mu_s' >> \mu_a$ assumption broke down for the background region.

Fixed-point has as disadvantage that its formulation does not allow other parameters to be easily set as unknowns. For the case of PA, the inversion will assume that information on scattering (and potentially thermoelastic efficiency) is fully available. In practice this is usually not the case. To cope with this, the studies above assumed a typical simplification: that scattering behaviour was homogeneous and known to be equal to the background scattering. This will bring errors, since the background assumed value itself may have uncertainty and will not properly reflect the behaviour of any heterogeneously scattering medium. Jetzfellner *et al* (2009) [110] assessed the experimental feasibility of fixed-point iteration at a single-wavelength, namely the impact of the number of iterations and of incorrect scattering amplitude information. This was done in scattering and absorbing phantoms and the DA was assumed as light-model. Regarding the number of iterations (at correct μ_s'), it was noticed that except for the first few iterations, increasing iterations considerably decreased the visual and quantitative quality, implying noise, artefacts and model inconsistencies were in place. Considerable inaccuracies for incorrect μ_s' definition were found, though recent results in another study have shown that the errors obtained may not always be that severe, especially if the average bulk scattering is reasonably estimated [111]. Suggestions were made that ideally some *a priori* information should be incorporated in the model, such as object geometry or background properties.

4.4.3 Model-based minimisation - least-squares minimisation

Model-based minimisations are a subset of Bayesian approaches and are one of the most general categories of approaches to solve an inverse problem. They find the desired unknowns by solving the forward problem iteratively based on the parameter estimates $\mathbf{u}$ at that given iteration, and then update those same parameter estimates for the next iteration $\mathbf{u} \leftarrow \mathbf{u}+\delta$. The update is always done in a direction that minimises the chosen error metric - known as the error functional ε. This error functional is usually formed by a data fidelity term (the difference between the forward model and measured data) and a regularisation term (based on some penalisation metrics of interest). Iterations are run until some stopping criterion is reached - either when a certain number of iterations has been reached, when no more downward steps can be found, when the gradient is too small or when the change in error functional or estimates between successive iterations is too small. Model-based minimisations are broad in their type: various ways exist to define the data fidelity and regularisation terms of the error functional and the minimisation algorithm (the way in which the search direction and parameter estimates are updated). For the data fidelity term, a least-squares approach - assuming Gaussian noise of zero mean - is often used. Least-squares error can be defined as $\left\|H^{model}(\mathbf{u}) - H^{meas}\right\|^2 = \sum_h \left(H_h^{model}(\mathbf{u}) - H_h^{meas}\right)^2$ where H^{meas} is the measured absorbed energy, $H^{model}(\mathbf{u})$ the forward modelled absorbed energy with input parameters $\mathbf{u}$ and the indexation h indicates the h^{th} voxel. Least-squares minimisations will have as aim minimising an error functional of the sort:

$$\underset{\mathbf{u}}{\operatorname{argmin}}\ \varepsilon = \frac{1}{2}\left\|H^{model}(\mathbf{u}) - H^{meas}\right\|^2 + \wp(\mathbf{u}) \tag{4.12}$$

where the first and second terms are the data fidelity and regularisation terms respectively. Minimising the data fidelity term in this manner is equivalent, in the Bayesian framework, to maximising the probability of the data H^{meas} given the parameters $\mathbf{u}$, $\underset{\mathbf{u}}{\operatorname{argmax}}\ p(H^{meas}|\mathbf{u})$.

Problem formulation, Unknowns A crucial advantage of model-based minimisation approaches is their high level of versatility. They are flexible enough to adapt to different types of unknowns, initial data and *a priori* knowledge. The problem needs to be formulated carefully though, to make sure it is well-posed and that it will converge in a reasonable time.

If the aim is to retrieve a μ_a spatial representation at wavelength λ_l from single-wavelength PA data $H(\lambda_l)$, with all other parameters known including scattering, the problem at hand is [149]:

$$\underset{\mu_a}{\operatorname{argmin}}\ \varepsilon = \sum_{h=1}^{Nh}\left[H_h^{meas}(\lambda_l) - H_h^{mod}(\mu_a, \lambda_l)\right]^2 \tag{4.13}$$

which should be unique.

If the aim is to retrieve images of a set of chromophore concentrations c_k with known specific absorption spectra $\alpha_k(\lambda)$ from multiwavelength data $H(\lambda)$, two main approaches

can be employed: either inverting for μ_a at each of the wavelengths separately using the single-wavelength inversion mentioned above and afterwards applying linear unmixing based on the knowledge of $\alpha_k(\lambda)$, or alternatively directly inverting for c_k based on the multiple-wavelength data and knowledge of $\alpha_k(\lambda)$ incorporated in the model [38, 149]. In the latter case, the problem can be formulated as:

$$\underset{c_k}{\operatorname{argmin}}\ \varepsilon = \sum_{l=1}^{L}\sum_{h=1}^{Nh}\Big[\, H_h^{meas}(\lambda_l) - H_h^{mod}(c_k, \lambda_l)\,\Big]^2 \tag{4.14}$$

where now the least-squares error is not only computed across all locations but also across all wavelengths. Most times, as long as the number of wavelengths L is greater than the number of unknown chromophores C (and assuming once more $\mu_s'(\lambda)$ is known and the spectra are unique), it should be possible to recover the concentrations in a unique manner.

As discussed, in reality μ_s' will usually not be known *a priori*. Contrary to fixed-point and linear unmixing strategies, model-based minimisation can include scattering as an additional unknown in the minimisation. Nevertheless, some additional information is needed, otherwise the problem may be non-unique (ill-posed). One way is to include PA information from multiple-illuminations [150]:

$$\underset{\mu_a,\mu_s'}{\operatorname{argmin}}\ \varepsilon = \sum_{p=1}^{P}\sum_{h=1}^{Nh}\Big[\, H_{p,h}^{meas}(\lambda_l) - H_{p,h}^{mod}(\mu_a, \mu_s', \lambda_l)\,\Big]^2 \tag{4.15}$$

where P is the number of illumination configurations [150] or patterns [151]. For these multiple illumination scenarios, Bal *et al* (2011) [152] have also mathematically showed that, given 3 unknown spatial entities (μ_a, μ_s', Γ), it is not possible (not unique) to reconstruct all 3 regardless of the reconstruction method used or the number of illuminations used, unless appropriate additional information is included (e.g. shown for multiple wavelength data to be possible and stable [114]; shown for imposed piecewise constancy to be possible though not stable [153]). It is however stable and unique to reconstruct any two with knowledge of a third. Though in theory any number of multiple illuminations (even 2) should be therefore enough to recover uniquely and stably a (μ_a, μ_s') pairing, it has been shown that at least $2n$, where n is the dimension of the space, should be used to in practice ensure convergence [154]. This is due to the low sensitivity of PA to scattering (local scattering does not directly weight the image, but only indirectly through the fluence term, therefore sensitivity is low, especially at increasing distances from the excitation source). In theoretical and simulation studies, multiple illumination is arguably the most popular and neat way of dealing with the unknown scattering and resultant absorption-scattering non-uniqueness in the inversion . However, not all illumination positions and/or profiles will be able to give the required uniqueness or equal levels of posedness, so this should be considered carefully [154, 155]. This approach also has not transitioned into experimental studies - multiple illuminations require practical changes in instrumentation and acquisition procedures, good access to information of illumination

profiles and positioning, and cause increased dimensionality of the data and increased acquisition time.

Another way to retrieve scattering is, for the case of multiwavelength PA, to include knowledge of the spectral dependence of the scatterer $\alpha_{scat}(\lambda)$, where it is assumed that $\mu_s'(\lambda) = k_{scat}\alpha_{scat}(\lambda)$ [38, 149]. In this case, the only scattering-related unknown to be recovered is the scatterer concentration/amplitude distribution k_{scat}:

$$\underset{c_k, k_{scat}}{\operatorname{argmin}}\ \varepsilon = \sum_{l=1}^{L}\sum_{h=1}^{Nh}\Big[\, H_h^{meas}(\lambda_l) - H_h^{mod}(c_k, k_{scat}, \lambda_l)\,\Big]^2 \tag{4.16}$$

This approach has been employed experimentally [35, 36, 104]. This may be because it is more practically feasible to acquire data at multiple wavelengths than at multiple illuminations (and multiple wavelength is usually acquired anyway because of chromophore differentiation). It only involves adding prior knowledge to the model rather than fundamentally changing acquisition systems or procedures.

Finally, by relying on joint multiple illumination and multiple wavelength data it is possible to simultaneously recover distributions of chromophores c_k, scattering components and Γ, as shown for instance in studies [114, 156, 157].

Minimisation approaches Once we have formulated our problem, a minimisation algorithm needs to be chosen to solve the problem, as finding the true solution means finding the minimum of scalar functional ε. There are many iterative minimisation strategies to choose from. Generally, the update can be given by:

$$\mathbf{u}^{(i+1)} = \mathbf{u}^{(i)} - \gamma \mathscr{H}(\mathbf{u}^{(i)})^{-1} g(\mathbf{u}^{(i)}) \tag{4.17}$$

where $g(\mathbf{u})$ represents the vector of functional gradients (first order derivatives), $\mathscr{H}(\mathbf{u})$ the Hessian matrix of second derivatives (which gives information on the curvature of the function), and γ the line-search weight. The term $\mathscr{H}(\mathbf{u}^{(i)})^{-1} g(\mathbf{u}^{(i)})$ is responsible for giving the direction of descent whilst γ gives the step-length. The way in which this direction is estimated defines the type of method. In the Newton method, the full Hessian matrix is calculated. For a convex problem, this will converge to the minimum in a few iterations - convergence is quadratic - but computing, storing, inverting and applying the Hessian at each iteration can be very computationally intensive and sometimes not practically feasible: e.g. a problem with 10^6 unknowns will require Terabytes of memory. Some strategies can ameliorate the burden of calculating the Hessian explicitly. For instance, the Gauss-Newton method approximates the Hessian based on the Jacobian J (matrix of first order partial derivatives), $\mathscr{H} \approx J^T J$ but would still need to store and invert Terabytes of data for the example given. Another way to alleviate the computation is by using quasi-Newton methods - these compute approximations of the Hessian matrix at each iteration based on stored functional gradient values and on the estimate of the Hessian at the previous iteration. These are known as gradient-based methods since they depend solely

on gradient estimates to step down the error functional. Limited-memory BFGS (L-BGFS) directly computes approximate estimates of the *inverse* of the Hessian $\hat{\mathscr{H}}^{-1}$ (therefore reducing additional burden of explicit inversion) and bases the calculation on stored gradient estimates from a finite number of previous iterations (therefore named limited-memory) [158]. Gradient-methods are much more memory-efficient and computationally manageable, but will typically take more iterations to converge than Newton or Gauss-Newton ones. Calculation of the functional gradient vector can traditionally be done by calculating each of its entries though finite forward differences - by perturbing the unknown of each current entry by a small amount δ and computing the slope. This is time-consuming, especially since it needs to be repeated in full at each iteration. Alternatively, the adjoint model can be implemented to efficiently and quickly obtain the full functional gradient vector in the same time as two runs of the forward model [149].

Other methods exist that rely on global search algorithms rather than on explicit information from the differentiation of the function (gradient-free) - e.g. simulated annealing, genetic algorithms and simplex methods. The latter typically sample the parameter space in the vicinity of the current estimate, fit a surface to the sampled points and then find the direction of descent along that surface. The Nelder-Mead simplex method is an example of that - e.g. for an error surface defined by two parameters, it will sample three neighbouring points to define a plane on which the steepest descent direction is computed; this can be seen as an extension of the secant method, which for an error surface dependent on one parameter will sample two points to define a line that dictates the direction of descent. Gradient-free methods will however converge very slowly. They are usually only useful in practice when there is a small number of unknowns - low-dimensional parameter space.

Both full-Newton (Hessian-based) [159], Gauss-Newton (Jacobian-based) [40, 128, 129, 160], gradient-based [39, 114, 149, 152, 161–164] and global-search strategies [35, 165] have been suggested and implemented at least in simulation for different variants of the qPAT problem.

Light model The choice of light model to be used in the forward model $H^{mod} = \mu_a \Phi(\mu_a, \mu_s, g)$ will depend on the accuracy and range of validity desired, the ease of implementation and computational burden. Most commonly, the DA has been used in model-based optimisations [40, 114, 128, 129, 149, 152, 160, 161], since it is fairly straightforward to implement and is valid for a large portion of most tissue-like domains. Nevertheless, since it is not valid close to the illuminated surface, especially when a collimated beam is used, the delta-Eddington approximation has also been suggested instead [35, 36, 163]. The most complete formulation would be to use the full RTE. This does increase the computational burden substantially due to the angular discretisation needed in FEM implementations, but has been tested in 2D simulation scenarios [40, 156, 160]. It has been shown that, if the case of interest is in the non-diffusive transport regime, apply-

ing DA-based inversion will not only cause inaccuracies due to data-model mismatch but will also be inherently more ill-posed in recovering scattering than a RTE-based inversion [40]. Due to the significant increase in computing capacity and parallelisation capabilities of GPUs, Monte-Carlo is also starting to be considered for iterative qPAT - both for global minimisation methods [166] and even for those that require functional gradients [164].

When considering the complexity of implementation and burden of calculations, it should be noted that this does not always strictly refer to challenges in formulating and evaluating the forward model itself but also to any functional gradient, Jacobian or Hessian calculations that may be involved in the minimisation scheme. Whilst for a small parameter space it may be sufficient to use a gradient-free method where the main mathematical calculations needed as input are the evaluation of the forward model, for most high resolution estimates of distributed parameters in 3D it will be necessary to, for all but the smallest imaging volumes, at the very least also derive and calculate functional gradient expressions through the adjoint method [164].

Regularisation and incorporation of prior knowledge Regularisation reduces the solution space in order to overcome ill-posedness (whether caused by non-uniqueness of the problem or because of the impact of noise). It is usually included as an additional term:

$$\underset{\mathbf{u}}{\operatorname{argmin}}\ \varepsilon = \frac{1}{2}\left\|H^{model}(\mathbf{u}) - H^{meas}\right\|^2 + \wp(\mathbf{u}) \tag{4.18}$$

where $\wp(\mathbf{u})$ is the regularisation or constraint-imposition term. In some cases, this formulation can be interpreted as part of a Bayesian framework, i.e. if we see the problem above as a maximisation of the posterior probability of the parameters, $p(\mathbf{u}|H^{meas}) \propto p(H^{meas}|\mathbf{u})p(\mathbf{u})$, which is equivalent to minimising its antilog, we will obtain two terms like the ones above: the first is the typical least-squares minimisation data fidelity term; the second term can be seen as a regularisation term based on the prior probability distribution $p(\mathbf{u})$, $\wp(\mathbf{u}) = -\log p(\mathbf{u})$.

More generally, regularisation $\wp(\mathbf{u})$ can be based on various types of information or expectations on the unknowns or measured data. For instance, it may be based on information on the minimum or maximum bounds of the values to be found, e.g. optical coefficients or concentrations are known to not fall below zero; also, a reasonable maximum may be imposed based on known information on typical physiological ranges. If a hybrid acquisition has been used (Section 4.2.3), the information from the other imaging modality can also be incorporated in the inversion, e.g. this has been demonstrated theoretically for a hybrid PA + surface light measurement scenario [167]. Alternatively, spatial information may be used, most commonly homogeneous spatial regularisers like total-variation (e.g. in [40, 160, 161]), which will impose piece-wise constancy and is therefore known as being edge preserving, and Tikhonov (e.g. in [38, 163, 168]), which will impose smoothness. Another option is to feed some information on the general shape of the structures, e.g. impose that they should be sparsely represented in a given basis, like Fourier or

Hadamard. It may also be possible to use even more specific structural information (from acoustic reconstruction, another imaging modality or an atlas) to define spatially varying probability maps for the optical properties (e.g. in [168]). Finally, regularisation may be related to the distribution of values statistics-wise rather than space-wise. For the case of chromophores known to be independent (see Section 4.3.1 for definition) it is possible to impose explicitly a term favouring independence, based on a mutual information penalty term. This has been shown to provide better results than standard minimisation when in the presence of model uncertainties [169]. Another option is, if each node can be classified into a tissue whose properties are known to some extent from the literature, to impose a regularisation in the reconstruction where the optical properties of that nodal value should be similar to expected ones. Recently, a new method was extended from this one, which does not assume known tissue properties or known attribution of each nodal value to those tissues but does assume that the nodes can be classified into one out of a fixed number of tissues, where each tissue has an expected distribution of values (μ_a, μ_s') following a Gaussian model with a certain unknown mean and standard deviation [170]. The unique characteristic of this approach is that the classification of each nodal value as a given tissue (class) and the characteristics of each class itself are re-assessed after each MBI reconstruction step - the distribution of unknowns and therefore optimal clustering of the nodes will have changed, leading to re-classification and update of the means of the classes (tissues) based on these new clusters (the concept is analogous to k-means). The following reconstruction step then has an updated regularisation imposition based on the new tissue classification of each node and the new mean of that tissue. The end result of this successive reconstruction-classification is that solutions are favoured where the cloud of nodes in feature space, (μ_a, μ_s') can be explained as belonging to a fixed number of tissues, each with a Gaussian distribution of optical properties. A multiwavelength approach has also been developed [171].

Single-step methods The optimisation approaches considered previously aimed to retrieve optical parameters such as (μ_a, μ_s', Γ) from the initial pressure distribution map $p_0(\mathbf{x})$, which was assumed to in turn have been reconstructed with an appropriate acoustic inversion from time-series at sensor locations $\mathbf{x}'$, $p(\mathbf{x}', t)$. These approaches can be referred to as two-step inversions. Another option for optimisation approaches is to perform a single-step inversion that incorporates both the optical forward problem and the acoustic forward problem in its formulation [172]. The parameters of interest such as (μ_a, μ_s', Γ) are now retrieved directly from the time-series data. One of the advantages of these methods is that both optical and acoustic unknown parameters can be incorporated in the inversion - as long as given sufficient data such as multiple illuminations. Namely, Ding *et al* [100] used such a scheme in a DA-FEM model to recover μ_a and speed of sound c_s. Another advantage of single-step methods is that any regularisation operations (e.g. spatial smoothening) can be applied directly to the parameters of interest taking into account the whole problem, instead of having to enforce them two-fold or having to choose

in which stage to enforce them, which may affect accuracy of quantification [172]. Finally, if the experimental data have been acquired with a system with simultaneously rotating illumination sources and acoustic partial view detectors around the object, it will not be suitable to use a two-step method - i.e. it will not be possible to reconstruct the initial acoustic pressure at each illumination in a stable manner due to the limited-view, and therefore also not possible to correctly apply optical inversion to these multi-illumination data to recover optical coefficients. Single-stage model-based minimisations may be able to do so [41, 155, 172].

4.5 Experimental implementations of model-based minimisations

Many of the MBI strategies suggested for PA are based on different variants of the above characteristics (error functional, minimisation strategy, light model, regularisation, domain dimensionality, one vs two-step, incorporation of scatter as unknown). There is a wide range of theoretical/simulation studies that have been suggested for the qPAT problem but only a small fraction of these have been extended to experimental scenarios. In this section we will describe the main studies that have experimentally - *in vitro* or in solid phantoms - implemented model-based minimisation strategies and dealt to various extents with the issues that arise once experimental implementation is considered.

Sun *et al* [12, 129, 168, 173] performed a series of studies with the aim of obtaining quantitative 3D photoacoustic imaging of the finger joints to inform the appearance and development of osteoarthritis (OA). A 3D inversion involving two coupled least-squares minimisation problems (one for the acoustic problem and another for the optical problem) was suggested. For the acoustic problem, a Gauss-Newton method and global convergence line search method was used to minimise the difference between measured PA values and a FEM frequency domain implementation of the Helmholtz photoacoustic wave equation (Equation 2.31) [128, 129]. A combined Marquardt and Tikhonov regularisation scheme is used. For the optical problem, a least-squares minimisation was used to try to recover μ_a from single-wavelength H information, using a DA-FEM model with scattering μ_s' considered homogeneous and known. A Gauss-Newton method was used for the minimisation, with two regularisation mechanisms added to reduce ill-posedness [129, 168]: Tikhonov regularisation and a spatial regularisation based on prior structural information from the acoustic reconstruction and segmentation. In a first experimental study [174], a solid phantom was developed mimicking the overall architecture and optical properties of the finger. Two bone-like structures were placed to emulate the distal and intermediate phalanx and in-between one cartilage-like layer was placed. Accurate absorption coefficients for 'cartilage' were obtained. Values of 0.016, 0.026, 0.031 and 0.043 mm^{-1} were obtained for true values of 0.015, 0.025 0.03 and 0.04 mm^{-1}, but no uncertainty figures were reported. In subsequent papers [12, 173], the authors applied the strategy on

the distal interphalangeal joint of human subjects, initially on a single volunteer [12] and subsequently on a small group of subjects, some of which were OA patients. Absorption coefficients for the phalanxes and the cartilage were recovered, which were consistent with the literature for healthy subjects. Mean μ_a was higher in diseased cartilage than in healthy, the same applying for the synovial fluid, which was also consistent with physiological characteristics of OA. Sun *et al* (2013) [175] then extended the study to the multiple wavelength case - inversion was still done wavelength-per-wavelength, but afterwards linear spectroscopic unmixing was applied to recover saturation and hemoglobin concentration. Outcomes showed that there were increased hemoglobin and reduced oxygen saturation levels for osteoarthritic phalanges and joint cavities when compared to control cases, and considered these trends believable indicators of angiogenesis and hypoxia expected in osteoarthritis development. The papers did however fail to provide any information on error and uncertainty and were unclear on how the regularisation parameters were chosen.

The multiple source illumination approach to overcome the absorption-scattering non-uniqueness has only been theoretically formulated and simulated (except for a study by Held *et al* (2016) [176] that aimed to estimate bulk background attenuation coefficient from illuminations at multiple successive positions with a handheld probe, to then use this in a 1D fluence correction - i.e. this study was not MBI-based). On the other hand, strategies that employ multi-wavelength data with prior scattering wavelength dependence knowledge $\alpha_{scat}(\lambda)$ have been used with experimental data [35, 36, 104], where $\mu_s'(\lambda) = k_{scat}\alpha_{scat}(\lambda)$ with unknown scatterer concentration k_{scat}. A series of *in vitro*/phantom studies were carried out by Laufer *et al* [35, 36, 104] which used a model-based inversion strategy: when fed multiwavelength PA data and a known wavelength-dependence of the scattering coefficient, it could retrieve distributions of chromophore and scatterer concentration through a least-squares minimisation approach. The aim of this series of studies was to pave the way and ultimately enable the *in vivo* attainment of blood saturation and concentration over the vasculature, in 3D and at high resolution. In the first of these studies [104], the simplest and most finely controlled setting was considered. Single PA waveform spectroscopic acquisitions of a tube with saline suspensions of red blood cells were made. Oxygen saturation levels were varied temporally between 2% and 100%. The endogenous chromophores considered were oxyhemoglobin, deoxyhemoglobin and water. Three quantification methods were considered. The first relied on the delta-Eddington diffusion approximation to model light transport for a large diameter collimated incident beam. The PA signal, including contributions from thermalisation and 1D acoustic propagation and detection, were modelled by the expression $S(t) = K\mu_a\Phi(c_s(t_0 - t), \mu_a, \mu_s)$ where K is a system response constant that accounts for incident fluence Φ_0, detector sensitivity, acoustic attenuation and thermoelastic coupling efficiency. The error metric compared the experimentally measured and forward computed PA amplitude spectrum $S_{p-p}(\lambda)$, and minimisation was done with the Nelder-Mead algorithm to recover unknowns c_{HHb}, c_{HbO_2}, k_{scat} and K (and SO_2). The second method

used simple linear unmixing based on the peak amplitudes. The third method relied on the shape of the curve at diffusion depths, with exponential curve-fitting used to extract μ_{eff} (similar to Section 4.4.1), making it independent of parameter K. The estimate $\mu_{\text{eff}}(\lambda)$ was then used in a second stage, to obtain estimates of unknowns c_{HHb}, c_{HbO_2} and k_{scat} through iterative inversion based on Equation 2.14. Accuracy of better than 4% SO_2 was obtained for the amplitude-based measurements (I and II), and of about 2.5% for the effective scattering-based measurements (III) was achieved. Larger systematic errors were also detected for the former, assumed to be because of inaccuracies in the wavelength dependent calibration factors or from not accounting for the laser output beam features as wavelength was shifted. All 3 methods exhibited a resolution of ±1%. Overall this study showed that using estimation based on the shape of the signal rather than its absolute values was advantageous, given its independence on variations in various scaling parameters including laser pulse energy or acoustic detector sensitivity.

The follow-up studies increased the degree of complexity of the imaged structure and extracted parameters by expanding on Method I. In a first-follow up study [35], the aim was to still acquire a 1D PA signal, but to extract from it depth-resolved information of the parameters of interest. The cuvette was discarded for a more informative phantom comprised of an '"intravascular" and an "extravascular" domain, where the "intravascular" space consisted of three tubes placed at a fixed distance from each other, perpendicularly to the transducer and in its line of sight. The tubes were filled with saline suspensions of red blood cells for which the oxygen saturation was gradually varied, like the cuvette content of the first study. The "extravascular" domain was made of Intralipid and further tested in three variants: only Intralipid; mixture of Intralipid and blood; mixture of Intralipid, blood and NIR dye. The problem was tackled through a least-squares minimisation approach between the modelled and measured PA time series. The forward model used once more the delta-Eddington approximation as light model, though now in 2D rather than 1D, and implemented through FEM instead of analytically. Geometric considerations from the PA data were used to partition the domain depth-wise and as a result 11 unknowns were present: "extravascular" concentration of the dye, oxy- and deoxyhemoglobin (c_{dye},c_{HHbev}, c_{HbO_2ev}), "intravascular" concentration of oxy and deoxyhemoglobin for each of the $i = 1, 2, 3$ tubes (c_{HHbi} ,c_{HbO_2i}), scattering parameter k_{scat} and a system parameter K. The wavelength dependence of scattering was assumed known as well as the specific absorption spectra of chromophores. The acoustic wave propagation $p(t)$ was modelled through a numerical time-domain propagation model (numerical implementation of Poisson's integral solution of the wave equation for an acoustically linear, isotropic, homogeneous and non-absorbing medium), with additional corrections for acoustic attenuation and finite detector geometry and relative sensitivity ($p^*(t)$). The PA waves were therefore modelled as:

$$S(t) = K\, p^*(t, \mu_a(\mathbf{r}), \mu_s(\mathbf{r})) \tag{4.19}$$

The same simplex-based search (Nelder-Mead) strategy used in the earlier study was

employed to minimise the error functional between the modelled and experimentally acquired PA time series $S(t)$ and estimate the eleven parameters of interest. The estimation of the c_{HHbi}, c_{HbO_2i} and SO_2 parameters compared fairly favourably with the gold standard CO oximetry outcomes for most background scenarios and tube oxygenation scenarios tested, both in terms monotony (a linear proportionality was seen) and considerable quantitative coherence. c_{HHbi}, c_{HbO_2i} from the two tubes closest to the light source were generally within a 15% error percentage, regardless of concentration. As for the farthest tube from the light source, errors were higher, partly due to lower SNR levels given the greater depth it was located at. Generally speaking, c_{HHbi} and c_{HbO_2i} tended to be overestimated for the most superficial tube and underestimated for the deepest one, which was assumed to probably be due to limitations in the FEM light transport model and its 2D geometry assumption. As expected, measurement resolution for c_{HHbi}, c_{HbO_2i} and SO_2, dependent on SNR, decreased with increasing depth from the light source plane. Visually, SO_2 recovery was better than c_{HHbi} and c_{HbO_2i}, probably due to some degree of error cancellation that comes with ratiometric metrics.

In a subsequent study [56], the method was extended to allow determination of chromophore concentrations from 2D (depth and laterally resolved) multiwavelength images [36] - piecewise constant areas were defined to reduce the problem dimensionality, meaning only a small number of unknown parameters had to be estimated. A similar "intravascular"/"extravascular" phantom was used as in the depth-resolved study, though now with either a 1 or 4 tube-architecture, and with oxy- and deoxyhemoglobin replaced by two inorganic dyes as analogues: copper(II)-chloride dihydrate ($CuCl_2.[2H_2O]$) and nickel(II)-chloride hydrate ($NiCl_2.[6H_2O]$), based on studies on their suitability [56]. Due to ramifications of the same study, the Grüneisen parameter was this time assumed to be a function of the chromophore concentration in the forward model, unlike other studies where the Grüneisen parameter was always assumed constant. The inversion followed a least-squares minimisation between the experimental PA image reconstruction and a purely model-based reconstruction of p_0. The full forward model included once more as light model a FEM implementation of the delta-Eddington approximation in pseudo-3D, i.e. originally computed in 2D and then extended into the assumed homogeneous direction of the phantom (along the tubes) according to a Gaussian distribution weighting. The k-Wave software package [76] was applied to account for 3-dimensional acoustic propagation and detection in a homogeneous, non-acoustically attenuating medium. Unlike the forward models for the previous two studies, a third step was incorporated in the forward model, which consisted of actually performing image reconstruction with the obtained data through a 2D Fourier Transform image reconstruction algorithm [85]. The unknowns to be found were: scattering parameter k_{scat}, acoustic sensitivity of the measurement system K, $CuCl_2$ and $NiCl_2$ concentration in each of the i tubes (c_{Cu_i}, c_{Ni_i}), as well as extravascularly (c_{Cu_e}, c_{Ni_e}). To minimise the error between estimated and experimental PA image $p_{0,recon}$ and retrieve the unknowns, the quasi-Newton Broyden-Fletcher-Goldfarb-Shanno (BFGS) method with numerical (FFD-based) functional gradient calculation was

used - feasible due to the reduced number of unknowns. In terms of outcomes, most concentration values fell within a 15% error margin and followed a satisfactorily linear increase in estimated value vs actual value. As for the estimation of the "intravascular" R value (an entity obtained from c_{Cui} and c_{Nii} and analogous to SO_2), most values fell within a 10% error range, and the average accuracy was 5%. Its uncertainty was found to worsen as concentration ratios dropped. It proved to be more robust than c_{Cui} and c_{Nii} given the fact that it could be determined from the shape of the spectrum alone. The tube farthest from the excitation surface revealed more considerable scatter of values.

Brochu *et al* (2017) [37] also suggested and applied a model-based minimisation strategy experimentally to data acquired in a commercial multispectral optoacoustic tomography (MSOT) system, with the main difference that the output of interest from the inversion was not the estimated optical coefficients, but rather the obtained approximation of the fluence map $\hat{\Phi}$, so that it could then be used to correct the PA image for the spatial distribution of the fluence in a manner somewhat similar to that discussed in Section 4.2. 3D initial pressure distribution from experimental data were reconstructed with a linear model-based reconstruction algorithm, corrected for the system impulse response and thresholded to remove negative values. Inversions were then done slice-by-slice and wavelength-per-wavelength, by defining as error functional the error between the reconstructed image and the modelled absorbed energy density for that slice, both normalised to their integral to deal with differences in data scaling. The forward model employed as light model the delta-Eddington approximation to the RTE in 2D, with piecewise constant absorption and scattering regions as defined by manual segmentation. Grüneisen coefficient was assumed spatially homogenous. Minimisation was achieved with Matlab's *fmincon* function, where the unknown parameters were the optical absorption and scattering values in each of the segmented regions of the slice. The method initialised scattering values to literature values and allowed them to oscillate within 10% bounds. Once convergence was obtained, the resultant modelled fluence was then used to divide the experimental PA data slice at that wavelength, in a hope to correct for non-linearity, spectral colouring and spatial distortion. Single-wavelength experiments on agarose phantoms with varying bulk and inclusion absorption levels showed that after fluence correction a linear relationship could be obtained between the image intensity and the reference optical absorption. Equally nominally-absorbing inclusions at different depths in a same phantom also approached equal image intensity after correction. Multiple-wavelength experiments in phantoms with highly spectrally absorbing background (caused by ICG) also showed that the spectral corruption on flatly absorbing inserts diminished after the correction. *In vivo* tests were also done on nude mice, where manual segmentation at the organ level was done and literature values for μ_s' were used for initialisation. Promising depth-wise recovery of feature intensity was seen as well as alteration of intensity spectra. SO_2 metrics under two oxygen challenge conditions did not show informative differences however. Recognised limitations to be improved on were the 2D nature of the limited fluence, the tight constraint on scattering, the assumption of spatially invariant system

response and Grüneisen parameter. Despite this, the study showed the feasibility and potential of this approach, especially in its phantom studies. Upscaling of this approach for highly-dimensional data rather than a few thresholded areas would need a more efficient minimisation implementation like gradient-based minimisation with calculation of gradients through the adjoint method. To improve robustness of the algorithm and avoid problems of scaling, a direct multiwavelength inversion with chromophores as unknowns would also be more favourable.

The appearance of a highly parallelised GPU implementation and increasing availability of highly-parallelised hardware, such as general purpose GPU clusters are beginning to encourage the use of Monte-Carlo methods. Kaplan *et al* (2017) [165, 166] implemented a model-based minimisation approach using Monte-Carlo as a light model, where the aim was to extract SO_2-equivalent information from multiwavelength 3D PA data. In the experiment, tube phantoms with mixtures of two absorbers were embedded in a background of Intralipid, imaged with a FP sensor and reconstructed with time-reversal. The forward model employed, besides incorporating a Monte-Carlo light model for the fluence, also carried out two other steps: acoustic propagation (k-Wave) and inversion/reconstruction (k-Wave time-reversal), to account for limited-view artefacts from the planar geometry contemplated by the imaging strategy. In a similar spirit to previous studies mentioned, a discrete number of regions with homogeneous optical properties was considered, through segmentation - in this case there were four regions: the background and three tubes. The background was considered to be fully known, as was the scattering in the tubes. Also, the model was such that the concentration of one chromophore informed completely the presence of the other chromophore i.e. the model knew that the tubes contained mixtures of the mother solutions themselves, whose absolute-valued spectra were known, $\mu_a[\mathrm{mm}^{-1}] = R * \alpha_{mother,1}[\mathrm{mm}^{-1}] + (1-R) * \alpha_{mother,2}[\mathrm{mm}^{-1}]$, $R = [0-1]$ (analogous to assuming the total concentration of hemoglobin to be homogeneous and known). As such the model only had 3 unknowns: the SO_2 equivalent ratios R for tubes 1, 2 and 3. The error functional tried to retrieve this by minimising the difference between modelled and measured normalised PA amplitude spectra. The error functional was calculated as follows: first, for each segmented tube region, all pixels were averaged, yielding a PA intensity spectrum $p_0(\lambda)$ for each tube. For each tube, a linear fit was then applied between the experimental and simulated PA average spectrum to deal with different data scaling, and, for the best scaling, the least-squares error metric was obtained. The summation of individual least-squares errors from the three tubes tube was then computed as the total error metric. The minimisation approach used was not gradient-based but parametric/global - coordinate descent algorithm. Promising results were obtained - less than 5% error in percentage points. Authors also alerted to the need of having a large enough domain to avoid boundary issues. Even though forward MC itself can be run fast, this method would not be directly upscaleable e.g. towards highly-dimensional quantification, due to the minimisation approach used - the parametric method was fine for the low number of unknowns, 3, but would have quickly struggled if increased. A gradient-based method

would be adviseable but, since MC has no analytical form, gradient calculation is not trivial - though some advances are being made in the direction of obtaining MC-based stochastically sampled gradients [164]. Another aspect to consider is that the current inversion looks at the PA spectral shape over an integrated spatial region - therefore disregarding the rate of decay therein - and also normalises the obtained spectra before comparing, therefore in its current form it would not be able to give absolute chromophore concentrations. This is the object of future studies.

4.6 Emerging machine-learning approaches

Machine learning has been playing an increasing role in various fields, especially for image segmentation, registration and classification. Its use for PAT has not been much explored yet, but there is potential. Kirchner *et al* (2017) [177] have recently proposed potentially the first machine-learning approach for qPAT, where the fluence is learnt and afterwards predicted at the voxel level, by looking at its local context. Optical absorption in that voxel is then found by dividing out the absorbed energy density by the predicted fluence. Supervised learning is done by using as training data voxels from a finite set of volumetric virtual phantoms to which a random forest regressor is applied, where each voxel is labelled with its true fluence (as found by MCX) and assigned a feature vector (or so-called context image) that takes into account the PA data obtained in a given vicinity of the voxel of interest and also a fluence contribution map, which informs on the probability with which light arriving at the voxel of interest has passed through each of the other voxels in the vicinity, assuming homogeneous background and a specific source position and shape. A few datasets were assessed in terms of prediction error with unseen data. In each, samples were made by varying either the vessel radius, the vessel optical absorption or the number of vessels (or a combination of these). A portion of the samples in each dataset was used for training whilst other portions were used either for either validation or testing. Results were promising in giving small fluence estimation errors - the algorithm seemed to be able to predict correctly fluence deviations from the standard homogeneous background as caused by insertions/vessels (i.e. could predict well the spatial distortion in fluence relative to a homogeneously absorbing background). Nevertheless, an issue that needs to be addressed or assessed in future studies was that in this study, all samples, regardless of dataset or on their allocation to the training or testing subset, were simulated with the exact same background optical properties. Also, these same true background optical properties were always plugged in the model *a priori* through the fluence contribution maps (used to generate the feature vectors for classification). No study was done on the generalisation error once any background variations in absorption were introduced and it is not clear how this dimension could be incorporated in the learning process. Other issues that remain open are the susceptibility to scattering variations and whether this voxel-by-voxel rather than full-image learning

approach, despite its benefits in speed, dataset size for training and such, can be as robust or deal with more global parameters, e.g. an unexpected global offset or scaling relative to the training data.

Tzoumas *et al* (2015) [178] suggested using a combination of machine learning and MBI to account for spectral colouring, even without knowledge of the optical properties or explicit formulation and computation of a light propagation model. It involved describing wavelength-dependent fluence distributions as a linear combination of a finite number of reference basis spectra (eigenspectra). These eigenspectra were found through principal component analysis on large simulated datasets of fluence in blood-rich virtual phantoms. This knowledge was then incorporated in a MBI framework minimising the difference between measured and modelled PA data, but where the model did not calculate fluence based on a typical optical propagation model and on updates of all optical estimates at that iteration but rather was given as a sum of a mean fluence map and a linear combination of three eigenspectra maps weighted by a scalar factor each that were also unknowns in the inversion. Results in simulation and *in vivo* were promising but more generalisation studies on robustness are needed, as well as stricter experimental validation. In this case machine-learning outcomes were incorporated to reformulate the forward model, but other strategies may use it to define new priors or regularisation terms or as interleaved classification steps in MBI (Malone *et al*'s (2015) study addressed before is an example in that direction, where clustering steps are intertwined with MBI steps to find, classify and update properties for a set of tissues, information which is then used to regularise/constrain the MBI search). These hybrid MBI/machine-learning approaches may show great promise as they can combine sturdy statistical information on typical behaviour (increasing robustness) with the greater grasp on theoretical accuracy and adaptability of MBI.

4.7 Discussion

This Chapter gave an overview of suggested and employed qPAT strategies, with a focus on experimental implementation. Conventional linear spectroscopic unmixing can provide accuracy in specific scenarios, besides being fast and easy to implement. Nevertheless, it will only apply for very constrained scenarios since its underlying assumptions do not mirror the real characteristics of the photoacoustic problem. Some approaches opt for dealing with spectral corruption by dividing out the fluence spectrum from the PA signal before inverting for the chromophores with linear spectroscopic unmixing, but not only is it hard to find an appropriate model and parameters to yield this estimate, if the estimate is not faithful enough (whether resolution or accuracy-wise), non-linearities between the PA data and μ_a will remain encoded in the corrected data and will not be properly dealt with during the subsequent linear unmixing step - for the current standing of practical and clinical studies though, this seems to provide the best compromise

between ease-of-implementation and reasonable data treatment (though not nearly the most accurate). Statistical linear unmixing strategies and machine-learning approaches are becoming fashionable, but still behave as a black-box. They will by definition rely on certain heuristics that, though certainly useful in certain situations, will never fully and properly reflect the true behaviour of the problem (namely due to the underlying assumption of linearity of some sort and due to inevitable generalisation errors in such approaches). Their generalised robustness and range of validity is hard to assess, therefore careful validation will be required on case-by-case scenarios.

Model-based minimisation strategies can be highly accurate given the explicit incorporation of a fluence model. They are inherently able to deal with non-linearity and to cope with spectral colouring and spatial distortion. They are also flexible enough to incorporate various assumptions, priors and to explain additional unknowns if given sufficient data and a carefully posed problem. Until recently, one of their biggest disadvantages was their lack of ability to deal with the high-dimensionality of the data, leading either to infeasible or prohibitively slow quantifications or a forced reduction of the number of unknowns to very few, which stifles some of the main selling characteristics of PA - its high resolution, depth of penetration and volumetric nature. This hindrance is changing thanks to improvements in computing power and efficiency of algorithms. What is the least trivial is seamlessly transposing algorithms from simulation to experiment due to assumptions that cannot be easily harmonised with the experimental reality. Often these algorithms assume perfect acoustic reconstruction of p_0 (e.g. assumptions of no noise, no artefacts, no incomplete data due to limited view, directionality or detector bandwidth, perfect acoustic reconstruction model, known acoustic properties), assume known and constant Γ, assume low to no uncertainty in many model input parameters (beam profile and position, scattering, spectral shape) or for instance assume an acquisition geometry with enough SNR to cope with the low sensitivity of PA to scattering. The light model itself also needs to be carefully considered depending on the application. Some experimental studies have focussed on this ensemble of considerations and showed promising qPAT outcomes in highly discretised or 2D scenarios. Once highly-resolved, volumetric and absolute quantifications of chromophores are pursued these issues will need to be dealt with even more carefully. After this, *in vivo* pre-clinical and clinical applications will be in reach.

Part II

Phantoms

Chapter 5

Review of phantom materials and characterisation methodologies

5.1 Motivation

Part I highlighted the potential of multiwavelength PAT as an imaging technique and the special interest in extracting quantitative information from these data. This quantification, especially when considering *in vivo* and clinical scenarios, requires algorithms that can give accurate estimates with low uncertainty, be applicable in various situations, be robust to experimental uncertainties and noise and have a demonstrated validity over the full range of scenarios in which the method will be applied. PA phantoms are invaluable to carry out proof-of-concept, validation and optimisation in qPAT with the rigour, ground-truth and repeatibility required. On one hand, studies with phantoms with realistic and known properties would be very valuable for state-of-art qPAT propositions that have only yet been implemented and tested in simulation and that wish to extend their scope and optimise their performance in experimental scenarios (e.g. [41, 157, 163, 179]). Likewise, phantom assessment would be of great aid to *in vivo* studies that have directly applied quantification algorithms of varying degrees of complexity and wish to assess their robustness, uncertainty and range of validity (e.g.[15, 22, 45]). With the advent of increasingly faster and higher resolution instrumentation [26, 180], as well as increasingly complex and efficient theoretical algorithms that allow high-dimensional and fine-resolution quantification both at single [162, 163, 181] and multiple wavelengths [157], having access to a qPAT phantom that is tissue-realistic, well-characterised, tunable, stable and spatially-detailed is even more pressing and desirable.

Usually a good starting candidate material/phantom to explore would be one that is already used in standardised routine image quality assessments. Standardised consensus test methods and phantoms exist for several biomedical imaging modalities, from MRI to x-ray tomography and ultrasound, and are traditionally used for quality assurance and

monitoring of laboratory and commercial systems during development, manufacture and repeated use. For photoacoustics however, there is no such standardised or consensual material or set of methods. Finding fit-for-purpose phantoms and chromophores for PA is still an outstanding challenge [56, 182]. The requirements for a photoacoustic phantom are more stringent than for many other modalities, largely due to its hybrid nature. For example, phantoms designed for use in diffuse optical imaging [183–185] may not have suitable acoustic properties; phantoms designed for use in ultrasound [186, 187] may not have suitable optical properties. Since, some studies have therefore focussed specifically on PA - namely on characterising materials that could be used for general, proof-of-concept PA studies [188–190] and more recently on the creation of a suite of phantoms for system characterisation and quality control of prospective commercial systems [191]. Progress is being made but it is still an open field of research.

When considering an ideal all-purpose PA phantom, the following general characteristics would ideally be met and known in a well-characterised manner:

- tissue-realistic, stable and controllable acoustic properties;
- tissue-realistic, stable and controllable optical parameters;
- tissue-realistic values for relevant thermoelastic properties;
- realistic and versatile architecture;
- photo- and mechanical stability during the imaging acquisition procedure;
- long-term stability under storage and repeated use;
- reproducibility, ease and high throughput of fabrication.

where the extent, accuracy and relative priority needed for each of these would depend on the application.

Namely, when considering PA phantoms for *multiwavelength* PAT or full *quantification* there will be additional layers of difficulty compared to phantoms for quality control or other proof-of-concept. A greater versatility will be desired and the characterisation demands will also extend beyond the typical characterisation suite, both in type (e.g. access to Γ) and breadth of information (e.g.access to *multiwavelength* optical properties, *broadband* acoustic properties) and stringency in the accuracy and uncertainty of the ground-truth (since the phantoms are to be used as benchmark for absolute quantification techniques).

The objectives in this Chapter are to:

- Highlight the need for standardised consensus PA phantoms and the need to gear these for qPAT applications;
- Review the existing options for PA - and qPAT - phantoms (Section 5.2) - the overview is divided in terms of structure/architecture, base materials and range of additives;

- Specify the requirements for an ideal qPAT phantom and what sets them apart from more general PA phantom requirements (Section 5.3);
- Highlight appropriate/desirable characterisation techniques for candidate qPAT materials and detail those used in this work Section 5.4;

Afterwards, in Chapter 6, a thermoplastic, PVCP, is fully assessed and characterised in terms of its potential for qPAT. In Chapter 7, aqueous solutions of sulphate salts are characterised in terms of their suitability as chromophores and eventual hemoglobin surrogates.

5.2 Review of PA phantom materials

When considering photacoustic phantoms, no extensive review is available, nor a general consensus on which type of material would be ideally suited for photoacoustics as a modality. In practice, it is hard to find a formulation that perfectly matches all the requirements of a so-called ideal phantom and that is accompanied by accurate and rich characterisation. An even greater deficit exists in finding and sufficiently assessing suitable phantom materials for multiwavelength qPAT. Until now, a range of phantom types and integration strategies have been employed depending on the need and application.

This section aims to provide a review on existing candidate materials for PA imaging. It draws information from existing reviews on a range of acoustic phantoms and optical phantoms, the existent PA-focussed phantom studies and the more general body of experimental PA studies where phantoms were used along the process. The review is divided according to 3 core aspects that need to be considered when deciding on creating a phantom for experimental studies from a practical perspective: the structural configuration and arrangement of the phantom, the matrix material used as a base and finally the range of additives to tune its properties. Ideally these aspects would be tackled independently and complement each other, but trade-offs need to be met most times. For instance, if a liquid phantom is chosen due to the advantageous extensive characterisation of the acoustic and optical properties of water in the literature and the ease to include absorbers as additives, some demands on structure (e.g. capability of suspending inserts or moulding the overall shape) may be compromised.

5.2.1 Structural aspects

The structural aspects considered when designing a phantom include overall geometry and size as well as the geometry, size, depth and number of the inserts of interest. The preferred overall configuration of the phantom will depend on what type of sample is typically under study, the type of scanning system available, the field-of-view, the end-application envisioned, the computational load of the algorithm and more. As for the

inserts, the preferred geometries will depend on the application or metric of interest - if a biomimetic phantom is desired, complex geometrical shapes may be chosen to emulate tissues or tubular shapes to emulate vessels; if a phantom is desired for image quality metrics such as resolution, uniformity, SNR or depth of penetration, more abstract shapes (e.g. spherical) or thin wires may be preferred.

Different matrix materials can be used to deliver the desired geometry (although sometimes materials and architecture restrict or condition one another). Broadly speaking, the type of phantoms used in PA can be summarised as *in vitro* (this would correspond to simple cuvette measurements, e.g. [104]), *in vitro* within water (cases in which tubular structures are used but within a medium such as a water tank, e.g. [16, 44, 118]), *in vitro* within another medium (where water is substituted by a more tissue-realistic medium such as Intralipid, e.g. [35, 36]), solid phantoms with high level of abstraction (e.g. [139, 146]) and solid phantoms emulating tissue structures (e.g. [174]).

Liquid-based phantoms bring advantages in terms of flexibility and ease of preparation, and are also usually better characterised in terms of material properties both with and without additives. Nevertheless, they need to be prepared anew each time, leading to variability, and might provide difficulties in achieving certain geometries or maintaining certain particle-based additives in an homogenised manner. On the other hand, solid phantoms can be made with certain materials that promote long-lasting use in a stable manner and facilitate the creation of complex shapes and suspension of particle additives. Nevertheless, as will be discussed in the next section, they may be less well characterised in terms of material properties, both in terms of the matrix itself and when additives are added. Manufacturing may also be more cumbersome, or even prohibit adding certain inclusions without degradation.

Recent developments in 3D printing technology [192] have allowed the creation of optical phantoms with detailed and controlled geometry and inclusions [193, 194]. Unfortunately, most available materials (PLA, ABS) that would be suitable for use in currently available off-the-shelf 3D printers have very high speed of sound (>2000 ms^{-1}) [195, 196], are rather non-elastic and are prohibitively hard - supporting shear waves. Hydrogels have been printed for tissue engineering applications [192, 197] and there are indications that it might be possible to apply the principles of 3D printing with paraffin wax or gel wax, though this is still a new field of study [198]. Also, the precision of these systems as well as minimum resolution achievable still need improvement [192].

5.2.2 Matrix materials

This section reviews the matrix materials that can be used as base for the phantom.

Matrix	Advantages	Disadvantages
Water/Coupling-gel [56]	• Easily obtainable; • Largely optically transparent; • Well defined optical and acoustic properties; • Sound speed similar to biological tissue, though somewhat lower [186]	• Cannot be used to easily sustain an insert; • Does not allow tuning acoustic properties; • Speed of sound varies significantly with temperature [186]; • Allows only reduced flexibility in architecture - shape, layering.
Hydrogels e.g. agar, bovine gelatin [56, 190]	• Solidity for suspending particle additives; • Can have dye absorbers added to it; • Largely optically transparent, with the precise levels dependent on the base material used; • Tissue-like speed of sound. • Relative ease of preparation.	• Concentration range typically used significantly affects sound speed [56]; • Well-defined inserts are short-lasting due to diffusion; • Absorption of water; Water soluble dyes need encapsulation [191]; • Reaction with nickel and copper ions, changing optical absorption [56]; • Differing dye optical absorption in solution from absorption in gelatin [190]; • Cross-linking time; • Susceptibility to dehydration and bacterial growth in storage, thus requiring additional careful mitigating measures [186, 190]; • High susceptibility to physical damage [186]; • Low temperature stability at physiological temperatures, causing structural integrity loss; • Limited re-use capability, heavily conditioned by imaging, handling and storage conditions. [186]
Polyvinyl alcohol (PVA) [199, 200]	• Solidity for suspending particle additives; • Adjustable intrinsic μ_s; • Tissue-like speed of sound; • Greater longevity and structural rigidity than hydrogels;	• Extensive preparation (several freeze-thaw cycles spanning each several hours) [186]; • Sensitive to humidity [186]; • Inhomogeneities due to differential heating and cooling rates [200].

Polyvinyl chloride plastisol (PVCP) [188, 191]	• Solidity for suspending particle additives, speed of curing mitigates precipitation; • Insoluble in water; • Largely optically transparent; • Tunable acoustic properties: hardener/softener; • Stable during storage, up to 6 months [191, 201]; • Can be used and re-used for imaging.	• Non trivial preparation; • 180^{o}C temperature needed for preparation might cause dye denaturation so only pigments should be used; • Higher acoustic attenuation than most soft tissues except breast; • Lack of a widely available supply chain by reference chemical suppliers.
Silicone e.g. room-temperature vulcanising (RTV), polydimethylsiloxane (PDMS) [189]	• Solidity for suspending particle additives; • Insoluble in water; • PDMS is largely optically transparent (for RTV some optically clear grades exist) • Can be embedded with inorganic optical scatterers and absorbers; • Capacity to be embedded with acoustic scatterers like e.g. glass and plastic microspheres; • Stable during storage - free of contamination [202]; • Can be used and re-used for imaging; • Variable Young's modulus (hardness), englobing biological tissue levels; • Relative ease of preparation. • For PDMS: Machineability and capability of creating microfluidic channels	• Limited by high acoustic attenuation (>9.8 @ 3 MHz, >39 @ 11 MHz) [203] and low speed of sound (<1000 ms^{-1}) [186]; • Organic dyes might not be suitable for addition [183]; • For RTV: Cost [183]; • Hardening time.
Paraffin wax	• Solidity for suspending particle additives; • Has had its optical absorption tuned with wax colors [204, 205] • Has had its acoustic attenuation tuned with glass microspheres and carnauba wax [206] • Non-toxic [206] • Stable during storage - free of bacterial contamination and dehydration [206]	• Material possibly already highly scattering, restricting tunability [207] • High temperature needed for preparation might cause dye denaturation; • Higher acoustic attenuation than most soft tissues except breast; • Lack of a widely available supply chain by reference chemical suppliers.

Table 5.1: *Advantages and disadvantages of several background media materials, in the context of Photoacoustic Imaging. Adapted with permission from [182].*

Important characteristics of the matrix include its longevity, resistance to fungal and bacterial infections, appropriate acoustic attenuation and dispersion, low optical absorption and no fluorescent background, solidity for suspending further particles, ease of preparation, processability and reproducibility [191, 202]. Candidate materials for the

background medium/matrix include water, hydrogels (agar, bovine gelatine), Polyvinyl alcohol (PVA), Polyvinyl chloride plastisol (PVCP), polyester resin, epoxy resin, room temperature vulcanising (RTV) silicone and paraffin gel wax.

Apart from the first example, water, all other materials will yield a solid phantom. Table 5.1 provides an overview of the various materials, alongside some of their advantages and disadvantages for PA. It should be noted that nominally identical materials may exhibit slightly different properties, especially if different suppliers or preparation techniques have been used. Materials such as polyester resin and epoxy resin, despite being popular optical phantom options due to their optical transparency and long term stability [183, 185], are not appropriate for photoacoustics due to their high sound speed and attenuation, and the support of fast shear waves [186], and were therefore not included in the list.

There have also been studies using animal tissues directly as matrix (e.g. turkey, chicken, pork) which may in some ways be thought to provide an ideal set of material properties, but these bring issues such as reproducibility, low temporal stability and cumbersomeness of use and characterisation.

5.2.3 Chromophores and other additives

Though the matrix material itself can provide some of the desired characteristics, it is common that additives are added to tune the properties of the phantom in a versatile and flexible way, usually beyond the bounds of what the preparation of the background matrix would allow.

One class of additives commonly considered are optical scattering elements, to emulate tissue scattering properties. These include titanium dioxide TiO_2; microspheres and Intralipid. Details for these can be found in Table 5.2.

In some instances acoustic scatterers such as aluminum oxide AlO_2 or glass microspheres may be considered to tune the acoustic scattering/attenuation behaviour [186].

Optical absorbers are arguably the main entities of interest when considering a phantom for photoacoustics, since they are the main providers of the source of contrast in PA imaging. They are even more essential for qPAT, as they are the main elements of interest to be quantified. An overview of endogenous and exogenous chromophores was given in Tables 2.1 and 2.2 respectively, though more focussed on their potential and utility for pre-clinical and clinical studies. Using endogenous chromophores in phantom studies - say blood - has the advantage that they often are what we want to estimate *in vivo*. However, they may not be easy to obtain or isolate and may present degradable or dynamic behaviour *in vitro* which is different from the *in vivo* scenario (e.g. blood clotting, blood deoxygenation). Exogenous contrast agents provide well-defined optical properties, and are available in a wide range (varying in peak wavelength, bandwidth, intensity, etc). However, various other factors should be considered. They may not be

Scatterer	Advantage	Disadvantage
Intralipid	• Empirical relationships of wavelength and concentration dependence of μ_s and g are available [208]; • In alternative, Mie Theory can be employed.	• Empirical method implies uncertainty and error; • Mie Theory is often precluded due to difficulty in assessing particle size distribution; • Speed of sound increases linearly with concentration; • Copper salt inclusion causes peroxidation [56]; • Organic dyes suffer changes in absorption spectrum [56]; • Poor temporal stability [209] • Intralipid in hydrogels afftects acoustic attenuation spectra [190]
Polymer microspheres; Quartz glass microspheres [183]	• Specific and defined size and shape information, facilitating Mie theory calculations; • "Gold standard" for characterisation.	• Needs a suspending medium; • Might be difficult to maintain suspension homogeneity.
Titanium dioxide	• Properties can be experimentally defined (e.g. diffuse reflectance + light model) [188, 210]; • Widely used for engineering applications.	• Needs a suspending medium; • Might be difficult to maintain suspension homogeneity; • Although Mie theory can be employed [211], aggregates are not perfectly spherical.

Table 5.2: *List of optical scattering agents that can be used, including some advantages and disadvantages.*

non-scattering absorbers (e.g. india ink) and may not accurately represent endogenous optical characteristics when used in a phantom scenario. Furthermore, some may not be photostable. Since photoacoustic techniques use high peak power light sources and sometimes prolonged imaging times, resilience to transient and permanent photobleaching is essential. Most organic dyes (namely cyanine-based [56, 140], azo-based [1] and basic dyes like cresyl violet [140]) have low transient and permanent photostability. Gold nanoparticles can also exhibit changes in absorption after prolonged exposure [189], with the added difficulty that their photoacoustic efficiency is not straightforward to model and characterise [51, 52]. The same prohibitive issues affect typical fluorescence proteins [54, 140], and although these proteins can be genetically modified into relatively stable chromoproteins with increased photoacoustic efficiency, the fabrication and purification is labour-intensive and complex, and gives final protein yields typically in the tens or hundreds of μl, which is usually not enough for phantom-based studies [54]. While inorganic absorbers such as prussian blue, $CuCl_2.2H_2O$, $NiCl_2.6H_2O$ were shown to be highly photostable and to have relevant spectra [56], the absorption of the latter two does not vary linearly with concentration or when mixed, therefore deviating from the typical

Beer Lambert assumptions, whilst prussian blue was found to not behave in a predictable manner when mixed with the most common background composition, Intralipid [56]. In fact, the matrix in which the chromophore of interest is meant to be embedded can often affect the specific absorption spectrum, e.g. there have been reports of red-shifting of the specific absorption spectrum of azo-dyes Direct Red 81 and Evans Blue in gelatin [190], of a blue-shift and amplitude rise of $CuCl_2.2H_2O$ in gelatin [56, 212] and of considerable changes in cyanine dye ICG when put in different solvents [213]. Whilst issues of absorption linearity with concentration, change in absorption behaviour when in mixture with other species or backgrounds and intricate photoacoustic efficiency behaviour may not be an issue in most PA studies of more qualitative nature, for multiwavelength qPAT they may pose a serious hindrance unless there is access to intuitive calibrating functions that can be efficiently incorporated and calculated in the model.

5.3 Requirements for a quantitative PA phantom

The previous section has shown that in the past few years there has been a growing realisation that phantoms and chromophores especially designed and characterised for PA are needed, especially for system characterisation and quality control once clinical translation fully occurs [191]. However, the criteria and characterisations in these studies still fall short of what is required for qPAT, as the existent studies are more focussed on the ability to assess qualitative or relative metrics (SNR, contrast, uniformity, spatial resolution, penetration depth, spatial accuracy and distortion) rather than aimed at studying algorithms that retrieve actual material physical properties in an absolute manner. More extensive phantom and additive studies are therefore needed, whether in their stringency (accuracy, confidence intervals), their breadth (expanding wavelength range, frequency range, fluence range) and their nature (e.g. accounting for photoacoustic efficiency). The aim below is to lay down which properties and characterisations are needed for a complete and versatile phantom for multiwavelength qPAT.

The requirements for the optical properties of a multiwavelength qPAT phantom are the main area of concern and focus compared to those for other PA phantoms. To summarise, an ideal set of chromophores for phantom studies of multiwavelength photoacoustic imaging will need to fulfil a set of characteristics, some or all of the following depending on the application:

- Low propensity for peak power dependent transient effects such as ground-state bleaching/saturation [56, 214]. This is necessary when using optical pulses with high peak power (pulsed photoacoustics), and when it is important that the specific absorption spectra are known accurately.
- Low propensity for permanent photobleaching [54, 56, 189]. This is essential when the imaging system requires the use of multiple illumination shots, or when the same

phantom will be used multiple times, both to prevent the absorption spectrum from changing over time and to maintain the photoacoustic signal strength.

- Absorption spectra at visible-NIR wavelengths that are good analogues, in a general sense, to endogenous chromophores and exogeneous contrast agents used *in vivo*. Note that for specific QA tests at commercial or clinical level, absolute agreement (a contrast surrogate) may be wanted to a given (pre-)clinical contrast source, but for most **QPAT!** (**QPAT!**) studies under development (early-research and development) what is crucial is mostly the uniqueness and interplay of spectral shapes of the chromophores and an acceptably similar magnitude (contrast analogues).

- Compatibility with the phantom matrix in which they will be embedded or mixed, i.e. they form stable and homogeneous mixtures, and the absorption spectra of the mixtures can be measured (or calculated). This is important when the absorber will be mixed directly with the matrix, rather than remaining separate within a channel, for instance. [56, 190]

- The absorption coefficient μ_a can be written as a linear sum of the molar absorption spectra of the constituent chromophores α_i weighted by their concentrations c_i:

$$\mu_a(\lambda) = \sum_{i=1}^{N} \alpha_i(\lambda) c_i, \tag{5.1}$$

  where λ is the optical wavelength and N is the total number of chromophores. This entails that:

  1. The specific absorption spectra $\alpha_i(\lambda)$ do not depend on the concentrations of the chromophores themselves, or, if they do, their dependence can be written using simple functional expressions. If this is not the case, then it would be necessary to measure and tabulate the spectra for all concentrations of interest, which could be very time-consuming.

  2. The specific absorption spectrum of one chromophore does not depend on the concentrations of the other chromophores present or any other constituents of the phantom [212].

  If this is the case, linear spectroscopic techniques can be used to estimate the concentrations from the absorption coefficients.

- Fast, simple, repeatable and cheap procedure that allows the chromophore to be produced in sufficient quantity.

For qualitative studies it may be sufficient that the added absorbers are stable and can provide absorption at tissue-realistic levels for a given single wavelength with some degree of tunability. For full multiwavelength qPAT, ideally all the above would be respected.

Besides suitable optical properties, for qPAT, it is crucial to have access to well-characterised thermoelastic efficiency (Grüneisen parameter Γ) of both the matrix material and the chromophores [56]. Γ does not need to be highly analogous to behaviour in soft tissues but should be significant enough to generate meaningful PA signal (higher Γ can actually bring useful gains in SNR). It should also be known, since most suggested theoretical qPAT algorithms will already assume Γ is either known *a priori* or constant throughout the domain [34]. Knowing Γ is also important as ground-truth in inversion frameworks where Γ is included as an additional unknown to be estimated [109, 156]. Typical Γ values for some tissues can be found in [112]. Usually minimal fluorescent behaviour (null quantum yield) will also be desirable, such that the thermalised energy is maximised and confounding parameters in the qPAT problem are minimised.

Regarding the acoustic properties, whilst for clinical quality control being able to closely match tissue levels is a primordial goal, for qPAT this may not be as crucial - being within a reasonable range will usually suffice. The main priorities are rather - having access to *well-characterised* sound speed and acoustic attenuation and doing so over a *broad range of frequencies*. This is needed to properly account for the acoustic behaviour during reconstruction: erroneous sound speed would lead to blurring or artefacts in the acoustic reconstruction, whilst incorrect estimation of acoustic attenuation would affect the retrieval of the correct amplitude of the initial pressure distribution. PA-generated signals extend to several tens of MHz [4], with the highest frequencies being responsible for much of the finer resolution features of interest, so ideally broadband data of acoustic properties will be available. Reference values for soft tissue can be found elsewhere [98, 215].

Finally, when choosing a phantom it will be important to assess the suitability of the material for imaging applications, namely the feasibility and ease of manufacturing and constructing various phantom structures with interest for imaging purposes, beyond classical image quality assessment geometries.

5.4 Material property characterisation

This section outlines the methods that can be used for the characterisation of phantoms and tissue mimicking-materials, offering a small overview of existent techniques and putting special emphasis on those chosen and used in this work. The essentials of the experimental setup and data processing are also given when necessary.

5.4.1 Optical absorption

Optical absorption μ_a in non-turbid media can typically be found through light transmittance measurements, with a spectrophotometer, according to:

$$\mu_a = A\, ln(10)\frac{1}{\Delta x} = -ln\left(\frac{I_{sample} - I_{background}}{I_{reference} - I_{background}}\right)\frac{1}{\Delta x}, \tag{5.2}$$

where I_{sample} is the detected light intensity when the sample is placed on the light path; $I_{reference}$ is the detected light intensity when a reference material (e.g. empty cuvette) is in place; $I_{background}$ is the background intensity/noise detected and is done with the light shutter closed; Δx is the sample/cuvette thickness; $A = -log_{10}\left(\frac{I_{sample}-I_{background}}{I_{reference}-I_{background}}\right)$ is absorbance, as typically reported by spectrophotometers. In this study, a dual-beam spectrophotometer (Lambda 750S, Perkin Elmer, Waltham, MA, USA) was used, capable of providing readings between 200-2500 nm for quoted maximum accurate absorbance of 6 A (i.e. minimum accurate transmittance of 0.0001%, below which reduced SNR with the sample in place jeopardises estimations). Measurements of solutions in a typical physiological range (e.g. 0.1-1 mm^{-1}) yielded residual uncertainty - with intra- and inter-sample deviations usually well below 1% of the absolute μ_a.

Another way of characterising the absorption coefficient is through photoacoustic spectroscopy (PAS). Such an approach can be important if the sample of interest has an absorption above the typical dynamic range of conventional spectrophotometers and its dilution is not straightforward or desirable. More importantly, whilst conventional spectrophotometers use a continuous-wave (CW) source, PAS uses the high peak power, ns-pulse sources typical for PAI measurements. This therefore allows assessing relevant phenomena such as long-term photostability (propensity for photobleaching) and transient photostability (e.g. occurrence of ground-state bleaching) that would go unnoticed with a CW source. The simplified schematic of a PAS experimental setup can be seen in Figure 5.1. The excitation is generally provided by a fibre-coupled Nd:YAG pumped wavelength-tunable optical parametric oscillator (OPO) system. The sample is placed within the water-filled tray (or, if a liquid, placed first inside a cuvette) and illuminated from the top. The resulting PA signal $S(t)$ [V] can then be detected by a transducer at the bottom of the tray [140] and, assuming the medium is homogeneous and non-scattering, is described as:

$$S(t) = K\Gamma_{sample}\Phi_0\mu_{a,sample}e^{-\mu_{a,sample}c_{sample}t}, \tag{5.3}$$

where K is a scaling parameter accounting for the sensitivity of the detection system, Γ_{sample} is the Grüneisen parameter, Φ_0 is the incident fluence on the sample, $\mu_{a,sample}$ the absorption coefficient and c_{sample} the speed of sound of the sample material. In the specific case of the system available, to know the light fluence Φ_0 for each $S(t)$ acquisition, online integrating sphere measurements are also made at the proximal end of the fibre, V_{pd}, and stored. A light fluence calibration procedure is then necessary, usually done at the beginning or end of the acquisition session, establishing the relation between these

integrating sphere voltage readings and the powermeter measurements at the distal end of the fibre (mJ), for each of the wavelengths of interest. The resulting calibration factor k [mJ/V] can then be used to find the incident fluence $\Phi_0 = k\,V_{pd}$ for each instance.

After PAS data have been acquired for these non-turbid, homogeneous samples (which will be a set of bipolar PA signals with exponential decay, one per wavelength and repeat - usually 150), retrieving $\mu_{a,sample}(\lambda)$ related information can be done in two ways: either spectral fitting is performed to the exponential curve, for which only knowledge of c_{sample} and the temporal resolution is needed, or the peak-to-peak amplitude can be found ($Vpp = S(t = 0) = K\Gamma_{sample}\Phi_0\mu_{a,sample}$) and normalised for the incident fluence Φ_0 at each wavelength, such that $\frac{Vpp(\lambda)}{\Phi_0(\lambda)} = K\Gamma_{sample}\mu_{a,sample}(\lambda)$. This latter method does not retrieve absolute $\mu_{a,sample}(\lambda)$ but only up to a multiplicative constant ($K\Gamma_{sample}$) of it. However, the advantage over the exponential fitting method is that its sensitivity and dynamic range are greater, since it does not require a well-defined curve.

PAS system characterisation within the group, against water or known IR-dyes in methanol, showed that the exponentially-extracted μ_a had as detection limits 0.5 to 15 mm^{-1}. Within this range, deviations in accuracy did not exceed 5% of the true absolute value. Furthermore, the deviation decreased with increasing true absorption (e.g. deviations were mostly below 2.5% and 1% above 1 and 2 mm^{-1} respectively). Considerable deviation in the estimation started to be introduced when SNR levels of acquired signals fell below 5 dB.

5.4.2 Permanent photostability

Photobleaching is a permanent, non-reversible phenomenon, where long-term excitation (minutes to hours) causes photochemical reactions that permanently alter the covalent bonds of the molecules and impair its ability to absorb photons or fluoresce. A substance that is resistant to photobleaching is said to possess permanent photostability. To verify photostability under long-term exposure to high peak power, PA signals of newly prepared samples can be monitored and recorded over a prolonged period with a PAS measurement system. The temporal evolution of the peak-to-peak amplitude or of the fitted μ_a can then be analysed (decreases in absorption indicate photobleaching) [54]. Assessing absorption behaviour through the amplitude of the PA signal ($\sim K\Gamma\mu_a$) has as disadvantage that amplitude over time can be affected by other concurrent effects besides μ_a changes. A concurrent trend of increasing Grüneisen parameter, which also increases PA amplitude, can occur due to the gradual heating of the sample being probed. On the other hand, though assessing absorption behaviour by exponential fitting of the PA signal is robust to fluctuations in fluence or Γ, it relies on probing a certain depth range where μ_a is assumed constant, which might not always be a suitable or robust approach when dynamic and spatially-variant photobleaching phenomena are expected to be occurring.

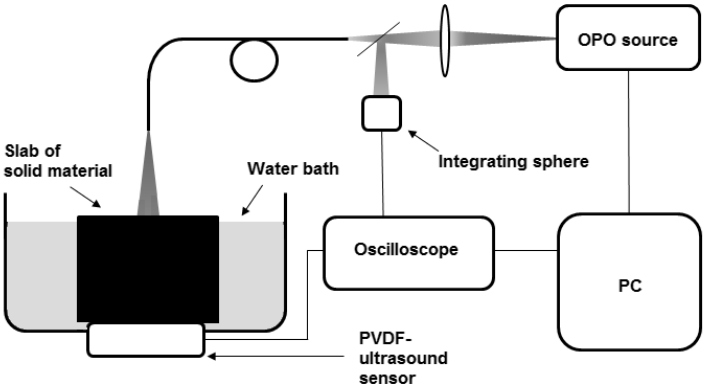

Figure 5.1: *Schematic of photoacoustic spectroscopy setup.*

5.4.3 Transient photostability

Apart from photobleaching, substances can also undergo a series of distinct and concurrent non-linear photophysical phenomena such as ground-state depletion, stimulated emission and excited state absorption [216]. These are transient, i.e. reversible, since they do not alter the composition or conformation of the molecules. Characterising these phenomena is not only important if a fully-characterised, stable and reliable qPAT phantom is desired, but also for *in vivo* studies, where a thorough knowledge of the photochemical and photophysical behaviour of the endogenous or exogenous chromophores of interest at high peak power is essential (PA relies on excitation pulses of nanosecond-order duration and power in the ~ MW). Chromophores that do not experience such phenomena are said to possess transient photostability.

The typical monitorisation of PA signal over time used to assess permanent photobleaching (with time resolutions in the tens of milisseconds depending on laser pulse repetition frequency (PRF)) would not be appropriate to assess transient photostability since these transient effects take place in the sub-nanosecond to nanosecond time regime [217], meaning their temporal onset and trend would go unnoticed.

Pump-probe (time-resolved) spectroscopy techniques are ideally suited to give a thorough and quantifiable characterisation of each of these phenomena [218]. A PAS-base variant has also been suggested recently [219] but these systems are not widely available.

A simpler way of assessing more generally whether a sample has transient photostability or not, adopted in this work, is by comparing the μ_a spectral behaviour of the absorbing species at low (~W) and high (~MW) peak power. Photostable samples should match in absolute values and spectral shape regardless of the modality. One possible comparison can be between the continuous-wave standard spectrophotometry and the PAS measurement system with a typical PA source [54], both described in Subsection 5.4.1. An alternative to PAS can be to perform classical optical transmittance (as in the spectrophotometer) but with high peak-power excitation from an OPO a typical wavelength-tunable ns-pulsed PA source. In our cases, a simple setup was created, as shown in simplified

diagram of Figure 5.2. Light detection was done by a powermeter (PowerMAX PM10V1, Coherent, Santa Clara, CA, USA). The procedure was roughly as follows: 1) zero the powermeter; 2) measure optical power with sample in the beam-path P_S; 3) measure optical power with no sample in the beam-path, P_B; 4) Correct both measurements for source intensity fluctuations based on the onboard pyroelectric powermeter of the OPO; 5) Estimate μ_a through $\mu_a = \ln(P'_B/P'_S)/\delta x$. It should be noted that this setup has not been optimised and standardised for detailed quantitative accuracy in itself. It was meant as a hypothesis-check of later-discussed causes of disagreement between the PAS and spectrophotometer data - i.e. it was used in a comparative analysis of spectral shape behaviour and of ballpark absolute values *versus* both PAS and the spectrophotometer (see Section 6.4.3).

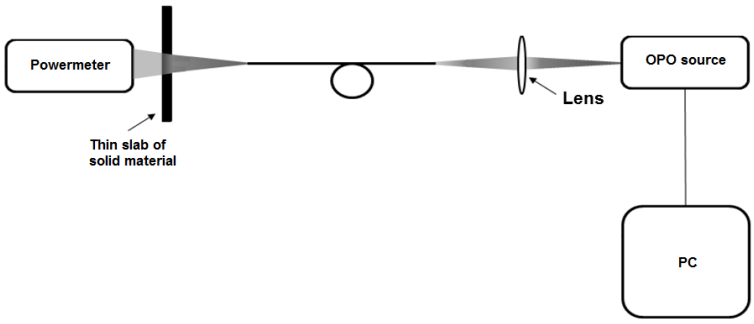

Figure 5.2: *Simplified schematic of high peak-power transmittance setup, for spectroscopic use.*

Furthermore, exploring the behaviour at high peak power as a function of concentration and power [56, 140, 214] can also provide insights on non-linear behaviour: photostable samples should display linearity of μ_a with concentration and no variation of μ_a with increasing fluence. Here, these studies were done with PAS as modality.

5.4.4 Optical scattering

To determine the scattering coefficient μ_s and anisotropy parameter g of a sample or substance, either direct, indirect or theoretical approaches can be employed.

A theoretical prediction of μ_s and g can be made through Mie Theory as defined by Bohren & Huffman (1983) [183, 220]. It assumes that the scatterer particles are spherical and requires as further inputs the particle size distribution $f(d)$ and refractive index m. It is therefore well-suited for assessing scattering properties of polymer microspheres with well quoted $f(d)$ and m and can serve as benchmark to evaluate the accuracy of other scattering characterisation methods. Mie Theory is not as straightforward to apply for other substances (e.g. TiO_2, Intralipid) where shape is more arbitrary or parameters $f(d)$ and m are not necessarily known. Particle size distribution $f(d)$ can eventually be assessed by scanning electron microscopy (SEM) [211, 221], backscatter confocal microscopy [202], with added advantage that these methods can ensure homogeneous dispersion of the particles and absence of agglomeration during sample preparation [202]. Refractive

index could be obtained with a refractometer [67] or indirectly from OCT information [211, 221]. These additional measurements do have as disadvantage that they add to the complexity and overall uncertainty of the method.

Alternatively, direct experimental retrieval of μ_s could be done by obtaining μ_t through a Beer-Lambert formulation of the type $\Phi = \Phi_0 e^{-\mu_t z}$ and spectrophotometry data, as long as μ_a is known or negligible and that the slab is thin enough to validate the assumption of single scattering (usually $\Delta x << \frac{1}{\mu_s}$). Manufacturing samples this thin or subsequently cutting into such thicknesses is also complex - respectively, electrospinning and crioslicing are sometimes considered. Furthermore, having *a priori* access to μ_a information is also seldom realistic. Direct experimental retrieval of g can be done with a goniometer [184], but once more very thin samples are needed.

An indirect manner of obtaining μ_s information involves measuring total transmission (M_T) and reflection (M_R) for a slab of the desired material and assimilating these measurements with a light modelling strategy that can account for the multiple scattering phenomena. This is an indirect strategy, as μ_a and μ_s are simultaneously retrieved by employing an inversion algorithm that iteratively minimises the difference between measured and modelled M_T and M_R. g has to be known, or in alternative a more complex method making measurements of total transmission, total reflection and collimated transmission (M_C) can be employed, which once plugged into a proper light model allows retrieving μ_s, μ_a and g jointly [222, 223]. When compared to the direct approach, the minimal thickness and known μ_a restrictions are now lifted. The measurements of M_T and M_R typically rely on a substitution procedure. Obtaining M_R requires 3 measurements - with the sample in place, with a traceable standard reference material in place providing near-total reflectance and a blocked beam measurement. Obtaining M_T also requires 3 measurements - with the sample in place, without the sample in place and a blocked beam measurement. As for the inverse light modelling stategy, implementations involving Monte-Carlo [184] or Kubelka-Munk [224, 225]) have been suggested, but the inverse adding-doubling (IAD) implementation of the RTE [222] is the most common framework. The adding-doubling algorithm that underlines IAD can provide an analytical solution to the RTE in terms of M_T and M_R for a thin homogeneous layer of material where single scattering is expected, and can then either double (for another layer with equal optical properties) or add (for a layer with different properties) the obtained values for successive layers until the desired thickness is achieved. As such, adding-doubling works under the assumption that the sample under study is a layer-like structure where each thin layer has homogeneous absorption and scattering. These assumptions are met for fabricated homogeneous slabs of material [222], reason why, besides its efficiency, it is the most common approach in many material characterisation studies.

Another way of indirectly obtaining μ_s information is to experimentally obtain time of flight measurements of photon propagation for a homogeneous slab of material and to compare them to theoretical predictions with an appropriate time-resolved light model

(e.g. DA, MC). These methods require careful deconvolution of system response and access to thick samples of material, which may not be feasible for biological tissues or even when fabricating other materials [202, 226].

In this study, the indirect approach, using integrating sphere principles and the IAD algorithm, was used for all reduced scattering assessments. The dual-beam spectrophotometer (Lambda 750S, Perkin Elmer, Waltham, MA, USA) with a 100-mm integrating sphere unit was used to obtain measurements of M_T and M_R, in a procedure involving three types of sub-measurements each, as outlined above. The accuracy of the instrument had been confirmed within the group by comparing Intralipid measurements at different concentrations and also by benchmarking with PAS-derived μ_{eff} decay at diffusive depths for turbid samples with known μ_a (therefore allowing μ_s' to be extracted). Similarity to literature-reported ranges was also confirmed.

5.4.5 Thermoelastic efficiency

The Grüneisen Parameter Γ, essential to PA generation, can in some instances be found through theoretical calculations and tabulated values from the literature, since $\Gamma = \beta c_s^2 / C_p$, where the volume thermal expansivity β, the speed of sound c_s and the specific heat capacity at constant pressure C_p are values commonly quoted in the literature for certain organic (e.g water, methanol, ethanol) and inorganic chemicals in liquid form, usually with temperature dependance [113]. This is however not the case for most complex chemicals or for materials in their solid form - as is the case with typical matrix materials. The variation with the inclusion of additives is also usually not known.

For these cases, the Grüneisen Parameter Γ can be estimated experimentally through photoacoustic spectroscopy [140], in a manner relative to Γ of water. Absolute values can then be derived since water has well tabulated values in the literature [113, 227]. The working principle is: PA measurements are made for both water and the sample of interest, their peak amplitudes will be defined by:

$$S_{0,water}(\lambda) = K\Gamma_{water}\Phi_0(\lambda)\mu_{a,water}(\lambda). \tag{5.4}$$

$$S_{0,sample}(\lambda) = K\Gamma_{sample}\Phi_0(\lambda)\mu_{a,sample}(\lambda) \tag{5.5}$$

Therefore,

$$\left(\frac{S_{0,sample}(\lambda)}{\mu_{a,sample}(\lambda)}\right) = \frac{\Gamma_{sample}}{\Gamma_{water}}\left(\frac{S_{0,water}(\lambda)}{\mu_{a,water}(\lambda)}\right), \tag{5.6}$$

where Γ_{water} is known from the literature [112], $S_0' = S_0/\Phi_0$ is the peak-to-peak amplitude normalised to the incident fluence Φ_0 and μ_a is optical absorption - all these can be found as defined in Section 5.4.1. If acquisitions are made at a single wavelength, a simple ratio will give Γ_{sample}:

$$\Gamma_{sample} = \frac{\frac{S'_{0,sample}}{\mu_{a,sample}}}{\frac{S'_{0,water}}{\mu_{a,water}}}\Gamma_{water}, \tag{5.7}$$

or if multiple wavelengths are available, equation 5.6 can be solved in a least squares manner, through linear regression.

In cases where it is not possible to find a single spectral region where both water and the sample are sufficiently absorbing to yield reliable S_0 data, a slightly different method can be adopted that relies on two spectral windows. First, a PA measurement is done for water in a suitable region, from which the sensitivity parameter K can be derived by solving Equation 5.4 in a least-squares manner. Γ_{sample} can then be found by solving equation 5.5 based on PA measurements done for another spectral region and incorporating the newly-found knowledge of K. This two-step method is similar to that suggested by Yao *et al* (2014) [112].

It should be noted that, unlike the case where a water-filled cuvette is placed in the water bath, when other samples are placed there is a considerable acoustic impedance mismatch at the interface with the water bath. This will result in a change in acoustic transmission, given by $T_{s,w} = \frac{2Z_w}{Z_w+Z_s}$, where Z_w and Z_s are the characteristic acoustic impedances of water and the sample respectively. To correct for this error, the measured amplitude S is divided by the appropriate transmission $T_{s,w}$ [112].

The accuracy and uncertainty achieved with this setup and method were tested with solutions well-characterised and reported in the literature - methanol and ethanol. The outcomes can be found in Table 6.3.

5.4.6 Speed of sound and acoustic attenuation

Measuring speed of sound $c(f)$ and acoustic attenuation $\alpha(f)$ can be achieved with a through-transmission substitution method. In this approach, a transducer, a sample holder and a hydrophone are co-aligned inside a tank filled with water. For each manufactured specimen, measurements are made with and without the sample in the sample holder within the water tank (Figure 5.3). Typically, the procedure is repeated with the hydrophone at a set of distinct distances from the source. From the measured difference in phase of the detected acoustic wave when the sample is present, $\phi_m(f) = 2\pi f\left(\frac{L-\Delta x}{c_w} + \frac{\Delta x}{c_m}\right)$, or absent, $\phi_w(f) = 2\pi f\frac{L}{c_w}$, the sound speed of the material can be estimated [228, 229]:

$$c_m = \frac{2\pi f c_w \Delta x}{2\pi f \Delta x - c_w d\phi}, \tag{5.8}$$

where Δx is the sample thickness, f is the frequency, L the distance between transducer and receiver, $c_w(f)$ the speed of sound in water [230] and $d\phi(f) = \phi_w(f) - \phi_m(f)$ the phase difference.

The same data can also be used to retrieve the acoustic attenuation coefficient α_m. When no sample is present, the measured amplitude is $V_w(f) \propto P_i 10^{-\alpha_w L}$, where P_i is the input pressure and $\alpha_w(f)$ the acoustic attenuation in water [227]. Once the sample is put in place, the amplitude is given by $V_m(f) \propto TP_i 10^{-[\alpha_w(L-\Delta x)+\alpha_m \Delta x]}$, where T accounts for

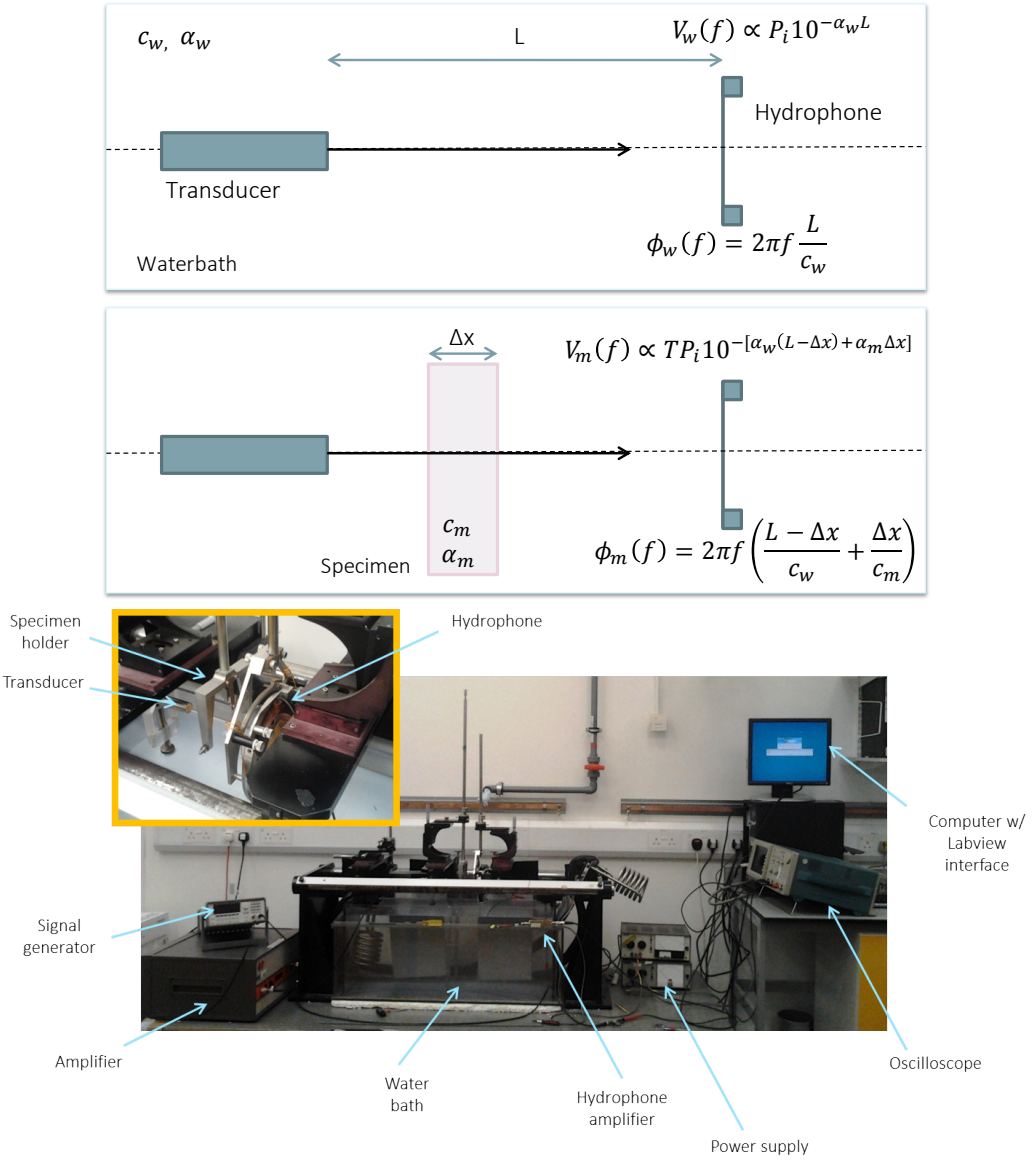

Figure 5.3: *Through-transmission substitution setup used for sound speed and acoustic attenuation measurements. (a) Schematic. Reproduced with permission from [182]. (b) Photo of setup and components.*

the transmission losses at the two water-material interfaces. The frequency-dependent transmission-loss (TL) is therefore given by:

$$TL\,[dB] = -20log\left(\frac{V_w(f)}{V_m(f)}\right) = -20\Delta x(\alpha_m - \alpha_w) + 20logT. \tag{5.9}$$

By computing transmission loss for two sample thicknesses Δx_1 and Δx_2, usually in the order of mm, α_m can be retrieved:

$$\alpha\,[dB\,cm^{-1}] = \frac{TL(\Delta x_1) - TL(\Delta x_2)}{\Delta x_1 - \Delta x_2} + \alpha_{w\,[dB]}. \tag{5.10}$$

In the case of our experiments, a National Physical Laboratory (NPL)-based through-transmission substitution setup was used [229]. The source was a broadband transducer (active diameter 12 mm, Medicoteknisk Institute, Denmark) and detection was achieved

with a broadband hydrophone (30-mm active element diameter bilaminar membrane hydrophone, Marconi). Both the hydrophone and the transducer were submerged in a large water tank, and aligned. Acquisition was controlled, recorded and pre-processed (to obtain mean and standard deviation of the 100 individual pulse waveform readings that comprise a reading and to map this information from the temporal into the frequency domain) using a custom in-house (NPL) program. Further analysis was then carried out according to the expressions above and UKAS uncertainty standards to obtain final results and confidence intervals.

5.4.7 PA excitation lasers

For studies of optical absorption, photostability and thermoelastic efficiency, a set of different PA excitation lasers was used throughout this work, depending on specifications (PRF, power, wavelength range) and availability. Table 5.3 gives an overview of the lasers employed throughout the studies, which will sometimes be referred to by the Shorthand nomenclature only.

Shorthand	**Product and Manufacturer**	**Type**	**Pulse length (ns)**	**PRF (Hz)**	**Wavelength range (nm)**
Innolas-OPO	Innolas Spitlight 600 (Innolas, Krailling, Germany)	Nd-YAG pumped OPO	6	30	420-680, 740-2400
GWU-Spectra Physics OPO	GWU VisIR (GWU-Lasertechnik GmbH, Erftstadt-Lechenich, Germany) + Spectra Physics Quanta Ray LAB170 (Spectra-Physics, Santa Clara, CA, USA)	Nd-YAG pumped OPO	8	10	500-680, 740-2100
Ultra Nd-Yag	Big Sky Laser Technologies	Q-switched Nd-YAG laser	8	20	1064

Table 5.3: *Lasers and OPO systems available for PA excitation.*

Chapter 6

PVCP

From the suite of materials available, Polyvinyl chloride plastisol (PVCP) was chosen as the most promising phantom material to be fully characterised and adapted for spectroscopic qPAT. This was due to its promising long-term stability, optical transparency and tissue-like acoustic properties and due to its good record in the recent literature in terms of suitability for general system characterisation PA phantoms.

Spirou *et al* (2005) [188] first suggested its use for PA, and it has more recently been proposed as a strong candidate for commercial PA measurement system characterisation and quality control [191, 231, 232]. PVCP has also been considered for other applications, e.g. as a phantom material in optical coherence tomography [233] or ultrasound-guided needle insertion [201]. Some optical properties of PVCP have been previously characterised at single [188, 191, 221] and more recently at multiple wavelengths [234]. Absorption has been tuned through the addition of black pigment colour, whilst reduced scattering has been increased mainly through the dispersion of titanium dioxide (TiO_2), though zinc oxide (ZnO) has also recently been suggested as an alternative scatterer, in the context of the development of an optical coherence tomography phantom [233]. Speed of sound and acoustic attenuation have been characterised at low frequencies for commercial PVCP formulations [188, 201]. Acoustic backscatter, the major source of contrast for conventional ultrasound, has been estimated for PVCP with added microspheres [231]. It has also recently been shown that by using custom-made dispersions of PVC in various plasticiser types, a wider range of sound speed and acoustic attenuation values could be obtained [231]. The use of PVCP - or in fact any material - for the assessment and validation of qPAT has however not been explicitly addressed.

In this Chapter, after detailing the PVCP fabrication process adopted (Section 6.1), we:

- Provided for the first time a frequency dependent characterisation of the speed of sound of PVCP up to 20 MHz, whilst previous reported values were given at a single frequency. This was done for three PVCP formulations (Section 6.2);
- Extended the characterisation of the acoustic attenuation of PVCP up to 15 MHz,

from previous efforts up to 4 MHz, and more recently to 9 MHz. This was once more done for three PVCP formulations (Section 6.2);

- Assessed the approximate density of PVCP for the three PVCP formulations (Section 6.3);
- Characterised the scattering coefficient with various concentrations of TiO_2, also in the 400-2000 nm range (Subsection 6.4.1);
- Characterised the intrinsic optical absorption of PVCP in the 400-2000 nm range - corresponding to the full range of wavelengths that would be accessible in a typical OPO excitation source used in PA (Subsection 6.4.2);
- Assessed the possibility of embedding chromophores with distinct spectral signatures - besides the already studied black plastic colour - and evaluated their linearity with concentration (Subsection 6.4.2);
- Assessed the optical behaviour of the embedded chromophores when exposed to typical PA ns-pulsed high peak power sources, to reveal transient or permanent non-linearities (Subsection 6.4.3).
- Characterised for the first time the expected Grüneisen parameter of PVCP (Section 6.5);
- Showed the fabrication of a series of phantoms with embedded inserts - either made of PVCP or vinyl - and with wall-less hollow channels that were then used successfully to obtain multiple wavelength 3D PAT images (Section 6.6).

6.1 Manufacture

The fabrication of PVCP phantoms was based on a previously reported protocol outlined by Bohndiek *et al* (2013) [191]. The main steps in the procedure were:

- prepare an oil bath, heated to ~200 ^{o}C, on a magnetic stirrer heating plate;
- pour 30 ml PVCP (Lure Flex Firm, Lure Factors, Doncaster, UK) into an Erlenmeyer flask alongside a magnetic stirrer bar;
- place the Erlenmeyer in the oil bath and allow it to stir continuously; (iv) turn on the vacuum line connected to the neck of the Erlenmeyer to eliminate air bubbles;
- as viscosity and translucency increase, reduce stirring speed;
- once the mixture becomes liquid again and considerably transparent, restore initial stirring speed;
- when PVCP reaches ~180^{o}C and the solution is homogeneous (single phase), release the vacuum and swiftly pour PVCP into an aluminium or silicone mould;

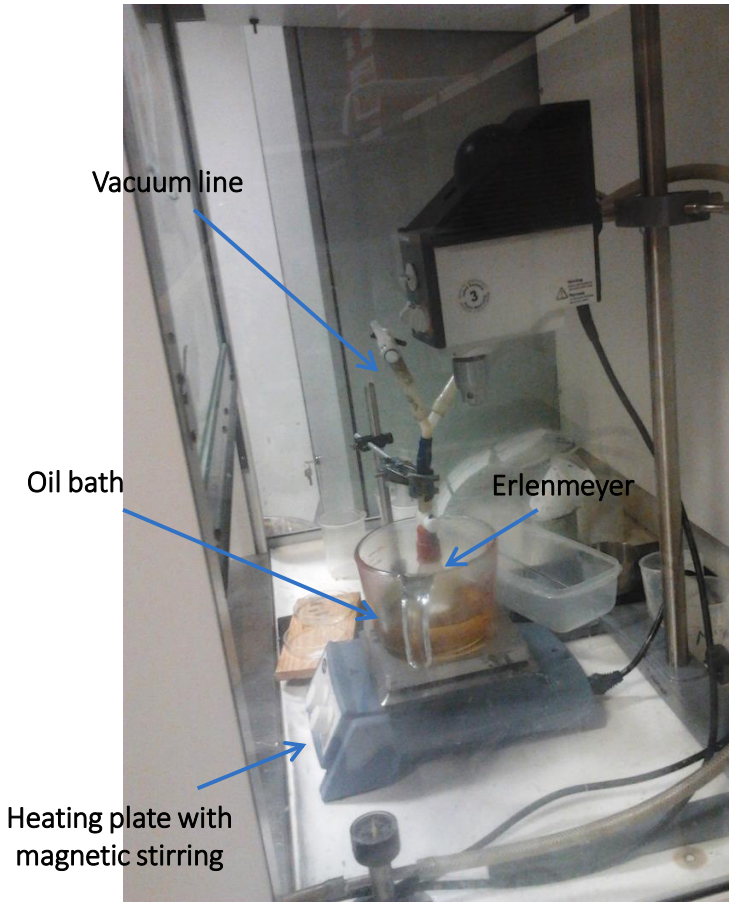

Figure 6.1: *Experimental setup for PVCP phantom preparation. A heating plate with magnetic stirring, an oil bath, a vacuum line, an Erlenmeyer flask and a clamp with support comprise the main elements of importance.*

- leave it to cure for several minutes.

Adding optical absorbers or scatterers was used to tune PVCP properties. These were mixed together with the PVCP mixture, placed in a sonicator for 10 minutes at $\sim 40^{o}C$ to ensure maximum homogenisation, and only then put in the oil bath. The volume of PVCP fabricated and its softness can also be increased to suit specific needs, within certain bounds - this is done by decreasing the concentration of PVC particles in the plasticiser, by adding more plasticiser (or so-called softener). It should be noted that when PVCP is harder (higher concentration of PVC particles), viscosity increases, meaning that stirring will need to be done more swiftly and for longer, to avoid the creation of two phases (one liquid and one solidified). The same issues occur at increasing overall volumes - a more upscalable production method is yet to be found; it may be helped in the future by contributions from the plastics industry. In both cases the yield of PVCP will lower since it will not pour out of the Erlenmeyer and into the mould as easily (especially thin gap moulds). Increasing volume or hardness may even become prohibitive at some point.

To achieve the desired shape and general architecture, PVCP cannot be 3D printed or laser cut, so imprinting the negative pattern in the mould itself is ideally done. Due to the

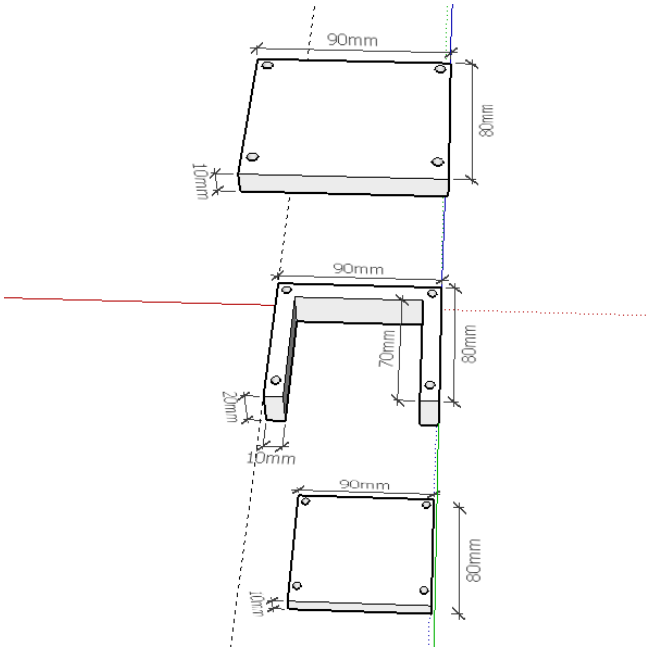

(a)

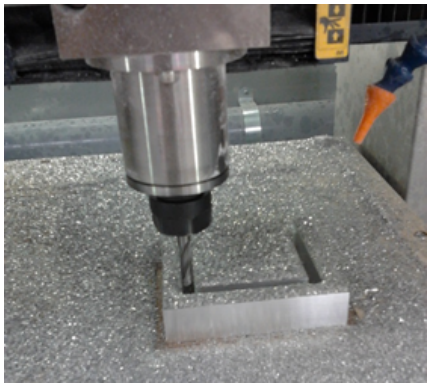

(a)

(b)

Figure 6.2: *Schematic and photos of phantom moulds. (a) Schematic of the 20 mm thickness mould; (b) Milling of the 20 mm spacer piece; (c) The finished 20 mm mould.*

thermal and curing characteristics of PVCP, only certain materials can be used for moulds - namely silicone, glass and aluminium. For some of the imaged phantoms, off-the-shelf silicone moulds were used to give cylindrical structures. In other cases, aluminium CNC machining was used as it can create more versatile/flexible mould geometries. For acoustic and optical characterisation of PVCP, it was necessary to be able to fabricate slabs with well-defined thickness and parallel walls. For that purpose, 'U'-shaped spacers were created with thicknesses of 20, 10 and 2 mm and inner 'U' dimensions of 70x70mm, with the shape and dimensions used (thickness and sides) being imposed by the acoustic measurement protocol. Two rectangular plates were also machined with outer dimensions matching those of the 'U' spacers. Both plates and spacers contained holes that could be aligned and lodge screws. Figure 6.2 shows the schematics and finished version of the 20 mm mould. The moulds were created with a CNC-machine (Modela ProII miller/router,

Roland, Japan) of aluminium (AW6082-T6/BS EN485/H30TF/BS 1470, Smiths Metal, UK).

Despite the general suitability of this approach, one issue that occurred for most samples was the formation of a meniscus at the top surface of the mould due to viscosity and surface tension. This complicated some of the sample volume estimation needed for density calculations given the irregular dimensions (Section 6.3). The use of a rotary plate during curing to avert the meniscus-formation would have been prohibitive due to curing speed (order of tens of seconds) and equipment logistics. Another disadvantage was that, for small spacer thickness levels (e.g. 2 mm), PVCP had difficulty to fully slide down the insert before curing, due to its viscosity. Lubricating and pre-heating the mould to ~50^{o}C led to a more controlled pouring process and also helped in driving the bubbles to the surface more effectively, since it slowed down the rate of curing.

6.2 Acoustic properties

PVCP was characterised in terms of its frequency-dependent sound speed $c(f)$ and attenuation $\alpha(f)$. The measurements were done for 3 different compositions of PVCP, by varying the portion of softener agent added (Softener, Lure Factors, Doncaster, UK) - 5, 10 or 20 % v/v. This was done to assess the potential to tune the acoustic properties. Samples at two main thicknesses were manufactured (10 and 20 mm, 2 specimens each). For the softest formulation, two 2 mm thick samples were also assessed to expand the frequency range. Spirou *et al* (2005) showed that optical additives such as TiO_2 and pigment based absorbers did not significantly affect the acoustic properties, therefore these formulations were not fabricated.

Properties $c(f)$ and $\alpha(f)$ were measured with the through-transmission substitution approach, as outlined in Section 5.4.6. The NPL setup was used [229]. The broadband transducer was driven by a single cycle electrical pulse with central frequency 9 MHz at a PRF of 1 kHz. For each manufactured specimen, measurements were then done with the broadband hydrophone at 3 successive distances from the source (this is advised in the protocol to randomise high-frequency diffraction phenomena) [229]. At each distance, four oscilloscope readings were taken with the sample in place and a further four readings without the sample in place, where each reading consisted of an average of 100 individual waveforms. This combination of readings at different distances was then combined in the subsequent analysis.

Figure 6.3 and Table 6.1 show the frequency-dependent speed of sound of PVCP up to 20 MHz and the acoustic attenuation up to 15 MHz. This discrepancy in final reported bandwidth is due to the fact that, though the same acoustic data are used to extract both parameters, the former relies on phase shift information whilst the latter relies on amplitude information (Section 5.4.6). The latter is less robust to noise. The table displays c at 5 MHz and attenuation behaviour in terms of power law parameters a and b ($\alpha(f) = a\, f^b$,

Composition	Softener	c_s	a	b	Samples	Temp.
	% v/v	[m s^{-1}]	[dB cm^{-1} MHz^{-b}]		#	[^{o}C]
Hard	5	1408.3±0.8 @ 5 MHz	0.67±0.02	1.55±0.01	4	(20.5-20.8)±0.03
Medium	10	1406.7±0.7 @ 5 MHz	0.62±0.03	1.54±0.02	4	(20.5-20.8)±0.03
Soft	20	1402.3±0.7 @ 5 MHz	0.55±0.05	1.53±0.01	4	(20.6-20.9)±0.03
Spirou 2005 [188]*		1400±20 @ 1MHz	0.57±1.01	1.51±0.06	3	-
Madsen 2003 [235]$^+$		1395	1.05 dB $cm^{-1}MHz^{-1}$ @ 4.5 MHz		1	22
Vogt 2015 [234]$^\#$		1380-1575	1-30 dB $cm^{-1}MHz^{-1}$ @ 4.0 MHz		-	-

Table 6.1: *Speed of sound c_s and acoustic attenuation (expressed through power law pre-factor a and exponent b), within one standard uncertainty. Literature values are given for other PVCP formulations: * MF Manufacturing; $^+$ unknown origin; $^\#$ range of custom formulations. Reprinted with permission from [182].*

where f is in MHz). Uncertainty is reported as one standard uncertainty, i.e. providing a coverage probability of approximately 68% (coverage factor k=1), having been carried out in accordance with UKAS requirements [236]. Uncertainties in sample thickness, temperature, literature reference values for water, repeated measurement variability and inter- and intra-sample variability were accounted for. Also, a comparison is made to previous literature-reported values for PVCP formulations from other suppliers. The acoustic properties were broadly comparable to tissue-like structures. The attenuation at 1 MHz was well within desired tissue range - between 0.6-1 among soft tissues - , but the power law b was above the typical range of b =1-1.35 [98], which might limit the depth to which high-resolution can be achieved. Increasing levels of softener lowered the acoustic attenuation, mainly in terms of the power law pre-factor, though attenuation was overall still too high. As for the speed of sound, c was ~10% lower than the typical soft tissue range (e.g. 1450 ms^{-1} for fat or 1590 ms^{-1} for liver [98]). Though increasing hardness caused an increase in the speed of sound, it was not considerable enough whilst further increases in hardness (through even higher PVC particle density in plasticiser) would not be feasible as they would exacerbate attenuation and also cause prohibitive difficulties in the fabrication process itself. Recently, it has been shown that the speed of sound can be increased to more tissue-relevant levels by using other types of plasticisers to suspend the PVC particles [231, 234] instead of just varying the concentration of particles. These plasticisers would however bring further increases in attenuation that, though some would be suitable for breast tissue up to 9 MHz, would be too high to be representative of most other soft tissues and further limit depth resolution and SNR. As for trying to reduce acoustic attenuation, the most suitable plasticiser found, DEHA, was equivalent to the

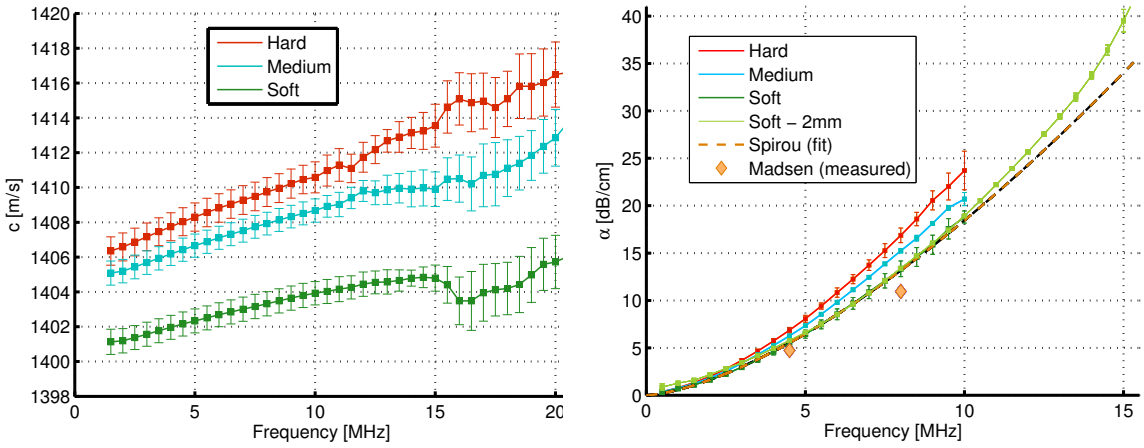

(a) (b)

Figure 6.3: *Speed of sound (a) and acoustic attenuation (b) for PVCP samples with various levels of hardness. The 2 mm soft PVCP slabs extend the frequency range for $\alpha(f)$ from 10 to 15 MHz. Error bars show standard uncertainty (coverage factor k=1), in accordance with UKAS requirements [236]. Uncertainties in sample thickness, temperature, literature reference values for water, repeated measurement intra-sample variability (i.e. due to the readings at three successive source-detector distances, due to the four readings per distance and due to the 100 individual waveforms per reading) and inter-sample variability were accounted for. The connecting lines are stylistic - a simple linear interpolation. Reproduced with permission from [182].*

one already used in commercial formulations, suggesting that if lowering attenuation at the expense of speed of sound is an option for the application, the best option is to simply use the current commercial formulation (or DEHA) and to make it as soft as possible by lowering PVC particle concentration (higher fraction of plasticiser/softener).

6.3 Density

The density ρ was assessed for the various compositions, which together with the speed of sound information can yield useful estimates of acoustic impedance $Z = \rho c_s$. The approximate density ρ of PVCP was found for the same acoustic samples by measuring their mass m as well as their volume V, where $\rho = \frac{m}{V}$. The mass was assessed with a weighing scale (Sartorius BP211D, resolution 0.01 mg (80 g)/ 0.1 mg (210 g)). The volume was found by measuring the 3 dimensions (thickness t, width w and height h) of the PVCP slabs with a calliper. However, all samples presented a slight meniscus on the top surface, so an approximate estimate of the missing volume V_e was made by assessing the amount of water needed to fill the meniscus, yielding a corrected total sample volume $V = t \times w \times h - V_e$.

Table 6.2 gives aggregate outcomes of density per PVCP composition, and its standard uncertainty. The estimates broadly agree with the literature [188, 201] and indicate density similar to water. There is a decrease of average density with increasing softness, but the

difference falls within the uncertainty. The existence of confounding values might be related to the inaccuracy in assessing meniscus volume V_e (even so, incorporating this measurement was still important since menisci volumes of the samples represented up to 2.2% of an otherwise meniscus-free volume). Higher resolving power in the density estimates could have been obtained if more rigorous total volume assessment had been employed, e.g. through a water-displacement approach or a commercial pycnometer.

Composition	**Density [g/ml]**
Hard	1.019 ± 0.008
Medium	1.014 ± 0.009
Soft	1.008 ± 0.006
Spirou 2005 [188]	0.95-1.05
Hungr 2012 [201]	0.74-0.98

Table 6.2: *Density for the various PVCP compositions (aggregate), with standard uncertainty. Intervals of values given in the literature are shown.*

6.4 Optical properties

PVCP has intrinsic, relatively low, optical scattering and absorption - desirable for a matrix material. This can be tuned and controlled through suitable additives.

6.4.1 Optical scattering

Scattering of PVCP was tuned by adding TiO_2 powder (Titanium IV Oxide, Anatase, 232033, Sigma-Aldrich, Germany), a commonly used optical scatterer [183]. Soft PVCP samples (2 mm thick) were prepared at 4 different concentration levels - 0.25, 0.5 ,1 and 2 mg/ml (0 mg/ml was not analysed since no meaningful total reflectance signal would be obtained in the used system - impairing scattering estimation). Integrating sphere measurements in the spectrophotometer coupled with the IAD algorithm were used to recover reduced scattering coefficient μ_s' and intrinsic absorption coefficient μ_a simultaneously, in the 400-2000 nm range. The main methodology is described in Section 5.4.4. The necessary total transmittance and total reflectance were made at four different spots on each sample (2 per side). The scattering anisotropy factor was set to $g = 0.6$, based on Mie Theory calculations from the literature for TiO_2 in PVCP [211].

Figure 6.4 (a) shows the reduced scattering spectra of PVCP with TiO_2. The resultant scattering was within the order of magnitude expected for biological tissue [63]. Also, the

values obtained were in the same range as those in other μ_s' characterisation studies [211, 234], though the absolute values differed among them. This is due to the fact that different TiO_2 products come in a variety of particle size distributions and even refractive indices [237], both parameters affecting μ_s'. This means that scattering measurements using different TiO_2 commercial products should not be directly compared. Ideally, scattering characterisation should be done per batch, even for products where the supplier specifies a mean particle size to a high degree of accuracy. Literature values should rather serve as a guideline for spectral behaviour and for preparing samples in the desired order of magnitude. As for linearity with concentration, an approximate linearity of μ_s' with increasing TiO_2 concentration was observed, except for the 1 mg/ml. This curve probably gives an erroneous portrayal of the expected behaviour of such a sample due to the visible homogeneity issues that had been noticed after preparing the sample, likely to do with lack of proper dispersion of the mixture. This was subsequently rectified for further dilutions (0.5 and 0.25 mg/ml) with increased mixing and sonicating.

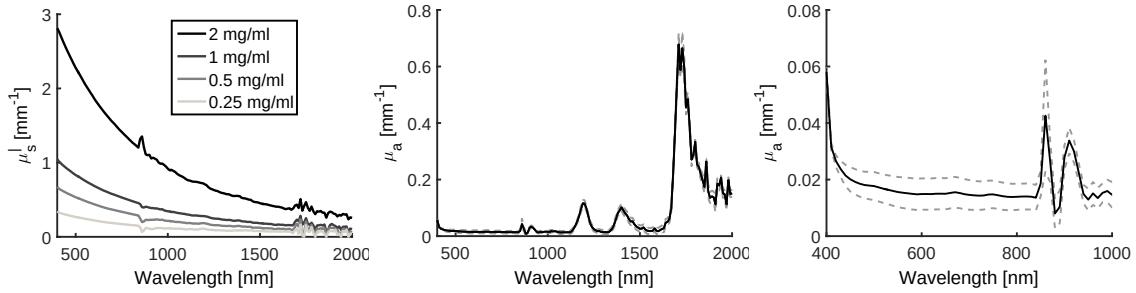

(a) $\mu_s'(\lambda)$ (b) $\mu_a(\lambda)$ (c) $\mu_a(\lambda)$ (detail)

Figure 6.4: *(a) Reduced scattering coefficient spectra of PVCP with varying concentrations of TiO_2. (b)-(c) Intrinsic absorption spectrum of soft PVCP. Variations at 850 nm are in fact artefacts due to the change of detectors within the spectrophotometer. The dashed lines correspond to the standard deviation between the estimated μ_a for the four slabs. Reproduced with permission from [182].*

6.4.2 Optical absorption

Figures 6.4 (b) and (c) show the intrinsic absorption spectrum of PVCP, averaged from IAD estimates from all samples. PVCP has intrinsic absorption peaks at 910, 1190, 1400 and 1720 nm, probably due to vibrational energy transitions (overtones) in PVC [238]. Overall, the absorption is conveniently low and analogous in range and magnitude to background biological tissue [63]. PVC has been reported to suffer a significant decrease in optical transmission when held at temperatures in the 190-205^{o}C range [239]. This is in principle above what we achieve. A standardised preparation of the material is advised [188, 239] to avoid absorption changing during the sample preparation process due to variabilities in heating rate or final heating temperature.

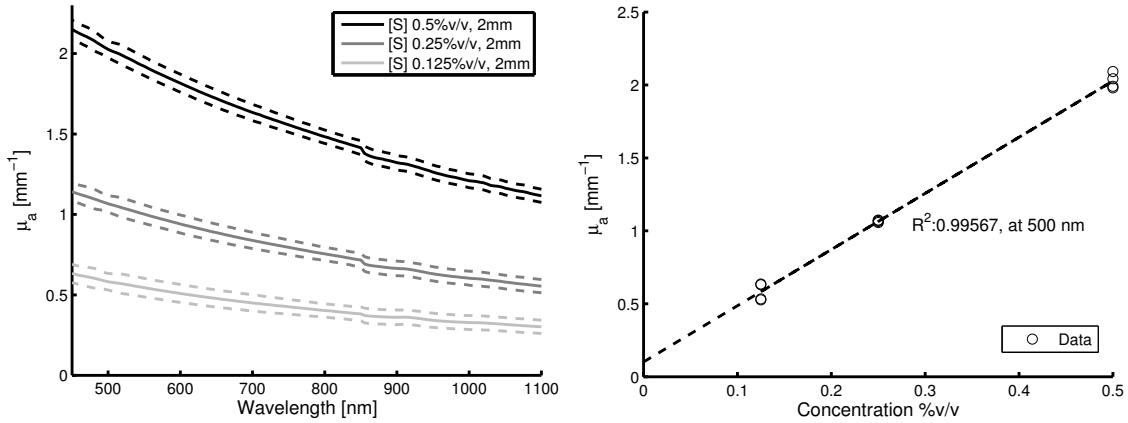

(a) Black

(d) Black

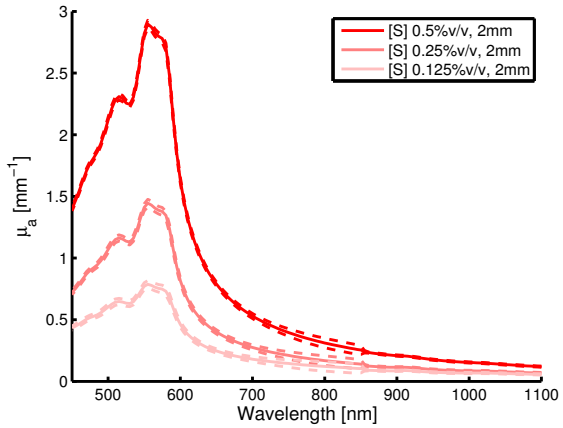

(b) Red

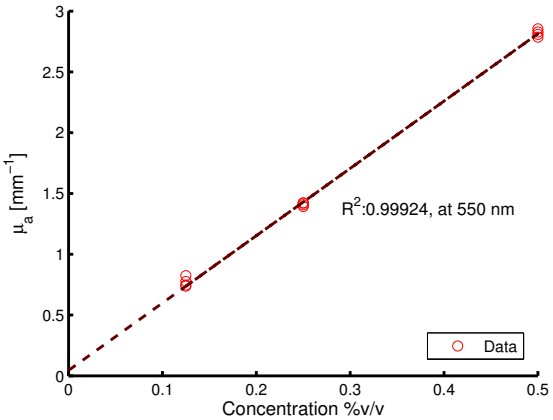

(e) Red

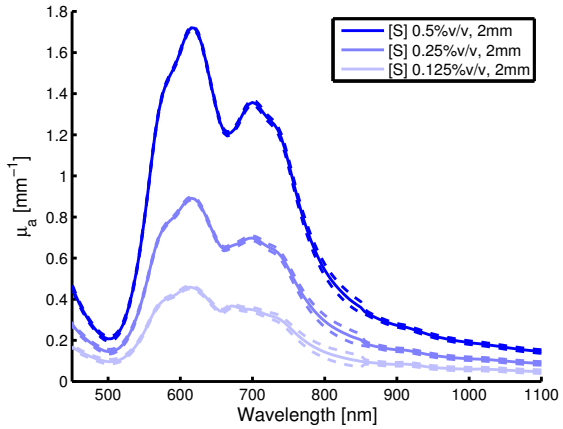

(c) Blue

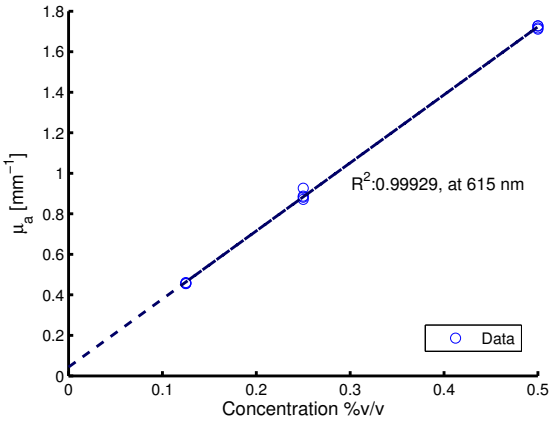

(f) Blue

Figure 6.5: *(a)-(c) Absorption spectra of PVCP slabs with embedded absorbers, at different concentrations; [S] - spectrophotometer acquired data. Dashed lines represent the standard deviation of the four measurements on the same sample. (d)-(f) Linearity of spectroscopic μ_a with increasing concentration at the peak wavelength. Reproduced from [182].*

Having established its background absorption, additives were asssessed that could tune the absorption. Soluble dyes are not suitable for use in plasticised PVC formulations since they migrate in the presence of the plasticiser [240]. Pigment dispersions - where pigments are pre-dispersed in a paste and then mixed with softener - are advised as colorants by manufacturers [240, 241]. Three pigment-based absorbers (black, red and blue) from the same supplier as the PVCP (Liquid Colour, Lure Factors, Doncaster, UK) were characterised. For these exploratory studies, one batch of each was acquired. 2 mm thick slabs of soft PVCP were prepared with added absorbers at 0.5, 0.25 and 0.125 %v/v concentration (serial dilution). Given that samples are non-turbid, the standard spectrophotometer was used for assessment, four points per sample. Three unique spectra were obtained (Figure 6.5, a-c) and linearity with pigment concentration was found to be respected for all pigments (Figure 6.5, d-f).

6.4.3 Absorption at high peak power

To investigate the absorption behaviour at high peak power, two modalities employing a high-peak power source were used. First, optical transmission measurements were made with the ns-pulsed Innolas OPO system rather rather than with the typical cw-source of the spectrophotometer, with the setup described in Section 5.4.3. Three repeat measurements were made. Secondly, PAS with μ_a retrieval through exponential fitting approach (Section 5.4.1) was employed, with the ns-pulsed GWU, Spectra-Physics OPO system (outputting ~ 14 mJ at 500 nm and 17 mJ at 630 nm, 10 Hz PRF). In this case, 1% v/v 20 mm slabs of the same fabrication batch as the spectrophotometer samples were used.

Figure 6.6 shows, for each of the three absorbers, that spectrophotometer- ([S]) and photoacoustic-derived ([P]) μ_a spectra differ, especially in absolute value. The red absorber shows the most significant mismatch, since the change in absolute absorption is accompanied by a clear and consistent change in the shape of the spectrum: the 550-580 nm plateau present in [S] measurements disappears in [P] measurements, in what becomes a more peak-like feature at 550 nm. The changes seen in [P] cannot be solely attributed to dynamic phenomena to do with PA thermoelastic efficiency or with volatility in the fitting procedure since high peak-power transmittance [T] measurements, performed on the 2 mm slabs, showed similar characteristics to [P] (Figure 6.6, a-c, [T]). The fact that this behaviour is seen in two high-peak power techniques operating through quite distinct mechanisms seems to indicate that the absorbers may be suffering photo-chemical or photo-physical changes in behaviour when exposed to high peak power nanosecond pulses [56, 214, 217, 242, 243] (~1 MW peak power) that do not occur when exposed to the low power continuous-wave illumination of the spectrophotometer (~W peak power).

To ensure that the absolute intensity mismatch was not a system or method fault, agreement between spectrophotometer and photoacoustic measurement systems and

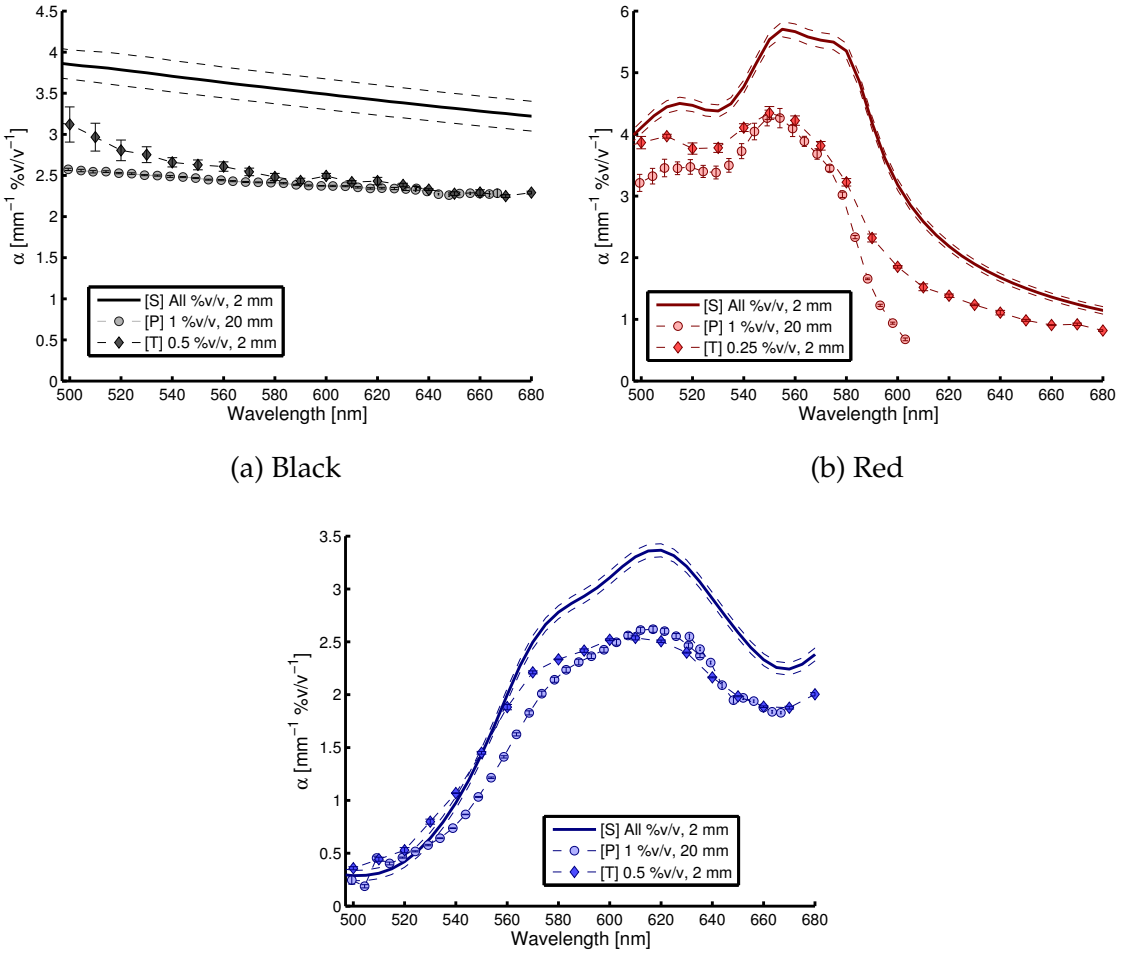

(a) Black

(b) Red

(c) Blue

Figure 6.6: *Comparison of extinction coefficient measured through: transmittance in spectrophotometer [S] (linear regression of results from samples at all concentrations) with cw-illumination, exponential fit of photoacoustic signal [P] and transmittance [T] with a high peak power OPO source. Measurement standard deviation is given. Reproduced with permission from [182]*

with ground-truth was studied to make sure they were working up to specification in the relevant absorption range. First, control measurements were made with a photostable $CuCl_2$ solution and found to agree. Measurements of water absorption between 1350 and 2000 nm (representing a range of μ_a up to 12 mm^{-1}) were then also made with the PA spectroscopy system to ensure that the exponential fitting methodology was accurate compared to literature reference values for a wide range [244]. The intrinsic absorption of PVCP (no added pigments) around the 1720 nm peak also agreed well between systems. This seemed to indicate that the pigments themselves were the source of the discrepancies.

To further study the behaviour of the pigment-embedded PVCP when exposed to high peak power, PA absorption measurements were made as a function of illumination time, of incident peak energy and of pigment concentration. The influence of the fluence on μ_a was assessed through photoacoustic spectroscopy. Different levels of fluence - 100, 80, 60, 40 and 20 % of Φ_{max} were used for excitation, where the non-attenuated energy

Φ_{max} is ~27 mJ at 500 nm and ~16 mJ at 680 nm with the Innolas-OPO system. Three variants were tested. In a first experiment, one point on the sample was illuminated with increasing fluence. In a second scenario, a different point was illuminated with decreasing fluence. Lastly, different points were illuminated with distinct peak energy levels - with minimised common history between points. These three approaches were used to differentiate effects due to instantaneous high peak power (leading to transient bleaching) from effects due to the accumulation of average power over an extended time (leading to permanent bleaching).

Overall, an increase in energy per pulse led to a decrease in μ_a (Figure 6.7). Though permanent photobleaching by accumulation of average power could explain the decreasing trend in μ_a when fluence is increased gradually over time (Figure 6.7 a,d), it would not explain why this μ_a is partially restored at timepoint [t6] when energy is reset to its lowest level. It also would not explain why when one point is illuminated with gradually decreasing pulse energy the μ_a levels increase (Figure 6.7 b,e). Illuminating different points on a sample with distinct pulse energies also shows that μ_a increases as pulse energy is lowered (Figure 6.7 c,f). These behaviours suggest that μ_a dependency on peak pulse energy is likely due to the transient/reversible occurrence of ground-state bleaching (saturable absorption) in the pigments [242].

The linearity of PA-derived μ_a with increasing concentration was then assessed (Figure 6.8). Red and blue 20 mm thick PVCP slabs were fabricated from a new batch, at 2, 1 and 0.5 %v/v pigment concentration. 3 acquisitions were made per sample in the 500-680 nm range with the Innolas-OPO system, each consisting of the averaging of 100 waveforms. Figure 6.8 shows the spectra, normalised to the mean spectrum for 2% v/v absorber concentration. Wavelengths where the exponential fit satisfied $R^2 > 0.98$ are shown. The blue samples displayed linearity with concentration whilst the red seemed to deviate from absorption linearity in the 540-580 nm region: the lower the concentration, the lower the relative absorption at 570-580 nm compared to 540-550 nm. This seems to go in line with the behaviour seen when [S] and [P] data (Fig. 6.6 b). Saturable absorption manifests itself not only at increasing peak energy, but also at lowered concentrations, since this also reduces the ratio between absorbing molecules per unit volume and number of photons.

To assess photobleaching, i.e. μ_a as a function of extended illumination time, black, red and blue 1% v/v PVCP slabs were continuously irradiated with the Spectra-Physics OPO laser for 30 minutes (18000 pulses) at their respective peak absorption wavelength - 500 nm, 550 nm and 615 nm. The beam pulse energy was ~ 5 mJ. PA signals were averaged over a minute, stored and afterwards exponential fitting was used to retrieve μ_a. The PVCP with embedded pigments displayed reasonable stability over the irradiation period. A decreasing μ_a trend is seen in Figure 6.9, though not exceeding 5%.

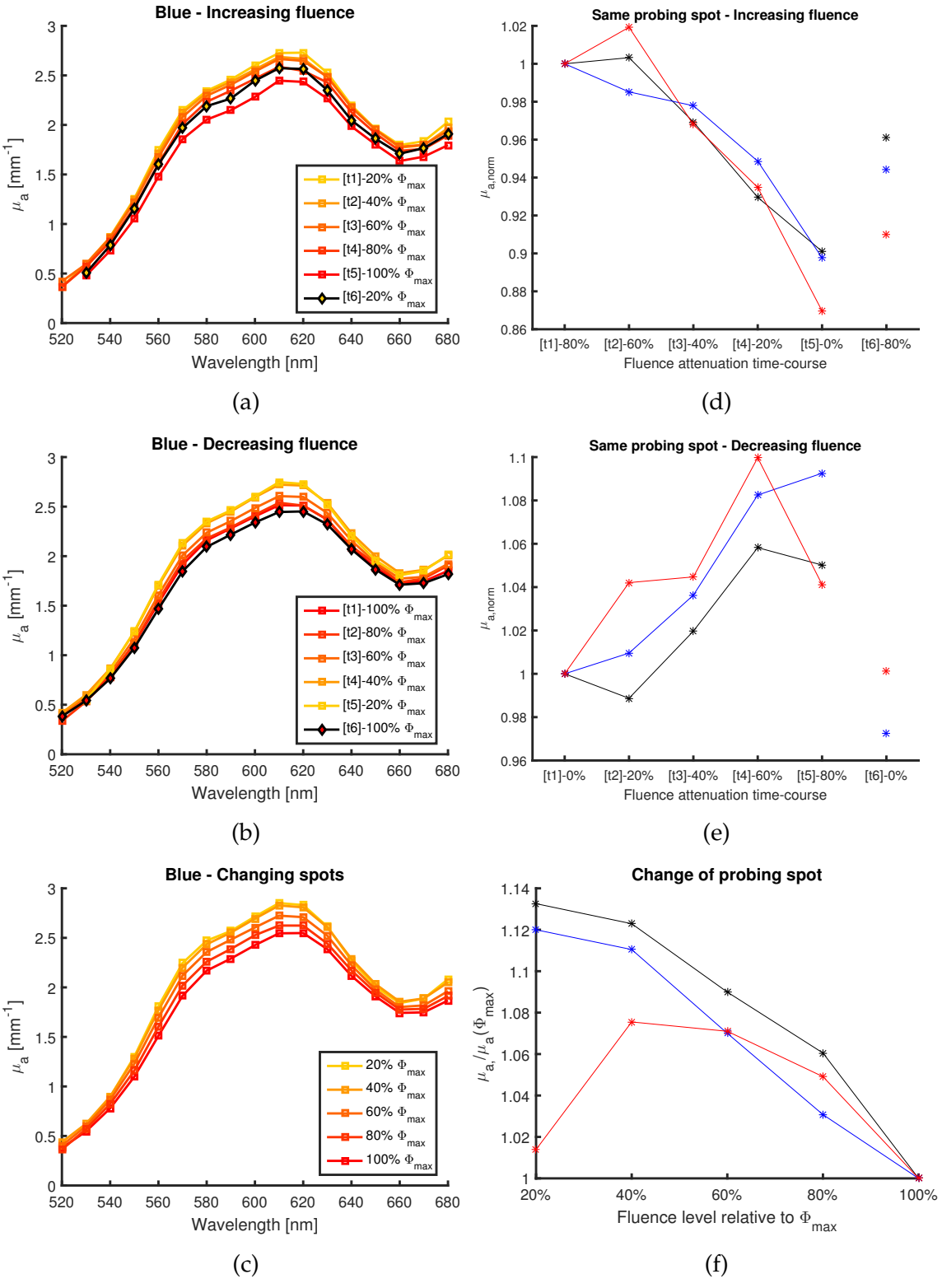

Figure 6.7: *(a)-(c) Influence of varying peak power energy on the μ_a of blue PVCP samples. Results are shown as peak energy is gradually increased over a same location for timepoints [t1-5] and restored to its initial (lowest) value in [t6] (a), as peak energy is gradually decreased over a second location for timepoints [t1-5] and restored to its initial (highest) value in [t6] (b), and as peak energy is varied over distinct locations/spots on a same sample (c). (d)-(f) Influence of varying peak power energy on μ_a of PVCP samples embedded with either of the three colours. Red and black values are shown for 550 nm whilst blue values are shown for 610 nm. Reproduced with permission from [182].*

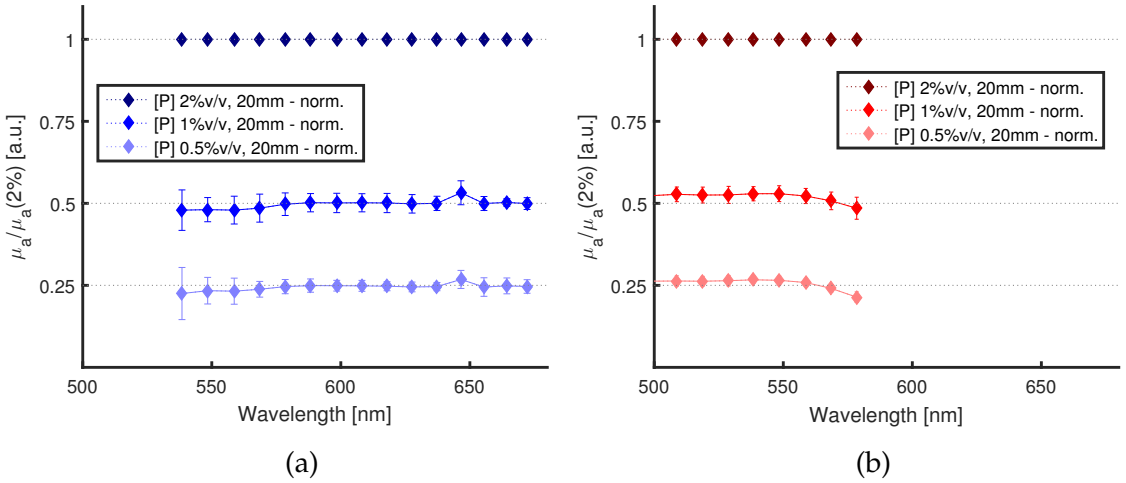

Figure 6.8: *PA spectra of PVCP with different absorber concentrations (0.5, 1 and 2 % v/v) normalised to the spectrum at 2 % v/v. 1/2 and 1/4 concentration ratios are broadly respected. Error bars account for inter-acquisition standard deviation and for the standard uncertainty in the exponential fitting procedure. (a) Blue absorber, (b) Red absorber. Reproduced with permission from [182]*

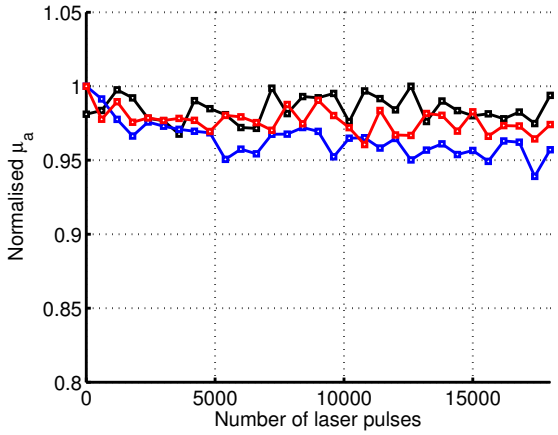

Figure 6.9: *Photobleaching of red, blue and black 20 mm slabs during 30 minute exposure (18000 pulses) at its respective peak wavelength.*

6.5 Thermoelastic properties

To assess the Grüneisen parameter, the PA spectroscopy method for two spectral windows was used, as described in Section 5.4.5. First, least-squares regression from PA measurements of water in the 1350-1850 nm spectral window, alongside $\mu_{a,water}$ and Γ_{water} from the literature [113, 244], were used to estimate sensitivity parameter K. This estimated value was then, alongside $\mu_{a,sample}$ values retrieved through curve-fitting at the relevant wavelengths, used in the equation for $S_{0,sample}$ to retrieve Γ_{sample}. Correction for impedance mismatch was applied.

A 20 mm slab of soft PVCP was used to make the measurements. Six acquisitions (each

formed by 300 averaged waveforms) were done in total for the 1700-1750 nm spectral region. Methanol and ethanol were also measured for method validation, with reference benchmark values taken from the literature (Table 6.3). Measurements for methanol, ethanol and also water were done by pouring the substances in turns into a cuvette, then placed within a water bath. Three acquisitions were done per substance. Wavelengths chosen were those that provided a reasonable fit, R^2>0.98.

The outcomes of the Grüneisen parameter characterisation are shown in Table 6.3. Error ranges take into account inter-acquisition standard-deviation as well as the standard uncertainty of the least-squares regression process applied to each acquisition. The estimated Γ values for ethanol and methanol are consistent with the literature. Γ of PVCP was found to be higher than some tissues [112], though this has as advantage that imaging can be done with higher SNR.

	T	C_p	c	β_v	ρ	Z	Γ_{lit}	T_{exp}	$\hat{\Gamma}_{exp}$
	[^oC]	[$Jmol^{-1}K^{-1}$]	[ms^{-1}]	[$^oC^{-1}$]		[$MRayl$]		[^oC]	
Water	20	75.3	1482.3	20.6×10^{-5}	1	-	0.116		
	21.7	-	1487.47 [230]		1		0.12	21.7±0.1	-
Eth.	20	112.3	1159	140×10^{-5}	0.7893	0.91	0.772	21.5±0.2	0.78±0.04
Meth.	20	81.1	1116	149×10^{-5}	0.7917	0.88	0.733	19.9±0.3	0.71±0.02
PVCP	20	-	1402 $_{(exp)}$	-	1.008 $_{(exp)}$	1.41 $_{(exp)}$	-	21.9±0.1	1.01±0.05

Table 6.3: *Tabulated properties in the literature vs experimental results (subscript $-_{exp}$) . All literature values taken from reference [113] unless otherwise indicated. T - temperature; C_p - specific heat capacity at constant pressure; c - sound speed; β_v - volume thermal expansion coefficient; ρ - specific gravity; Z - acoustic impedance $Z = \rho c$; Γ_{lit} - Literature-derived Grüneisen coefficient $\Gamma = \alpha_v c^2/C_p$; $\hat{\Gamma}_{exp}$ - Estimated Grüneisen coefficient. Reprinted with permission from [182]*

The variation in Grüneisen parameter with added blue or red pigments was also studied for 20 mm thick PVCP slabs with concentrations of 2, 1 and 0.5 %v/v. The PA spectroscopy method at a single spectral window was employed, where K cancels out. A single wavelength was used, corresponding to where intrinsic PVCP absorption is highest and pigment absorption is residual - 1715 nm, meaning that measured variations in $S_{0,sample}$ with pigment concentration should be mainly due to changes in Γ rather than μ_a [56]. Figure 6.10 shows that there was a negligible change in Grüneisen parameter with pigment addition up to 2% v/v.

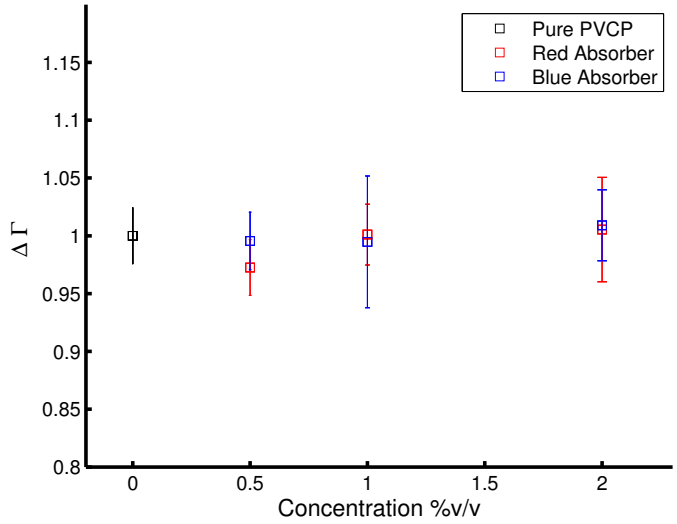

Figure 6.10: *Relative variation in the Grüneisen Coefficient of PVCP with increasing red and blue absorber concentration. The variation is negligible. Reproduced with permission from [245].*

6.6 Architecture and imaging

In this Section we will show some phantom constructs achieved with PVCP, as well as obtained PAT images. Before that, the FP sensor and acquisition setup will be described.

6.6.1 Fabry-Perot sensor

A Fabry-Perot polymer film sensing interferometer (FPI) approach was used in PAT experiments to measure PA waves and map the acoustic field. The FP sensor is typically formed by a parylene C polymer spacer on which two dichroic mirrors are deposited in a sandwiched manner, with a further poly(methyl methacrylate) (PMMA) backing stub on one of the sides that is wedged to avoid parasitic interference [78, 246, 247]. Compared to typical piezoelectric sensor arrays, FP sensor arrays have as advantages that they have broad bandwidth (from DC to 39 MHz for a typical spacer thickness of 22μm, -3 dB), good directionality characteristics thanks to the small element size (minimum 40μm) and exceptional sensitivity characteristics (a noise equivalent pressure of $\sim$ 200 Pa peak amplitude) [78]. Furthermore, delivering photoacoustic excitation light through the sensor is possible due to its high transmittance at wavelengths of interest for imaging (backward mode PA).

In terms of working principle, the pressure time-series information at a given location (A-line) is encoded in terms of a time-varying reflected power modulation, measured through interrogation of the Fabry-Perot interferometer (FPI) location with a focused laser beam. This procedure is then repeated for all locations of interest by 2D raster scanning the interrogation beam on the surface, yielding analogous data to typical array measurements [28, 78, 247]. The transduction mechanism can be described as follows:

PA waves that propagate to the surface of the FPI modulate the physical and therefore optical thickness of the spacer layer. As the sensor location is interrogated continuously with a laser beam at a fixed wavelength, the light will suffer a change in phase inside the spacer element, which will in turn change the reflectivity due to interference phenomena. The interferometer transfer function (ITF) describes this relation between reflected optical power and phase at each point.

To guarantee proportional change and maximum sensitivity in the transduction mechanism from phase change to reflected power change, the interrogation wavelength (and therefore baseline phase) at each location is optimally chosen such that it is tuned to the point of maximum slope of the ITF. This process is known as pre-tuning or biasing, and is typically done for all locations before the full scan area measurements. The slope of the ITF is also stored, so that correction for variations in sensitivity between locations can be done.

6.6.2 Fabry-Perot based planar scanner

FPI based scanners usually employ a single planar array. Such a geometry is preferred due to simplicity of production and interrogation. A general schematic of such a scanner can be found in Fig. 6.11. A fibre coupled ns-pulsed laser source provides the photoacoustic excitation light. The PRF of the laser will determine the speed of the raster scanning based acquisition. Illumination can be made in forward mode or in backward mode (through the sensor), since the dichroic mirrors are designed such that they reflect at longer wavelengths typically used for interrogation (1500 to 1600 nm) but transmit at wavelength of interest for imaging (600 to 1200 nm) [78]. A wavelength tunable cw laser is used for interrogation, with the focussed beam being scanned through a custom x-y comprising a pair of orthogonal galvanometer mirrors. An InGaS photodiode with a transimpedance amplifier is used to detect the reflected power, giving DC and AC coupled outputs. The former is connected to an analogue-to-digital card and used to perform the pre-tuning operation, whilst the latter is connected to a digitizer card and records the reflected optical power modulation (which encodes the acoustic data $S(t)$).

The main disadvantage of such a scanner with planar detection area is its incomplete view of the acoustic field. This issue, known as the limited-view problem, causes artefacts in the reconstructed images (distortion, lack of absolute pressure fidelity, non-physical negative values) and a deterioration in lateral resolution with increasing distance from the sensor. This will be discussed further in Section 9.1, where a system with two sensors in an orthogonal arrangement is used to tackle the issue.

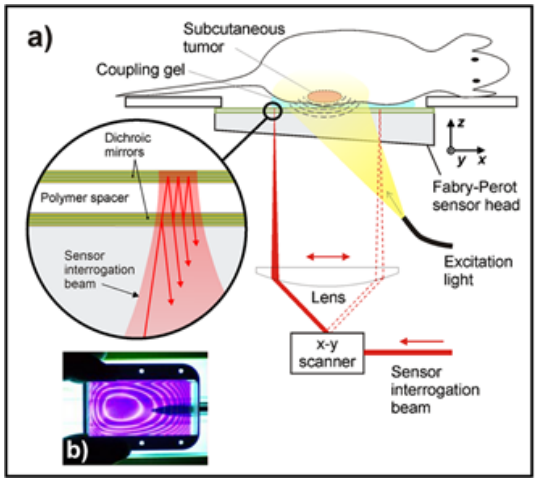

Figure 6.11: *Schematic illustrating the operation of the FP planar scanner system in its pre-clinical form. In this diagram PA illumination is done in backward-mode (through the sensor) but for imaging PVCP forward-mode was employed (from the top). Reprinted with permission from [28]. Copyright 2012 Society of Photo-Optical Instrumentation Engineers.*

6.6.3 Fabricated constructs and obtained images

To establish feasible manufacturing strategies and configurations for PVCP, three simple phantoms were developed. These were made with soft PVCP with 0.5 mg/ml of TiO_2 (Sigma Aldrich, Germany), into a purchased silicone mould with 39 mm diameter cylindrical pockets. The motifs embedded were respectively: a simple sub-500 μm-wide line made of self-adhesive black vinyl film (created with a commercial vinyl cutter); a 'UCL' pattern made of self-adhesive black vinyl film (created with a commercial vinyl cutter); a pair of 2 mm thick soft PVCP square inserts with 2% and 8% v/v black pigment respectively (both cut out from 2 mm thick PVCP slabs with a sharp square mould). During manufacturing, the inserts of interest were placed on a first layer of PVCP that had been poured and allowed to cure (Figure 6.12). To fully encapsulate the inserts, a second layer of PVCP was then poured and allowed to cure.

(a) (b)

Figure 6.12: *PVCP imaging constructs with insertions. (a) Photos of PVCP phantoms are shown before the second layer of PVCP was poured. Reproduced with permission from [182]. (b) Diagrams of the constructs.*

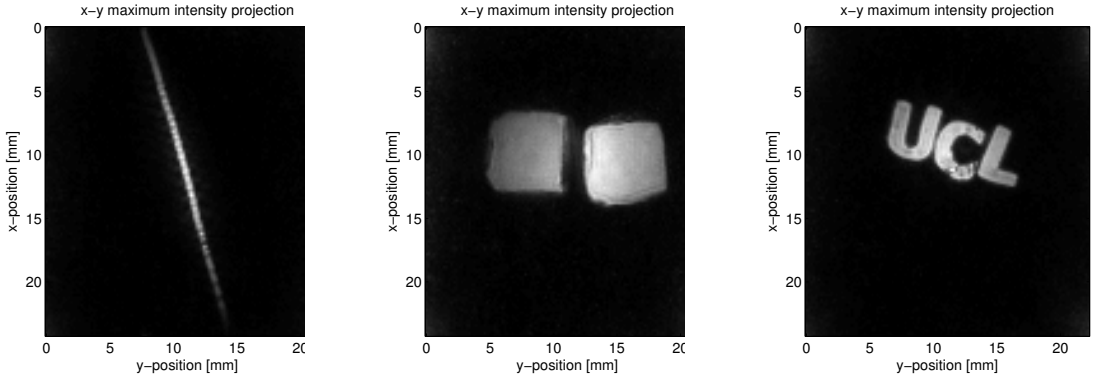

(a) Line phantom. (b) Embedded squares phantom. (c) 'UCL' phantom.

Figure 6.13: *x-y maximum intensity projections of the obtained PAT images of the constructs. In (b), the 2%v/v and 8%v/v black PVCP inserts are positioned left and right respectively. Reproduced with permission from [182].*

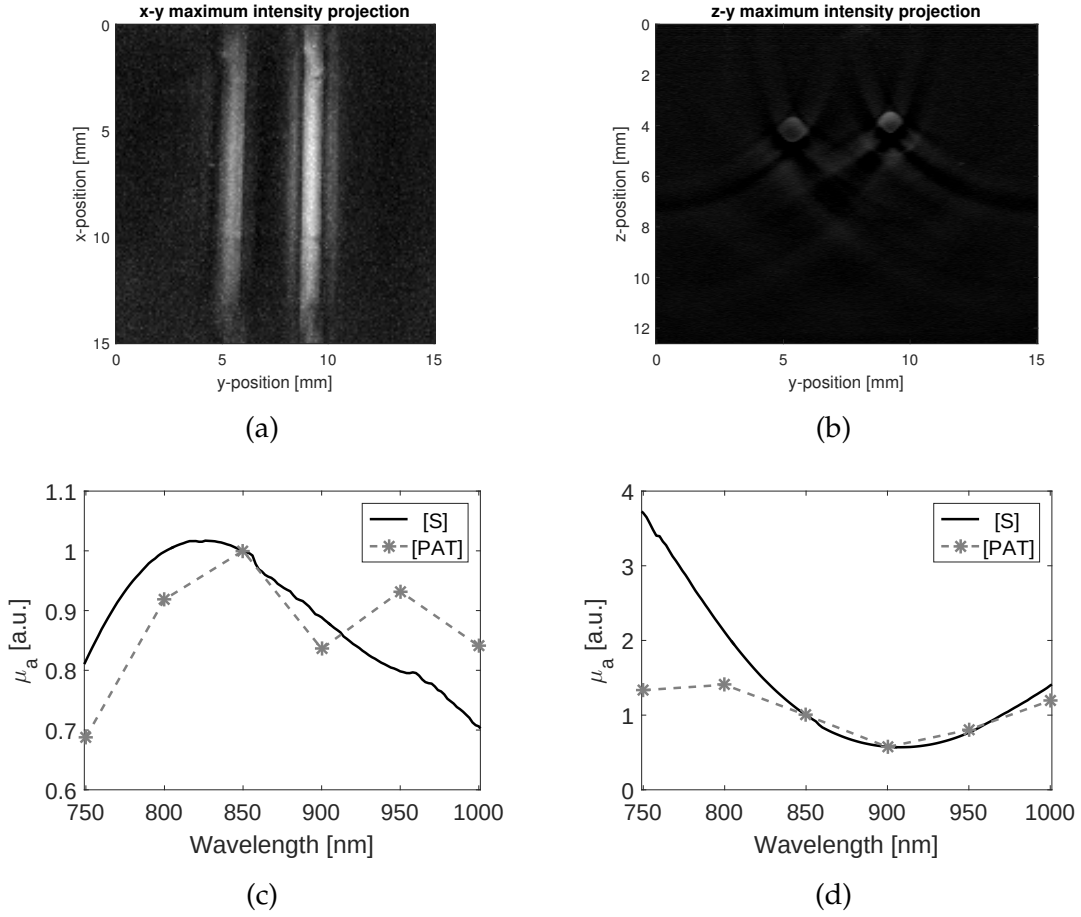

Figure 6.14: *Obtained PAT images of the hollow-channel PVCP constructs filled with absorbing solutions. (a) x-y MIP of a 3 mm slice for the channelled phantom, at 850 nm. Left: $CuCl_2$; Right: $NiCl_2$; (b) y-z MIP of the central 1 mm portion; (c)-(d) 850 nm normalised spectra for $CuCl_2$ and $NiCl_2$ respectively, comparing the spectrophotometer result ([S]) with the PAI intensity result ([PAI]). Reproduced with permission from [182].*

Photoacoustic imaging was performed using a Fabry-Perot scanner measurement system, with forward mode illumination at 500 nm being provided by the Innolas OPO system, with a beam diameter of 1 cm. Imaging parameters were: spatial resolution of $dx = 200\,\mu$m, $dy = 200\,\mu$m, $dt = 4$ ns, field of view $Nx \times Ny = 24 \times 22$ mm. The k-space back-projection algorithm in k-Wave [76], with $c = 1402\,\text{ms}^{-1}$ was used for reconstruction. Acoustic attenuation not accounted for in post-processing as this would exacerbate noise in the visualisation, though other strategies could have been employed if such correction was deemed necessary for other reconstruction purposes. The reconstructed 3D images obtained are shown in Figure 6.13 as x-y maximum-intensity projections (where the z-axis represents the depth direction). The main features can be perceived in all phantoms.

It is also possible to create PVCP phantoms with wall-less channels, given that PVCP is not prone to water absorption [211, 232]. This would allow the characteristics of the absorbing regions of interest to be changed easily between experiments, by changing the injected dye or pigment, and would also circumvent the issue with incorporating suitable absorbers in PVCP. Fewer reconstruction artefacts will also be present when compared to phantoms with walled-channels (where the wall is a different material such as a polyethylene tube), unless the wall material is explicitly accounted for. A double-channelled phantom was built to illustrate its potential use for multiple wavelength PAT. A silicone mould was used, with two 1 mm needles traversing it. After PVCP was poured and cured, the needles were removed, leaving two 1 mm diameter channels in the sample that were then filled with a solution of 34.7 g/l copper chloride ($CuCl_2.[2H_2O]$) and 440.6 g/l nickel chloride ($NiCl_2.[6H_2O]$) respectively. Note how this still creates an extra- to intra-luminal impedance mismatch interface (matrix/solution), but one less than for the walled phantom case (matrix/tube; tube/solution). Its composition is also more realistic.

Photoacoustic imaging was performed with a similar setup, with imaging parameters were: spatial resolution of $dx = 100\,\mu$m, $dy = 100\,\mu$m, $dt = 4$ ns, field of view $Nx \times Ny \times Nt = 15$ mm$\times$15 mm$\times$18 μs. Images were in this case acquired at multiple wavelengths, from 750 to 1000 nm in steps of 50 nm and corrected for incident fluence. x-y and y-z maximum intensity projection (MIP)s are shown in Figures 6.14 (a)-(b) respectively. Figures 6.14 (c)-(d) compare the 850 nm normalised absorption spectrum measured in the spectrophotometer to a metric on the total intensity inside the tubes, found through a thresholding operation. The spectra are distinct, which is expected due to the effect of spectral colouring, to the reconstruction artefacts partially associated to limited-view and to the limitations in the accuracy of the tube segmentation and choice of total intensity as a metric. Some artefacts are also due to the fact that a 600 kHz 6^{th}-order high-pass filter was in place during acquisition, which was later found to cause some phase shifting and group phase delay of the signals (and to manifest itself in reconstructed images somewhat like an edge operator).

6.7 Summary

• *In this Chapter, PVCP was characterised as a phantom material for multiwavelength qPAT. A good number of its characteristics were found to be well-suited.*

Speed of sound c(1 MHz)= [1402.3-1408.3] ms^{-1} was within ~ 10% of soft tissue, considered satisfactory for qPAT studies as long as well characterised. In the low frequency range, acoustic attenuation $\alpha(f) = [0.55 - 0.67]f^{[1.53-1.55]}$ dB cm^{-1} MHz^{-1} was analogous to most soft tissues. The density was shown to be similar to water, meaning that acoustic impedance was only mismatched to water by less than ~ 10%, less than for most polymer formulations reported, helping therefore to reduce acoustic reflections and artefacts. The Grüneisen parameter was found to be $\Gamma = 1.01 \pm 0.05$ for the soft formulation, its high value being beneficial in yielding a high SNR in qPAT acquisitions. It is also not too dissimilar from some soft tissue findings (e.g. ~25% higher than subcutaneous fat tissue, 0.81 [112]). No significant variations of Γ were found within relevant pigment absorber concentrations. Some satisfactory aspects were found in terms of optical properties, namely that the intrinsic absorption in the 400-1000 nm range was similar in magnitude to typical reported tissue background levels, around ~ 10^{-2} mm^{-1} order of magnitude, with higher absorption peaks above 1000 nm. The reduced scattering was also successfully tuned to tissue equivalent levels, around ~ 10^{0} mm^{-1} order of magnitude. Finally, fabrication and imaging of different geometries with various embedded structures or hollow channels was also possible, showing the versatility of the material. The main reservations are two-fold.

• *As a first reservation, the acoustic attenuation may be too high to properly represent some soft tissues and give proper SNR in validation settings.*

Though in the low frequency range the attenuation is overall low and matched to tissue, its trend with frequency is steeper than desired and leads to unnecessarily high attenuation at increasing frequencies, even when compared to most soft tissues except breast - as shown by the power law parameter $b = [1.53 - 1.55]$. To put in context, tissues such as the fat, liver, kidney, brain and breast have reported a of 0.6, 0.35-0.9, 1, 0.6-0.8, 0.75 dB cm^{-1} MHz^{-1} respectively, and reported b of 1, 1.1, 1 and 1.20-1.46 and 1.5 respectively [98, 248] Independent of attenuation matching or not real tissues, the sharp frequency-dependent behaviour and high attenuation may be problematic in initial qPAT studies since imaging PVCP may lead to low data SNR, especially of many structures of interest that intrinsically generate characteristically high frequencies, and may more generally create an additional non-linear confounding factor in the already difficult qPAT problem. From the acoustic point-of-view, PVCP may be a more attractive resource if used in a more complex follow-up step to a first qPAT step that has been optimised under low acoustic attenuation scenarios in a simpler phantom. Based on observations from this study and by Vogt *et al* (2016) for different plasticiser formulations, it seems that the most suitable formulation would probably be to use a commercial PVCP formulation (LureFactors or

MF-Manufacturing) with a high fraction of plasticiser (softener). This approach would lower the attenuation in PVCP the most possible, close to the upper soft tissue range.

• *A second reservation relates to the ability to find absorbers that will behave as desired, especially in terms of photostability.*

Though the optical characterisation of three different absorbing pigments dispersed in PVCP revealed that they all displayed absorption linearity with concentration and distinct and interesting optical spectra, further experiments revealed non-linear behaviour, possibly attributable to saturable absorption caused by ground-state depletion in the high-peak power regime [218]. This was manifested through mismatch between standard and PA specroscopy estimates, - both in absolute value and even in spectral shape for the red pigment - and non-linearities as a function of incident fluence (and more subtly as a function of concentration). There was also some permanent photobleaching, but the transient effects were more pronounced. For spectroscopic qPAT, these non-linearities and behavioural uncertainties are problematic. To obtain the desired stable absorption needed for qPAT, one option would have been to explore different pigments. The particular pigments studied in this work had been chosen to ensure compatibility to the matrix and resistance to the high temperature fabrication process - having come from the same supplier as the PVCP -, but there would be scope to explore pigments from different suppliers in the plastic materials colouring industry [240, 241] and perform appropriate absorber characterisation studies. The main obstacle would be short-listing the most promising variants from the large repository of colourants, especially since the type of tabulated features (such as hue, light and weather fastness, fastness to bleeding, tinting strength, particle size distribution, pigment dispersibility and minimum limiting concentration) are industry-geared and do not give direct indication about their better or worse propensity for absorption non-linearities. Another option that exploits PVCP in a stable absorption scenario is to use a PVCP phantom matrix with no embedded chromophores - only relying on the intrinsic PVCP absorption spectrum - and where wall-less channels have been created that can be filled with stable and well-characterised absorbing solutions. This circumvents the need to disperse absorbers in PVCP directly, both for the background of the phantom and for highly absorbing regions. Wall-less, channelled phantoms come with other advantages: they provide a more vasculature-realistic geometry, the absorbers can be changed quickly by flushing the solutions in and out the channels and contrary to liquid phantoms no acoustically mismatched capillary tubes are needed.

Despite all the previous, it may be that the issues with the used pigments are not that compromising for more general and less quantitative PA applications, assuming that the varying region in the red absorber is avoided. On one hand, despite some deviations, the pigments did mostly display μ_a linearity with concentration even at high peak power; on the other, the 5-fold variation in peak power that led to a maximum 13% variation in μ_a was done under the worst case scenario of direct surface incidence on the pigments. It may be that further investigation for scenarios where absorbing inserts are at greater

depth and where light has been attenuated and diffused show that the dynamic range of the non-linear variation is less pronounced (as fluence lowers less saturable absorption phenomena occur - as seen in Figure 6.7 (f) where the μ_a variation with fluence plateaus).

6.8 Conclusion

To conclude, PVCP does have the potential to be a useful and versatile phantom material for qPAT and other multiwavelength applications, but for now its acoustic absorption may limit its use to lower frequency (larger scale) systems, and care must be taken because of the possibility of nonlinear optical behaviour at high peak powers for some absorbers. Ideally, other promising materials like PDMS and gel wax should in the future also be characterised more broadly for quantitative and multiwavelength PA. It seems though that irrespective of matrix material, the main issue and limiting step in the implementation of well-controlled, characterised and tunable qPAT studies is finding suitable chromophores as additives, rather than fundamental inadequacies in properties of some of these matrix materials themselves. This should be the main focus of future studies, whether for chromophores for *in vitro* or contrast agents for *in vivo* applications. Meanwhile, to move forward with our key qPAT experimental study objectives, which required having meticulously controlled, stable and defined optical properties, it was considered wisest to focus primarily on the absorbers themselves and then choose the medium that best enabled high confidence in this characterisation whilst still satisfying satisfactorily other phantom criteria.

Chapter 7

The sulphates

As discussed in Section 5.3, and as further concluded from the studies with PVCP, finding suitable chromophores for spectroscopic studies and quantitative studies (i.e. that respect the criteria defined in Section 5.3) is not trivial. In this Chapter, we assess the suitability of sulphate salts as chromophores for well-controlled spectroscopic and quantitative experiments. This was motivated by encouraging results from previous studies and literature values.

Sulphates have well tabulated information on molecular weight and solubility. Knowing solubility becomes especially relevant when trying to assess what is the maximum optical absorption that can be achieved before linearity is compromised. Table 7.1 summarises the literature-reported properties, with solubility values shown for 20^{o}C, a typical room temperature (solubility increases with temperature) [113].

Compound	**Molecular formula**	**Molecular weight (g/mol)**	**Solubility at 20^{o}C**
Copper sulphate pentahydrate	$CuSO_4.5H_2O$	249.68	320 g/l ≃ 1.28 M
Nickel sulphate hexahydrate	$NiSO_4.6H_2O$	262.85	625 ≃ 2.37 M

Table 7.1: *Some literature-reported properties of Copper and Nickel Sulphate*

Su *et al* 2010 [249] used a 3-tube phantom filled with three different sulphate salts respectively (nickel, copper and ferrous) in a background of Intralipid to study post-processing procedures on a whole-body PAT measurement system. Tubes filled with nickel sulphate have also been used to illustrate the merits of a new model-based iterative acoustic reconstruction technique experimentally [250]. Further, there is some indication that the compounds may be transiently photostable, since a study by Balderas-López & Díaz-Reyes 2011 [251] reported similar optical absorption estimates for copper sulphate at 658 nm between a spectrometer-based method and a photoacoustic method.

Based on this knowledge, we aimed to fully characterise and assess the suitability of the compounds, in their aqueous form, for full *multiwavelength* photoacoustic imaging scenarios. This mainly involved assessing:

- Optical absorption behaviour in terms of absorption linearity with individual species concentration and also in mixtures of different sulphate species (Section 7.1.1);
- Relevancy and informativeness of their spectral absorption shapes and their potential as oxy- and deoxyhemoglobin surrogates (Section 7.1.1);
- Permanent and transient photostability (Section 7.1.2);
- Physical and optical behaviour when mixed with a common scatterer, Intralipid (compatibility) (Section 7.2);
- Thermoelastic efficiency as a function of concentration (Section 7.3);

The characterisations in the next sections were all done for the compounds in their hydrated form, but for ease of notation, they will often be referred to simply as copper sulphate, $CuSO_4$, and nickel sulphate, $NiSO_4$.

7.1 Optical absorption properties

To measure some of the optical absorption characteristics of the sulphate solutions, namely the specific absorption spectra, maximum absorption before saturation, absorption linearity with concentration and absorption linearity of mixtures, the dual-beam spectrophotometer was used. The mother solution for each species was chosen to be close to the solubility limit, $c_{NiSO_4,b} = 2.2\,M$, $c_{CuSO_4,b} = 1\,M$ and diluted in order to obtain solutions with $c_{NiSO_4} = \{0.55, 1.1, 1.65, 2.2\}\,M$ and $c_{CuSO_4} = \{0.25, 0.5, 0.75, 1\}\,M$ respectively. Mixtures of $NiSO_4$ and $CuSO_4$ were also prepared according to the following ratios of $c_{NiSO_4,b}$ to $c_{CuSO_4,b}$: 1:3, 2:2 and 3:1.

7.1.1 Absorption spectra and linearity with concentration

Figure 7.1 shows the measured absorption spectra of the solutions of either $NiSO_4$ or $CuSO_4$, at various dilution levels. It can be seen that both have linear absorption characteristics with concentration, where linear fits yielded coefficients of correlation R^2 >0.99. Figure 7.2 shows measured absorption spectra of mixtures of $NiSO_4$ and $CuSO_4$ (*meas*). These spectra are compared with those predicted (*pred*) by considering the measured mother batch spectra and applying equation $\mu_a(\lambda) = \mu_{a,CuSO_4,b}(\lambda) f_{CuSO_4} + \mu_{a,CuSO_4,b}(\lambda) f_{NiSO_4}$, where f_{CuSO_4} and f_{NiSO_4} are the fractional concentrations of $NiSO_4$ and $CuSO_4$ relative to the respective mother batch concentrations. It can be seen that the measured spectra for the

mixtures give an accurate reflection of the linear sum of the individual unmixed absorptions.

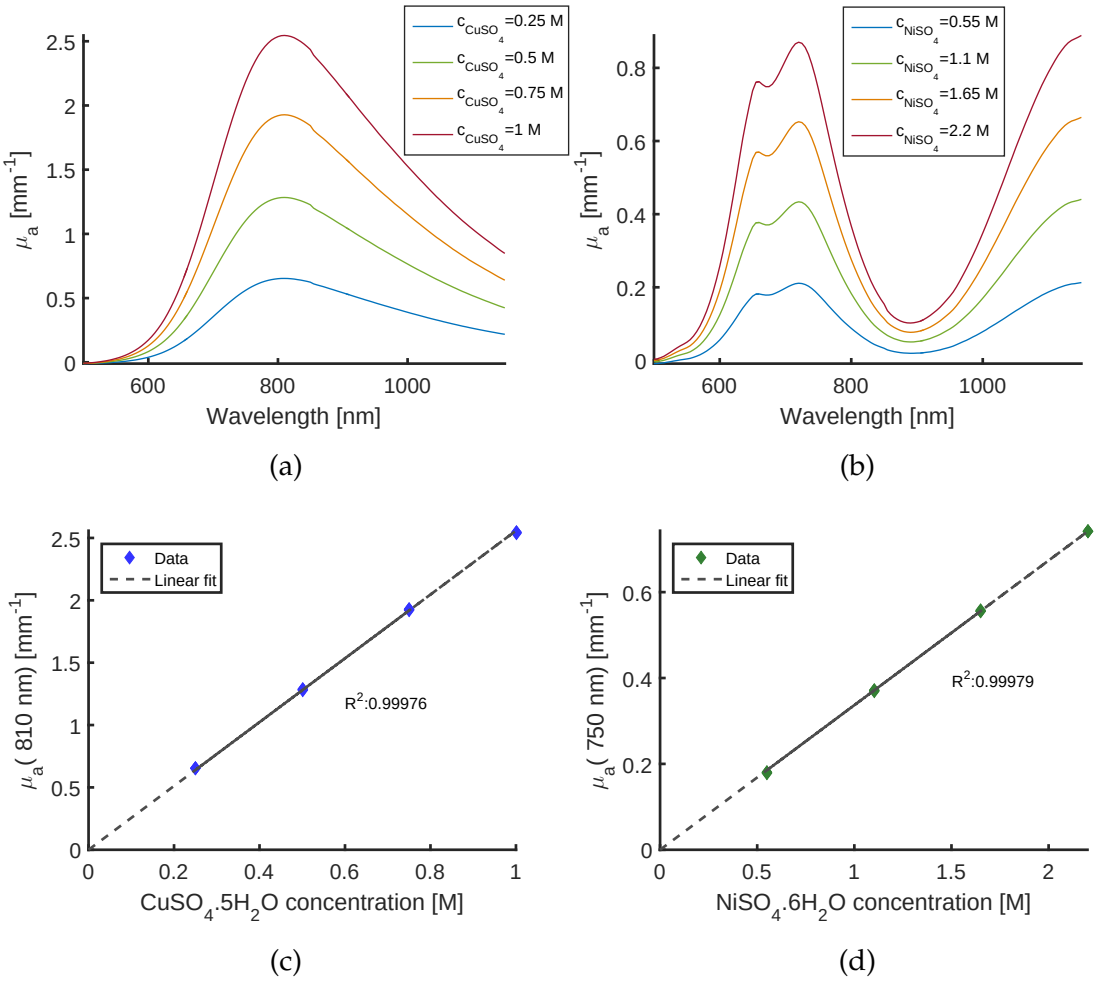

Figure 7.1: *Absorption spectra of four levels of dilution, for both (a) $CuSO_4$ and (b) $NiSO_4$. Absorption linearity with concentration is respected, as shown in (c) and (d), where absorption near peak wavelength is plotted as a function of concentration.*

Figure 7.3 (a) shows the specific (molar) absorption spectrum of each compound, $\alpha(\lambda)$. The spectra for the two compounds are distinct from one another, where each has different features and gradients. It was also found that the compounds could be adequate surrogates for oxy- and deoxyhemoglobin in terms of their spectral shapes and magnitude. Figure 7.3 (b) makes this suitability clearer, by plotting the absorption spectra of oxy- and deoxyhemoglobin in a typical physiological blood sample (total hemoglobin concentration c_{HbT}=150 g/L and oxygen saturation SO_2=80% [63]), as well as the spectra of a 0.137 M $CuSO_4$ solution and 0.489 M $NiSO_4$ solution, where these molar concentrations were chosen to match the absorption of oxy- and deoxyhemoglobin at 800 nm respectively (near the isosbestic point of hemoglobin). Analogous behaviour can be seen for both pairs in the NIR window (650 nm onwards) - namely, in both cases the pairs of spectra cross-over once and near 700 nm ; also, $CuSO_4$ and oxyhemoglobin (HbO_2) have similar spectral shapes, with a broad main peak, though one is centred at 815 nm and the other closer

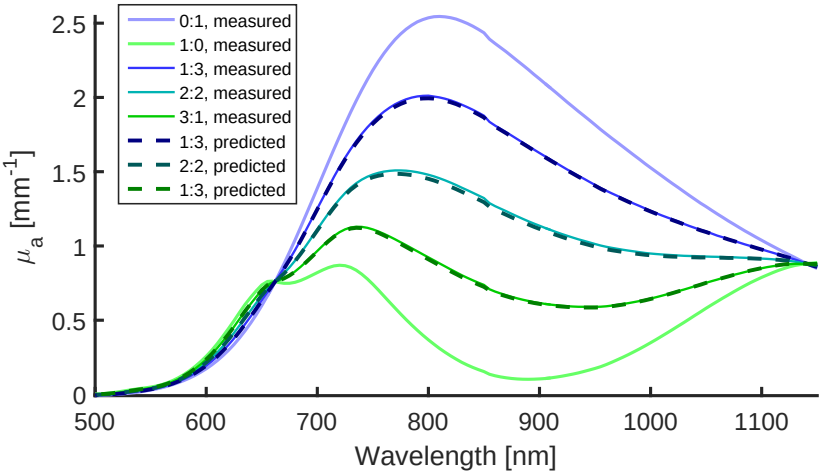

Figure 7.2: *The mixtures have a measured absorption spectrum that matches the predicted spectrum from the simple linear combination of the measured spectra of the mother batch solutions of nickel sulphate, $c_{NiSO_4,b}$, (1:0) and copper sulphate, $c_{CuSO_4,b}$, (0:1).*

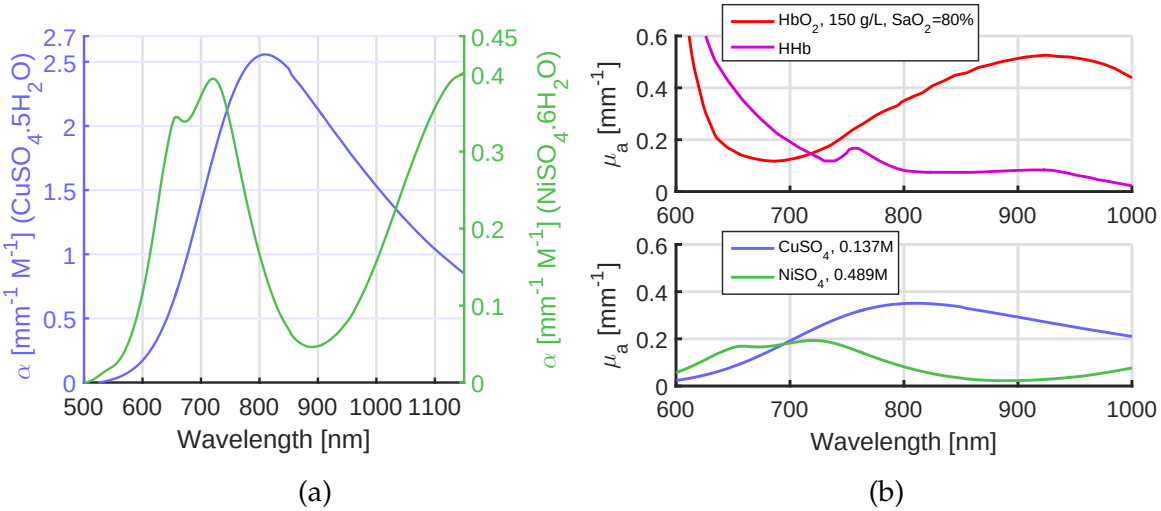

Figure 7.3: *a) Specific absorption spectra of $NiSO_4$ and $CuSO_4$; b) $NiSO_4$ and $CuSO_4$ as analogues for deoxy- and oxyhemoglobin. Spectra for deoxy- (HHb) and oxyhemoglobin (HbO_2) are shown as their individual/partial contributions to blood with 150 g/L hemoglobin and 80% saturation. The spectrum for $NiSO_4$ is plotted for a concentration where absorption would match that of partial deoxyhemoglobin at 800 nm. The spectrum for $CuSO_4$ is plotted for a concentration where absorption would match that of partial oxyhemoglobin at 800 nm.*

to 950 nm; similarly, deoxyhemoglobin (HHb_2) has a mainly decreasing or plateauing behaviour that is fairly well mirrored by $NiSO_4$. However, at wavelengths below 650 nm (outside the NIR window), it should be noted that the sulphates do not accompany the rise in absorption by orders of magnitude seen for oxy- and deoxyhemoglobin.

If there is interest in emulating the isosbestic point of hemoglobin (i.e. the wavelength where, for a certain hemoglobin concentration c_{HbT}, the total absorption will remain unchanged regardless of the level of oxygen saturation, SO_2), then the following rule of thumb could be followed: mixtures should be made from mother batch solutions of $NiSO_4$ and $CuSO_4$ that have a relative molar ratio of 14.28 to 1, i.e. $c_{NiSO_4,b2}\,[M] = 14.28\; c_{CuSO_4,b2}\,[M]$.

7.1.2 Absorption at high peak power

To assess whether the compounds studied were stable when exposed to the high peak power ns-pulsed sources typical in PA, transient and permanent photostability were tested through the methods described in Section 5.4.3 and Section 5.4.2 respectively. The Innolas OPO system was employed for all high peak power measurements.

To assess transient photostability, the absorption spectra of the mother solutions obtained with the spectrophotometer (employing low power CW illumination) were compared to those derived from photoacoustic spectroscopy measurements (μ_a was obtained through curve-fitting - only the wavelengths that yielded a goodness of fit $R^2 > 0.98$ are considered and displayed). Figure 7.4 (a) shows that there is overlap in the spectroscopically ([S]) and photoacoustically ([P]) derived absorption spectra, both in shape and absolute units. This supports the hypothesis that there is no transient photobleaching occurring.

To probe the permanent photostability, newly prepared samples of 2.2 M $NiSO_4$ and 0.5 M $CuSO_4$ were continuously excited for 30 minutes (this equates to 54000 pulses at 30 Hz) with the PAS system. The wavelengths chosen were close to the absorption maximum of each compound in the NIR window - 750 nm for $NiSO_4$ and 810 nm nm for $CuSO_4$, for which the Innolas source had an incident energy of ~ 7.3 mJ and ~ 6.2 mJ respectively. The PA signals were recorded every 3 minutes. The temporal evolution of the curve-fitted μ_a can be seen in Figure 7.4, indicating an overall stable behaviour during the full exposure and therefore absence of permanent photobleaching signs.

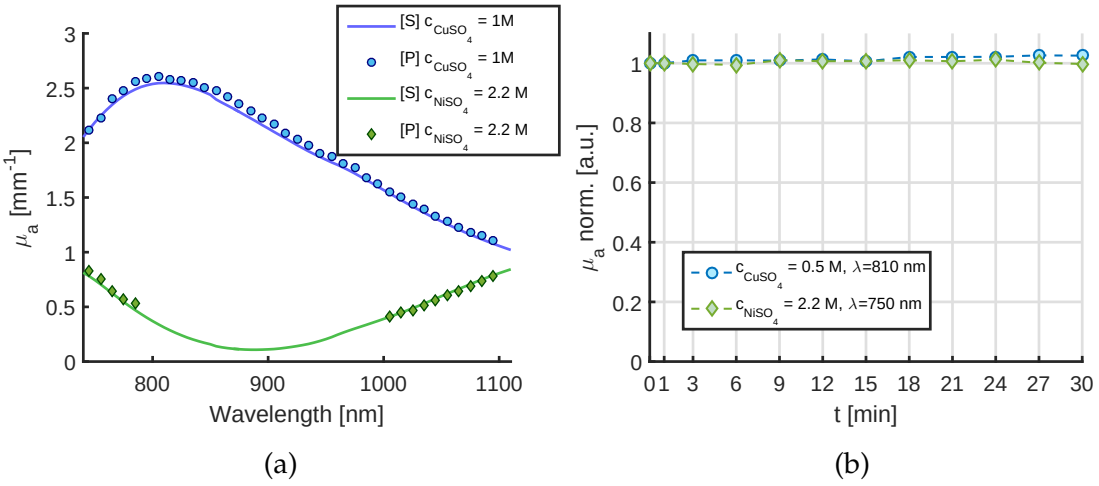

Figure 7.4: *Transient and permanent photostability of $NiSO_4$ and $CuSO_4$. (a) Spectroscopically (solid line) and photoacoustically (data points) derived absorption spectra; (b) Photostability under 30 minute irradiation (54000 pulses)*

7.2 Optical scattering properties

Aqueous solutions $CuSO_4$ and $NiSO_4$ have negligible scattering. Intralipid is commonly used to confer tissue-like scattering properties to solutions and media [183]. Nevertheless, mixing sulphate (or chloride) based solutions with Intralipid results in non-stable mixtures [252] - emulsions are quickly disrupted forming 2 phases. Salts are known to disrupt hydrophobic/hydrophilic interactions among molecules [253]. Figure 7.5 shows the overnight stability of 1% w/v Intralipid mixtures with different additives: whilst Intralipid-only (v) and Intralipid+india ink (i) mixtures were stable, those with added sulphates (b-d) were unstable, creating two phases - a rim rich in Intralipid on top of an aqueous translucent phase. This phenomenon occurred in fact as soon as an hour after mixing.

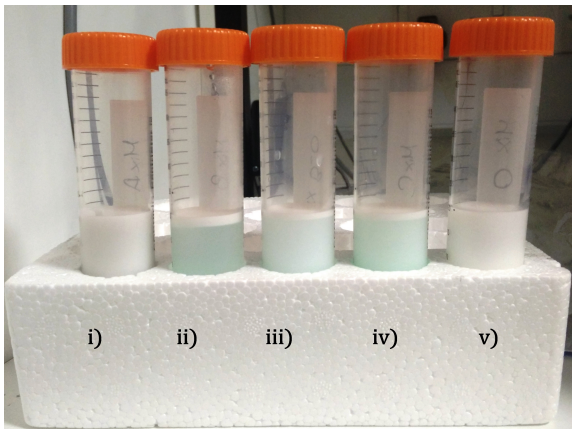

Figure 7.5: *Overnight stability of mixtures. All solutions are made of 1% w/v Intralipid in water. From left to right, they have different absorbers: i) added india ink, yielding $\mu_a \simeq 0.008\,mm^{-1}$ at 750 nm; ii-iii) added nickel and copper sulphate, yielding $c_{NiSO_4} = 0.011\,M$, $c_{CuSO_4} = 0.005\,M$; iv) added nickel sulphate, yielding $c_{NiSO_4} = 0.033\,M$; v) no additional absorber.*

It was hypothesised that adding an emulsifier like Tween-20 could potentially stabilise Intralipid emulsions [254]. To test this, 1% w/v Intralipid solutions with 0.033 M $NiSO_4$ were prepared, with concentrations of Tween $c_{Tween} = \{0, 0.05, 0.5, 5\}$% v/v. A control 1% w/v Intralipid solution was also prepared, with no added sulphates or Tween. The control solution and all Tween solutions presented a single homogeneous phase for up to 48 hours after sample preparation and homogenisation, whilst the sample with added sulphate but no Tween started separating into two phases - with a rim as soon as an hour after preparation (Fig. 7.6). This seemed to indicate, at least visually, that Tween could stabilise the solutions, even when as little as 0.05% v/v Tween-20 was used.

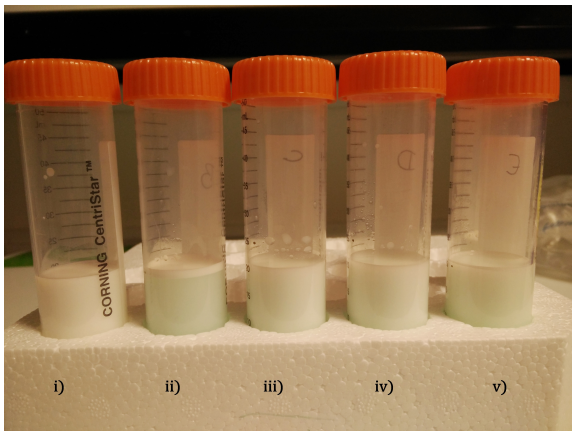

Figure 7.6: *Overnight stability of mixtures with Tween. All solutions are made of 1% w/v Intralipid. From left to right, they have different compositions: i) standard solution; ii) added $NiSO_4$, yielding $c_{NiSO_4} = 0.033\,M$. iii-v) added $NiSO_4$ and varying levels of Tween, yielding $c_{NiSO_4} = 0.033\,M$ and $c_{Tween-20} = \{0.05, 0.5, 5\}\%v/v$ respectively*

To confirm this trend in a more quantifiable manner, the reduced scattering coefficient μ_s' was characterised for a new batch of solutions of interest (Table 7.2) - immediately after preparation and also 48 hours after. Mixtures were always properly mixed and rehomogenised before measuring. To characterise the reduced scattering coefficient μ_s' of the solutions of interest, total transmittance (M_T) and total reflectance (M_R) were measured and the IAD algorithm was then employed, where the scattering anisotropy factor was fixed at $g = 0.6$ [208]. Measurements were performed on the 100 mm integrating sphere, between 500 and 1200 nm, with the solution poured into a 1 mm quartz cuvette. This was done 3 times per solution, where in-between the cuvette was always emptied and re-filled.

Figure 7.7 (a) shows that the addition of sulphates - whether $NiSO_4$ or $CuSO_4$ - to Intralipid significantly affects the measured reduced scattering coefficient and that this behaviour varies in a non-trivial manner with sulphate concentration. This was observed in readily prepared samples and where proper homogenisation had been attempted before measuring, meaning that the change in characteristics of the emulsions with sulphates is due to more than simple macroscopic phase separation or degradation over time. For all cases, the pre-addition of Tween to the solutions before mixing with Intralipid successfully yielded a reduced scattering coefficient analogous to the Intralipid-only sample.

Samples	Intralipid (% w/v)	$NiSO_4$ (M)	$CuSO_4$ (M)	Tween-20 (% v/v)
3.a	1	0	0	0
3.b	1	0	0	0.025
3.c	1	0.0165	0	0
3.d	1	0.0165	0	0.025
3.e	1	0.0495	0	0
3.f	1	0.0495	0	0.075
3.g	1	0	0.0037	0
3.h	1	0	0.0037	0.025

Table 7.2: *Samples with different combinations of Intralipid, $CuSO_4$, $NiSO_4$ and Tween-20, for reduced scattering measurements.*

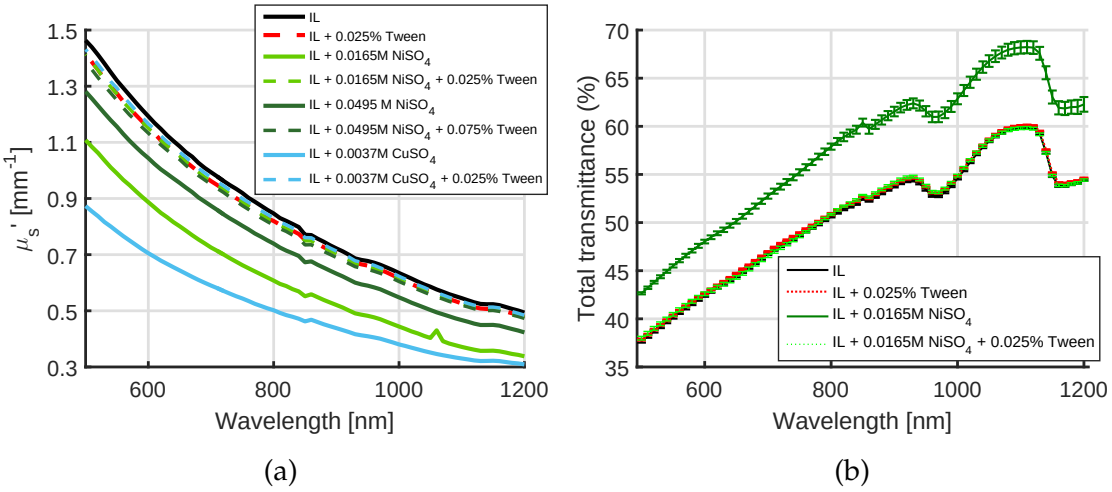

Figure 7.7: *Scattering behaviour of samples with different combinations of Intralipid, $CuSO_4$, $NiSO_4$ and Tween-20. (a) Reduced scattering coefficient; (b) Total transmittance.*

The effect of the sulphates and Tween can also be observed clearly through the total transmittance curves in Figure 7.7 (b). Theoretically, the addition of 0.0165 M of $NiSO_4$ should residually increase absorption and thus residually reduce total transmittance. However, measurements show a considerable increase in total transmittance for sample 3.c (similar behaviour for 3.e and 3.g - data not shown). Pre-addition of 0.025 %v/v of Tween (sample 3.d) successfully averted that phenomenon, yielding similar total transmittance to the Intralipid-only sample.

7.3 Thermoelastic properties

To characterise the Grüneisen behaviour of the sulphates, namely concentration dependency, solutions at five concentrations were prepared for each compound:
$c_{NiSO_4} = \{0.275, 0.55, 1.1, 1.65, 2.2\}\,M$ and $c_{CuSO_4} = \{0.125, 0.25, 0.5, 0.75, 1\}\,M$. Grüneisen parameter estimates were obtained with the photoacoustic spectroscopy setup, through the strategy described in Section 5.4.5 for a single spectral window. Measurements were

done at wavelengths where the water absorption has a prominent peak and is dominant - 1400 to 1500 nm.

The Grüneisen parameter of the aqueous solutions was found to follow a linear trend with increasing concentration of either $CuSO_4$ or $NiSO_4$ (Figure 7.8). The slope of each (β_{NiSO_4} and β_{CuSO_4}) was found through linear regression and is given in Table 7.3. Overall, the Grüneisen parameter of an aqueous solution of $CuSO_4$ and $NiSO_4$ could be described as a first approximation by the following empirical equation:

$$\Gamma_{solution} = \Gamma_{water}\left(1 + \beta_{NiSO_4} c_{NiSO_4} + \beta_{CuSO_4} c_{CuSO_4}\right), \tag{7.1}$$

where concentrations are in Molar. This type of behaviour is consistent with some previous observations. Petrova *et al* (2013, 2014) [255, 256] characterised the relative change of Grüneisen parameter with temperature for both sulphates, and found that the temperature point of null PA signal (null Grüneisen parameter) changed linearly with salt concentration. Laufer *et al* (2010) had also shown that the Grüneisen behaviour in aqueous solutions of chloride salts varied linearly with salt concentration [56].

The Grüneisen levels found are higher than water, which can be good for SNR, and are overall within a tissue-realistic range. We can for instance consider the hypothetical sulphate mixture shown in Figure 7.3 (b) (bottom), which emulates absorption at 800 nm for oxy- and deoxyhemoglobin in blood with 150 g/L hematocrit at 80% saturation. According to the empirical formula, this mixture would have a $\Gamma_{solution} = 0.206$, which is within the 0.152-0.226 range reported for blood [257]. Another physiologically relevant characteristic of the Grüneisen behaviour may be the linear dependence with concentration itself: it has been shown that the Grüneisen parameter in red blood cell suspensions also displays a linear type of behaviour with hemoglobin concentration [112]: $\Gamma_{RBCS} = 0.124 + 0.04995\, f_{150g/L}$, measured at 22ºC, where $f_{150g/L}$ is the concentration of hemoglobin given as a fraction of 150 g/L, a typical physiological hematocrit. Also, if we redefine this as a function of $\Gamma_{water} = 0.124$, where 0.124 is a realistic literature value for water in the 22-23ºC range [113], we obtain $\Gamma_{RBCS} = \Gamma_{water}(1 + 0.403\, f_{150g/L})$, which illustrates how the baseline and slope are comparable in magnitude to the behaviour seen for the sulphate solutions.

The previous calculations assumed that the Grüneisen parameter has no dependence on wavelength. Figure 7.9 shows, for the 740-1100 nm range, the ratio between the peak-to-peak reading corrected for pulse energy ($V_{pp}(\lambda) = \frac{V'_{pp}(\lambda)}{\Phi_0(\lambda)}$) and the fitted μ_a of the PA signal. This will in principle be proportional to the Grüneisen, $\frac{V_{pp}(\lambda)}{\mu_a(\lambda)} = \kappa\Gamma(\lambda)$, where κ is a scalar. Though there is some variation, the ratio does not have a prominent dependence on wavelength (Fig. 7.9). The plotted discontinuity for $NiSO_4$ is due to insufficient SNR for those wavelengths.

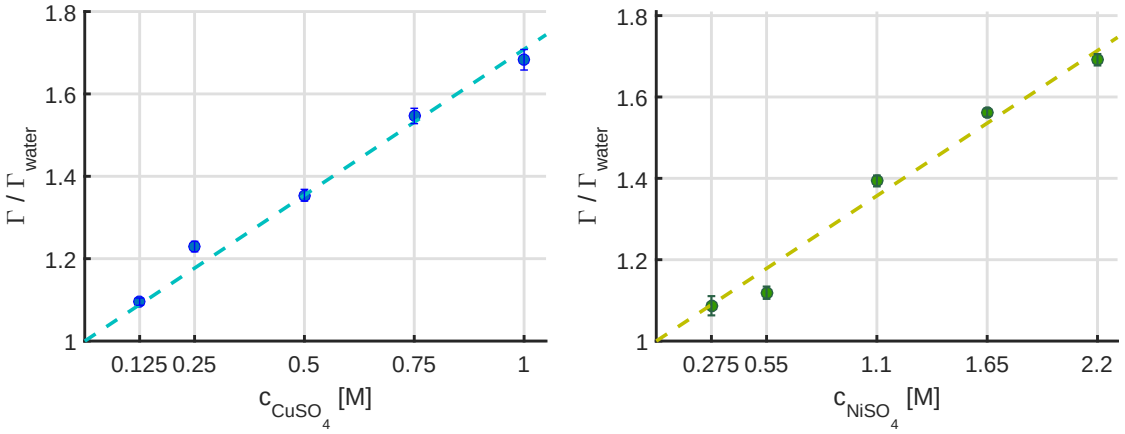

Figure 7.8: *Grüneisen dependency of $NiSO_4$ and $CuSO_4$ aqueous solutions with concentration, measured relative to water. Linearity is observed.*

Compound	β **factor** $[M^{-1}]$	β **factor standard uncertainty**	**Temperature in solution** $[^oC]$
$CuSO_4.5H_2O$	0.708	0.025	23.0±0.2
$NiSO_4.6H_2O$	0.325	0.015	22.6±0.2

Table 7.3: *Calculated factors accounting for concentration-dependency of the Grüneisen parameter of Copper and Nickel Sulphate aqueous solutions.*

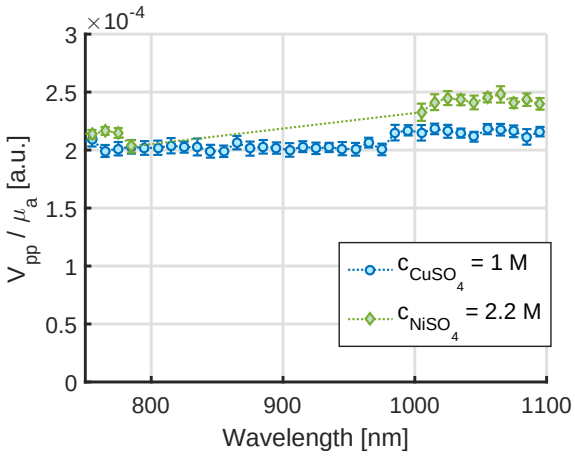

Figure 7.9: *Ratio between peak-to-peak voltage reading V_{pp} and exponentially-fitted μ_a for $NiSO_4$ and $CuSO_4$ measured with photoacoustic spectroscopy.*

7.4 Summary

• *Aqueous solutions of $NiSO_4$ and $CuSO_4$ are chromophores that present the characteristics desired for* in vitro *photoacoustic imaging studies, namely those studies where multiwavelength information is relevant.*

Regarding absorption characteristics, the spectra of the sulphates are unique and rich in spectral features. The absolute absorption varies linearly with concentration and, more generally, respects the Beer Lambert law when mixed with other linearly behaving species. Importantly, the concentrations needed to yield absolute absorption values within the physiological range are below the solubility limit. The sulphates displayed long-term as well as transient photostability, being therefore suitable for exposure to typical photoacoustic sources, even for the extended periods of time that may be required when using some PA measurement systems and acquisition frameworks based on raster scanning [4]. Presence of either $NiSO_4$ or $CuSO_4$ in aqueous solutions led to linear increases in the Grüneisen parameter with concentration. Having access to and incorporating this information is often essential when performing quantitative PA studies. Another potential advantage is that, since increasing solute concentration contributes to rises in both μ_a and Γ - both of which will boost PA signal -, improved SNR can be obtained. Attention should however be given to temperature - as this will also affect thermodynamic behaviour.

• *Aqueous solutions of $NiSO_4$ and $CuSO_4$ may act as appropriate surrogates for oxy- and deoxyhemoglobin*

The specific absorption spectra of $NiSO_4$ and $CuSO_4$ in the NIR window range have spectral shapes that reasonably emulate deoxy- and oxyhemoglobin respectively. The signature isosbestic point of blood near 800 nm can also be emulated by preparing appropriate mother-batch solutions. Furthermore, the concentrations of the solutions can be varied to match expected absorption levels of blood at typical physiological hematocrit levels. For those concentrations, the Grüneisen parameter will also be similar to blood. The fact that aqueous solutions were shown to have Grüneisen parameter that varies linearly with concentration could be exploited - it has been that the shown the Grüneisen in red blood cell suspensions also follows a linear behaviour with hemoglobin concentration, and that it is of comparable baseline and slope [112].

• *Intralipid emulsions can be mixed with $NiSO_4$ and $CuSO_4$ for increased reduced scattering, as long as a proper emulsifier is used.*

It was found that solutions with relevant and predictable optical absorption and scattering can be prepared with sulphates as absorber and Intralipid as scatterer, as long as an appropriate emulsifier (e.g. Tween) is used. When no emulsifier was used, the sulphates were found to disrupt the emulsions, even at residual concentrations - with reduced scattering decreasing considerably and the mixture becoming visibly cloudy and separated in

two phases. For solutions with added Tween, emulsions were stable and had the expected reduced scattering behaviour compared to the equivalent Intralipid-only solution.

7.5 Conclusions

$NiSO_4$ and $CuSO_4$ aqueous solutions were found to have all the desired properties for qPAT and can therefore be readily incorporated in capillary tube-based phantoms or solid phantoms with hollow channels (e.g. PDMS and PVCP) to obtain stable and reliable ground-truth information that is also tissue-relevant. Apart for the optical scattering studies in Intralipid, all other characteristics were tested with water as the solvent - using other solvents or mixing the sulphate salts in matrices meant for solid phantoms (e.g. PVCP, hydrogels) was not tested and may lead to unexpected behaviour which should be studied on a case-by-case (matrix-by-matrix) basis. This is true more generally for any untested additive-matrix pairs.

Part III

Experimental Quantitative Photoacoustic Tomography

Chapter 8

Sensitivity to sources of experimental uncertainty

8.1 Motivation

We have in previous Chapters illustrated that optical model based inversion (MBI) is a general framework for solving the qPAT problem that can in principle provide high accuracy. Crucially, it has been demonstrated in simulation that it can, under the right conditions, successfully deal with inherent issues such as non-uniqueness, non-linearity and spectral colouring [34, 39, 114, 150]. Throughout Part III, we will work towards experimentally obtaining, under well-controlled and characterised conditions and with an optimised acquisition protocol, estimates of chromophore concentration and ratiometric parameter distribution, in 3D and at high resolution.

We have noted in Section 3.2.3 that experimental translation comes with a series of additional challenges. Understanding and dealing with these issues is especially important for the successful translation of quantitative PAT frameworks to *in vivo* pre-clinical and clinical scenarios. One concern is that the accuracy of MBI methods depends on the validity of the model assumptions, which include assumptions on the quality of the inputs, often assumed ideal and fully known in simulation studies. However, in real experimental scenarios they are measured or estimated and therefore affected by a range of sample-related and setup-related issues. We address this outstanding issue in this Chapter by assessing in simulation the effect that uncertainties in the optical inputs have on the success of model-based inversions. We do this for the inputs we have least confidence in. The main questions to be addressed are:

- How sensitive are typical model-based minimisations to uncertainty in explicit input parameters?;
- Is it feasible to include the uncertain parameters as additional unknowns in the model-based inversion, or to use additional priors, or mitigate the effect of uncer-

tainties with simple model adaptations?

- MBI can provide high accuracy, whilst heuristic decomposition approaches (e.g. simple linear unmixing or 1D fluence-corrected linear unmixing) will intrinsically lead to error. However, once typical uncertainty levels in parameters used in otherwise accurate MBI are considered, will it affect accuracy and uncertainty to a point that does not justify the added implementation complexity and running time?

The starting point is a simulated multiwavelength set of images of the initial pressure distribution. The uncertainties dealt with are those on the inputs to the optical problem: overall data calibration, scattering amplitude, beam profile and beam positioning. In this study it was assumed that the acoustic inversion was performed perfectly because it is deemed well understood. (It will be seen in the actual experimental study in Chapters 9 and 10 that, in fact, the accuracy of the acoustic reconstruction proved to be a critical factor.)

8.2 The virtual phantom data

Two 2D virtual phantoms were created - one emulating a cross-section through straight tubes and another one emulating vasculature.

The first virtual phantom replicated a typical experimental phantom design. The mesh domain was 6x6 mm, formed by $Ne = 7200$ regular triangular elements yielding $Nh = 3721$ nodes. 4 tubes with 600 μm diameter were included, represented in 2D by their circular cross-section. Copper chloride $CuCl_2$ and nickel chloride $NiCl_2$ were used as the main absorbers, given their known suitability for *in vitro* studies [56]. The concentration distributions of all chromophores and of the scatterer are shown in Figure 8.1 (a). Considering the tubes by row, from top left to bottom right, the concentration of $CuCl_2$ was $c_{CuCl_2} = \{0.25, 0.75, 1, 0\}$, and the concentration of $NiCl_2$ was $c_{NiCl_2} = \{0.75, 0.25, 0, 1\}$, defined as a fraction of the concentrations of the respective mother batches $c_{CuM} = 35.5069\ g/l$ and $c_{NiM} = 399.783\ g/l$. This yielded values of 75 %, 25 %, 0 % and 100 % for a ratiometric quantity analogous to oxygen saturation SO_2, $R(\%) = \frac{c_{NiCl_2}}{c_{NiCl_2}+c_{CuCl_2}} \times 100$. The background was filled with $c_{NiCl_2,bkg} = 0.005$, $c_{CuCl_2,bkg} = 0.005$ ($R = 50\%$). Water H_2O, the solvent, was an additional chromophore that was present and known in the entire domain. Spectra for $CuCl_2$, $NiCl_2$ and H_2O are given in Figure 8.1 (b). Reduced scattering μ_s' was matched to literature values for a 1 % w/v Intralipid solution [208], the typical concentration used in experiments that wish to mimic tissue reduced scattering properties ($\sim 1\ mm^{-1}$). For simplicity, it was assumed to be spatially constant in concentration ($a_1(x, y) = 1$).

The second phantom was designed to emulate a typical *in vivo* scenario of interest - with vasculature. The domain and mesh dimensions were the same as the previous case but the phantom was now constituted primarily by two vessels. The chromophore and scatterer concentration distributions are shown in Figure 8.2 (a). The vessel areas were

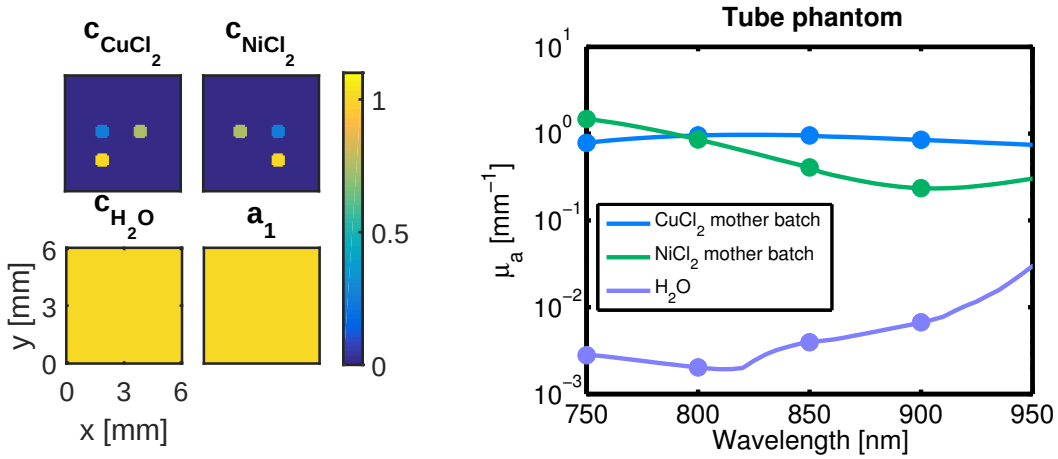

(a) (b)

Figure 8.1: *Tube phantom. (a) Distribution and concentration of the chromophores (c_k) and scatterer (a_1) of interest. Concentration units for each constituent are given in respect to its respective reference spectrum. (b) Reference absorption spectra for the chromophores present in the domain. $CuCl_2$ and $NiCl_2$ were measured experimentally in a spectrophotometer, whilst values for water were taken from the literature [244]. Reproduced with permission from [258].*

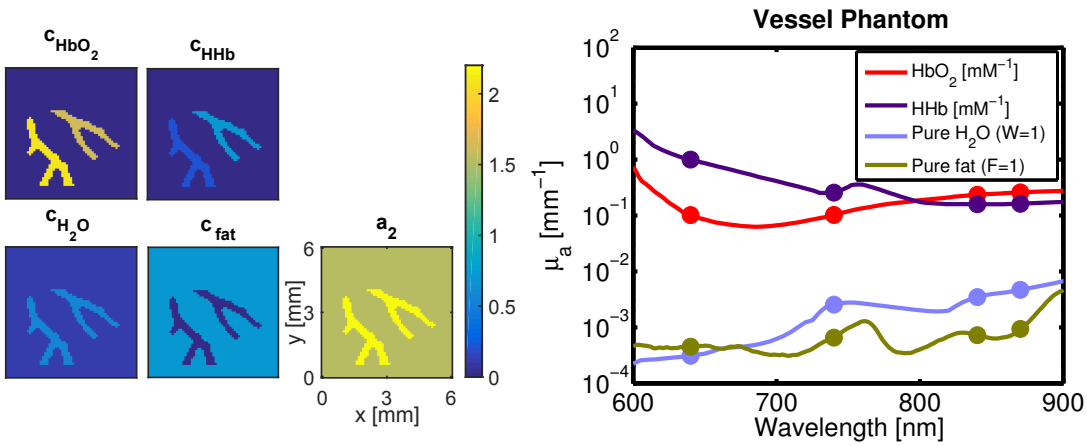

(a) (b)

Figure 8.2: *Vessel phantom. (a) Distribution and concentration of the chromophores (c_k) and scatterers (a_2) of interest. Concentration units for each constituent are given relative to its respective reference spectrum. (b) Reference absorption spectra for the chromophores present in the domain. Values were taken from the literature - water [244], hemoglobin [259], fat [260, 261]. Reproduced with permission from [258].*

assigned a hemoglobin concentration of $c_{HbT} = 150$ gl^{-1} $\simeq 2.327$ mM, typical for human blood [63]. Oxygen saturation levels of SO_2=90% and SO_2=70% were assigned to the left and right vessel respectively, falling in the typical range for artery and vein [262]. Water was also present inside the vessels at a fractional volume of $W = 0.55$, which is a typical fraction for the plasma component of blood (plasma itself is mainly constituted by water) [262]. The background properties were chosen to match abdominal tissue, such that c_{HbT} =0.0125 mM≃0.8057 gL^{-1} and SO_2=76%, with water volume fraction $W = 0.11$ and fat volume fraction $F = 0.69$ [63, 263]. For the inversion, the distribution of c_{HbO_2} and c_{HHb} were the unknowns, whilst c_{H_2O} and c_{fat} were considered known throughout the domain. Figure 8.2 (b) shows the spectra for oxyhemoglobin HbO_2, deoxyhemoglobin HHb and H_2O and fat. In this phantom, scattering was spatially varying. The vessel areas were assigned scattering typical of whole blood [63, 64] and the background was assigned a value typical for subcutaneous-adipose tissue [63, 264], $a_{2,(vessels)} = 2.2$ and $a_{2,(background)} = 1.54$ where $\mu_s' = a_2 \frac{\lambda}{500nm}^{-0.68}$. The power law values for whole blood and adipose tissue are similar enough ($b = 0.66$ and $b = 0.68$ respectively) therefore a common value of 0.68 was used for simplicity.

8.2.1 Light model

The light model used to generate the 'measured' data was the 2D DA with a FEM implementation - Toast++ [68]. Four wavelengths ($L = 4$) were considered - 750, 800, 850 and 900 nm for the tube phantom and 640, 740, 840 and 870 nm for the vessel phantom. The illumination source was shaped as top hat and incident on the top of the domain, $Q_{pos} = (x_Q, y_Q) = ([0.5\ 5.5], 6)$ mm (diameter $Q_{diam} = 5$ mm). To ensure the suitability of the DA for this case, the structures of interest in both phantoms (tube cross-sections, vessels) were positioned at a minimum depth d from the source such that the condition $d >> \frac{1}{\mu_t}$ was respected by having d be greater than $\frac{1}{\mu_t}$ by at least a five-fold factor [34]. The background in both cases also respected $\mu_s' >> \mu_a$.

The 'measured' dataset that was used as a starting point for the inversions was the scaled initial pressure distribution, defined as $p_{0,meas} = K_{true}\mu_a\Phi$, or in matrix notation for a single nodal point:

$$\begin{bmatrix} p_0(\lambda_1) \\ p_0(\lambda_2) \\ p_0(\lambda_3) \\ p_0(\lambda_4) \end{bmatrix} = K_{true} \begin{bmatrix} \Phi(\lambda_1) & \cdots & 0 \\ \vdots & \ddots & \vdots \\ 0 & \cdots & \Phi(\lambda_4) \end{bmatrix} \begin{bmatrix} \alpha_{c_1}(\lambda_1) & \alpha_{c_2}(\lambda_1) & \cdots & \alpha_{c_M}(\lambda_1) \\ \alpha_{c_1}(\lambda_2) & \alpha_{c_2}(\lambda_2) & \cdots & \alpha_{c_M}(\lambda_2) \\ \alpha_{c_1}(\lambda_3) & \alpha_{c_2}(\lambda_3) & \cdots & \alpha_{c_M}(\lambda_3) \\ \alpha_{c_1}(\lambda_4) & \alpha_{c_2}(\lambda_4) & \cdots & \alpha_{c_M}(\lambda_4) \end{bmatrix} \begin{bmatrix} c_1 \\ c_2 \\ \vdots \\ c_M \end{bmatrix}, \tag{8.1}$$

where $\Phi(\lambda_l)$ is the fluence at wavelength λ_l, $\alpha_{c_m}(\lambda_l)$ is the reference absorption spectrum for chromophore m at wavelength λ_l, M is the total number of chromophores and $K_{true} = 1$ is a spatially-constant factor that encompasses thermoelastic efficiency Γ and acoustic

sensor response. Because of this factor the acoustic pressure is considered to be 'scaled' to arbitrary units. Fig. 8.3 shows the modelled absorption μ_a, the fluence Φ and the absorbed energy density $H = \mu_a\Phi$ for the tube phantom, at the four wavelengths of interest.

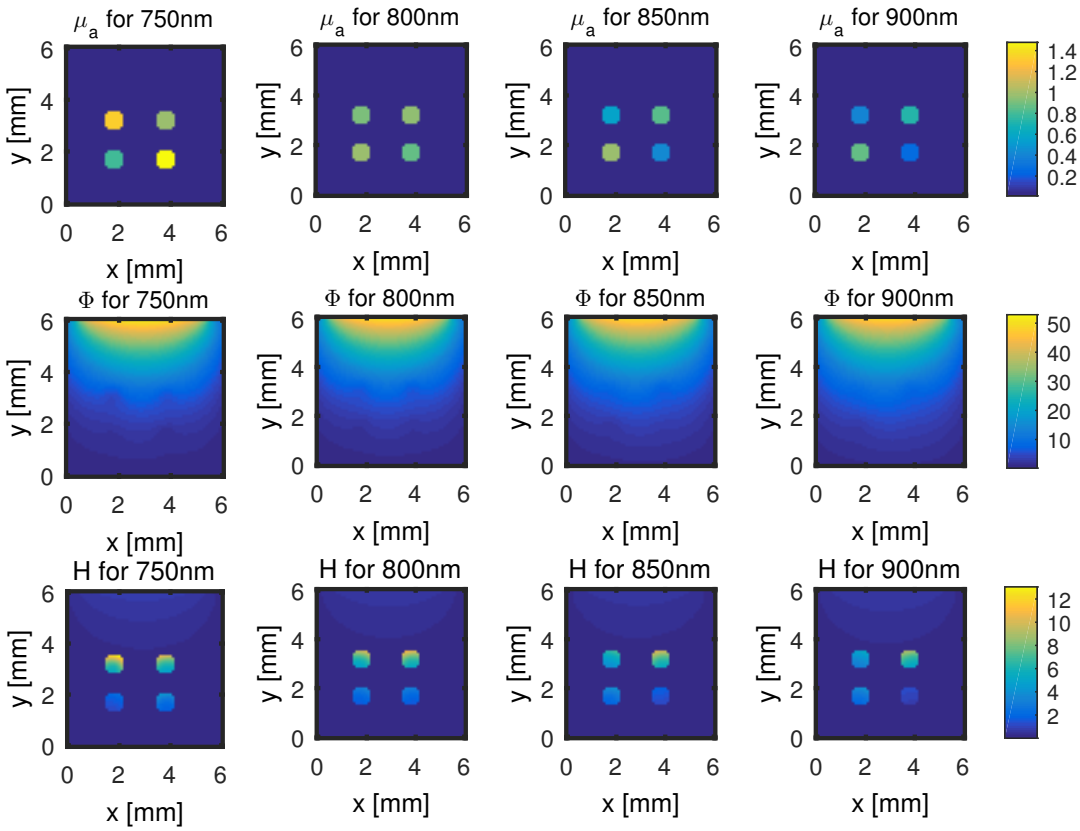

Figure 8.3: *[Tube phantom] True absorption coefficient (μ_a), true fluence (Φ) and true absorbed energy (H) at wavelengths 750, 800, 850 and 900 nm. Reproduced with permission from [258].*

8.3 Inversion strategies

The aim of the qPAT strategies is to retrieve the distributions of the concentrations of the chromophores of interest (c_{NiCl_2} and c_{CuCl_2} for the tube phantom and c_{HbO_2} and c_{Hb} for the vessel phantom) from multiple-wavelength and single illumination data. From these, the ratiometric parameter R can also be retrieved.

For the model-based inversion, a least-squares minimisation strategy is employed to retrieve c_k from the initial pressure maps, a very common and consensual error functional for MBI-qPAT studies. The forward light model is given by the 2D DA-FEM as outlined in the previous section (to match forward and inverse strategies; inverse crime is not an unwelcome paradigm since we are focussed on relative behaviour and benchmarking). More complex light models could have been applied, but for the aims of this study the type of outcomes would not have considerably changed in nature to justify or reward

the added complexity. The acoustic problem is assumed to be perfectly solved up to a constant factor K in order to keep the focus on the optical problem at this stage. The error functional is defined as:

$$\varepsilon = \sum_{l=1}^{L} \sum_{h=1}^{Nh} \left[p_{0,meas_h}(\lambda_l) - p_{0,sim_h}(\mathbf{u}, \lambda_l) \right]^2, \tag{8.2}$$

where $p_{0,meas_h}(\lambda_l)$ is the 'measured' initial pressure distribution and $p_{0,sim_h}(\mathbf{u}, \lambda_l)$ is the estimated initial pressure distribution for a given iteration with estimates $\mathbf{u}$ for the unknowns, where subscripts l and h denote different wavelengths and nodal positions respectively. For considerations of speed and efficiency, the gradient-based, quasi-Newton, limited-memory BFGS (L-BFGS) [158] was chosen as the minimisation scheme, and the functional gradients $\frac{\partial \varepsilon}{\partial c_k}$ and $\frac{\partial \varepsilon}{\partial a}$ were calculated using the adjoint method [111, 149]. It is important to note that for the purpose of assessing the degree to which the uncertainties in the experimental parameters move the minimum of the error functional (and hence the estimated quantities) any minimisation scheme could have been used (assuming it is able to find the minimum): the location of the perturbed minimum will be independent of the minimisation algorithm used.

Three different inversions were performed:

- MBI-($\hat{c_k}$) - estimates both chromophores concentration distributions c_k from single-illumination and L=4-wavelength data, which gives a number of unknowns $N_{unknowns} = 2 \times Nh = 7442$.
- MBI-($\hat{c_k}, \hat{K}$) - estimates c_k and the overall calibration factor K (a factor that encompasses thermoelastic efficiency Γ, mechano-electrical coupling) from single-illumination and 4-wavelength data. $N_{unknowns} = 2 \times Nh + 1 = 7443$.
- MBI-($\hat{c_k}, \hat{a}$) estimates c_k and the scatterer concentration distribution a from single-illumination and 4-wavelength data. $N_{unknowns} = 3 \times Nh = 11163$. The spectral signature of the scatterer is assumed known. This inversion was only performed for the unknown, erroneous scattering scenarios.

All simulations were allowed to run until the difference in the error functional from one iteration to the next was less than 10^{-6} or otherwise for a maximum of 1000 iterations. Given the 1.5 fold increase in unknowns for the MBI-($\hat{c_k}, \hat{a}$) case, the maximum number of iterations was 1500. The former took approximately 8 hours to run on an Intel Core i7-3770 CPU at 2.40 GHz with 16 GB RAM, though a later code improvement (one-off pre-loading of a DA-FEM system matrix rather than calculation at each iteration) showed these routines could be run on the same machine in just over an hour.

To lend greater certainty to the assumption that the global minimum was found, the simulations were run for two different initialisations - first, the starting values were set as the unperturbed ground-truth (this is therefore the global minimum in the unperturbed case, which we hypothesise will be sufficiently close to the minimum in the perturbed case,

therefore helping ensure that the shifted/perturbed global minimum is found); secondly, initialisation was set at 90% of the true background (note that it is common practice in the theoretical literature to initialise at the true background, so 90% is already a stricter imposition).

For comparison, the linear unmixing scheme was also employed, such that (defined for each nodal position):

$$\begin{bmatrix} K'\,c_1 \\ K'\,c_2 \end{bmatrix} \approx \begin{bmatrix} \alpha_{c_1}(\lambda_1) & \alpha_{c_2}(\lambda_1) \\ \alpha_{c_1}(\lambda_2) & \alpha_{c_2}(\lambda_2) \\ \alpha_{c_1}(\lambda_3) & \alpha_{c_2}(\lambda_3) \\ \alpha_{c_1}(\lambda_4) & \alpha_{c_2}(\lambda_4) \end{bmatrix}^{\dagger} \begin{bmatrix} p_0(\lambda_1) \\ p_0(\lambda_2) \\ p_0(\lambda_3) \\ p_0(\lambda_4) \end{bmatrix}, \tag{8.3}$$

where $K' = K\gamma$ is the adapted calibration factor accounting for light fluence, $\dagger$ denotes the pseudo-inverse and c_1 and c_2 are the chromophores of interest ($CuCl_2$ and $NiCl_2$ for the tube phantom and HbO_2 and Hb for the vessel phantom), with contribution from any remaining chromophores assumed negligible since their absorption is orders of magnitude lower. Linear unmixing was performed both without (LU) and with (LU_C) a simple 1D fluence correction ($\Phi_{approx} = e^{-\mu_{\text{fit}}(y_Q - y)}\ \forall\, x$) being applied to p_0, where the value μ_{fit} was obtained through an exponential fit to the laterally (x-wise) integrated background signal decay [115] .

8.4 Sensitivity analysis and performance comparison of the inversion schemes

The scenarios that were considered as potential experimental-related error are given in Table 8.1.

Type of parameter assignment error	Range
Calibration factor K	$\delta(K) = \{-50, -40, -30, -20, -10, 0, 10, 20, 30, 40, 50\}\%$
Reduced scattering coefficient μ_s', though with known spectral dependence	$\delta(\mu_s') = \delta(\mu_s) = \delta(a) = \{-50, -40, -30, -20, -10, 0, 10, 20, 30, 40, 50\}\%$
Lateral positioning of the beam Q_{pos}	$\delta(Q_{pos}) = \{-10, -8, -6, -4, -2, 0, 2, 4, 6, 8, 10\}\%$ Q_{diam}
Beam diameter Q_{diam}	$\delta(Q_{diam}) = \{-20, -16, -12, -8, -4, 0, 4, 8, 12, 16, 20\}\%$

Table 8.1: *Types of parameter assignment error and associated ranges used in the sensitivity analysis.*

The following metrics were computed to assess the resultant errors in the qPAT strategies:

- Relative error in c_k estimation: $RE(c_k) = \frac{||\hat{c_k} - c_{k,true}||}{||c_{k,true}||} \times 100$;
- Relative error in a estimation: $RE(a) = \frac{||\hat{a} - a_{true}||}{||a_{true}||} \times 100$;
- Relative error in intra-luminal R^{IL} estimation: $RE(R^{IL}) = \frac{||\hat{R}^{IL} - R^{IL}_{true}||}{||R^{IL}_{true}||} \times 100$;

where $||$ $||$ denotes the Euclidean norm and R^{IL} is defined: intra-tube for the tube phantom, $R^{tubes}(\%) = \frac{c^{tubes}_{NiCl_2}}{c^{tubes}_{NiCl_2} + c^{tubes}_{CuCl_2}} \times 100$, and intra-vessel for the vessel phantom $R^{vessels}(\%) = SO_2^{vessels}(\%) = \frac{\mathbf{c}^{vessels}_{HbO_2}}{c^{vessels}_{HbO_2} + c^{vessels}_{Hb}} \times 100$.

8.4.1 Uncertainty in overall calibration factor K

The overall calibration factor K was allowed to vary between $\delta(K) = \{-50, -40, -30, -20, -10, 0, 10, 20, 30, 40, 50\}$%, meaning from K=0.5 to 1.5. The effect of this error in both phantoms was tested for the MBI-($\hat{c_k}$) algorithm, as well as for the self-calibrating MBI-($\hat{c_k}, \hat{K}$) algorithm. As seen in Figures 8.4 (a-b), setting an erroneous fixed K greatly affects the error in c_k estimation for MBI-($\hat{c_k}$). Even the intra-luminal error for the ratiometric parameter R^{IL} (Figure 8.4 c-d) is still quite prominent (up to 40% and 25% for tube and vessel phantom respectively), though lower than that for the concentration estimation. For the ratio to have successfully cancelled K, the images would have needed to be divided before entering the inversion pipeline. A similar effect can be achieved by including K as an unknown in the inversion pipeline: as expected, the self-calibrating MBI-($\hat{c_k}, \hat{K}$) manages to correctly estimate both K and vector $\hat{c_k}$ from any initial erroneous K estimate since the problem is well-posed. Figure 8.5 - pink curves - show how the self-calibrating algorithm can deal with K initially underestimated by 50%, whilst the standard algorithm will diverge. Including K as an unknown does come at the expense of a slower convergence (Figure 8.5 - blue curves).

Comparisons to linear unmixing strategies (with and without 1D fluence correction) show that algorithm MBI-($\hat{c_k}$), despite its shortcomings, still performs better than linear unmixing unless there is underestimation of 30% or more in K.

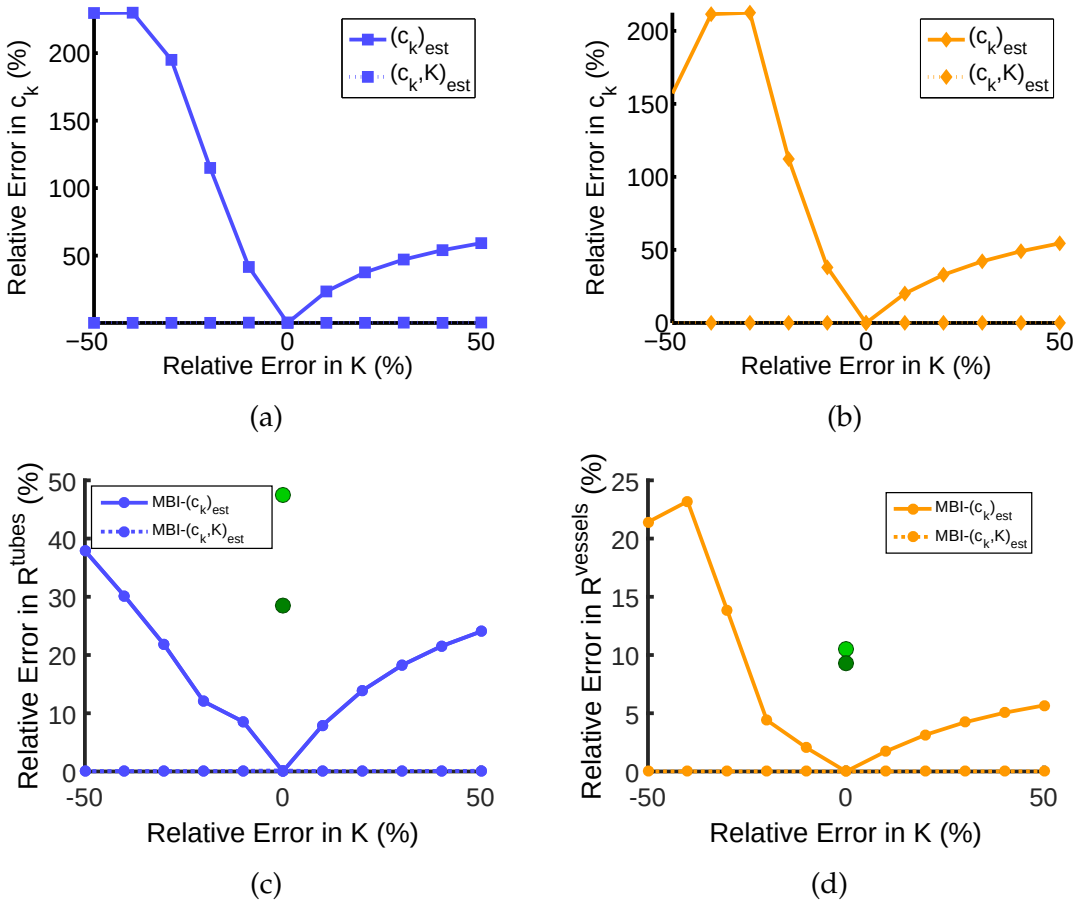

Figure 8.4: *Relative error in chromophore concentration vs error in calibration factor K for (a) Tube phantom and (b) Vessel Phantom. Relative error in intra-luminal R vs error in calibration factor K for (c) Tube phantom and (d) Vessel phantom. LU - light green; LU_C - dark green. Subfigure (c) reproduced with permission from [258].*

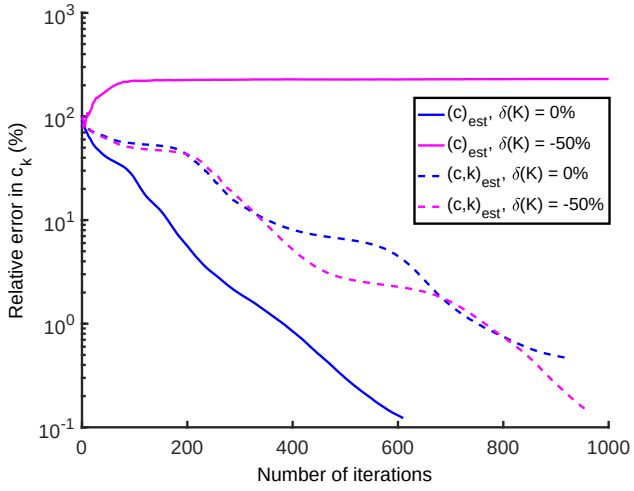

Figure 8.5: *[Tube phantom] Relative error in chromophore concentration vs number of iterations - initialisation from 90% background. Blue - inversion for c_k, with K assumed known. Pink - inversion for both c_k and K, with K_0 initial estimate.*

8.4.2 Uncertainty in reduced scattering coefficient

To assess the effect that uncertainty in the reduced scattering coefficient has in approaches that assume it is known, the reduced scattering coefficient was varied by a constant multiplicative factor, meaning that the relative wavelength-dependence was always maintained, but the concentration of the scatterer at each point $a(x, y)$ was altered: $\delta(\mu_s') = \delta(\mu_s) = \delta(a) = \{-50, -40, -30, -20, -10, 0, 10, 20, 30, 40, 50\}\%$.

For both phantoms, errors in the assumed scattering coefficient led to considerable error in c_k estimation by MBI-($\hat{c_k}$), especially when scattering was assumed to be higher than its true value: a 50% over-estimation of scattering led to errors up to 140% (Figure 8.6 (a-b)). The self-calibrating algorithm, MBI-($\hat{c_k}, \hat{K}$), led to considerable improvement in the estimation, though as seen in Figure 8.7 for the $\delta(a) = 10\%$ case, improvement in c_k estimation still eventually stabilises at a non ground-truth local minimum (dotted pink line). The fact that the estimation is seen to stabilise at this local minimum and does not further converge to the ground-truth is expected, since adding one free floating spatially-constant parameter K is not enough for the model to fully explain disparities caused by a widespread change in scattering which will affect fluence and p_0 both intensity-wise, spectrally and spatially. Nonetheless, though K is not expected to be able to explain the spatially dependent error, it seems it can help mitigate/absorb the average error in the initial pressure intensity, which is why the local minimum that is reached is an improvement on the local minimum of MBI-($\hat{c_k}$). Finally, the MBI-($\hat{c_k}, \hat{a}$) algorithm, which minimises for the spatially-dependent scatterer concentration with a known wavelength behaviour, was employed. In theory this algorithm should be able to converge to the true minimum since the problem is unique and fully explains the data. In practice it does not within the 1500 iterations due to slow convergence and poor sensitivity to scattering away from the source. The algorithm does still mostly outperform MBI-($\hat{c_k}$) in chromophore estimation. The improvements are sometimes not that considerable compared to MBI-($\hat{c_k}, \hat{K}$) though (in some instances even worse), which is worth noting since MBI-($\hat{c_k}, \hat{a}$) would theoretically be more apt to model the true physical deviations introduced. This similar performance is also note-worthy since MBI-($\hat{c_k}, \hat{a}$) is memory-intensive ($\sim 50\%$ more unknowns) and needs a longer computation time per iteration. Figure 8.8 further illustrates, for the tube phantom, how accurate the three inversions are for $\delta(a) = -50\%$, compared to the ground-truth. Note how for MBI-($\hat{c_k}, \hat{a}$) improvement on the estimated a is significant mainly close to the source.

Once more, errors in the ratiometric parameter R^{IL} are lower than those for absolute concentration. As seen in Figures 8.6 (c-d), the relative performance of the 3 model-based inversions in estimating R^{IL} is mostly similar to that seen for concentration estimation in (a-b), though now, for the vessel phantom, MBI-($\hat{c_k}, \hat{K}$) matches or even outperforms MBI-($\hat{c_k}, \hat{a}$), which did not happen for the chromophore estimation. As for the comparison with the linear unmixing frameworks, MBI always perform better, except when scattering is overestimated by 40% or more in the least accommodating MBI: MBI-($\hat{c_k}$).

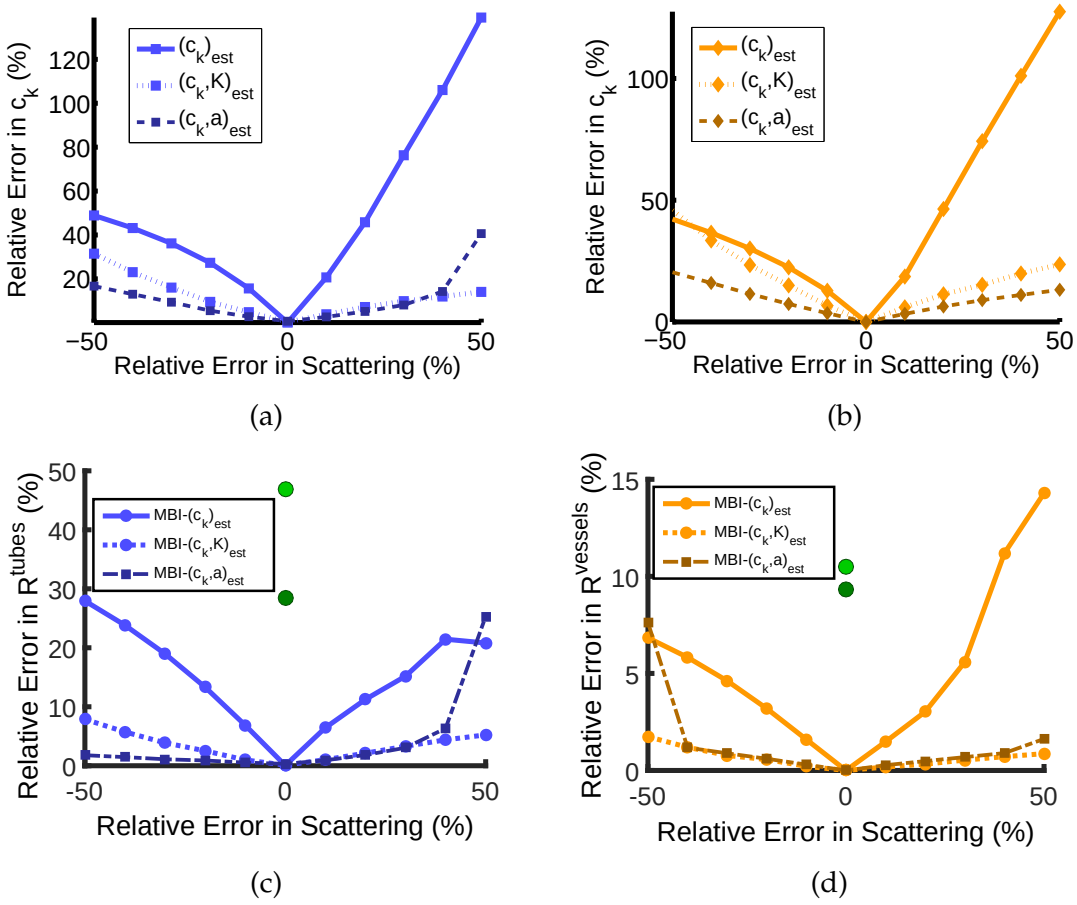

Figure 8.6: *Relative error in chromophore concentration vs error in scatterer concentration a for (a) Tube phantom and (b) Vessel Phantom. Relative error in intra-luminal R vs error in scattering for (c) Tube phantom and (d) Vessel phantom. LU - light green; LU_C - dark green. Subfigure (c) Reproduced with permission from [258].*

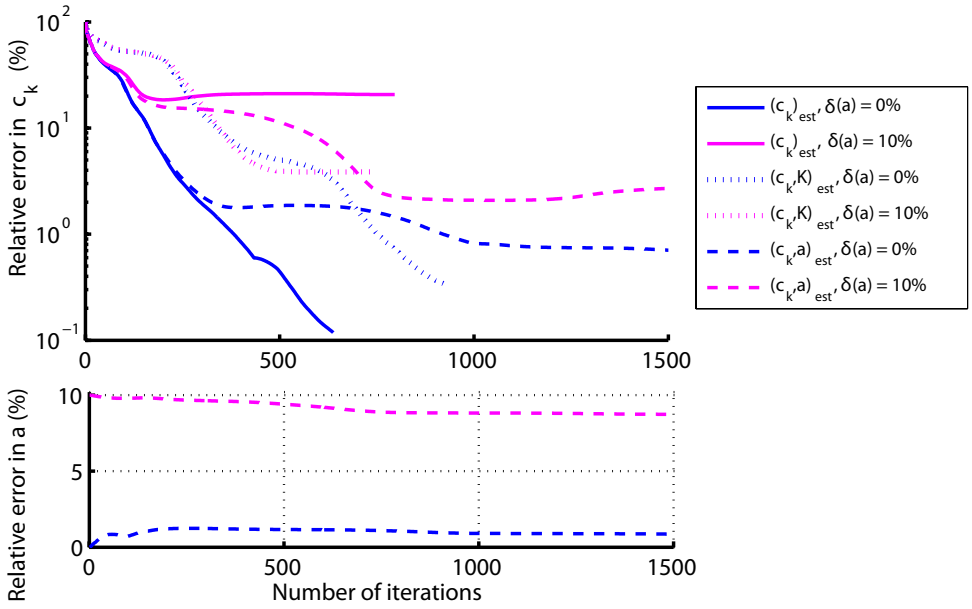

Figure 8.7: *[Tube phantom] Relative error in chromophore concentration (top) and scatterer concentration (bottom) vs number of iterations - initialisation from 90% background. Reproduced with permission from [258].*

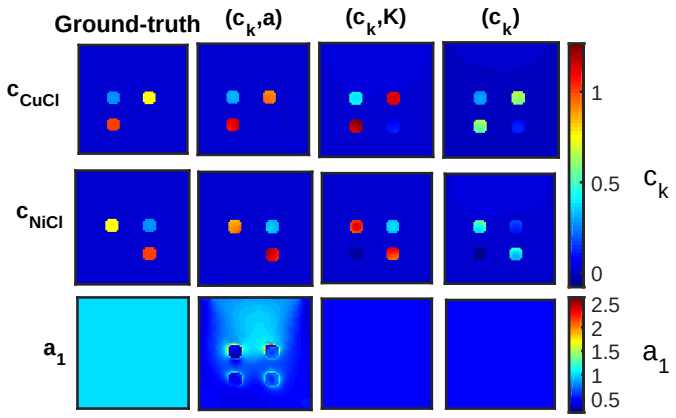

Figure 8.8: *[Tube phantom] Comparison of outcome between inversions with wrong scattering estimate a. First column gives ground-truth for c_{CuCl_2}, c_{NiCl_2} and a. Second column shows inversion outcome when both c_k and a are unknowns to be inverted, and $a_0 = 50\% a_{true}$. Third and fourth columns show outcome for MBI-(c_k,K) and MBI-(c_k) respectively, where scattering is fixed as $a = 50\% a_{true}$. Reproduced with permission from [258].*

8.4.3 Uncertainty in excitation beam configuration

Here, the impact of errors in beam positioning Q_{pos} and diameter Q_{diam} is described. The beam is defined as top hat in all instances. Total incident energy remained unchanged.

8.4.3.1 Uncertainty in beam positioning

The beam positioning was varied from its central position to its most leftward and rightward possible position in the domain, at incremental steps of 0.1 mm. More specifically, $\delta(Q_{pos}) = \{-10, -8, -6, -4, -2, 0, 2, 4, 6, 8, 10\}\%\ Q_{diam}$. Figure 8.9 (a-b) shows that changing positioning led to an expected error in optical property estimation with MBI-($\hat{c_k}$) but the error did not exceed 14% for a 10% shift. The self-calibrating MBI-($\hat{c_k}, \hat{K}$) inversion seemed to slightly improve results for most cases - except for some instances in the vessel phantom. This general improvement probably happens because adjusting K can slightly compensate for variations in average energy distribution (caused by beam displacement) around the central area where the structures of interest are. Once more, MBI-($\hat{c_k}, \hat{K}$) only improves estimation up to a certain point, after which it seems to stabilise at a local minimum (data not shown) since the fixed wrong positioning means the model can only explain and compensate the data to a certain extent.

Model-based inversions also fared significantly better than linear unmixing strategies, for errors in positioning up to 10% of the beam diameter (Figure 8.9 c-d).

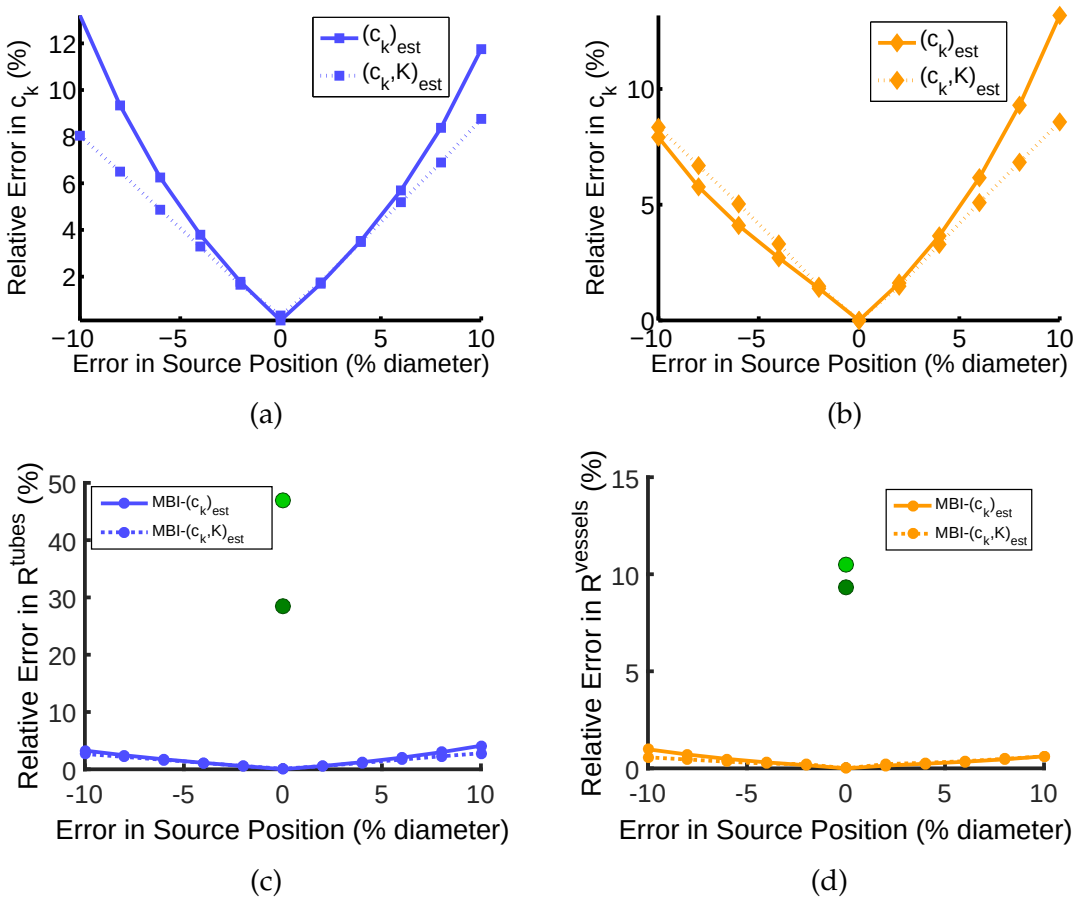

Figure 8.9: *Relative error in chromophore concentration vs error in source position Q_{pos} for (a) Tube phantom and (b) Vessel Phantom. Relative error in intra-luminal R vs error in source position Q_{pos} for (c) Tube phantom and (d) Vessel phantom. LU - light green; LU_C - dark green. Subfigure (c) reproduced with permission from [258].*

8.4.3.2 Uncertainty in beam diameter

The beam diameter was varied up to where it would cover the whole lateral domain. $\delta(Q_{diam}) = \{-20, -16, -12, -8, -4, 0, 4, 8, 12, 16, 20\}$%, i.e. variation between 4 to 6 mm. The source intensity per node was adapted so that the total incident energy remained constant despite diameter variations. As seen in Figure 8.10 (a-b), for the MBI-($\hat{c_k}$) inversion, changes in diameter led to errors in c_k estimation up to 40%, larger than the error caused by position shifting across the domain. When applying MBI-($\hat{c_k}, \hat{K}$) the total error in c_k fell below 2.5% for all cases. The fact that scalar adjustment greatly improves estimates indicates that actually the error in MBI-($\hat{c_k}$) when beam diameter is changed stems more heavily from an erroneous energy incidence per pixel in the central surface region (scalar effects) rather than from more intricate deviations in fluence spatial distribution or in spectral distortion throughout the domain. Since the tubes are placed quite centrally relative to the beam, and at a reasonable depth, light has become diffuse enough that small variations in diameter have little impact. Robustness to changes in beam positioning and diameter would probably not be as great if the subjects of interest were in the sub-diffuse or ballistic regime, or if they were not located quite centrally relative to the source.

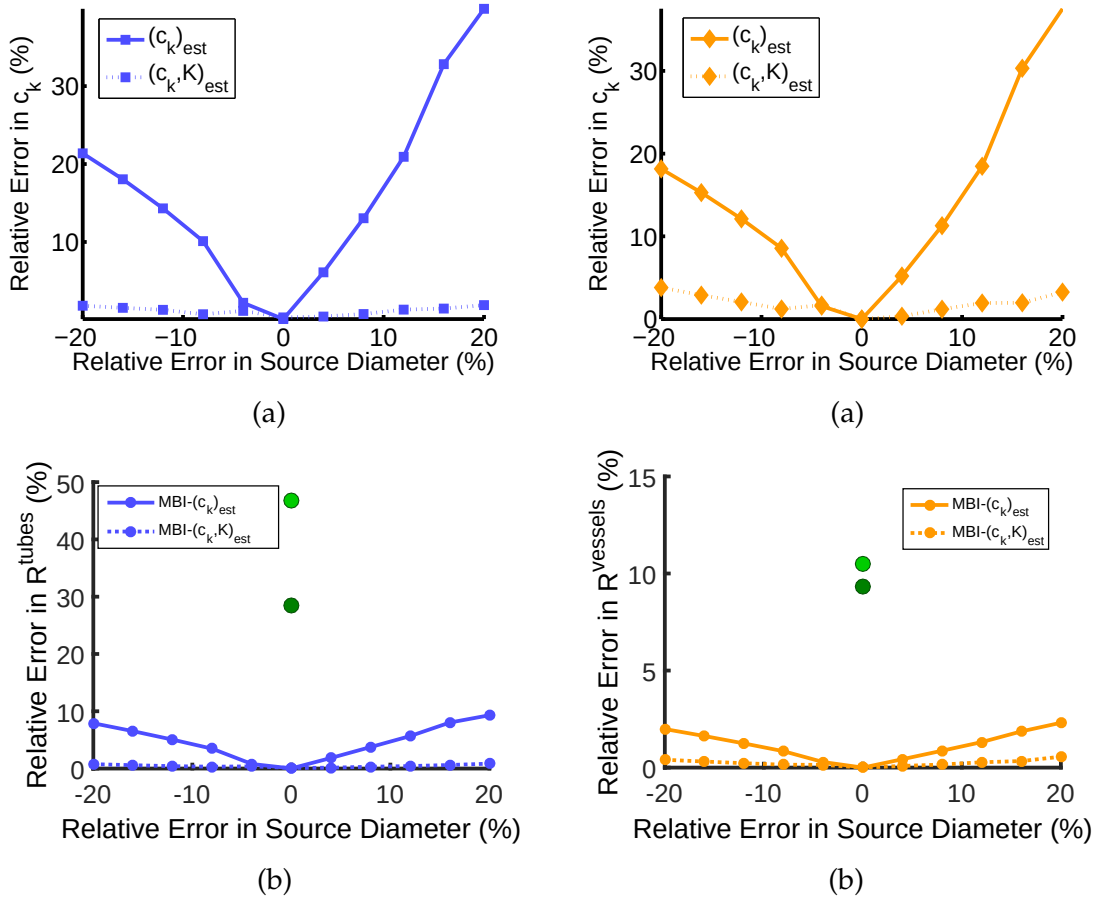

Figure 8.10: *Relative error in chromophore concentration vs error in source diameter Q_{diam} for (a) Tube phantom and (b) Vessel Phantom. Relative error in intra-luminal R vs error in source diameter Q_{diam} for (c) Tube phantom and (d) Vessel phantom. LU - light green; LU_C - dark green. Subfigure (c) reproduced with permission from [258].*

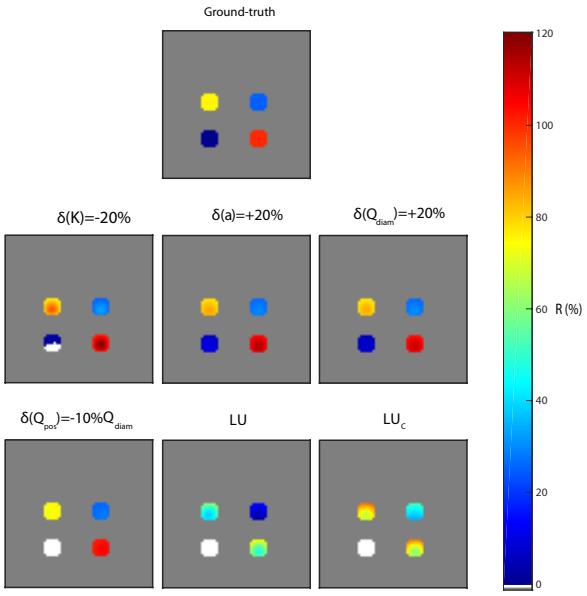

Figure 8.11: *[Tube phantom] Comparison of inversion outcome for the ratiometric quantity R^{tubes}, using MBI-($\hat{c}_k$) with erroneous calibration factor K, reduced scattering coefficient μ_s', source diameter Q_{diam} or position Q_{pos} and using linear unmixing strategies with and without 1D background decay correction. Source incident from the top of the domain. White - negative; Gray - background; Darkest blue - zero. Reproduced with permission from [258].*

Once more, the estimation of R^{IL} (Figure 8.10 c-d) leads to smaller error than c_k. Model-based inversions also outperformed by far the two linear unmixing strategies for all studied levels of diameter uncertainty.

In order to have a more visual and comparable sense of the impact of different types of uncertainty, $R^{(tubes)}$ of the tube phantom is plotted in Figure 8.11 for the ground-truth, versus both linear unmixing strategy (LU and LU_c) outcomes and the MBI-($\hat{c_k}$) algorithm outcomes with parameter uncertainty $|\delta| = 20\%$ (since there are two cases where $|\delta| = 20\%$, the case where $RE(c_k)$ was largest is presented). For the case of source positioning, since the parameter error is not relative to itself, the case leading to the worst $RE(c_k)$ was plotted, i.e. $\delta(Q_{pos}) = 10\%\ Q_{diam}$.

8.4.4 Choice of initialisation

Figure 8.12 compares, for the tube phantom subject to perturbations in source positioning and diameter, outcomes for the two initialisations - (I) initialisation at 90% of the true background, (II) initialisation at the ground-truth (global minimum of the unperturbed case). A complete overlap is seen for all cases. The same overlap of minimisation outcomes with different initialisations was seen for other computed scenarios, as long as the minimisations were convergent. Given that the results were independent of the starting estimates, this meant that a correct depiction of the global minimum of the perturbed error functional (and consequently of the shift relative to the true unperturbed minimum) was obtained for the various perturbed situations.

8.4.5 Influence of noise

All the results above were computed with measured data devoid of noise so as to be able to look at the isolated effect of different uncertainties. In this case, noise was added to the tube phantom case to see in which way it affected the outcomes of the inversions. Figure 8.13 compares the results of the inversion between cases where initial data are noiseless or where they have 5% added noise (additive gaussian noise of zero mean and standard deviation equal to 5% of the mean data intensity over all wavelengths). For the unpertubed case, there is an increase in the error but once in the presence of other uncertainties, noise does not play a relevant role in further affecting the minimisation - the curves for the noisy and noiseless case are seen to converge and eventually overlap as the magnitude of the perturbation increases. Gaussian noise therefore does not seem to be an additional destabiliser when in the presence of input uncertainty.

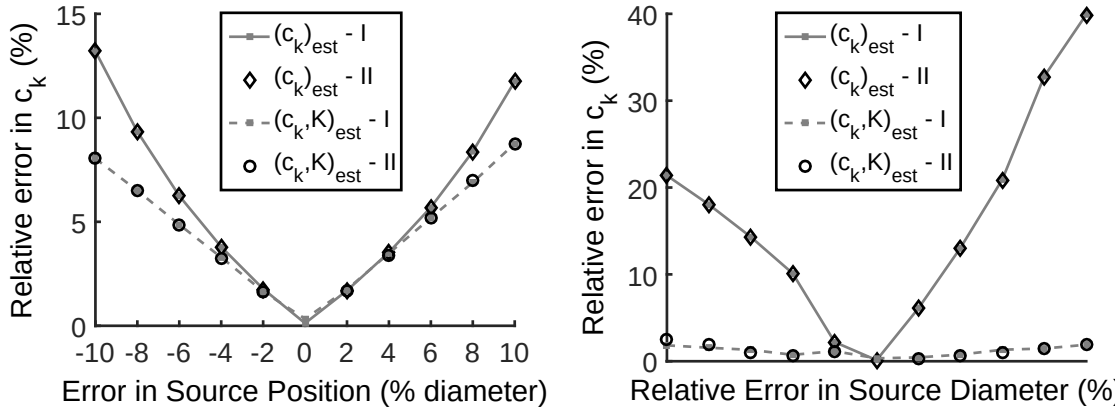

Figure 8.12: *[Tube phantom] Comparison between cases with initialisation from 90% background (I) and from the ground-truth (II). Outcomes are shown for the MBI-($\hat{c}_k$) and MBI-($\hat{c}_k, \hat{K}$) algorithms when (a) the beam location is perturbed; (b) the beam diameter is perturbed.*

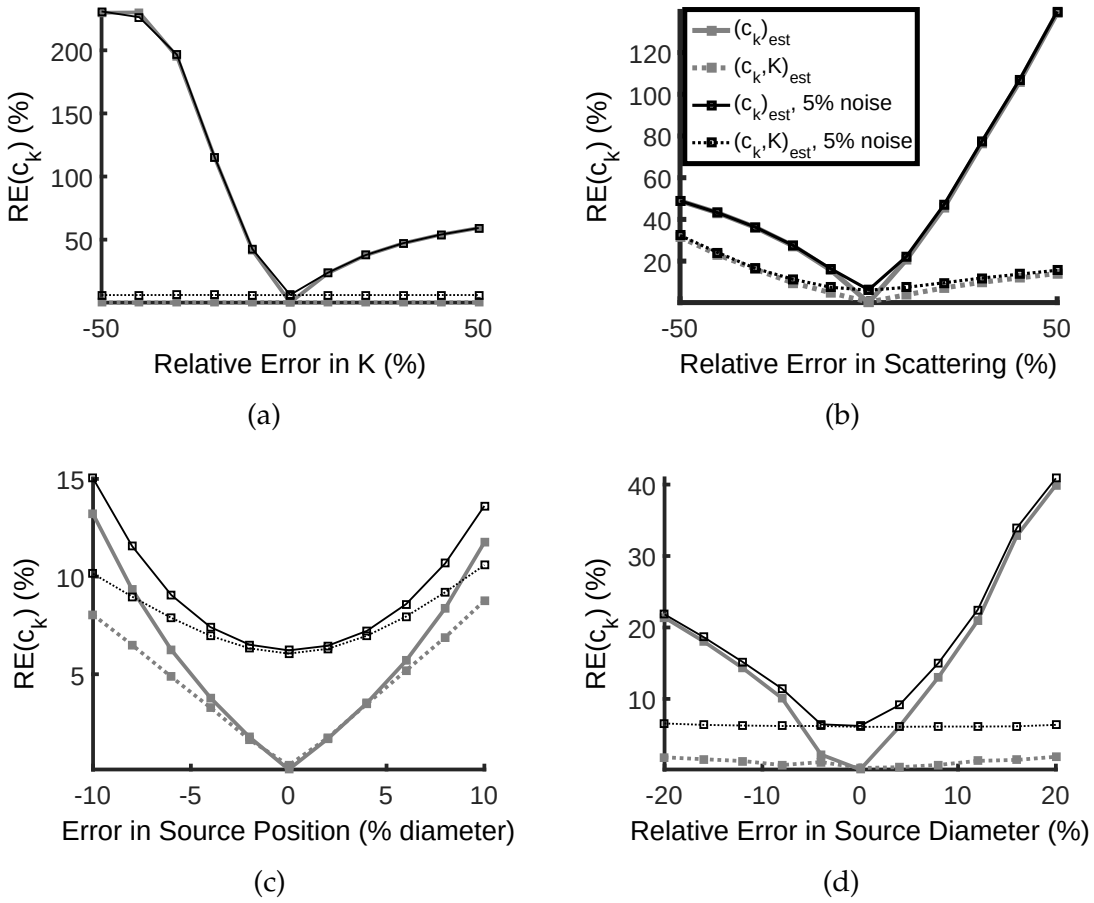

Figure 8.13: *[Tube phantom] Comparison between cases with no noise and 5% added Gaussian noise. Outcomes are shown for the MBI-($\hat{c}_k$) and MBI-($\hat{c}_k, \hat{K}$) algorithms when there is a perturbation in (a) calibration factor; (b) scatterer concentration; (c) source location; (d) source diameter.*

8.5 Summary

An *in silico* study was used to determine the degree to which the accuracy of model-based inversion is sensitive to uncertainty in the optical input parameters which must be passed to the forward models used in the inversions. The main findings were:

- Experimental uncertainties in *a priori* fixed parameters - especially calibration factor and scatterer concentration - can affect accuracy of model-based inversions considerably. For all cases, this error is larger when estimating concentrations c_k than when estimating the ratiometric parameter R^{IL}.
- Including a global floating scaling parameter in the inversion appears to improve quantification estimates subjected to an input perturbation even if the data are originally scaled correctly, probably by absorbing the mean error that different types of parameter uncertainty produce.
- For the case of uncertainty in scattering, including the scatterer concentration as an unknown (with known spectral dependence) increased the accuracy in c_k and R^{IL} estimates, but did not converge quickly due to ill-posedness caused by the diffuse nature of light. The scattering estimate was mainly correct close to the source. In some cases, inverting for the chromophores and the global floating scaling parameter outperformed inverting for the chromophores and the full scatterer concentration map;
- For realistic levels of experimental uncertainty in model-based input parameters, the studied model-based inversions still outperformed linear unmixing approaches (both with and without 1D fluence correction).

It is important to perform studies such as these to have an understanding of which input parameters are most likely to result in errors in the estimates, as then mitigating measures can be taken. For example, for a given problematic parameter an additional experimental step could be used to obtain this parameter with a higher degree of certainty, or a different physical model that does not require that input could be used, or the parameter could be included as a variable in the inversion [114, 152]. Care should still be taken to assess whether the re-formulated problem is well-posed enough, robust to noise and not prohibitive memory- or time-wise.

Chapter 9

Designing a qPAT experiment

Throughout this Chapter and Chapter 10, the feasibility of achieving fully-resolved (voxel-by-voxel), volumetric chromophore distribution estimation in experimental scenarios is assessed by conducting a rigorous and fully characterised phantom study. An efficient model-based inversion was implemented and a highly-resolved (segmentation-free) approach was used in order to preserve the outstanding qualities of PAT - its capability to image deep structures with high-resolution and in 3D.

Overall, the study had as its aim:

- Assessing the feasibility of obtaining volumetric, high-resolution estimates of chromophore concentration (both in relative and absolute units) and estimates of ratiometric quantities analogous to SO_2 from PAT data by performing a well-controlled and characterised phantom experiment enabled by state-of-the-art theoretical qPAT frameworks;
- Identifying the main bottlenecks towards successful experimental qPAT, in all its stages (phantom, setup and acquisition, acoustic and optical reconstruction);
- Optimising the experimental design and identifying further directions of research or focus for qPAT, for both theoreticians, experimentalists and clinicians.

Designing an experiment for highly-resolved volumetric qPAT requires careful attention to all stages of the problem, especially since the high-dimensional nature of the approach could mean higher susceptibility to any model-experiment discrepancies. The design of this extensive and thorough phantom-based study had as priorities:

1. Phantom - use a stable, characterised and realistic phantom in terms of its optical, acoustic and thermoelastic properties that can serve as a known ground-truth to which qPAT estimates can be reliably compared;
2. Setup and acquisition - increase knowledge and reduce all foreseeable uncertainty in the experimental acquisition process, both in terms of knowledge of illumination characteristics and faithful representation of the acoustic field (PA time-series at op-

timised bandwidth, aperture, directionality and expressed in meaningful physical units);

3. Acoustic reconstruction - choose a method that will give the most faithful reconstruction of the initial pressure distribution, with minimal artefacts and noise and no unphysical values;

4. Optical reconstruction - choose a method that will be able to recover concentration estimates in 3D, voxelwise and at high resolution in an efficient manner and be flexible enough to account or accommodate for other specifications such as scattering or Grüneisen parameter, if necessary.

In this Chapter we will outline these various considerations and decisions taken regarding the design of the experiment. Results and discussion of the outcomes will follow in Chapter 10.

9.1 The experimental setup

One of the aspects to be considered for a successful, well-controlled qPAT experiment is having an experimental setup from which a faithful representation of the true acoustic field can be obtained. To achieve this it is necessary to consider the directionality of the detectors, their frequency bandwidth, their sensitivity and the existence of a reasonable *visible region* (where data can be reconstructed without limited aperture issues).

With this in mind, Fabry-Perot sensors were used to measure the PA signals, given their wide bandwidth (DC to ~40 MHz), low noise-equivalent pressure (<200 Pa peak amplitude) and near omni-directionality [78]. To overcome the limited view problem that occurs in planar detection arrangements [265, 266], a system with a V-shaped detection geometry was used [20]. Such a geometry enhances the field of view and creates a clear *visible region* as long as an appropriate iterative reconstruction is used, therefore reducing limited-aperture artefacts and increasing resolution within the region-of-interest. A measurement system with two Fabry-Pérot sensors in an orthogonal arrangement was employed [20]. The two sensors in this system were rigidly connected in a water-tight tray. Two interrogation systems were used to simultaneously interrogate the two sensors. 300 kHz 2nd order high-pass filters were connected to the scope of each PA data acquisition channel to dampen effects of unwanted baseline oscillations, which would otherwise necessitate an increase in dynamic range of the scope and an inherent increase in quantization noise, to a point that would compromise feature discrimination. PA excitation could be provided by any ns-pulsed source (laser or OPO). Figure 9.1 gives a schematic overview of the system and sensor arrangement.

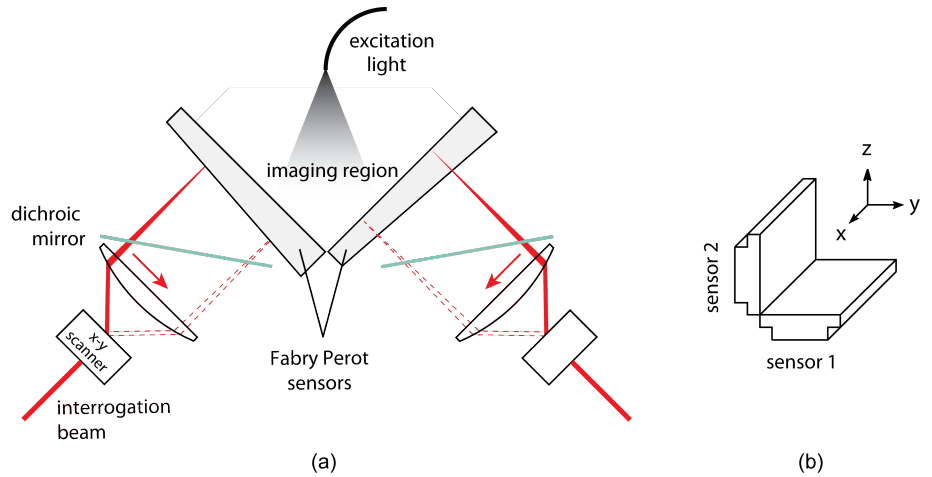

Figure 9.1: *(a) Schematic of experimental setup, in cross-section. (b) Orthogonal arrangement of FP sensors, in perspective. Adapted from [20]. Diagram not to scale.*

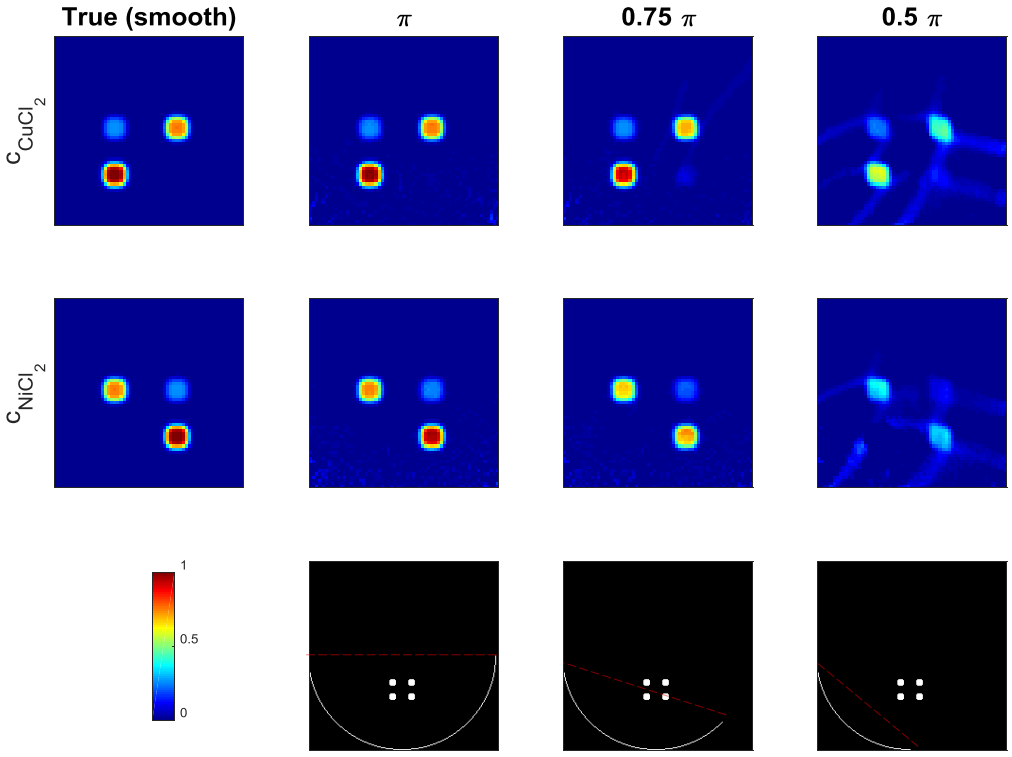

Figure 9.2: *Outcomes of the L-BFGS-($\hat{c}_k$) quantification when the input initial pressure data have been reconstructed from PA data acquired over different acoustic apertures are shown in the first two rows. Three detection apertures were considered, in a circular geometry: $\{0.5, 0.75, 1\}\pi$. The scale bar is shown on the bottom left and is valid for all reconstructions in the first two rows. The last row of the image shows a mask of the sensors and of the circular inclusions of interest. The red dashed line indicates the edge of the visibility region for each case. The case-study used was a smoothened version of the Tube Phantom scenario in Chapter 8. The source is incident from the top edge. Iterative time-reversal (it=10) was used for acoustic reconstruction.*

On the effects of partial view in qPAT If data have been acquired with partial view, not only will the reconstruction of the initial pressure distribution suffer, but also the down-

stream quantification. Figure 9.2 illustrates this for a virtual phantom - a smoothened version of the Tube Phantom used in Chapter 8. Three detection apertures were considered, corresponding to the following solid angles in circular geometry: $\{0.5, 0.75, 1\}\pi$. The L-BFGS-($\hat{c_k}$) MBI was applied to the initial pressure data that had been reconstructed from the various geometries using iterative time-reversal, it=10 (this method is described in more depth in Section 9.4.3). It can be seen that, for the 0.5π angle case, where the structures are completely outside the *visible region*, reconstruction of the chromophore concentrations is very poor since artefacts, distortion and erroneous intensities can be seen. The π angle case can be considered full-view since the features of interest are completely inside the *visible region* - the chromophore concentrations are well reconstructed. In the 0.75π angle case, only part of the structures are in the *visible region*- there is little distortion of the structures, but the concentrations are not correctly recovered.

9.2 The phantom

In this section an overview of the chosen phantom is given.

9.2.1 Liquid-based tube phantom vs other candidates

Liquid-filled tube phantoms, submerged in Intralipid, were used for these studies as the phantom type/architecture of choice. The advantages of this type of phantom are that they can be made with tubes available commercially in a variety of sub-mm sizes of interest, and are versatile: their liquid composition can be easily modified between experimental runs, whether in terms of background medium or absorbers of interest in the intraluminal space. Though it is true that certain solid tissue mimicking materials offer long-term stability/use and can be fabricated into shapes or with compositions not possible with liquid phantoms, it was considered that the latter are currently better positioned for precise qPAT studies, since they respect more closely the ideal optical and thermoelastic characteristics (Section 5.3). This is largely due to the fact that in tube phantoms, absorbers can be inserted and imaged in their native solution form, for which material properties are easier to estimate and control. Solid matrix materials require embedding or mixing of absorbers, for which there is a limited range of options for proper mixing and even then, it is harder to characterise or reproduce material properties in the mixture in a stable and repeatable manner. For tube phantoms, there is also potential to in the future make the relative arrangement (architecture) of the tubes more reproducible and adjustable: studies have explored laser cutting and 3D printing to obtain stable, reproducible frames with tailored inserts for tube phantoms [267]. From the perspective of the acoustic properties, aqueous solutions have a very similar speed of sound to soft tissue. An issue may arise from the acoustic impedance and speed of sound mismatch between the media and the tubes - this will be addressed below. The acoustic attenuation in 1% w/v Intralipid will be

much lower than in most soft tissues [190] but for these qPAT feasibility studies this may actually be desirable since it will lead to higher SNR and one less confounding factor.

9.2.2 Geometry / construction

The phantom architecture consisted of a support frame onto which the tubes of interest were glued. A 1 mm-thick PMMA sheet was laser-cut into a U-shaped frame. Two additional holes were also cut in the frame to lodge screws to hold the phantom in the upright position inside the sensor tray. The initial aim was to have a total of 6 tubes, arranged in two columns as seen in Figure 9.3 (a) (somewhat like the Tube Phantom in the simulation studies), but it was found that this arrangement would exacerbate multiple reflections between the tubes due to acoustic impedance mismatch and even partially block the signals of each tube column of reaching the opposite sensor. The tubes were instead aligned along a single line depth-wise - this maintained the optically-challenging nature of the phantom whilst minimising the acoustic reflection phenomena. This arrangement, with 4 tubes, is shown in Figure 9.3 (b). Whilst *in vivo* it may be necessary to deal with acoustically mismatched structures, we wanted to minimise this in phantom studies, as they would act as confounding factors in the already complex qPAT problem.

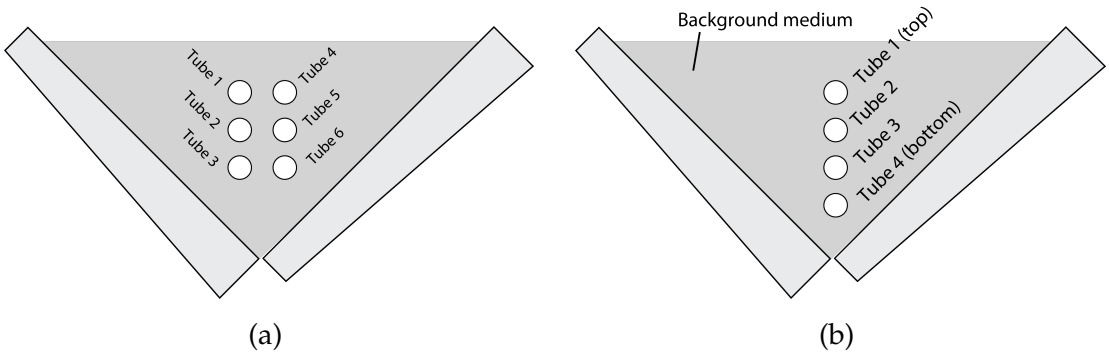

Figure 9.3: *Diagram of the cross-section of the phantom in the orthogonal sensor tray. (a) Two-column 6-tube phantom; (b) Co-aligned 4-tube phantom. The numbering of the tubes shows the convention that will be used to refer to the tubes in the remainder of the studies. Diagrams not to scale*

9.2.3 Tubing

Ideal specifications for the capillary tubes would be: high levels of transparency/clarity, speed of sound and acoustic impedance similar to aqueous media to avoid reflections and distortions, sub-mm inner diameter sizes, high inner/outer diameter ratio, flexibility and low brittleness.

In initial studies, silicone tubes had been used (inner diameter 508 μm, wall thickness 229 μm, inner/outer diameter ratio of 0.526, silicone SF1291, Trelleborg) but these led to

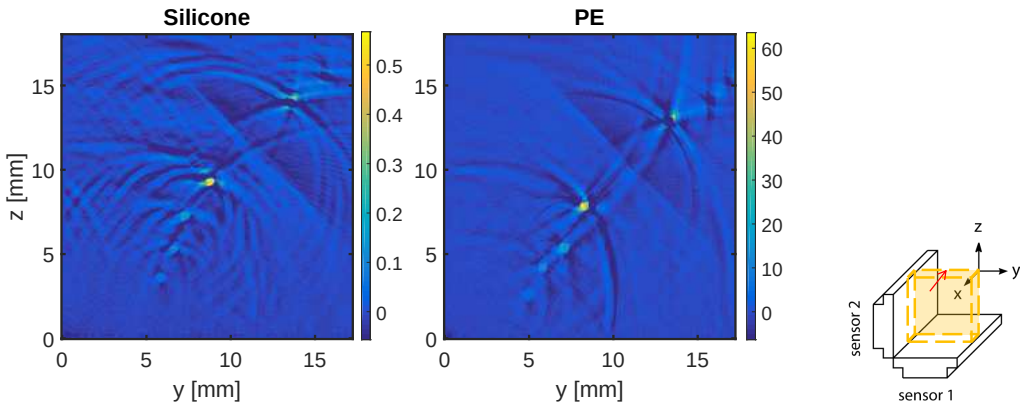

Figure 9.4: *Comparison of two PA experiments, one of them using silicone tubes and the other using low density polythene (PE) tubes. Both cases had the same composition ($NiCl_2$ in the top and third tube and $CuCl_2$ in the second and fourth tube, and identical Intralipid based background). They were acquired for the same field-of-view and reconstruction of p_0 was done with iterative time-reversal, it=3. The figures display the MIP of the central 0.8 mm-thick yoz slice, for 830 nm excitation. The colour mapping range was capped on the negative end to 10% of the maximum absolute intensity.*

large acoustic reflections and artefacts caused by their low speed of sound (and acoustic impedance) [268] compared to water ($Z_{silicone} \sim [1 - 1.1]$ MRayl vs $Z_{water} \sim 1.49$ MRayl) and by their greater tube wall thickness.

When surveying literature values of speed of sound, density, acoustic impedance and acoustic attenuation for a range of more than 35 plastic materials/grades [195], it was found that low density polyethylene (LDPE) was one of the best performers: its acoustic impedance is $Z_{LDPE} = [1.73 - 1.79]$ MRayl and its acoustic attenuation is $\alpha_{LDPE} =$ 2.4 dB/cm at 5 MHz. Of the plastics examined, its acoustic impedance was closest to water except for ethyl vinyl acetate (EVA) ($Z_{EVA} = [1.6 - 1.69]$ MRayl) and its acoustic attenuation was the lowest except for a specific grade of polystrene ($\alpha_{LDPE} = 1.8$ dB/cm at 5 MHz). LDPE also possessed high optical clarity, with relevant available sizes and a useful level of malleability and flexibility. Arconada-Alvarez *et al* (2017) [267] made an extensive study of some commercial tubes made of different materials and sizes, with the purpose of choosing the best for PA contrast agent characterisation and found that overall, polyethylene (PE)-based tubes would be best-suited. On one hand, they saw, by comparing PA spectra of pixel intensity, that PE exhibited a 3- to 4-fold higher PA signal than Teflon (PTFE) in the 750-970 nm region (and up to 10-fold in the 680-750 nm region), indicating potentially less comparative optical clarity, but the overall signal was only detected when high gain (~39 dB) was used to highlight the tube signal. In most practical scenarios, this signal would be undetectable when in the presence of typical contrast agents. Among tubes from different suppliers, it was noticed that the change in PA signal was more related to overall tube size than with the material itself. Teflon, despite having high clarity, has a high melting point, being not very malleable and therefore difficult to handle or seal. It also would have an inconveniently high acoustic impedance and speed of sound.

Based on all the previous considerations, LDPE tubes were chosen for further testing (inner diameter 580 μm, wall thickness 190 μm, inner/outer diameter ratio of 0.604, LDPE, Scientific Supplies). Figure 9.4 shows the relative performance of two experiments where identical experimental setups and reconstructions were used, but in one the phantom was made of silicone tubes and in the other LDPE tubes. The acoustic artefacts and number of reverberating effects are fewer for the LDPE case.

9.2.4 Absorbers

Initial experiments used $CuCl_2$ and $NiCl_2$ as the main absorbers. Despite them possessing characteristics that warranted their use in other qPAT studies (photostability and interesting spectral features), they do not exhibit absorption linearity with species concentration or when mixed together. This meant that when using different levels of dilution of either species, all solutions had to be independently characterised in the spectrophotometer. More crucially, aqueous solutions of chloride salts $CuCl_2$ and $NiCl_2$ could not be mixed with each other in a linear or even easily predictable manner. This meant that the two had to be kept in separate tubes during experiments. Given that one of the most relevant metrics of interest for *in vivo* studies is SO_2, a ratio of two chromophores mixed together, this posed a problem. As discussed in Chapter 7, sulphate salts $CuSO_4$ and $NiSO_4$ were characterised and found to retain all the fundamental advantages of the chloride compounds, whilst also respecting absorption linearity with concentration and when mixed with one another. This meant that qPAT phantoms could be created in which $CuSO_4$ and $NiSO_4$ could be mixed and act to some extent as surrogates for oxy- and deoxyhemoglobin. Besides these chromophores, water itself was a chromophore present in the solutions. For each individual qPAT experiment, the absorption spectra of the mother solutions were characterised with the spectrophotometer in the range of interest. Absorption for water was taken from the literature [244]. It is important to remember that the Grüneisen parameter of the sulphate compounds was empirically found to have a linear dependence with concentration (Section 7.3).

9.2.5 Phantom background

The background medium was comprised of Intralipid 1% w/v in water, which yields tissue-realistic levels of reduced scattering μ_s' in the wavelength range of interest. For each individual qPAT experiment, the reduced scattering spectrum $\mu_s'(\lambda)$ was characterised with the integrating sphere mounted in the spectrophotometer, for the wavelength range of interest. The IAD algorithm was then applied (Section 5.4.4).

The optical absorption of the background was raised in all qPAT experiments by including an additional absorber, given the low absorption of water itself in the 750 - 930 nm imaging window. The contribution of Intralipid towards absorption was found to be

negligible in the full range, based on literature values [260, 261]. In most experiments, india ink (Windsor) was added to the medium, to ensure that the background had a minimum absorption of at least $\mu_{a,bkg} \sim 0.01$ mm^{-1}. The reason india ink was chosen despite its flat absorption spectrum was because the other stable, more spectrally unique, absorption compounds - $CuCl_2$, $NiCl_2$, $CuSO_4$ and $NiSO_4$ - did not mix with Intralipid in a stable manner (in later *in vitro* studies, emulsifier Tween-20 was found to stabilise Intralipid emulsions with added salts and yield mixtures with reproducible and stable reduced scattering, Section 7.2). Though in itself india ink did not provide a very interesting spectral profile, water contribution in the 930 nm upwards region did ensure there was some spectral variation in the background absorption. Also, at the levels of dilution used, reduced scattering for india ink could be considered negligible.

9.3 Measurements

Having introduced the PA experimental setup and the phantom of interest, this Section outlines the acquisition procedure in terms of the pipeline, parameters and additional measurements of interest.

9.3.1 PA data acquisition

The data acquisition procedure with the orthogonal FP measurement system consisted of the following main steps:

1. Define a 2D region of interest to be interrogated on each sensor and the step size;
2. Optimise measurement sensitivity of FP sensors - Fine-tune adjustment of the manual translation and tip/tilt stages associated with each sensor in order to maximise reflectivity, whilst obtaining the most uniform reflectivity map possible (the higher the reflectivity, the higher the sensitivity);
3. Acquire PA data for sensor co-registration with dedicated registration phantom (see Section 9.4.1);
4. Acquire the multiwavelength PA dataset for the phantom of interest;
5. Acquire a PA image of the medium surface, by interrogating the phantom at the water absorption peak (see Section 9.3.2);
6. Acquire a PA image of the beam profile, by placing a dedicated acetate sheet with a grid of dots on the medium surface (see Section 9.3.2);
7. Acquire a second PA dataset with the registration phantom (see Section 9.4.1);

All PA images/acquisitions above were acquired without re-adjusting the physical positioning mentioned in step 2, and using the same ROI. Each PA acquisition was preceded

by a new pre-tuning operation (pre-tuning meaning, at each location of the ROI, finding and storing the ITF wavelength of maximum slope, then biasing the wavelength of the interrogation laser accordingly during PA acquisition - more details on this step and further Fabry-Perot working principles in Section 6.6.1). The repeated tuning was done because each full experiment lasted several hours, a period during which temperature changes could alter the characteristics of the ITF and therefore the optimal bias wavelength. As for the recording of the actual PA signal traces from systems 1 and 2 (respectively through channels 1 and 2), scope settings such as the time step dt and total number of temporal points acquired Nt were set *a priori* and left unaltered. On the other hand, due to the considerable changes in PA amplitude between acquisitions at different wavelengths, the channel resolution dV (in Volt per division) was altered for each case in order to find the finest resolution that did not allow the acquired signal to exceed the dynamic range (range defined by the product between the channel resolution and the finite number of discrete bins for acquisition, $\Delta V = dV \times Nbin$).

Besides the main measurements with the orthogonal FP measurement system, a set of complementary measurements was made for each experiment: calibration for the fluence intensity at each wavelength (Section 9.3.3), measuring both room and bath temperature (Section 9.3.4) and, as discussed previously, characterising the optical absorption properties of the mother solutions in the spectrophotometer as well as the optical scattering of the background medium through integrating sphere measurements and IAD inversion.

9.3.2 Beam profile

The initial pressure generated by the fluence incident on the surface of the medium creates an imprint of the beam profile. If the medium is illuminated at a wavelength at which optical absorption is high, obtaining a good representation of the beam profile should be possible. For our studies, 1450 nm, where water has a very prominent water peak, was chosen ($\mu_a(1450\,\text{nm}) = 30.9\ \text{cm}^{-1}$ [244]). In practice though, this approach did not yield the desired reconstruction. This was found to be related to the planar (and therefore highly directional) nature of the generated acoustic field/wavefront and the fact that this wavefront will mainly travel at a ~45º angle relative to each sensor. The pressure generated in the central strip will propagate as a wavefront that will travel directly to the edge area of the sensor array (the region where the two FP sensors are joined together), where in practice acoustic detection is not possible due to a gap where the sensors meet. This undesired gap is partially due to constraints in engineering - there will be a physical gap between sensors - and partially due to the fact that FP sensor interrogation scanning to the very bottom of each sensor array may not be possible. As a consequence of this gap in acoustic detection, reconstruction leads to artefacts - a curving of the planar surface in the image (e.g. see the curving in Fig. 10.5 when just one system/sensor is used) and insufficient data to reconstitute the planar behaviour in the middle, leading instead to a crossover feature. Another factor that could have some influence is the fact that

the incoming pressure waves will come at a strict-range ~45º acceptance angle, which, despite the good directionality characteristics of the FP, could have some effect.

Since the main problem seems to stem from having an initial pressure field that is planar, leading to the propagation of a planar, directed, wavefront, it was considered that a way to tackle this problem would be to ensure that the initial pressure field was comprised of point sources - these would propagate as spherical wavefronts, meaning that the acoustic detectors would be able to acquire information from a wider range of acceptance angles and more importantly, that pressure generated at points on the surface that are aligned with the gap-region will still spread as a spherical wave in all directions, being seen by multiple acoustic detectors. With this in mind, densely packed points arranged in a grid and separated by 1 mm were printed with black ink onto an acetate sheet. To map the beam, the sheet was dropped on the surface of the bath and imaged at a wavelength where absorption from the background medium was negligible, in order to guarantee that the printed points were the predominant acoustic generators (Fig. 9.5) - usually the range 750-850 nm was chosen. The mapping of the field was much improved. As a consequence of using point absorbers to generate the pressure, the beam profile will be sparsely sampled.

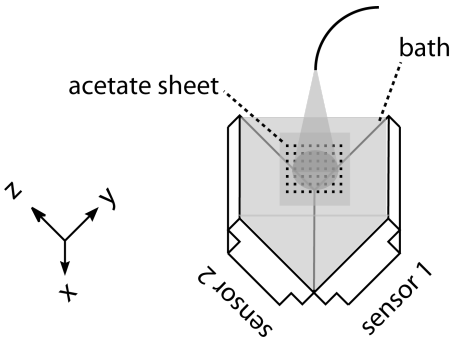

Figure 9.5: *Simplified diagram of the acquisition of beam-related data on the acetate sheet with printed densely packed points in a grid arrangement.*

9.3.3 Beam fluence

The pulse energy at the output of the laser was measured from pulse-to-pulse using an integrating sphere, and related to powermeter measurements of pulse energy at the distal end of the fibre (in Joule). The incident fluence employed in the theoretical light model was matched to the measured incident fluence.

More specifically, these variations in pulse-to-pulse energy were probed and corrected for by redirecting a small portion of the excitation light into an integrating sphere. The voltage reading from the integrating sphere for each given pulse was sent to the DAQ card and associated to the PA signal readings on systems 1 and 2 originated from that same pulse. A calibration step was further necessary since the integrating sphere is not equally reflective for all wavelengths of light, i.e. an identical voltage reading at two

given wavelengths does not translate to a same fluence level in Joule. This implied, for the wavelength range of interest, making simultaneous measurements of the fluence collected by the integrating sphere (measurement unit, V) and the fibre coupled distal fluence incident on a commercial powermeter (measurement unit, J). The obtained calibration factor could then be used to put all measurements in meaningful units of unitary incident fluence, Joule.

9.3.4 Temperature

Information on temperature can be important to inform on the absolute values or relative changes in certain material properties. The Grüneisen parameter and speed of sound are known to be temperature-dependent for most materials. Namely, for water, better absolute value estimates can be obtained from the literature if the temperature is known [113, 230].

Room temperature was measured with a thermometer (Digi-Temp sensor, ±0.05ºC) at the start and end of each acquisition to have an overall idea of the temperature trend during the full acquisition procedure. The temperature of the bath was also measured with a thermocouple before the first and at the end of the last acquisition with the phantom in place. This was not done for each acquisition/run (each wavelength) in order minimise the chance of accidentally disturbing the setup positioning (light fibre, phantom, tray alignment) between runs.

9.4 Acoustic reconstruction

Figure 9.6 shows the overall pipeline adopted for the acoustic reconstruction procedure. This involves a series of operations: first, the coordinate systems of each sensor are co-registered. The measurements are then converted to meaningful units of pressure (Pa) based on a calibrated measurement and they are normalised at each wavelength to 1 Joule incident fluence. Once the data for all wavelengths are available as $p_{meas}(\mathbf{r}', t, \lambda)$ [Pa/$J_{incident}$], they undergo some pre-processing steps - filtering and baseline correction. Finally, the acoustic reconstruction algorithm is applied to obtain multiwavelength images of initial pressure distribution, $p_{0,meas}(\mathbf{r}, \lambda)$ [Pa/$J_{incident}$].

9.4.1 Sensor co-registration and calibrations

The PA data acquired will be of the sort $p^{(1)}(\mathbf{r}'_1, t)\,[V]$ and $p^{(2)}(\mathbf{r}'_2, t)\,[V]$ for sensors 1 and 2 respectively. The superscripts are there to indicate that, although both sensors probe indirectly the pressure through a voltage reading, their sensitivity (mechano-electrical transduction) will be different, i.e. equal voltage readings may not correspond to equal

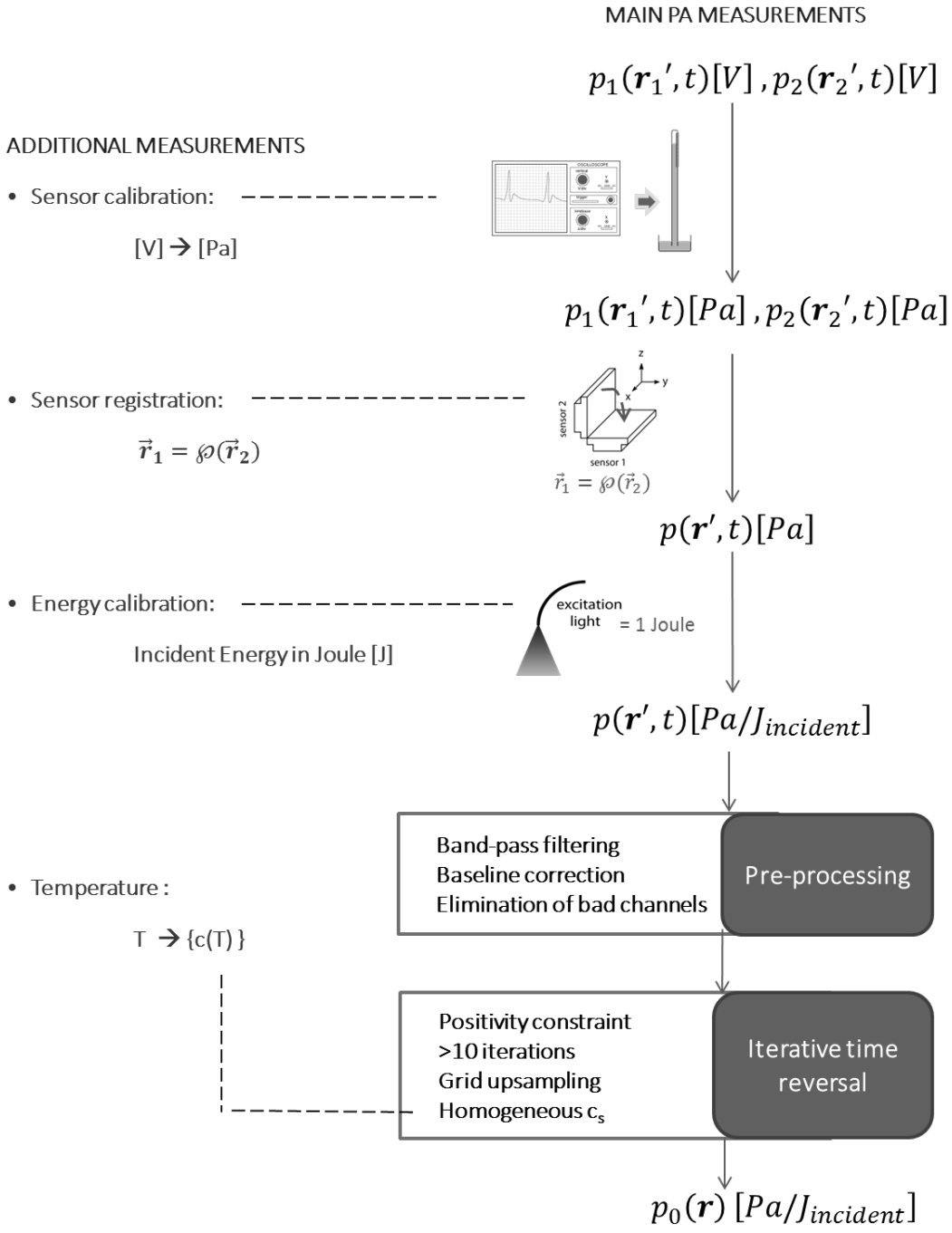

Figure 9.6: *Diagram of the acoustic pipeline, including co-registration, calibrations, pre-processing and acoustic inversion steps. Additional measurements needed are highlighted. The diagram shows the procedure for one wavelength.*

pressure. To pass all data into meaningful absolute pressure units of Pascal, the time-traces from each sensor are divided by calibration factors $K_{sys1}[V/Pa]$ and $K_{sys2}[V/Pa]$ obtained through characterisation of each sensor with a calibrated transducer.

The next step is to harmonise the data $p(\mathbf{r}'_1, t)\,[Pa]$ and $p(\mathbf{r}'_2, t)\,[Pa]$ into a common coordinate system $\mathbf{r}$. This is done by finding the transformation between the two local, on-plane, coordinate systems: $\mathbf{r}_1 = \wp(\mathbf{r}_2)$. The PA data acquired with the calibration phantom are used for that effect (Figure 9.7). The phantom data acquired with each sensor are reconstructed separately using time reversal at a speed of sound matched to water at the bath temperature, yielding volumetric images $p_0(\mathbf{r}_1)$ and $p_0(\mathbf{r}_2)$. Thresholding is applied to each, to obtain a cloud of points originating from the phantom. A rigid body transformation [269] is then applied to find the translation T and rotation R matrices that can best co-register the two point clouds, and therefore best represent the transformation between coordinate systems. Based on this, PA data acquired on systems 1 and 2 can be expressed through a common coordinate system $\mathbf{r}$, as $p(\mathbf{r}', t)[Pa]$.

The next step involves normalising the initial pressure data to equal levels of Joule incident, irrespective of wavelength - 1 Joule incident was chosen for simplicity. The data acquired will already have been corrected online for pulse-to-pulse variations in energy based on integrating sphere measurements, as explained in Section 9.3.3. The fluence calibration data $\left(K_{calib}(\lambda) = \frac{\text{Diverted energy into integrating sphere [V]}}{\text{Energy at distal end of fibre, powermeter [J]}}\right)$ will still need to be applied offline to translate this normalisation into meaningful absolute energy units. This calibration is done assuming linearity, through a simple multiplication of the PA data by $K_{calib}(\lambda)$. The PA data $p(\mathbf{r}', t)$, now in units of $[Pa/J_{incident}]$, are ready to be pre-processed and inverted.

9.4.2 Pre-processing

The measured time-series are pre-processed prior to image reconstruction. First, a baseline correction is employed to all time-series, by subtracting from each the respective baseline - defined here as the median value of time-samples between an early time-period where meaningful PA signals have not yet arrived. The time-series are then low-pass filtered to remove high-order noise. Finally, the noisiest channels are eliminated - this is defined as 5% of the channels with the highest variance in the baseline region.

9.4.3 Acoustic reconstruction algorithm

An iterative time-reversal scheme, including a positive initial pressure constraint, was employed as the acoustic reconstruction algorithm [270, 271], being considered the most appropriate for this type of orthogonal configuration [20]. The pseudospectral time-domain propagation model, k-Wave [76], was used as the acoustic forward model. The algorithm was typically run for >10 (usually 20) iterations to obtain a volumetric image

of initial pressure. A two-fold grid upsampling was typically applied compared to the scanning step size.

In terms of acoustic properties, the speed of sound in the medium, c_s, could be matched to that of literature values of water at bath temperature [230], since Intralipid concentration of 1% w/v has been shown to have negligible effect on the speed of sound in water [56]. Acoustic attenuation was neglected.

On iterative time-reversal Iterative time-reversal techniques are ideally suited to optimally reconstruct data acquired in an V-shaped geometry [20]. If given sufficient data, they will converge to the right solution - in terms of pressure distribution, amplitude and absence of artefacts/blurring. No non-iterative reconstruction strategy would be capable of providing an exact reconstruction. The technique works by adding successive terms (images) in a Neumann series. This can be formulated in the following way [270, 271]:

$$p_0(\mathbf{r})^{(m+1)} = p_0(\mathbf{r})^{(m)} + T(p(\mathbf{r}', t) - Ap_0(\mathbf{r})^{(m)}), \tag{9.1}$$

where $p(\mathbf{r}')$ is the measured time-series data at the detectors, T is a standard time-reversal operator mapping $p(\mathbf{r}')$ back into the domain as initial pressure distribution $p_0(\mathbf{r})$ (i.e. a time-reversal reconstruction operation) and A is a forward operator that maps $p_0(\mathbf{r})$ to $p(\mathbf{r}')$ through acoustic propagation. Constraints of non-negativity and zero initial particle velocity are imposed at each iteration, which is critical for the reconstruction to converge to the true solution.

Explained in a more intuitive manner, the technique starts by reconstructing an estimate of the initial pressure distribution through standard time-reversal, $p(\mathbf{r})^{(1)} = T(p(\mathbf{r}', t))$. Whilst time-reversal would stop here, iterative time-reversal attempts to maximise the agreement between data and model. This is done by comparing the true measured pressure time-series $p(\mathbf{r}', t)$ with the one generated by propagating the reconstructed field $p(\mathbf{r})^{(1)}$ forward and sensing it at the same detectors (using operator A). Any differences between these two sets of time-series, $p(\mathbf{r}', t) - Ap_0(\mathbf{r})^{(m)}$, are used to form an update to the image through time-reversal T. This will be perceived as pressure wrongly left unaccounted in the model and will be added onto the previous estimation of the reconstructed field, yielding $p_0(\mathbf{r})^{(2)}$. This process of forward propagation and time-reversal can then be repeated for more cycles, m, in the hope of converging to maximum agreement.

For illustrative purposes, Fig. 9.8 shows the outcome of applying iterative time-reversal to data from a virtual phantom that is placed entirely in the visibility region of a V-shaped configuration (the delimitation of this region is marked with a red dashed line). The results are compared to those obtained with non-iterative time-reversal and also to those obtained with a planar sensor - which provides only limited view and no *visible* region (since regardless of where a feature of interest is placed in the domain, there will always be feature edges whose normals are parallel to the sensor, and therefore never be detected - see red arrows). It can be seen that iterative time-reversal in the V-shaped configuration

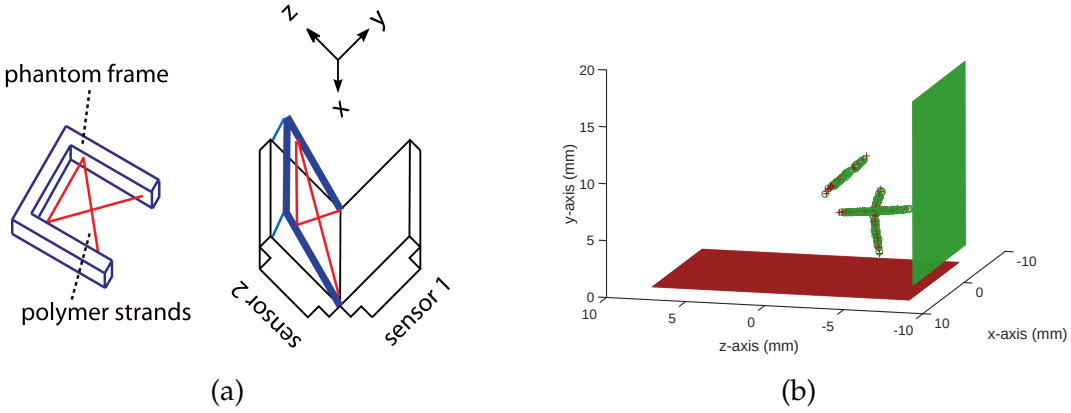

Figure 9.7: *(a) Diagram of the registration phantom, composed by a 17 µm black polymer strand (shown here in red for clarity) stringed onto a transparent PMMA frame. The general way in which the phantom is positioned in the sensor array is also shown. (b) Representation of the sensor surfaces (1 - green, 2 - red) and a portion of the point cloud of the phantom data taken by each sensor, after alignment.*

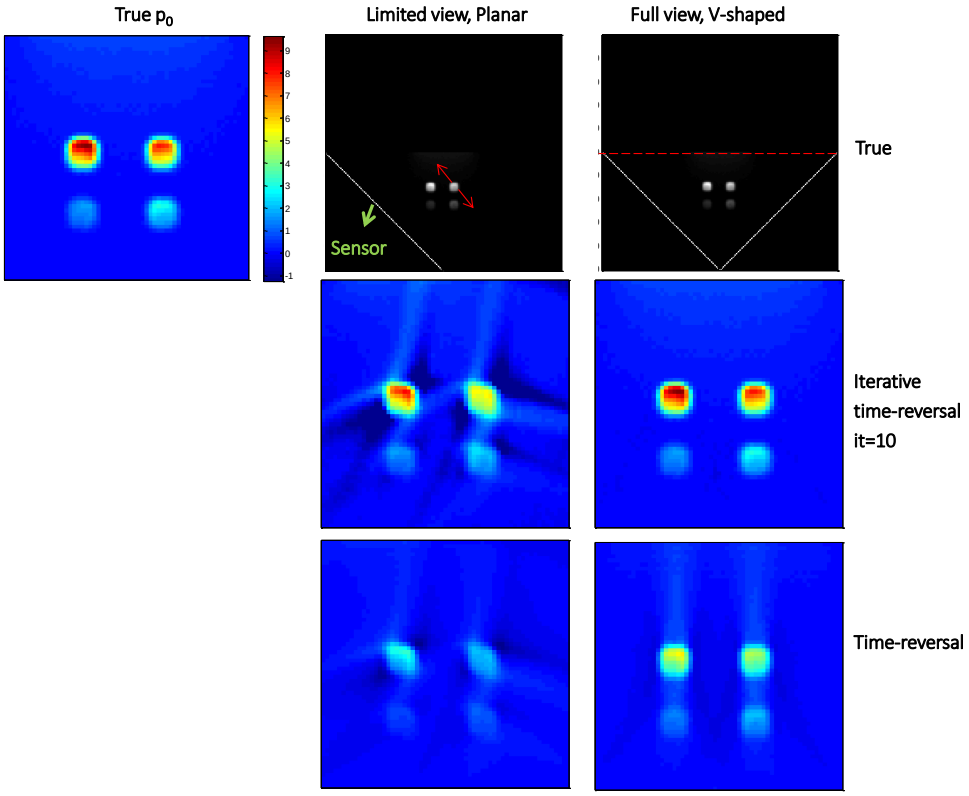

Figure 9.8: *Outcomes of applying either non-iterative or iterative time-reversal (it=10) to data acquired with a planar or V-shaped geometry (acquisition geometry shown by the gray lines in the top row figures). The true initial pressure distribution used for testing was obtained from a spatially smoothened version of the tube phantom in Chapter 8 (smoothening was done to avoid instabilities in k-Wave forward and backward propagation), at 750 nm. The source is incident from the top edge. All initial pressure distribution images are colour-coded for the same range (that of the colourbar). The red dashed line indicates the top edge of the visible region. The red arrows indicate how waves generated from feature edges orthogonal to the detector, and therefore travelling parallel to the sensor, will never be detected regardless of the spatial location of the feature.*

perfectly reconstructs the true initial pressure field p_0. On the other hand, when only a planar array is used for detection, the field is erroneously recovered (whether with non-iterative or iterative time-reversal) - both in terms of feature distortion, incorrect absolute intensity, artefacts in the background and the appearance of non-physical negative values. The results also show that even in the V-shaped configuration, if only non-iterative time-reversal had been applied, it would not have been possible to recover the full field information. For non-iterative time-reversal to have successfully recovered the full field information, the detection geometry would have needed to be closed (features of interest enclosed within).

9.5 Optical reconstruction (quantification)

After a multiwavelength dataset of the initial pressure distribution is obtained, $p_0^{meas}(\mathbf{r}, \lambda)$, these images can be used to help retrieve distributions of the chromophore concentrations, ideally by maintaining the volumetric and highly-resolved nature of the PA data. Model-based inversion was chosen as the preferred method. More specifically, a least-squares minimisation was adopted, with the fluence being modelled with a 3D diffusion approximation to the RTE, implemented through FEM with Toast++ [68]. In practical terms, the optical inverse (or optical reconstruction) pipeline can be described as follows:

1. Creation of a mesh for FEM implementation
    - Definition of ROI - delimitation of top surface based on water surface data and centre of beam profile based on grid data;
    - Construction of mesh;
2. Interpolation from the regular k-Wave grid onto the unstructured FEM mesh - acoustic reconstruction data defined on the gridpoints is interpolated onto the nodes of the mesh (inherently involves rotation and translation);
3. Scaling
    - Step 1 - Division of data by the Grüneisen of water, Γ_{H_2O}
    - Step 2 - Unit conversion from Pa to J mm^{-3}
    - Step 3 (only applied if theoretical and experimental p_0 data are deemed incorrectly scaled) - Re-normalisation of the experimental H data by a scaling factor given by the ratio of the maximum of the experimental H data to the maximum of the Toast++ ground-truth simulated H data;
4. Definition of the MBI framework and its relevant inversion parameters;
5. Running the MBI and plotting outcomes.

9.5.1 Mesh creation and data interpolation

An overview of the mesh creation is given in Fig. 9.9. The first step involved establishing the ROI over which the meshing is to be done. One approach could involve meshing the entirety of the medium - i.e. all the imaged space enclosed by the two sensor surfaces and the liquid surface. This would make the domain potentially unnecessarily large when considering the location of the features of interest (tubes) and would also require the domain to be irregular. Instead, the ROI was always defined to be cubic, with its top surface co-aligned with the liquid surface of the phantom (Fig. 9.9 c). A mesh with irregular tetrahedral elements was then created for the cubic ROI, using application *gmsh* [272] - the average desired side length of the elements was usually set to 100 μm or 200 μm.

The medium surface was found by first reconstructing for the initial pressure distribution at water peak excitation with iterative time-reversal (iTR), $p_0(1450\,\text{nm})$, then obtaining a cloud of point locations through binary intensity thresholding and fitting a plane to it (Fig. 9.9 a). A first approximation of the location of the centre of the beam and its diameter was found by reconstructing the grid phantom data with iTR, then thresholding the data to isolate the points on the grid, projecting these data onto the medium surface plane and finally fitting a Gaussian distribution intensity profile to the data projected on the plane (Fig. 9.9 b).

(We will express the mesh ROI through coordinates X, Y, Z and the acoustic reconstruction grid (k-Wave) ROI in coordinates x, y, z for clarity)

9.5.2 Model-based inversion algorithm

The model-based inversion algorithm considered the chromophore concentration distributions c_k as unknowns, implemented such that both the optical absorption μ_a and Grüneisen behaviour Γ could be defined through a known dependence on c_k. The reduced scattering coefficient and data scaling were usually considered fully known (a few cases considered either the scatterer concentration scalar a or the data scaling K as unknown). Based on this, the problem could be formulated as follows:

$$\underset{c_k,a,K}{\operatorname{argmin}}\, \varepsilon = \frac{1}{2}\sum_{l=1}^{L}\sum_{h=1}^{Nh}\left[\, p_{0,h}^{meas}(\lambda_l) - p_{0,h}(c_k, K, a, \lambda_l)\,\right]^2, \tag{9.2}$$

where subscripts l and h denote wavelength index and nodal position index respectively, c_k denotes the vector of unknown concentration distributions for a set of k chromophores [170], $p_{0,h}^{meas}(\lambda_l)$ is the experimental initial pressure distribution interpolated from the k-Wave grid (acoustic model) into the nodes of the mesh (optical model) and $p_{0,h}^{model}(c_k, \lambda_l)$ is the modelled initial pressure distribution where the forward model is defined as

$$p_0(c_k, a, \lambda_l) = K\,\Gamma(c_k)\,\mu_a(c_k, \lambda_l)\,\Phi(\mu_a(c_k), \mu_s'(a), \lambda_l), \tag{9.3}$$

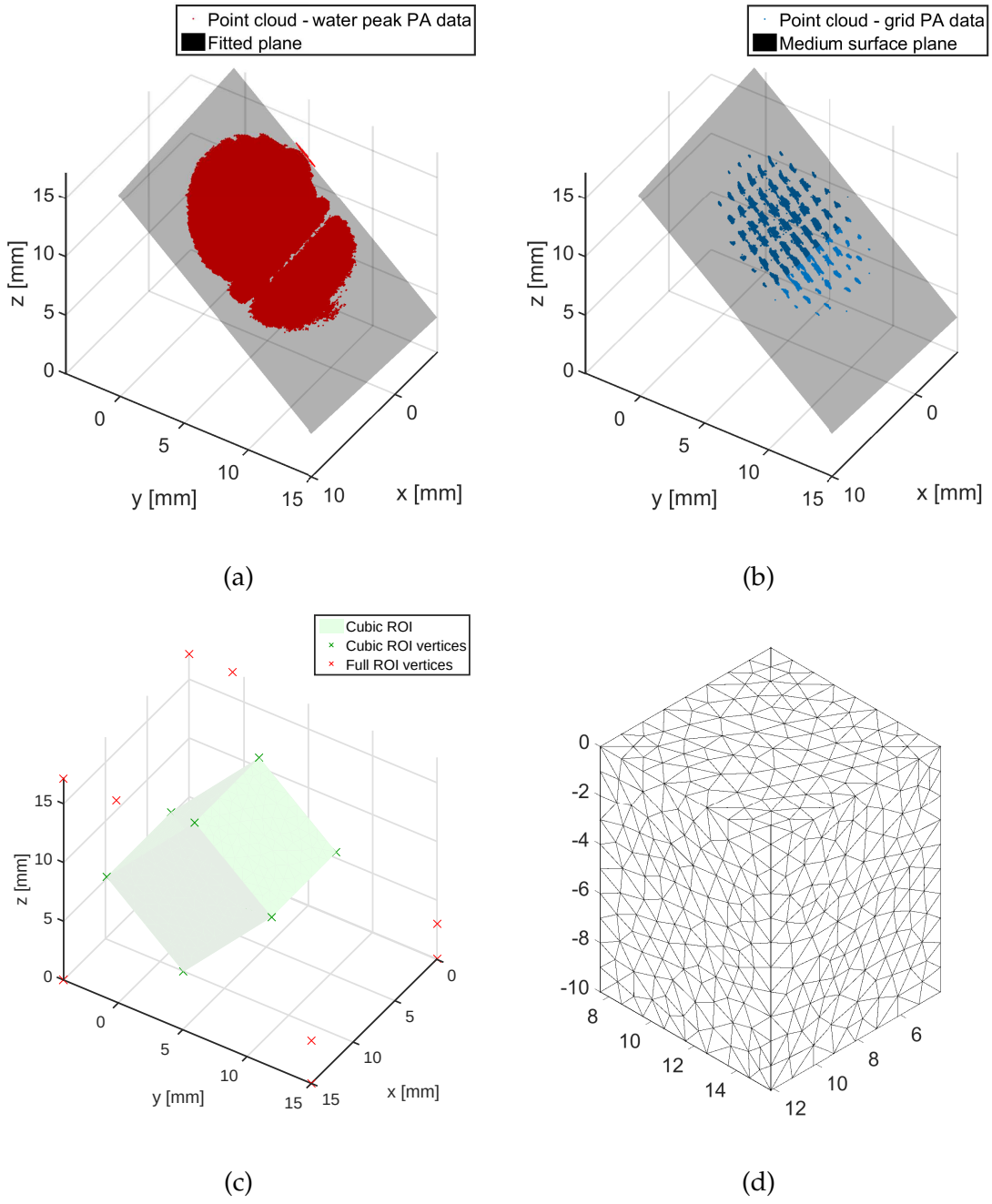

Figure 9.9: *(a) Example of the cloud of points from the water peak acquisition and the respective fitted plane for the surface; (b) Example of the cloud of points from the grid phantom projected onto the surface plane; (c) Example of the cubic ROI and its vertices. Vertices of the full imaged liquid medium are also shown. (d) Example of a cubic mesh with tetrahedral elements of average side length 1 mm (purposefully very coarse for ease of visualisation).*

where

- $\Gamma(c_k)$ is the Grüneisen parameter distribution normalised for water Γ_{H_2O} and related to the chromophore concentrations through an empirical relationship of the type $\Gamma(c_k) = c_{H_2O} + \sum_{i=1}^{k} \beta_i c_i$;
- $\mu_a(c_k) = \sum_{i=1}^{k} \alpha_i c_i$ is the optical absorption distribution with known chromophore spectra $\alpha(\lambda)$;
- $\mu_s'(a) = a\alpha_{scat}$ is the optical reduced scattering with known scatterer wavelength dependence $\alpha_{scat}(\lambda)$.
- Φ is the light fluence distribution computed using 3D DA-FEM (Toast++ [68]), with incident beam characteristics fixed and known through experimental characterisation.

The minimisation algorithm employed was the limited-memory BFGS (L-BFGS) and the functional gradients needed as input, $\frac{\partial \varepsilon}{\partial c_k}$, were calculated with the adjoint method [111, 149] rather than with forward differences (reducing forward-model runs from $Nh \times k$ to only 2 per iteration). Core inputs are the multiwavelength PA data, $p_{0,meas}(\mathbf{r}, \lambda)$, the absorption spectra of the chromophores, $\alpha_i(\lambda)$, the reduced scattering spectrum $\alpha_{scat}(\lambda)$ and the characteristics of the beam (location, diameter).

The functional gradient $\frac{\partial \varepsilon}{\partial c_k}$ can be expressed as follows:

$$\begin{aligned} \frac{\partial \varepsilon}{\partial c_k} &= \sum_{l=1}^{L} \left[\frac{\partial \varepsilon}{\partial \mu_a^l} \frac{\partial \mu_a^l}{\partial c_k} \right] + \frac{\partial \varepsilon}{\partial \Gamma} \frac{\partial \Gamma}{\partial c_k} = \\ &= \sum_{l=1}^{L} \left[\alpha_k^l \frac{\partial \varepsilon}{\partial \mu_a^l} \right] + \beta_k \frac{\partial \varepsilon}{\partial \Gamma} \end{aligned}, \tag{9.4}$$

where $\alpha_k^l \equiv \alpha_k(\lambda_l)$ is the absorption spectrum of the kth chromophore at wavelength λ_l, $\frac{\partial \varepsilon}{\partial \mu_a^l}$ is the functional gradient with respect to the absorption coefficient μ_a^l, $\frac{\partial \varepsilon}{\partial \Gamma}$ is the functional gradient with respect to the Grüneisen parameter and β_k is the empirical factor that gives the relative contribution of chromophore k towards the overall Grüneisen parameter.

The gradient w.r.t. the Grüneisen parameter is given by:

$$\frac{\partial \varepsilon}{\partial \Gamma} = K \sum_{l=1}^{L} \sum_{i=1}^{Nh} \left[\Phi_i^l \, \mu_{a_i}^l \left(p_{0_i}^{l,meas} - p_{0_i}^{l,model} \right) \right]. \tag{9.5}$$

The gradient w.r.t. the optical absorption coefficient at node i, $\mu_{a,i}^l$, can be calculated independently for each wavelength as (we will drop the subscript l for clarity):

$$\frac{\partial \varepsilon}{\partial \mu_{a,i}} = -\left(\frac{\partial p_0}{\partial \mu_{a,i}} \right)^T \left(p_0^{meas} - p_0 \right), \tag{9.6}$$

where:

$$\frac{\partial p_0}{\partial \mu_{a,i}} = K\Gamma \left(\frac{\partial \mu_a}{\partial \mu_{a,i}} \Phi + \mu_a \frac{\partial \Phi}{\partial \mu_{a,i}} \right). \tag{9.7}$$

Equation 9.6 therefore becomes:

$$\begin{aligned}\frac{\partial \varepsilon}{\partial \mu_{a,i}} &= -K\Gamma\left(\frac{\partial \mu_a}{\partial \mu_{a,i}}\Phi + \mu_a\frac{\partial \Phi}{\partial \mu_{a,i}}\right)^T\left(p_0^{meas} - p_0\right) = \\ &= -K\Gamma\Phi^T\frac{\partial \mu_a}{\partial \mu_{a,i}}^T\left(p_0^{meas} - p_0\right) - K\Gamma\frac{\partial \Phi}{\partial \mu_{a,i}}^T\mu_a^T\left(p_0^{meas} - p_0\right)\end{aligned}. \tag{9.8}$$

Recalling that $A\,\Phi = q$ (equation 2.18), where A is the DA-FEM system matrix and q the source vector, and finding its derivative w.r.t. $\mu_{a,i}$, we obtain:

$$A\,\frac{\partial \Phi}{\partial \mu_{a,i}} + \frac{A}{\mu_{a,i}}\Phi = 0 \tag{9.9}$$

$$\frac{\partial \Phi}{\partial \mu_{a,i}} = -A^{-1}\frac{A}{\mu_{a,i}}\Phi, \tag{9.10}$$

which, substituting into 9.8 yields:

$$\frac{\partial \varepsilon}{\partial \mu_{a,i}} = -K\Gamma\Phi^T\frac{\partial \mu_a}{\partial \mu_{a,i}}^T\left(p_0^{meas} - p_0\right) + K\Gamma\Phi^T\left(\frac{\partial A}{\partial \mu_{a,i}}^T(A^T)^{-1}\right)\mu_a^T\left(p_0^{meas} - p_0\right), \tag{9.11}$$

where matrix relations $(A^T)^{-1} = (A^{-1})^T$ and $(B\,C\,D)^T = D^T\,C^T\,B^T$ were used. $\frac{\partial A}{\partial \mu_{a,i}} = \int_\Omega u_i u_j u_k d\Omega$ is the derivative of the system matrix w.r.t. $\mu_{a,i}$. The first term can be solved straightforwardly, whilst for the second one the adjoint method can be employed to solve the computation with two runs of the forward model instead of Nh runs. The adjoint field Φ^* is defined as:

$$A^T\Phi^* \equiv \mu_a^T(p_0^{meas} - p_0^{model}) \tag{9.12}$$

and therefore:

$$\Phi^* = (A^T)^{-1}\mu_a^T(p_0^{meas} - p_0^{model}) \tag{9.13}$$

The expression for the adjoint can now be substituted into Equation 9.11:

$$\begin{aligned}\frac{\partial \varepsilon}{\partial \mu_{a,i}} &= -K\Gamma\Phi^T\frac{\partial \mu_a}{\partial \mu_{a,i}}^T\left(p_0^{meas} - p_0\right) + K\Gamma\Phi^T\frac{\partial A}{\partial \mu_{a,i}}^T\Phi^* = \\ &= K\Gamma\Phi^T\left(\frac{\partial A}{\partial \mu_{a,i}}^T\Phi^* - \frac{\partial \mu_a}{\partial \mu_{a,i}}^T\left(p_0^{meas} - p_0\right)\right)\end{aligned}. \tag{9.14}$$

Furthermore, adaptations could be made to the algorithm to also minimise for the scattering or concentration-independent Grüneisen related parameters. To invert for the Grüneisen parameter directly, the functional gradient expression found above, Eq. (9.5), can be used straightforwardly. To invert for scattering, the spectral behaviour $\alpha_{scat}(\lambda)$ will for instance need to be known to reduce ill-posedness. In that case, only the scatterer concentration distribution a needs to be inverted for, where $\mu_s'(\lambda) = a\,\alpha_{scat}(\lambda)$. The functional gradient w.r.t a can be defined as follows:

$$\frac{\partial \varepsilon}{\partial a} = \sum_{l=1}^{L}\left(\alpha_{scat}(\lambda_l)\frac{\partial \varepsilon}{\partial \mu_s'^l}\right), \tag{9.15}$$

where $\mu_s'^l \equiv \mu_s'(\lambda_l)$. The gradient w.r.t. $\mu'_{s,i}$, i.e. reduced scattering coefficient at a given nodal position i and wavelength λ_l (index l omitted for clarity) can also be found through the adjoint method, where similar calculations to those used for $\frac{\partial \varepsilon}{\partial \mu_{a,i}}$ will yield:

$$\frac{\partial \varepsilon}{\partial \mu'_{s,i}} = K\Gamma\Phi^T \frac{\partial A}{\partial \mu'_{s,i}}^T \Phi^*, \tag{9.16}$$

where $\frac{\partial A}{\partial \mu'_{s,i}} = 3D_i^2 \int_\Omega u_i \nabla u_j \cdot \nabla u_k d\Omega$ is the derivative of the system matrix w.r.t. $\mu'_{s,i}$.

9.5.3 Defining further model-based inversion settings/options/inputs

Model-based minimisation strategies are characterised by their versatility and flexibility. Table 9.1 gives an overview of the qPAT algorithm implemented, including the options that can still be taken (the Table is not meant as an exhaustive list of all options pertaining to all MBI frameworks, but only as an overview to those easily accessible via the implemented MBI set of scripts in this project). Some of the aspects, and the way in which choices are made, have been discussed above, namely those pertaining to the reconstruction, calibration and normalisation of the data, to the characteristics of the mesh and of the source. Other aspects mentioned in the Table that also remain open for decision before a MBI can be run are:

- **Choice of the unknowns** - for the chromophores, it may be decided to invert for all chromophores species or to set some as fixed and known; for the scattering, it may be decided to set its amplitude as fully known based on experimental/literature information or to set it as unknown (albeit with known spectral behaviour, otherwise the problem would be too ill-posed) and finally it may be decided to set the Grüneisen parameter as known or unknown, and, if the latter is chosen, to decide whether it should act as an independent variable or as a known function of concentration. The scalar factor K could also be set as unknown or fixed. Another decision to be made in terms of the unknowns is whether any of the parameters should be expressed by a single, piecewise constant or fully spatially-resolved (i.e. node-per-node) set of unknowns;

- **Initialisation** - for the unknowns defined for minimisation, it will be necessary to initialise their values in some way;

- **Stopping criterion** - given the iterative nature of the minimisation, a stopping criterion will need to be set, which may be related to e.g. the number of iterations, a tolerance on the relative change in error functional, a tolerance on a relative change in the estimates of the unknowns.

- **Other *a priori* information** - Decisions also need to be made about the bounds of the values to be found, and on the inclusion of regularisation (smoothing, edge-preserving, etc) and its relative weight to the error functional.

9.5.4 Displaying outcomes

To display and analyse the outcomes, the MBI results obtained for the cuboid mesh were interpolated onto a regular voxel-based structure with 50 μm voxel size, though with the same overall cuboid ROI. The next Chapter will also present some error metrics of interest to be computed on this ROI, to quantitatively assess performance and to better compare different scenarios. For this, values within a *selection mask* that probes behaviour inside the tubes were considered. The starting point for the mask was an approximate full tube segmentation. Then, the mask was adapted to only consider a more central cross-section rather than the whole tube cross-section. This was done to avoid the effect of mesh interpolation errors and partial volume effects close to the edges of the tubes. The updated mask was thus found by finding the centroid of each tube in each cross-section slice of the ROI and then by performing a dilation operation with an element of the desired cross-section size. Finally, the mask was updated to only consider half the full length of each tube along the longitudinal axis from the centre of the ROI, to avoid the effect of expected DA-FEM model inaccuracies close to the physical boundaries of the ROI.

9.6 Overview of contributions

The experimental qPAT experiment described in this Chapter and in Chapter 10 was a project that resulted from a joint effort between a group of researchers from the Photoacoustic Imaging Group and the Centre for Medical Image Computing (Lu An, Simon Arridge, Paul Beard, Ben Cox, Rob Ellwood, Felix Lucka, Emma Malone). Since the project involved a range of considerations from instrumentation development and calibration, to material characterisation, data acquisition, theoretical acoustic reconstruction and qPAT considerations, a multidisciplinary approach was essential for increasing the success of the project. Besides the invaluable role of the joint discussions and troubleshooting, I would like to acknowledge the following specific contributions to this work:

- Rob Ellwood developed the V-shaped system, provided scripts for system co-registration and for iterative time-reversal and performed the mechanoelectrical calibration of the two sensors with calibrated transducers;
- Lu An performed studies on the accuracy and repeatibility with which reduced scattering estimates are obtained through IAD+integrating sphere measurements;
- Emma Malone scripted the main MBI pipeline and also performed reconstructions with initial acquired datasets;
- Felix Lucka performed the acoustic pre-processing and reconstruction on the main experimental datasets and also optimised the MBI speed-wise and memory-wise in order for it to run more efficiently for the 100μm cases.

I was largely in charge of the design of the main experiment and various other preliminary experiments, of the acquisition of the PA data, auxiliary data and material characterisation data, of early data pre-processing (calibration, sensor data alignment, preliminary acoustic reconstructions) and of the computation of most batches of optical inversions. I also implemented and performed various adaptations to the main MBI - as presented in the next Chapter - and did extensive and critical analysis of the data (performance metrics, visualisation, comparison between MBI inversions, comparison with LU, sensitivity analysis, convergence analysis, critical factors) and assessment of relevant future work.

9.7 Summary

In this Chapter we designed and adopted an overall methodology to be able to perform a controlled, well-characterised and informative qPAT experiment where the high-resolution and volumetric estimation of chromophore concentration could be within reach. To obtain the most faithful images of initial pressure distribution, a V-shaped Fabry-Perot measurement system was used in order to optimise detection bandwidth, directionality, sensitivity and resolution. Iterative time-reversal was chosen as the acoustic reconstruction strategy to, together with the orthogonal sensor arrangement, allow near full-view acquisition. The acquisition protocol contemplated performing additional measurements - measuring the temperature to obtain better estimates of speed of sound and thermoelastic efficiency; measuring the position and profile of the incident beam; obtaining calibrations for incident energy and for the sensitivity and mechanoelectrical transduction of the sensors. Polyethylene tubes filled with absorbing aqueous solutions of $NiSO_4$ and $CuSO_4$, in a bath of intralipid and india ink, were adopted as the phantom of choice. This yielded known and appropriate acoustic, thermodynamic and optical properties and enabled ease and versatility of usage. For optical reconstruction, a least-squares model based inversion was adopted with the DA as the fluence model. To deal with the high-dimensionality of the data and to ensure a non-prohibitive computational load when estimating 3D high-resolution maps of concentration, the quasi-Newton L-BFGS method was chosen as the minimisation algorithm, with the functional gradients computed through the adjoint method.

Overview of options available in the used MBI pipeline	
	Choices on physical parameters
Chromophore concentration	{water,india ink,NiXX,CuXX} - choose which ones are Known vs unknown Homogeneous vs piecewise constant vs fully resolved
Scatterer concentration	Known vs unknown Homogeneous vs piecewise constant vs fully resolved
Grüneisen	Known vs unknown (function of chromophore concentration) vs unknown (independent) Homogeneous vs piecewise constant vs fully resolved
	Choices on the measured PA data
Scaling	Steps 1 and 2 vs Step 3
	Choices on the light model
Light model	FEM Diffuse approximation vs FEM Delta-Eddington approximation
Mesh	Domain size: (NX× NY× NZ) Average size of tetrahedral elements: *var*
Source	Profile: Gaussian vs Customised Radius: *var*
	Choices on the cost function
Data fidelity term	Least-squares
Regularisation term	None vs Tikhonov zeroth order vs Tikonov first order Weighting factor
	Choices on the minimisation
Algorithm	L-BFGS with adjoint method for functional gradient calculation
Initialisation	Homogeneous vs Initial estimate vs Other
Stopping criterion	Number of iterations vs Tolerance on estimate updates vs Tolerance on gradient

Table 9.1: *Overview of optical inversion algorithm, including the various options/settings available.*

Chapter 10

Outcomes of experimental QPAT

In this Chapter, we will describe and show the results of the qPAT experiment whose methodology was described in the previous Chapter.

10.1 Overview of the experiment and PA data

Region	**Q** (%)	c_{H_2O} [a.u.]	$c_{indiaink}$ [a.u.]	c_{NiSO_4} [M]	c_{CuSO_4} [M]	**Intralipid** [% w/v]	Γ/Γ_{H_2O}
Background	n.a.	1	1	0	0	1	1
Tube 1	25%	1	0	0.55	0.375	0	1.444
Tube 2	100%	1	0	2.2	0	0	1.714
Tube 3	75%	1	0	1.65	0.125	0	1.624
Tube 4	0%	1	0	0	0.5	0	1.354

Table 10.1: *Composition of each of the four tubes and of the background. Unitary water concentration is defined as corresponding to a unitary partial volume of water at typical room temperature and pressure. Unitary india ink concentration has been set to correspond to the concentration used in the phantom background - which is 0.4% of a mother batch solution ($M10_b$). The unitary absorption spectra are given in Fig. 10.1 (a) and (c).*
n.a.- not applicable.

In this experiment, copper sulphate ($CuSO_4.5H_2O$) and nickel sulphate ($NiSO_4.6H_2O$) were used as the main chromophores. The phantom comprised 4 low-density polyethylene tubes in a background of 1% w/v Intralipid and 0.4% v/v of a mother batch solution of india ink (such that $\mu_{a,indiaink}$ (750 nm) $\simeq 0.0064$ mm^{-1} in the medium). The tubes were filled with mixtures of a 0.5 M copper sulphate mother solution and a 2.2 M nickel sulphate mother solution, such that $Q = \{25, 100, 75, 0\}$% from top to bottom tube respectively (Figure 10.2), where the ratiometric quantity

$$Q(\%) = \frac{\frac{c_{NiSO_4}}{2.2}}{\frac{c_{CuSO_4}}{0.5} + \frac{c_{NiSO_4}}{2.2}} \times 100 \tag{10.1}$$

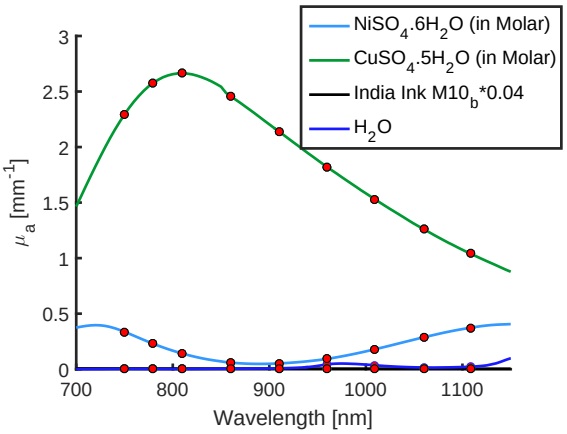

(a) Optical absorption of chromophores

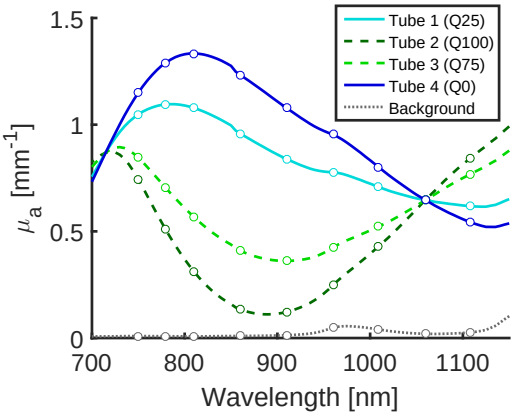

(b) Optical absorption per region

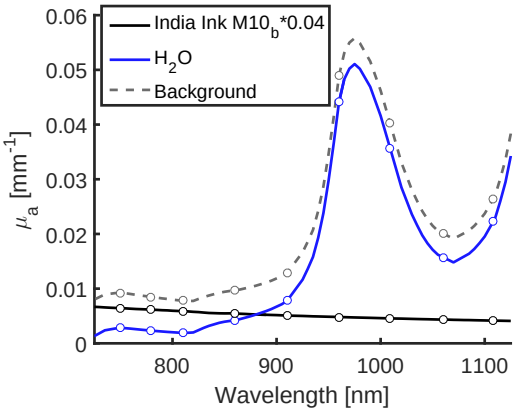

(c) Background optical absorption

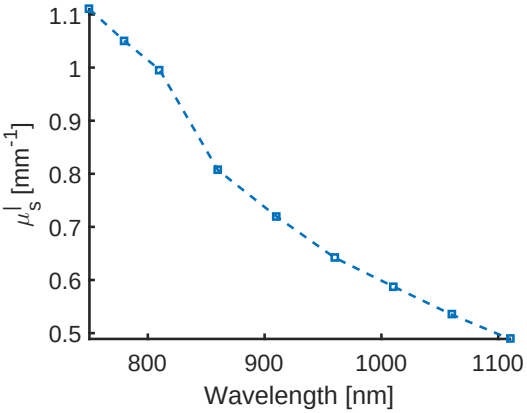

(d) Background reduced scattering

Figure 10.1: *Overview of the PA tube phantom optical characteristics. (a) Absorption spectra of each of the four chromophores, as given to the qPAT inversion schemes; (b) Optical absorption spectra of each of the four tubes and of the background. (c) Breakdown of the background optical absorption contributions. (d) Reduced scattering of the background medium. (b,d) Reproduced with permission from [273]*

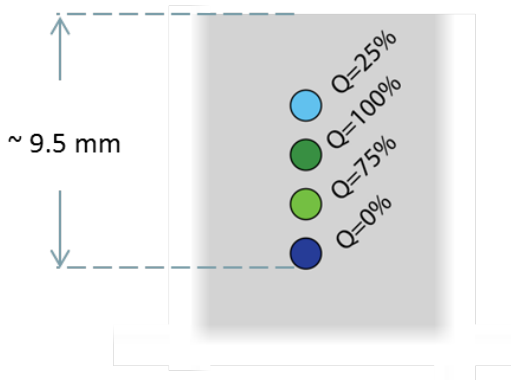

(a) Tube arrangement schematic

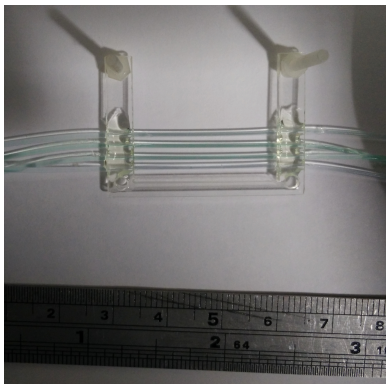

(b) Image of tube before submersion

Figure 10.2: *Overview of the PA tube phantom architecture. (a) Schematic of the tubes, filled with mixtures of $CuSO_4$ and $NiSO_4$, in a background of Intralipid and india ink. Indication of rough distance of bottom tube to the surface is given. Reproduced with permission from [273]; (b) Image of tube phantom before submersion.*

is introduced as an analogue for oxygen saturation, SO_2 (Q is similar to ratiometric parameter R used in Chapter 8). The composition breakdown is given in Table 10.1. The resulting absorption coefficient spectra of the four tubes are shown in Figure 10.1 (b), as measured by the dual-beam spectrophotometer. The absorption of the background is displayed in (b-c), having been computed as a joint contribution of water absorption [244] and india ink (mother batch solution M10b measured in spectrophotometer). Figure 10.1 (d) shows the measured reduced scattering characteristics of the background medium - obtained through total transmittance and reflectance measurements followed by application of the IAD method [222]. As for the tubes and their contents, they are largely non-scattering, which clashes with the DA assumptions, but given their dimensions it was considered to be acceptable to consider uniform background-level scattering in the model and in that way also bypass the DA violation. Figure 10.2 shows the relative tube arrangement and composition.

The placement of the phantom in the V-shaped scanner can be seen in Fig. 10.3. During imaging, the bath was covered with acetate film to minimise water evaporation (noticed in previous experiments to be non-negligible otherwise). The phantom was scanned over 12×16.2 mm on each sensor, at a step size of dx=dy=100 μm and a temporal resolution of dt=8 ns. The GWU Spectra-Physics OPO system was used for delivery of excitation light, with a pulse energy of ~19 mJ at 800 nm (at the distal end of the fibre) and PRF of 10 Hz. Length of acquisition per image was limited by the PRF and the number of scanned points - each image was acquired in approximately 33 minutes with a few additional minutes needed before for pre-tuning the FP sensor. The excitation source was positioned above the phantom. Data were acquired for 9 wavelengths: 750, 780, 810, 860, 910, 960, 1010, 1060 and 1110 nm plus the 1450 nm water peak acquisition to probe the surface. The characterisation of the beam profile was also done with the grid phantom placed on the medium surface and photoacoustically imaged at 800 nm. Unfortunately this last acquisition did not yield a clear cloud of points due to partial submersion. Initially, this was not judged to be too compromising since MIPs from preliminary reconstructions still looked appropriate. Nevertheless, when point cloud extraction was attempted in post-processing, it was actually concluded that reflections caused by this submersion impaired proper extraction. As such, the radius was instead based on previous estimates of beam diameter at an approximately similar height, measured on a scanner with a planar FP-sensor. The centre of the beam on the surface was still found with the grid data, with the source in the model then being placed depth-wise one mean inverse reduced scattering depth into the mesh domain as is standard practice when using the DA approximation.

Having acquired the data, the measured PA time-series were calibrated for incident fluence and FP pressure sensitivity, after which data from both sensors were co-registered into a common coordinate system, as discussed in Section 9.4.1. The data were then pre-processed (Section 9.4.2): the time-interval between 392-1192 ns for each time-series was used to define the baseline used for baseline correction; 15 MHz low-pass filtering

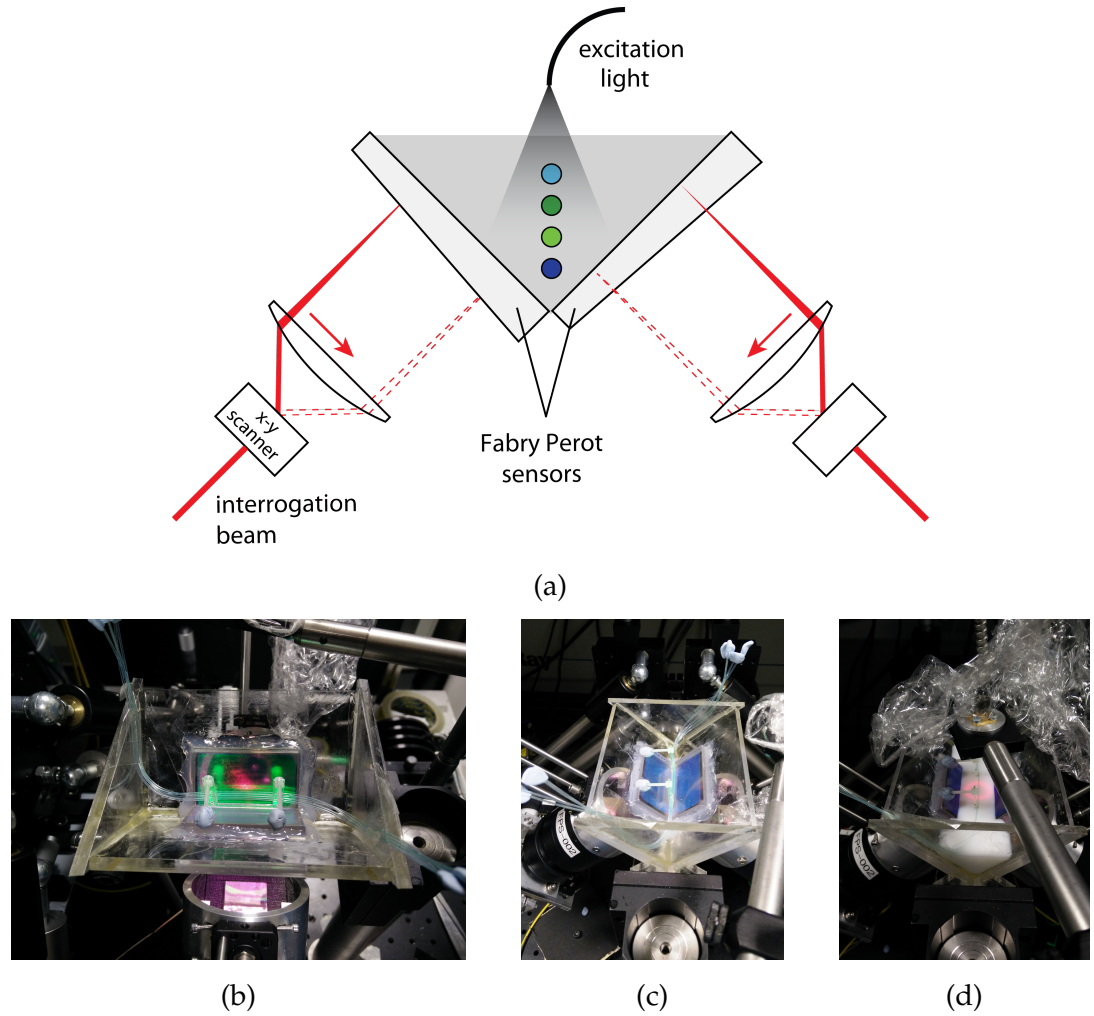

Figure 10.3: *Overview of phantom and its placement in the setup. (a) Schematic of experimental setup, in cross-section. Reproduced with permission from [273]; (b-d) Photo of tubes placed in the tray, in side view (b), front-view (c) and front-view where the background medium has been filled up to the top tube (not fully filled yet) and with the red guiding light coupled through the fibre on, to indicate the centre of illumination (its perimeter does not indicate true beam perimeter).*

was then employed; finally, removal of noisy channels was done by eliminating the 5% with the highest variance in the previously defined baseline (392-1192 ns). The iterative time-reversal scheme was employed and run for 20 iterations. The grid was upsampled two-fold, to obtain a $13.2 \times 17.9 \times 18$ mm^3 volumetric image of initial pressure with 50 μm voxel size, for each of the 9 wavelengths. Figure 10.4 shows the resulting initial pressure map for the 1060 nm acquisition. Tube structures are successfully recovered with minimal limited view artefacts - although some artefacts due to reflections from the tube are visible. Figure 10.5 shows the effect of applying either non-iterative or iterative time-reversal and also of reconstructing with only one sensor. Figure 10.6 highlights the spectral nature of the data by showing zoomed insets of a z-y cross-section at 3 wavelengths.

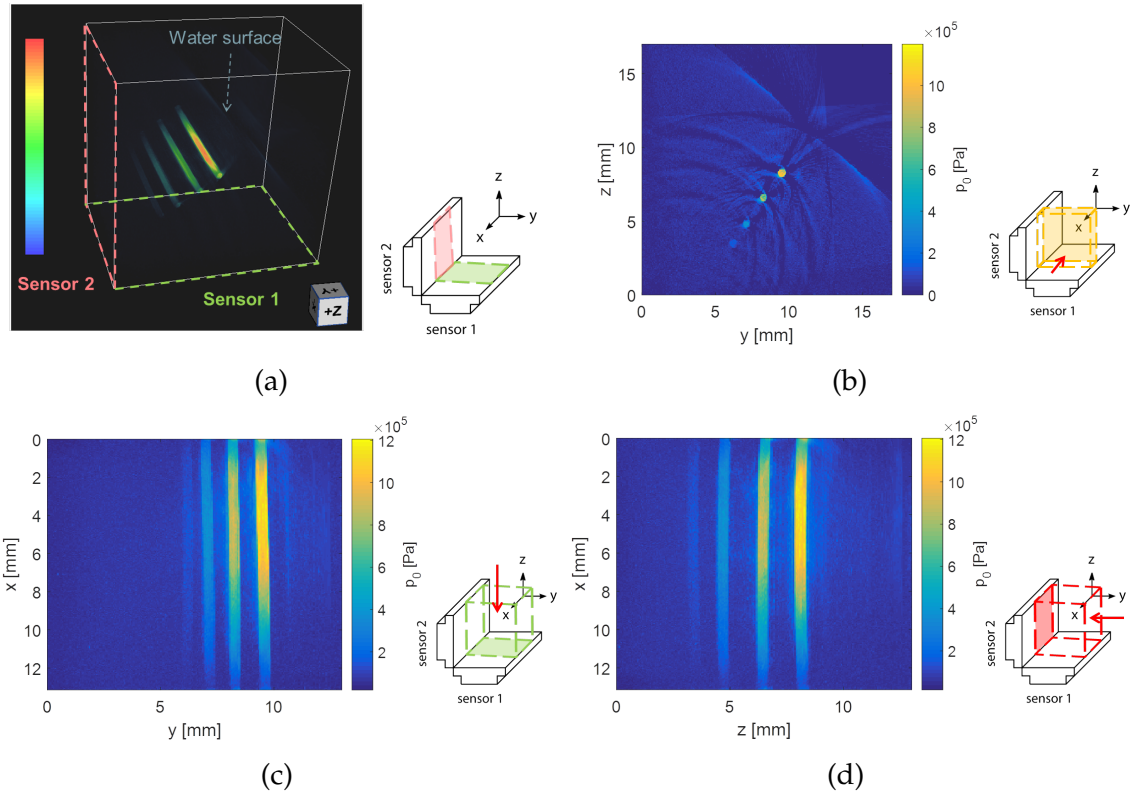

Figure 10.4: *Acoustic reconstruction at 1060 nm. (a) Volume rendering of the 13.2 × 17.9 × 18 mm³ volume. Pressure amplitude is colour encoded. 10% lowest values thresholded out. Opacity increases linearly. Colour-bar represents pressure for the range 0-1.207 MPa. Reproduced with permission from [273]; (b) MIP of the central 1 mm z-y cross-section - 17 × 17 mm² inset; (c) MIP of xoy plane (onto sensor 1); (d) MIP of x-z plane (onto sensor 2).*

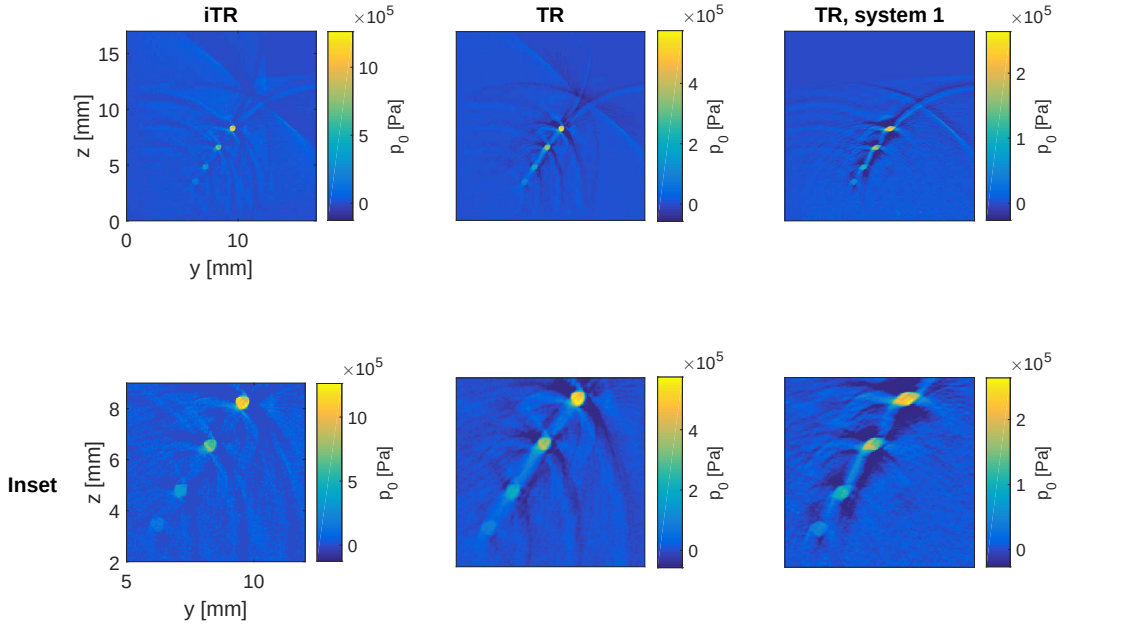

Figure 10.5: *Acoustic reconstruction at 1060 nm, comparing iterative time-reversal with 20 iterations (iTR) to non-iterative time-reversal (TR) and classic time-reversal done with only data from sensor 1 (TR, sys1). MIP of the central 1 mm z-y cross-section - 17 × 17 mm² inset shown on top row; 7 × 7 mm² inset shown in bottom row.*

Main Fine (Coarse) Inversion	
	Choices on physical parameters
Chromophore concentration	{water,india ink,$NiSO_4$,$CuSO_4$} - All unknown Fully resolved
Scatterer concentration	Known and Homogeneous (a=1) $^{\triangledown}$
Grüneisen	Unknown (function of chromophore concentration, $\Gamma(c) = c_{H_2O} + \beta_{NiSO_4} c_{NiSO_4} + \beta_{CuSO_4} c_{CuSO_4}$) Fully resolved
	Choices on the measured PA data
Scaling	Steps 1 and 2
	Choices on the light model
Light model	FEM Diffuse approximation
Mesh	Domain size: 8× 8× 10 mm Average size of tetrahedral elements: 100 (200) μm Number of nodes: 418490 (60247)
Source	Profile: Gaussian Radius: 3 mm $*$
	Choices on the cost function
Data fidelity term	Least-squares
Regularisation term	None
	Choices on the minimisation
Algorithm	L-BFGS with adjoint method for functional gradient calculation
Initialisation	{1, 1, 0, 0} i.e. True background values
Stopping criterion	400 iterations
	Computation details
Fine: ~12h (1673960 unknowns, 400 its) on an Intel Xeon CPU with 12 cores at 2.70 GHz, 256GB RAM	
Coarse: ~1h (240988 unknowns, 400 its)	

Table 10.2: *Overview of optical inversion algorithm for the Main Fine Inversion example (1673960 unknowns). The Main Coarse Example uses identical parameters but is carried out on the mesh with 200 µm average tetrahedral element size (240988 unknowns).*
$*$ radius defined to a realistic level based on planar FP sensor measurements of the beam, due to limitations in the grid phantom data for this experiment; $^{\triangledown}$ reduced scattering was always set to that of 1% w/v Intralipid throughout the whole domain, though in fact there is no Intralipid inside the tubes.

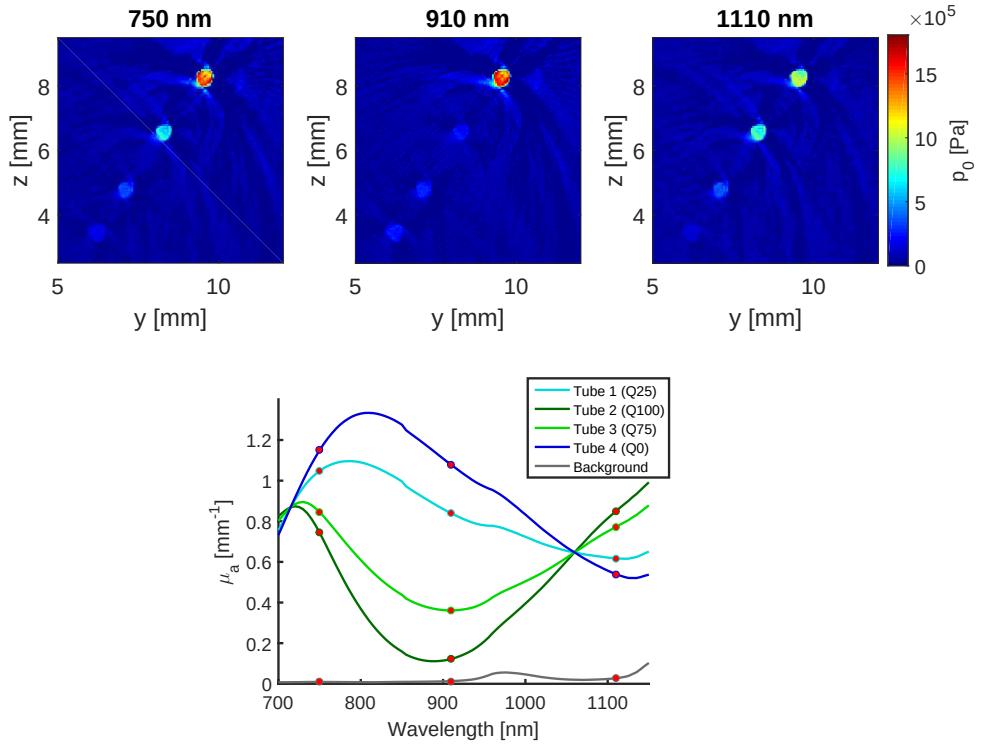

Figure 10.6: *Zoomed MIP of the central 1 mm z-y cross-section of the reconstructed PA data at 750, 910 and 1110 nm. Colour scale is equal for all. Some characteristics: in absolute terms, the top tube (Q25) at 1110 nm has weaker signal than at 750 and 910 nm - this is because the absorption of the solution is weaker here, and also because the background absorption is stronger. The bottom tube is clearly weakest at 1110 nm for the same reasons - absorption of Q0 (pure $CuSO_4$) is weakest at 1110 nm and background absorption is strongest. When looking at the relative absorption between the 2^{nd} tube compared to the 1^{st}, at 910 nm the 2^{nd} tube is much less prominent than at 750 or 1110 nm. This tube is filled with pure $NiSO_4$, which at 910 nm has very low absorption compared to the top tube. On the other hand, at 1110 nm the 2^{nd} tube has a more comparable signal to the 1^{st} one despite its greater depth since the stronger optical absorption at 1110 nm in the 2^{nd} tube (Q100) compared to the 1^{st} tube (Q25) counter-balances the attenuation with depth.*

Having obtained the multiwavelength images of initial pressure distribution, the model-based inversion framework described in the previous Chapter was employed for quantification. In the main example, the unknowns to be estimated were the spatial distributions $\mathbf{c}_k$ of the 4 chromophores of interest - water, india ink, $CuSO_4$ and $NiSO_4$. The sulphates are given in Molar whilst water and india ink are normalised such that the true concentration to be expected in the background is unity. The Grüneisen parameter is also set as unknown, but defined as a known function of concentration. The domain ROI was set as a cuboid region, 10 mm deep starting from the surface of the medium and with 8 x 8 mm lateral dimensions, aligned with the estimated centre of the beam. A mesh formed by tetrahedral elements was created, with a 100 μm average element size. This led to a total of 418490 nodes and a total number of unknowns of 1673960. The unknowns were initialised at the true background values and the minimisation was allowed to run for 400 iterations. Table 10.2 shows the overview of the choices made for the main quantification approach whose results will be shown in Section 10.2 (including

computation specifications). We will name this case the *Main Fine Inversion* throughout the Chapter. We will also refer to this same case reconstructed on the 200 μm average element size mesh as the *Main Coarse Inversion*. Throughout the Chapter we will discuss and display the effect of error in various parameters, the effect of different initialisations and also show the outcome of inversions with different model formulations. Usually these alterations will be done through departures from the *Main Fine* or *Coarse Inversions*.

10.2 Results of the quantitative inversion

Volume renderings of the chromophore distribution estimates for the *Main Fine Inversion* are shown in Figure 10.7 (a), normalised to the mean intensity of the tube with highest concentration. This visualisation shows the good agreement between the ground-truth and the estimate in terms of relative concentration. Similarly, Figure 10.7 (b) plots the normalised concentration averaged over each tube. For each tube, a selection mask is formed by all values within the central 4 mm length-wise and 150 μm diameter-wise (to avoid, respectively, model discrepancies expected close to the physical boundary of the ROI and mesh interpolation errors), from which mean and standard deviation estimates are computed. These are then represented as errorbars (labelled (c_k)) and overlaid on the expected value of normalised concentration in each tube (gray bars). The estimation procedure was able to correctly detect the presence of $NiSO_4$ in the top three tubes, and also found a low level of $NiSO_4$ in the bottom tube (low cross-talk/ false-positives). Furthermore, the comparison of colours in the tubes shows that there is good agreement in the relative concentrations, with the main deviations occurring for the third tube, over-estimated on average by a 0.098 offset. Similar trends are seen for $CuSO_4$ in terms of accurate detection, reduced cross-talk and relative inter-tube agreement. In this case, the main deviation was seen for the first tube, under-estimated on average by a 0.178 offset. Potential causes of discrepancy are discussed later on, but it is generally thought that the top tube is more affected by error on one hand due to falling more closely to the sub-diffusive regime and on the other due to being further away from the acoustic detectors and hence being more susceptible to limited view issues. Figure 10.7 (c) shows the outcome in terms of the ratio of absolute chromophore concentrations, Q (Equation 10.1). Estimates for the four tubes were 31.8±1.6, 97.5±1.1, 73.7±2.7 and 2.5±2.8 (mean±standard deviation of the point cloud), for ground-truth values of 25, 100, 75 and 0% respectively. The global relative error in the selection mask was 6.9% whilst the global mean absolute error was 3.4 p.p. (errors defined in Section 10.4). Despite the estimates in normalised concentration and chromophore concentration ratio agreeing reasonably with the true values, absolute estimates (concentrations in Molar) do not agree as well, with an overall overestimation in all cases - see Figure 10.8. Nevertheless, the extent of the absolute concentration overestimation is similar for $NiSO_4$ and $CuSO_4$ (a factor of about 1.5), which is why the ratiometric quantity Q still yields good results.

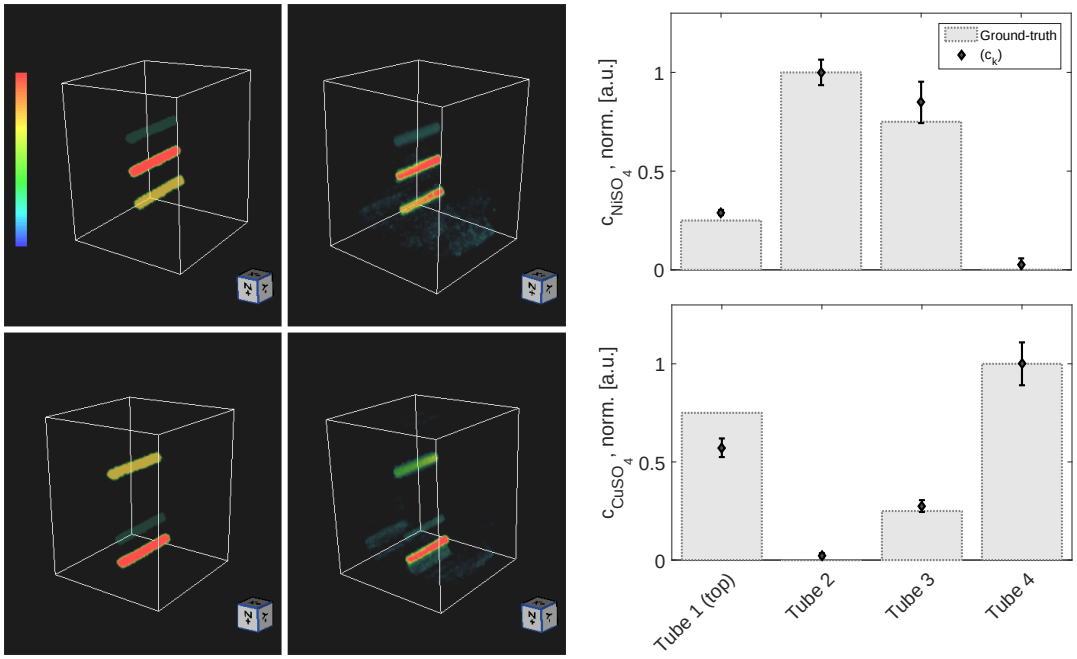

(a) (b)

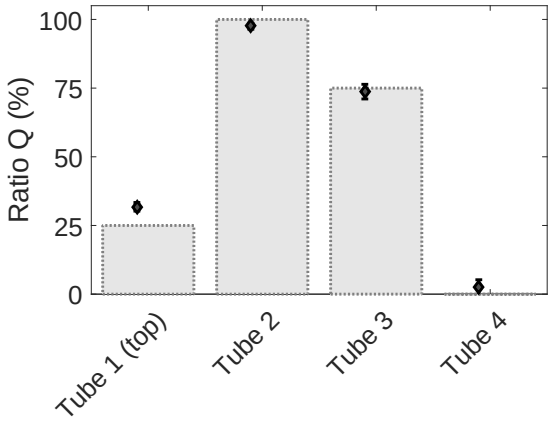

(c)

Figure 10.7: *(a-b) Comparison between true and (c_k) main fine inversion estimates of normalised concentration distributions of $NiSO_4$ (top row) and $CuSO_4$ (bottom rom), displayed as (a) volume rendering; (b) tube-by-tube metric. For the volume renderings, the colour-bar ranges between zero and one, where in each case one is matched to the mean intensity of the tube with highest concentration. The first column shows the ground-truth whilst the second shows the estimations. (c) Ground-truth for ratio Q(%) is compared to (c_k)-inversion outcomes. Values computed for the selection mask. Reproduced with permission from [273]*

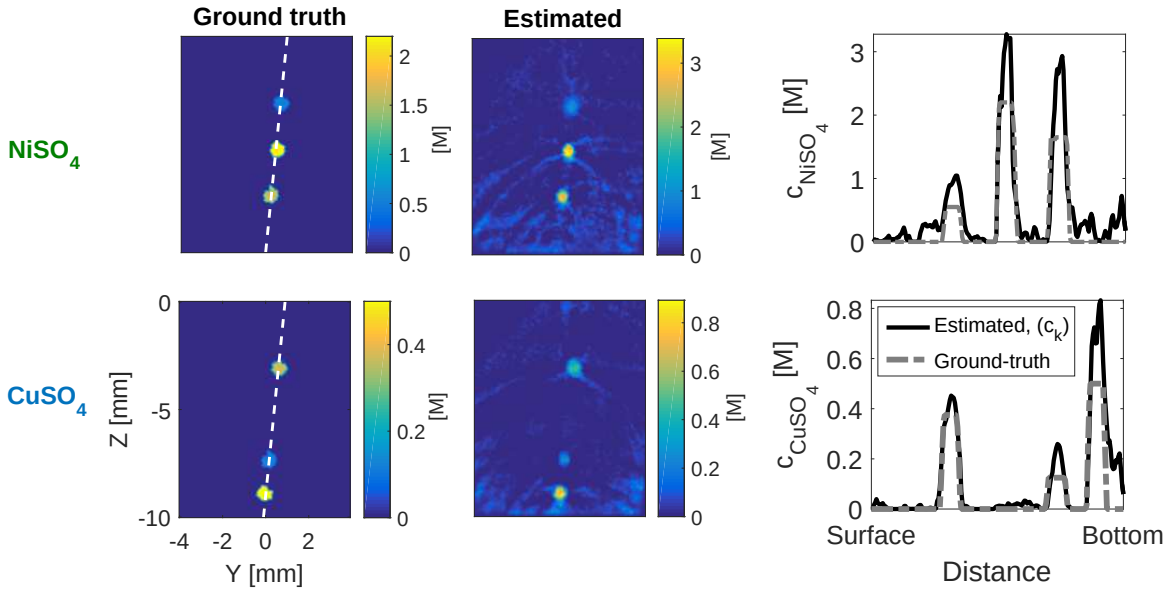

Figure 10.8: *Comparison of ground-truth and estimated absolute concentrations of $NiSO_4$ and $CuSO_4$. The left and middle columns display comparison through a central slice of the ROI. Colourmaps are adjusted to the maximum of each image. The right column plots depth profiles (along the white dashed line), highlighting that although relative concentrations are promising, absolute values are overestimated.*

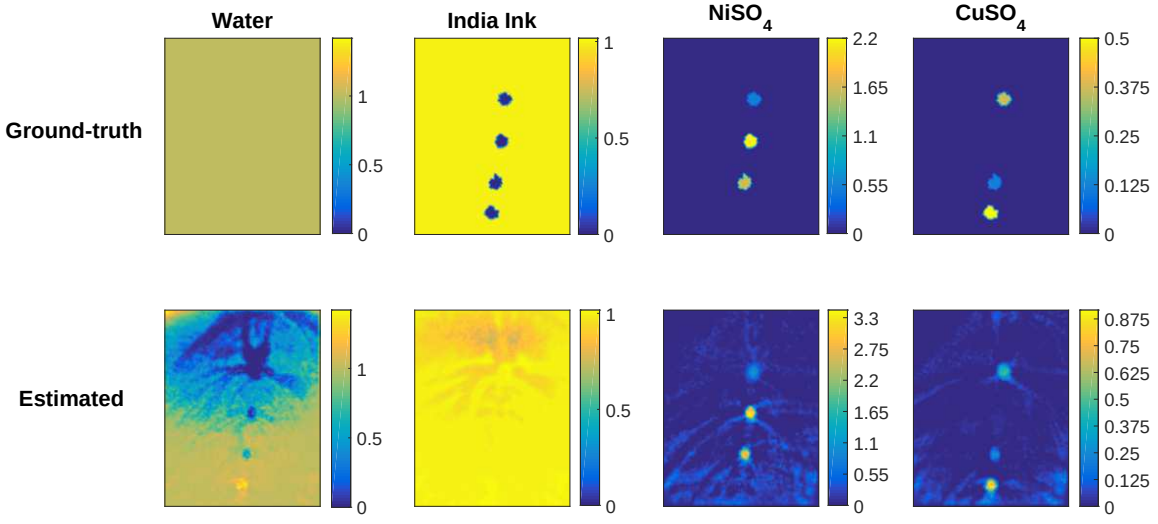

Figure 10.9: *Comparison of ground-truth and estimated absolute concentrations of the four chromophores, in terms of a central slice of the ROI. Colourmaps of the sulphates are adjusted to the maximum of each image. Colourmaps of water and india ink are matched to the overall maximum between ground-truth and estimated.*

Until now we have mainly shown $CuSO_4$ and $NiSO_4$ results even though inversion was done for all four chromophores - including water and india ink. Fig. 10.9 plots the outcome for all four chromophores. We can see that at depths greater than 5 mm, both india ink and water remain at the background ground-truth levels they were initialised with, but in the upper half of the domain there is a divergence towards very low (almost null) concentrations - this seems to indicate some discrepancy between measured and modelled absorbed energy density in that region, with water and india ink concentration unknowns being used to accommodate and cope with the discrepancies. This issue and its potential sources are discussed in Section 10.6. Another thing to note is that the inversion cannot pick up the absence of india ink inside the tubes, mainly leaving it at the background level of 1 it had been initialised with - this indicates weak sensitivity of the data to india ink concentration. This may be both because india ink has very weak wavelength dependence and also because it has low contribution towards overall absorption.

10.3 Adapting the problem formulation or its initialisation

One of the great advantages of MBI is their versatility and adaptability, which allows including different priors, assumptions, model formulations and initialisation choices. In this Section we will show outcomes from a selection of reasonable user-led adaptations in the formulation of the main MBI or on the initialisation choice.

Variable scaling factor to improve absolute quantification We have seen that despite the potential for relative quantification with the MBI scheme, there are still problems with absolute quantification. It was hypothesised that these were due to errors/uncertainty in the calibration of the data, i.e. in the set of operations that relate the raw measured time-series to meaningful units of pressure (Pa) per incident energy (in J). Note however that with our efforts (accounting for sensitivity, transduction mechanism, thermoelastic efficiency, pulse energy) we were able to bring the mismatch to what seems to be of about 50% overestimation - this would otherwise have been off by several orders of magnitude and we would also have no authority to claim images of pressure were given in pressure units or that they were given in respect to a Joule incident source. To try to address the remaining, acceptable to deal with mismatch, a new inversion procedure was devised, the so-called (c_k, K)-inversion, inverting for the previous unknowns but also for an additional calibration parameter K (a single scalar value) [36], which acts as a global scaling of the modeled p_0 in equation 9.3. That is, we let it be acknowledged in the model that the amplitude of the measured data may differ from the model by a factor. This idea also goes in line with the *a posteriori* observations of the previous example, where it seems that the chromophore concentrations, regardless of tube or $NiSO_4$ or $CuSO_4$, were approximately out by a similar factor.

This new strategy was run after 400 iterations of the *Main Coarse Inversion*, (c_k)-inversion, using its outcome as initialisation. The (c_k, K)-inversion was then applied to the latest estimate and only stopped when the infinity norm of the gradient hit machine-precision (in this case 1545 iterations). Due to the slow rate of convergence, all results were run on a coarser mesh, of average element size 200 μm. This mesh was formed by a total of 60936 nodes which leads to totalling 243744+1 unknowns considering the four chromophore scenario.

Figure 10.10 shows an improvement in estimates of absolute concentration with the (c_k, K)-inversion, compared to the (c_k)-inversion only. New estimates are promising especially for $CuSO_4$ content, with main deviations seen only for the 3rd tube. $NiSO_4$ content was still overestimated, but to a lesser extent. Estimates for the central slice are also shown in Fig. 10.11 - bottom row.

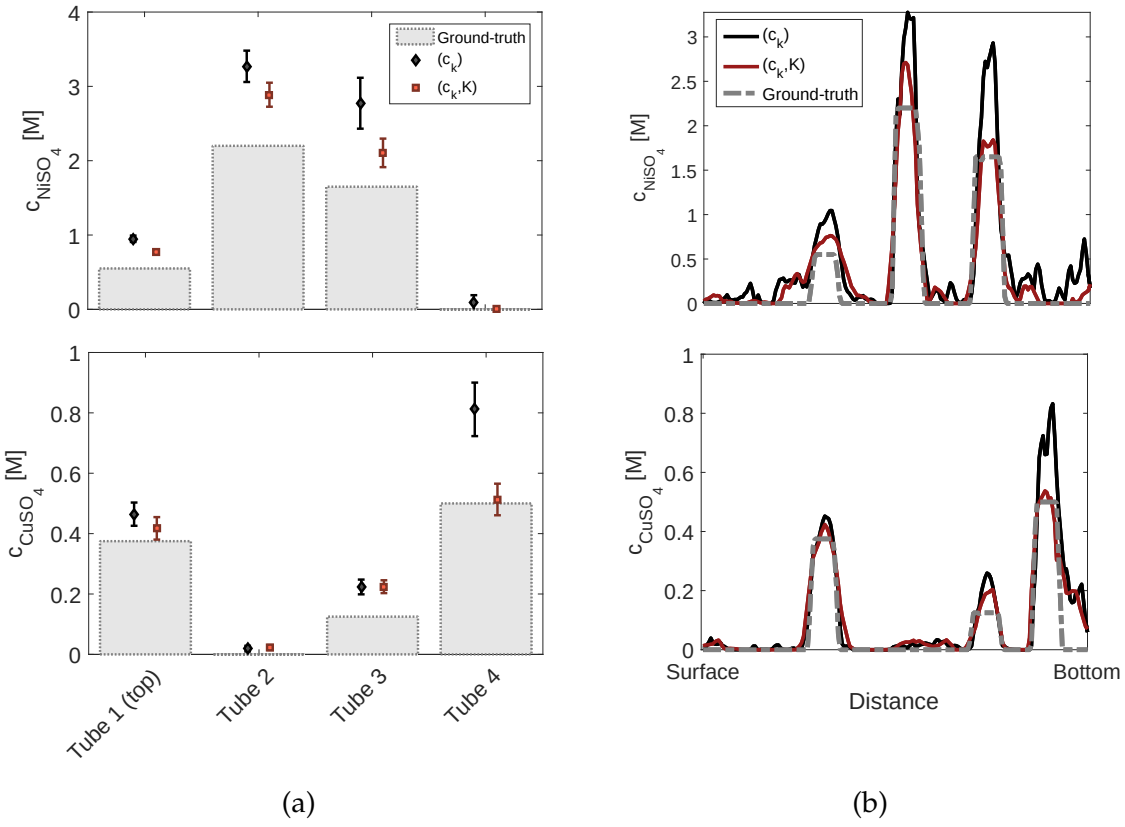

Figure 10.10: *Absolute chromophore concentration of $NiSO_4$ and $CuSO_4$. Ground-truth is compared to the Main Inversion, (c_k), and to the inversion with an added scalar actor K as unknown, (c_k, K). (a) Outcomes within the selection mask. Reproduced with permission from [273]. b) Profiles: The profiles are those defined in Fig. 10.8.*

Quantification with Tikhonov regularisation Another strategy that also improved absolute outcomes was when 1st order Tikhonov regularisation was employed in the algorithm.

Fig. 10.12 and 10.11 show the outcome of running 400 iterations of the MBI with

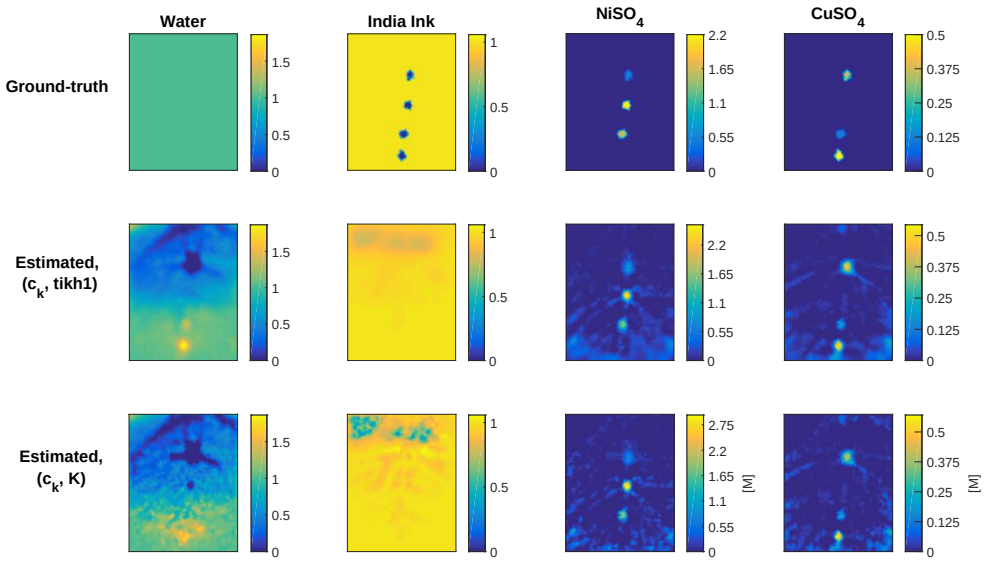

Figure 10.11: *Assessing the effect on absolute quantification of incorporating a scalar unknown in the inversion or of incorporating Tikhonov first order regularisation, $\beta_{tikh1} = 10^{-5}$. Run with all other parameters equal to Main Coarse Inversion. Ground-truth and estimated absolute concentrations are shown for a central slice of the ROI. Colourmaps of the sulphates are adjusted to the maximum of each image, expressed in Molar. Colourmaps of water and india ink are matched to the overall maximum among ground-truth and estimated images and are expressed relative to unitary concentration (background).*

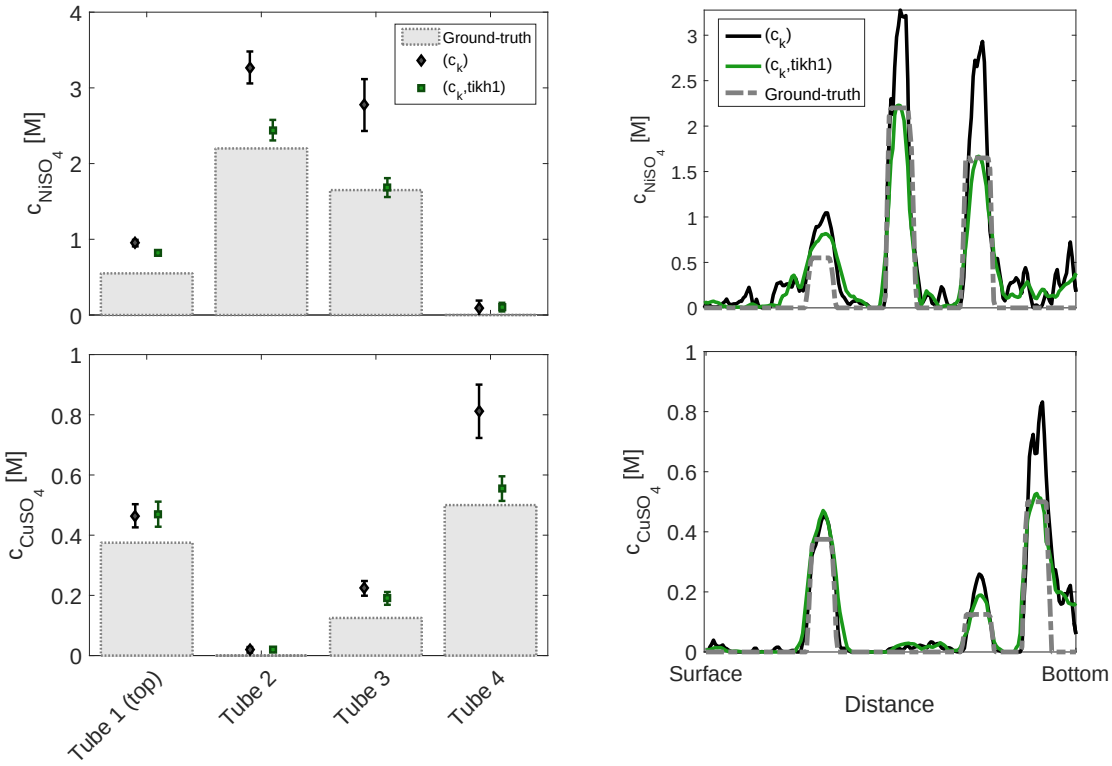

Figure 10.12: *Absolute chromophore concentration of $NiSO_4$ and $CuSO_4$. Ground-truth is compared to the Main Inversion, (c_k), and to the inversion with 1^{st} order Tikhonov regularisation, $(c_k, tikh1)$. The histograms show outcomes within the selection mask. The profiles are those defined in Fig. 10.8.*

this added regularisation term, with a weight factor of $\beta_{tikh1} = 10^{-5}$ (chosen for being the lowest order of magnitude leading to non-negligible change in behaviour relative to the no regularisation scenario). The initialisation was the background ground-truth. A clear improvement in quantitative agreement can be seen, to the point where estimates match or mimic closely the ground-truth (i.e. see similarity of colourbar range values in Fig. 10.11 and similarity of traces in Fig. 10.12). Further studies are needed to see if this approach is robust or of extensible use given that, despite the lowest possible yet still meaningful β_{tikh1} having been chosen, it is still not quite clear whether the improvement in absolute quantification was due to the merits of smoothness itself as prior knowledge or if it was a consequence of the dampening side-effect that occurs when regularisation is imposed too strongly. Namely, when inversions were run for $\beta_{tikh1} = 10^{-6}$ absolute estimated values were lowered further. A useful counter-example to study that would decouple dampening from robust increase in accuracy due to prior information would be to consider an experiment where the non-regularised MBI had underestimated the absolute values, and assess whether regularisation could improve (and thus necessarily increase) estimates.

Initialising from the ground-truth In simulation, initialising from the ground-truth gives an expected null error in the error functional. However, with experimental data this null evaluation does not occur and, by running the inversion, it was also observed that this point was not a minimum of the error landscape since the MBI could find directions of descent. After 200 iterations (Fig. 10.13), the algorithm seems to be updating estimates towards those seen in the Main Coarse and Fine Inversions (Fig. 10.9) - namely in terms of the dip in water estimates in the sub-surface region, the overestimation of water in the bottom tube and the overestimation of sulphates in all tubes.

Setting certain chromophores as fixed knowns Setting water (and eventually india ink) as fixed and known did not seem to help in achieving greater accuracy - relative spatial concentrations between tubes were not as accurate and also $NiSO_4$ and $CuSO_4$ were not off by the same factor (the former were overall underestimated whilst the latter overall overestimated) - Fig. 10.14. This greater mismatch might seem rather counter-intuitive as in theory, setting the background to its ground-truth and therefore having the fluence colouring fixed *a priori* to its true behaviour should help the inversion (in simulation this did indeed help towards the faster accurate convergence of the algorithm). In practice it is thought that by restricting the unknowns to solely $NiSO_4$ and $CuSO_4$ (and eventually india ink) with experimental data it also means that the only way the model can now accommodate for any source of uncertainty or error is by explaining it directly through unwarranted changes in the $NiSO_4$ and $CuSO_4$ estimates. Namely, the shortcomings in matching the background behaviour close to the surface (whether because of wrong fluence model, shortcomings in acoustic reconstruction or because of the unmodelled effect of the high-pass filter on the detector) can no longer be accommodated by altering

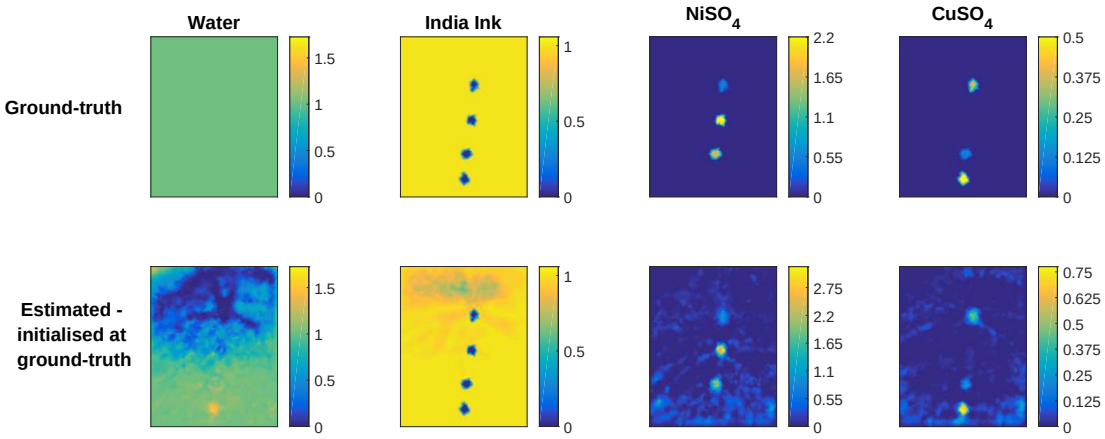

Figure 10.13: *Assessing the effect of initialising the MBI from the full ground-truth estimate, in experimental data. 200 iterations were used. Run with all other parameters equal to the Main Coarse Inversion. Ground-truth and estimated absolute concentrations are shown for a central slice of the ROI. Colourmaps of the sulphates are adjusted to the maximum of each image, expressed in Molar. Colourmaps of water and india ink are matched to the overall maximum among ground-truth and estimated images and are expressed relative to unitary concentration (background). Note how estimated amplitude ranges for each sulphate compound - seen in colourbars - are much more similar to the range for the ground-truth than in the case in Fig. 10.9.*

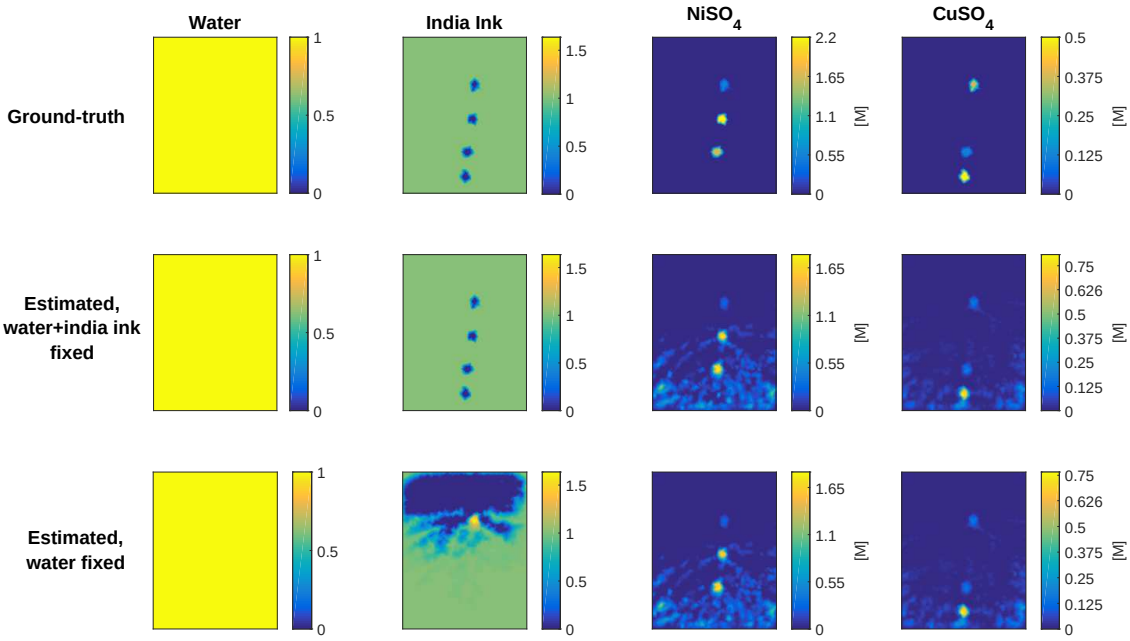

Figure 10.14: *Assessing the effect of fixing knowledge of different chromophores, in experimental data. Run with all other parameters equal to the Main Coarse Inversion. Ground-truth and estimated absolute concentrations are shown for a central slice of the ROI. Colourmaps of the sulphates are adjusted to the maximum of each image, expressed in Molar. Colourmaps of water and india ink are matched to the overall maximum among ground-truth and estimated images and are expressed relative to unitary concentration (background).*

the water concentration. When only water is fixed, we now see the estimated india ink distribution taking on this role - i.e. lowering its values in the upper region of the domain as much as possible. When both india ink and water are fixed, the model can only explain unexpected behaviour in experimental data through the sulphate distributions themselves but struggles to do so since concentration is already at its minimum in the background, leading to poor estimations.

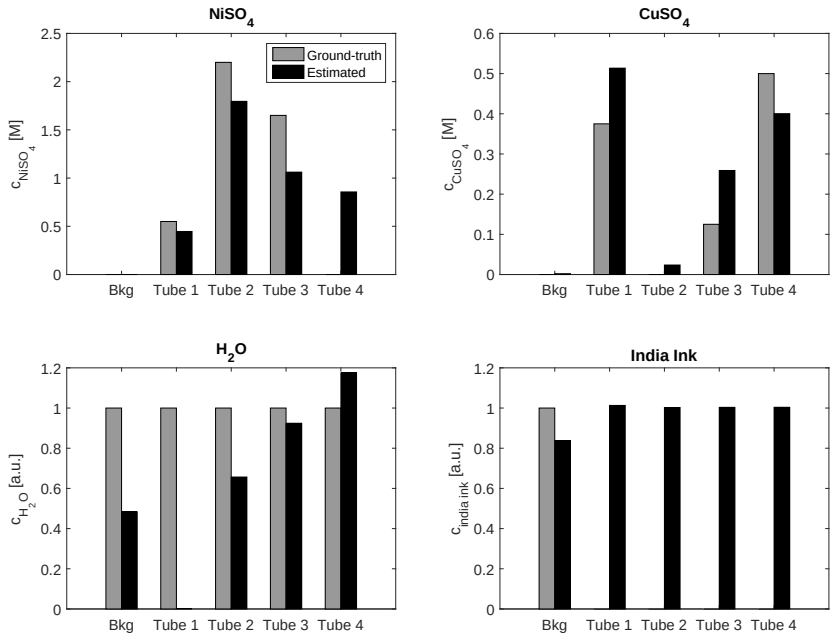

Figure 10.15: *Assessing the effect of enforcing piecewise constant regions in the experimental inversion - 5 regions were defined, for the 4 tubes and the background (bkg). Run with all other parameters equal to the Main Coarse Inversion but stopped after 118 iterations (convergence reached). Bars compare the outcomes in terms of absolute concentration between the MBI estimation and the ground-truth values of the 5 regions.*

Enforcing piecewise constancy In this example we show the effect of imposing piecewise constancy on the parameters to be estimated. Five regions were defined, one for each of the tubes and one for the background, based on a segmentation of the PA images. This meant that the inversion only had 20 unknowns (5 regions for 4 chromophores). In simulation this helped the inversion to converge quicker to the right solution. The outcome for experimental data is shown in Fig. 10.15 (run with similar parameters to the *Main Coarse Inversion* but imposing piecewise constancy as indicated). Relative inter-tube agreement for $NiSO_4$ and for $CuSO_4$ is not as good as for the main inversion studied and there is higher cross-talk (namely undesired $NiSO_4$ presence in tube 4). Important to note is that the estimation for the sole water background parameter is underestimated by ~50% and the sole india ink background parameter is underestimated by ~16% - probably to deal with the aforementioned model-data background discrepancies. This raises the hypothesis that for experimental data it may not always be preferable to enforce strict piecewise constancy even if it is known that the underlying structures respect that prop-

erty, since it also substantially decreases the degrees of freedom through which the model could accommodate for model-experiment mismatches/shortcomings.

Inverting for scatterer concentration In most of the inversions tested here, the reduced scattering coefficient was fixed based on experimental characterisation. A set of exploratory inversions were also run where, besides the unknown chromophore concentrations (of which optical absorption and Grüneisen parameter are a function of), the scatterer concentration was also set as unknown, albeit with known wavelength dependence Its gradient formulation is given in Eq. (9.15). This is somewhat similar to the MBI-($\mathbf{c}_k$, $\mathbf{a}$) formulation in Chapter 8, but in this case only a single scalar scatterer concentration value a was searched for the whole domain, instead of a spatial mapping (other differences being namely that in the previous case the Grüneisen was fixed and known and that simulations were in 2D). Inverting for scatterer concentration was done for a case with similar initial conditions as the *Main Coarse Inversion* and i) initialising at the background ground-truth; or ii) initialising from the outcome of the *Main Coarse Inversion*; or iii) initialising at the background ground-truth with an initial scatterer concentration overestimated by 20%. Overall, the trend seen was that parameter a was consistently being lowered in any of the inversions as much as it was allowed by the parameter bounds instead of converging to the correct value or stabilising at any other. In terms of the true scattering behaviour itself, this downward trend of parameter a in the MBI did not seem realistic since the characterisation of scattering done experimentally was of low uncertainty and also matched expectations from the literature. It was hypothesised that the decreasing trend in a was instead a collateral effect related to the data scaling issue, where lowering it performs a similar role to that of raising K in a MBI-(c_k, K) inversion (Section 10.3). I.e., in a similar way that raising K multiplies the modelled data by a factor, reducing the scalar mismatch to the experimental data, lowering a reduces attenuation, meaning that overall there will be higher fluence and higher initial pressure in the model, once more reducing the mismatch to the experimental data (this is a first order simplifcation since there will be more intricate wavelength and spatial effects when a is changed). The idea that an MBI-(c_k, a) strategy lowers a as a means to improve estimates of an underestimated model scaling would also be consistent with observations in Chapter 8 for the complementary/reverse case: when scatterer concentration a is fixed at an erroneously low value, the MBI-(c_k, K) strategy also improved estimates by lowering K in the inversion (Section 8.4.2).

10.4 Adapting experimental strategies

In this Section, we examine the performance of MBI estimation assuming that certain individual aspects could not have been so exhaustively and meticulously addressed beforehand to maximise accuracy but had instead been dealt with based on plausible

estimates or approaches that someone trained in PA could have reasonably made. The aim was to help illustrate which decisions, though reasonable, could affect the qPAT estimates most and to what extent. Cases assessed related to system calibration (normalising estimates instead of fully calibrating), acoustic reconstruction (assuming acquired data from planar sensors; reconstructing with commonly used non-iterative algorithms), thermoelastic efficiency (assuming a homogeneous, background tissue matched Γ) and light model input parameters (assuming the user had set reduced scattering or beam diameter to within a reasonable range from the true value, not having had ground-truth available). Table 10.3 shows comparison between cases where one aspect is altered relative to the *Main Coarse Inversion*, for the error metrics:

- Relative error in normalised concentration: $RE(c_k^{(norm)}) = \frac{\left\| c_{k,true}^{(norm)} - c_{k,est}^{(norm)} \right\|_2}{\left\| c_{k,true}^{(norm)} \right\|_2} \times 100\,(\%)$
- Relative error in ratiometric parameter: $RE(Q) = \frac{\|Q_{true} - Q_{est}\|_2}{\|Q_{true}\|_2} \times 100\,(\%)$
- Mean absolute error in ratiometric parameter: $MAE(Q) = \frac{\|Q_{true} - Q_{est}\|_1}{N_{mask}}$ (percentage points, p.p.)

where $c_{k,true}^{(norm)}$ is the true normalised concentration of the kth chromophore and $c_{k,est}^{(norm)}$ the estimated normalised concentration of that chromophore, where normalisation is done to the average of the brightest tube. Similarly, Q_{true} is the true ratiometric parameter and Q_{est} is the estimated one. $\|\,.\,\|_2$ is the euclidean norm and $\|\,.\,\|_1$ is the L1-norm. In all these metrics, only values within the *selection mask* are considered (N_{mask} is the number of points in the *selection mask*).

The default scenario (i.e. the scenario where no aspects or parameters were perturbed) yielded, according to the chosen metric, a 6.5% error for $NiSO_4$, 14.7% error for $CuSO_4$ and a 7.1% relative error for Q (mean absolute error of 3.7 percentage points). Alterations towards non-optimised scenarios mainly led to an increase in this error. Also, increases in erroneous concentration exceeded increases in erroneous ratio of chromophores Q.

Altered scattering or changing the radius estimate to half its initial estimate (both optical inputs) led to a small overall increase in error, but this was much less severe than the increase in error caused by sources of uncertainty in upstream stages of the inverse problem - i.e. those related to the acoustic reconstruction or thermoelastic efficiency. Fixing the Grüneisen to that of the background $\Gamma = \Gamma_{H_2O}$ led to large, though expected, errors. Likewise, normalising both modelled and experimental data to their maxima (applying the step 3 normalisation) by assuming lack of access to good acoustic pressure calibration also led to large errors. This approach should in theory have given a good calibration (and would have worked perfectly in simulation) but in experiment it was not successful - whether because of noise, model mismatch, compounded effect of other uncertainties.

High levels of error were also obtained for the alternative acoustic reconstruction approaches (non-iterative and/or in planar geometry), which are commonly used. Non-

Source of explicit uncertainty/error	$RE(c^{norm}_{NiSO_4})$	$RE(c^{norm}_{CuSO_4})$	$RE(Q)$	$MAE(Q)$
None (Main Coarse Inversion)	6.5%	14.7%	7.1%	3.7 p.p.
μ_s': 20% overestimation	7.4%	17.9%	6.2%	3.2 p.p.
Beam radius set to 1.5 mm	5.8%	17.2%	8.3%	4.2 p.p.
Grüneisen: $\Gamma = \Gamma_{H_2O}$	39.6%	48.3%	13.1%	6.0 p.p.
No acoustic pressure calibration (step 3 normalisation applied)	14.4%	20.8%	11.0%	5.2 p.p.
One-step (non-iterative) time reversal	26.5%	32.5%	20.7%	10.4 p.p.
One-step (non-iterative) time reversal: sensor 1 only	50.7%	54.6%	n.a.	n.a.
Simple linear inversion (no MBI)	38.1%	71.9%	23.5%	11.5 p.p.

Table 10.3: *Error in normalised $NiSO_4$ and $CuSO_4$ concentration and in ratiometric Q is compared between the default case and various scenarios where a given parameter or aspect is perturbed, whilst other parameters remain equal to the* Main Coarse Inversion. *Mean absolute error in Q is also shown.*
n.a. - not applicable (selection mask not appropriate for one sensor only reconstructions given the distortion in shape).

iterative time-reversal led to more than 4-fold and 2-fold increases in relative error in $NiSO_4$ and $CuSO_4$. The majority of this error is due to the ability of iterative time-reversal to correct for the partial detection surface and of its positivity constraint to avoid negative artefacts. In the more extreme limited-view scenario, where only data from sensor 1 was used for reconstruction (planar geometry), error were increased by almost 8-fold and 4-fold for estimation of $NiSO_4$ and $CuSO_4$ respectively, compared to the *Main Coarse Inversion*. Ratios could not properly be computed in the mask since the reconstructed features were in this case distorted. Fig. 10.16 better shows, through central cross-sections, the effect of using sub-optimal acoustic reconstructions as measured initial pressure data.

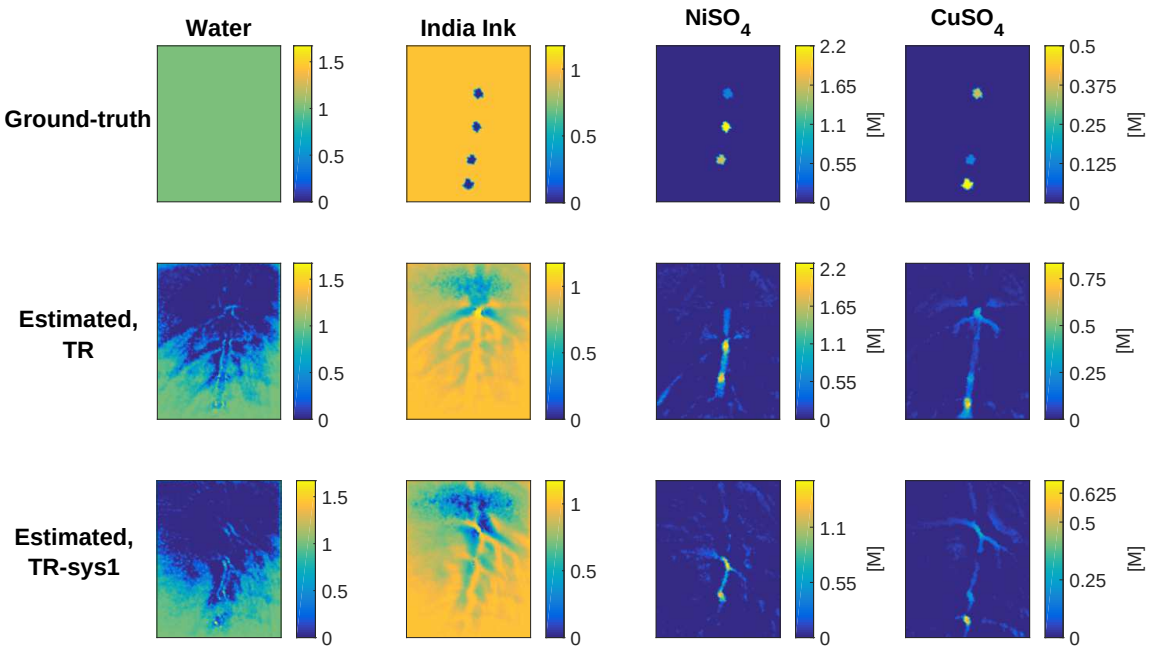

Figure 10.16: *Assessing visually the effect of applying the MBI to data that have been acoustically reconstructed with classic time-reversal, with both sensors (TR) and with only sensor 1 (TR-sys1). All other parameters equal to the* Main Fine Inversion *(100 μm resolution). Comparison of ground-truth and estimated absolute concentrations of the four chromophores, in terms of a central slice of the ROI. Colourmaps of the sulphates are adjusted to the maximum of each image, expressed in Molar. Colourmaps of water and india ink are matched to the overall maximum among ground-truth and estimated images and are expressed relative to unitary concentration (background).*

10.5 Sensitivity study in simulation

To have a more controlled understanding of the effect of uncertainties, a similar simulation study to that in Chapter 8 was conducted, but now with a phantom and characteristics analogous to the experimental scenario of this Chapter.

10.5.1 The Main Coarse Inversion in simulation

In the Main Coarse (and Fine) Inversion computations, the four chromophores were considered as unknowns, without any piecewise constancy restraints, and initialised at their expected background value: chromophores of interest $CuSO_4$ and $NiSO_4$ were initialised to 0 Molar, whilst water and india ink were initialised to 1 (since mother batch spectra of these were normalised accordingly). Fig. 10.17 shows the behaviour of this exact inversion in a simulation-only scenario (where the 'measured' pressure has been simulated with true parameters, by multiplying the true absorption and Grüneisen by the fluence outcome of Toast++ on the 3D cuboid mesh). From the outcomes, we can see that water has remained mostly stable at 1, indicating that the previous behaviour seen for water in experimental inversions is indeed related to discrepancies in model

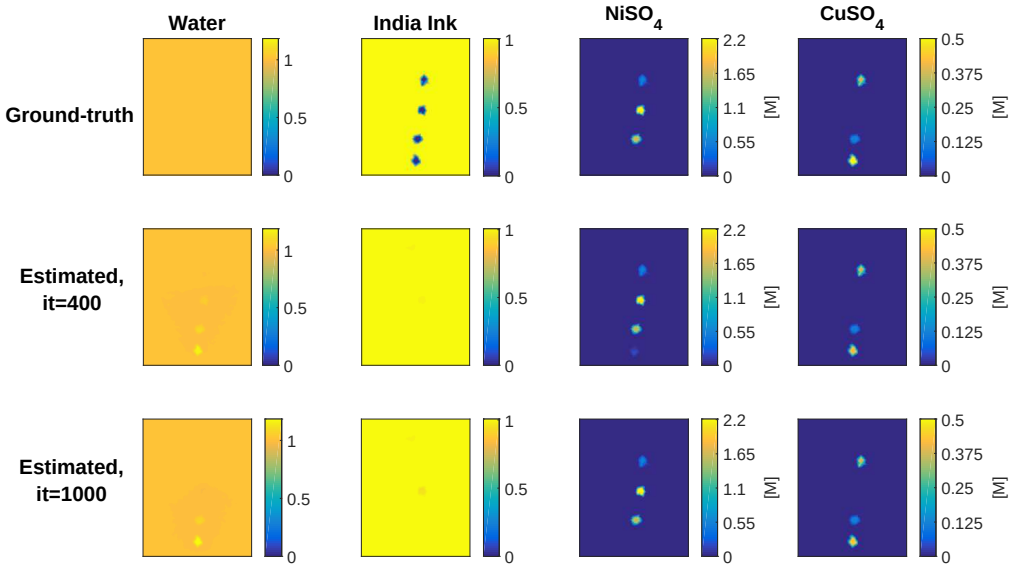

Figure 10.17: *Model-based inversion when run for simulated-only data, 200 µm mesh. Ground-truth and estimated absolute concentrations are shown for a central slice of the ROI. Results are shown both after 400 and 1000 iterations. Colourmaps of each of the chromophores are matched to the overall maximum among ground-truth and estimated images from the respective chromophore.*

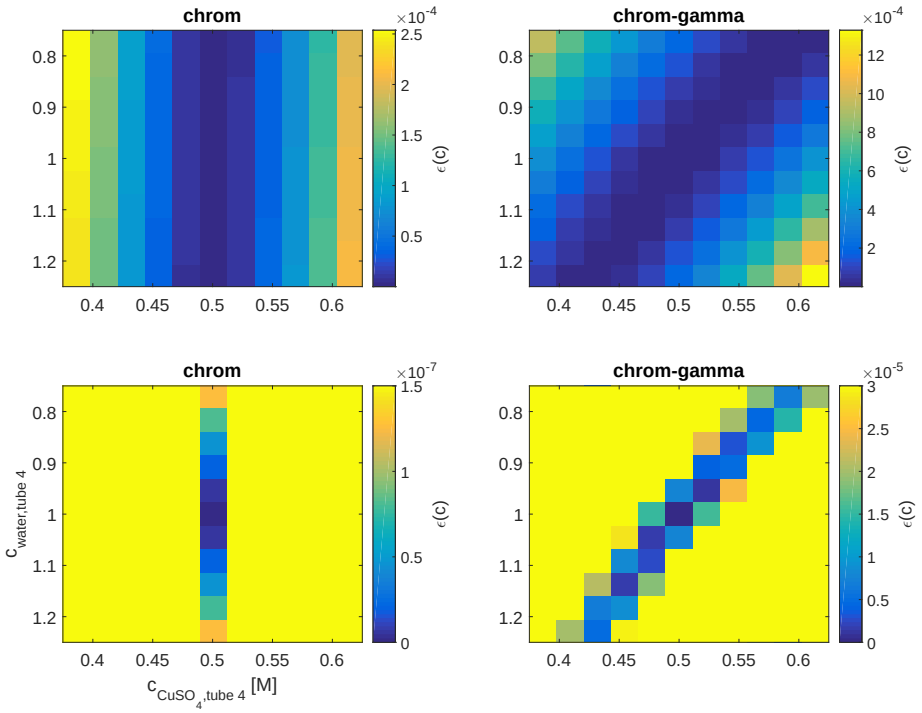

Figure 10.18: *Error functional landscapes, plotted versus the concentration of $CuSO_4$ and water in the bottom tube, with all other parameters set to ground-truth. chrom-gamma and chrom indicate respectively inversion with and without Grüneisen dependence on concentration, $\Gamma(\mathbf{c})$. Bottom row shows the same plots but with a different colour mapping, in order to highlight that chrom is convex whilst chrom-gamma has a local minimum at ~ (0.45,1.15) besides the global one at (0.5,1).*

and data. As for india ink, similar to the experimental case, in simulation the algorithm did not manage to reveal the absence of india ink in the tubes, - from the perspective of reducing the error functional, changes in india ink were probably too marginal in contribution to the change in error functional given its low concentration and spectral flatness. Estimations for $CuSO_4$ and $NiSO_4$ were mainly accurate after the 400 iterations, except for the bottom tube where $CuSO_4$ was ~10% underestimated and water was ~15% overestimated. This was found not to be a problem of convergence, as running the model for 1000 iterations gave similar outcomes, nor to be related to the lack of sensitivity of the algorithm to india ink, since when another inversion was run with fixed and known india ink this behaviour in the bottom tube was also seen (not shown). The behaviour of the error functional was therefore assessed. Fig. 10.18 shows the error functional landscapes for the concentration of $CuSO_4$ in the bottom tube versus the concentration of water in the bottom tube, $f(c_{tube4,CuSO_4}, c_{tube4,H_2O})$, with all other parameters and regions set to ground-truth. It was noted that including Grüneisen dependence on concentration in the model, as $\Gamma(\mathbf{c}) = c_{H_2O} + \beta_{NiSO_4} c_{NiSO_4} + \beta_{CuSO_4} c_{CuSO_4}$, affected the posedness of the problem: though there is still only one absolute minimum, $f(0.5, 1)$, indicating the problem is unique, there appeared to be a local minimum at $f(\sim 0.45, \sim 1.15)$, which happens to correspond to the point the inversion in Fig. 10.17 converged to. This did not occur for the case where the Grüneisen was fixed and known, i.e. where only the absorption had a dependence on concentration (*chrom*-inversion). For this case, only a single minimum was found, indicating convexity for these two parameters.

Further qPAT inversions in simulation showed that this problem could be avoided for other types of initialisation: e.g. setting water as fixed and known; or assuming known Γ dependence (*chrom*-inversion). Formulating the $\Gamma(\mathbf{c})$ function in different ways could also help posednesss - ultimately this formula is empirical and simplified, so there may be scope to alter it in a way that improves posedness whilst still being sound as a model of physical behaviour. Namely, it was found that formulating the dependence as $\Gamma(\mathbf{c}) = 1 + \beta_{NiSO_4} c_{NiSO_4} + \beta_{CuSO_4} c_{CuSO_4}$ (i.e. imposing unitary contribution of water to the Grüneisen, rather than setting it as a fraction of the water concentration) gave a much better behaved error landscape for the case above, which could be explored in the future. It should be noted that dealing with this posedness problem may not be peculiar to sulphates, as, for example, hemoglobin shows a similar type of Grüneisen dependence with concentration [112].

10.5.2 Sensitivity assessment

The sensitivity studies in simulation were carried out in an 'inverse crime' environment (equal domain resolution and models in forward and inverse computations and no added noise), to assess the exclusive effect of a given single perturbation on the inversion. The perturbations studied were errors in source diameter, in source position, in the reduced scattering coefficient and in accounting for thermoelastic efficiency. This would have been

burdensome, if not prohibitive, to do experimentally. Also, it would be very difficult to ensure true static behaviour of all conditions except one parameter. The inversion parameters were equal to those in the *Main Coarse Inversion*, with the exception that the chromophore water was considered fixed and known - meaning inversion was done for india ink, $NiSO_4$ and $CuSO_4$ - and run for 800 iterations for better convergence. The error metrics shown are those introduced in Section 10.4, in addition to the relative error in absolute (non-normalised) concentration, defined as:

- $RE(c_k) = \frac{||c_{k,true} - c_{k,est}||_2}{||c_{k,true}||_2} \times 100\,(\%)$

Another difference is that the errors in concentration take into account both $NiSO_4$ and $CuSO_4$ together instead of separately.

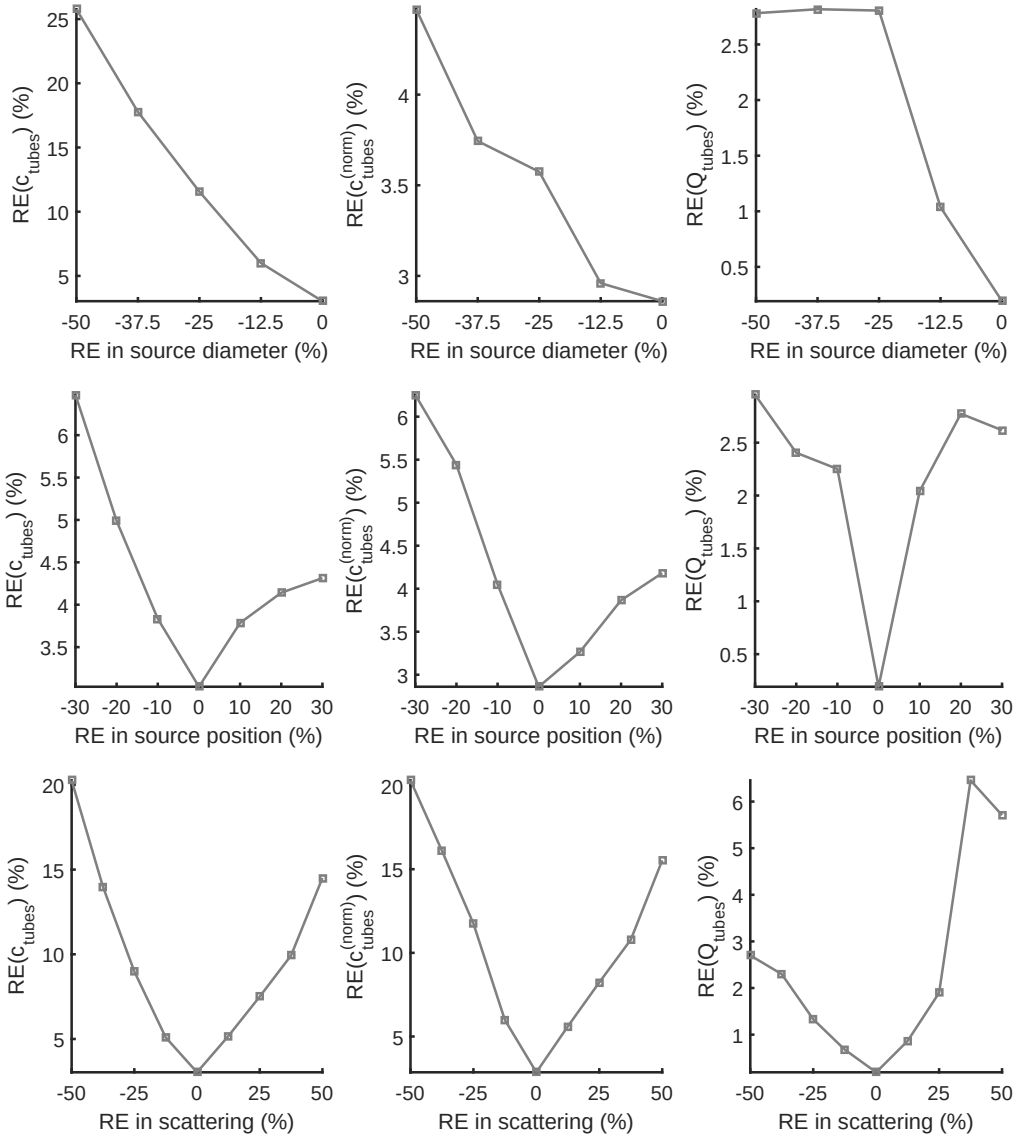

Figure 10.19: *Assessing in simulation-only the effect of uncertainties in individual parameters on the outcome of the MBI. Inversions were run for the simulation only case, it=800, with water fixed. All other conditions were equal to the Main Coarse Inversion.*

Fig. 10.19 shows the outcomes. Overall, these perturbations resulted in relatively small

errors in the ratiometric parameter Q_{tubes}. As for the concentration estimates, for the case of the beam position, displacement errors up to 30% of its diameter did not yield more than 7% error in either concentration or normalised concentration estimates. Errors in source diameter also did not severely affect normalised concentration (4.5% error when diameter has halved), but had a more prominent effect in absolute concentration estimates (25% error), though sublinear. This error in absolute quantification was not due to changes in total energy with source diameter, as the beam was normalised to unity for each case, but was likely related to the fact that a smaller diameter increased incident fluence near the centre of the domain, under which the tubes lie. Finally, reduced scattering under- and overestimation by 50% led to errors up to 15-20% in concentration (both normalised and non-normalised behaved similarly). Though the error is non-negligible, its behaviour is sub-linear, and 50% can be considered a quite harsh perturbation range, showing that reduced scattering behaviour may not always really be the main limiting step in qPAT studies despite the focus that has been placed on dealing with it in simulation studies.

An additional inversion was also run to assess the effect of disregarding the Grüneisen parameter behaviour (i.e. setting it fixed to Γ_{H_2O} instead of inverting for it), as in Table 10.3. As expected, for the non-normalised concentration, error was very large, $RE(c_{tubes})$ = 92.8%. Errors for normalised concentration and for the ratiometric parameter were much smaller but not inexistent - $RE(c_{tubes}^{(norm)})$ = 6.4%, $RE(Q)$ = 2.6%.

10.6 Considerations on the discrepancy in the background

Despite the promising results obtained for the concentration of the sulphates, there is still much room for improvement. One of the symptomatic outcomes that show that improvements are needed is the severe dip to low water concentrations in the region close to the top surface (where the source is). This indicates that there is a mismatch between the modelled and measured absorbed energy density. If the source(s) of this mismatch can be found, better quantitative outcomes can be achieved.

The light model One plausible cause of mismatch close to the surface is the fact that the diffuse approximation to the RTE was used as light model, which is known to be inaccurate in the sub-diffusive regime. An alternative would have been to run the inversion with a light model of higher accuracy in the ballistic and sub-diffusive regime, for instance the δ-Eddington approximation or the RTE [39, 163]. For reference, a δ-Eddington based MBI was implemented and run for the experimental data. The functional gradients specific to the δ-Eddington case were calculated using the adjoint-method [163]. Contrary to the previous case where the mesh could be unstructured, in this case the way the algorithm was implemented required the use of a structured mesh (in theory an unstructured mesh could be used for the δ-Eddington, but the implementation and calculation of the forward model and of the functional gradients would become much more complex). Fig. 10.20

shows results for such an inversion, with most parameters equal to the main DA case. The ROI was also the same, but a structured mesh was chosen with 8-noded regular voxel elements of side length 200 μm. Early results look promising but further work is needed. Regardless, given that the dip in background estimations is still observed this suggests that fluence model mismatch to experimental reality may not be the main issue.

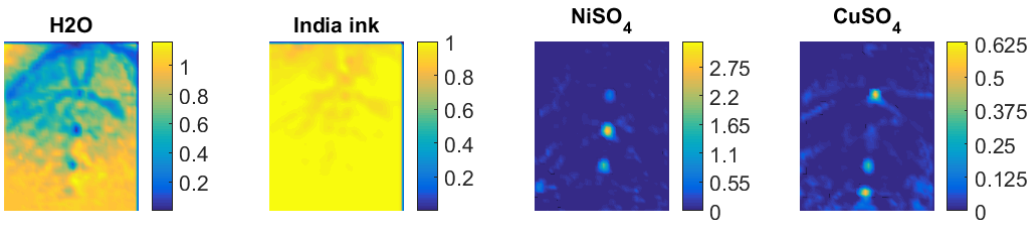

Figure 10.20: *Assessing the effect of using a MBI that incorporates the delta-Eddington approximation as fluence model, in experimental data. Run on 200 µm structured mesh for 283 iterations due to convergence. Run with all other parameters equal to Main Coarse Inversion Concentration maps shown for central slice of ROI. Sulphates expressed in Molar. Water and india ink expressed relative to unitary concentration (background ground-truth).*

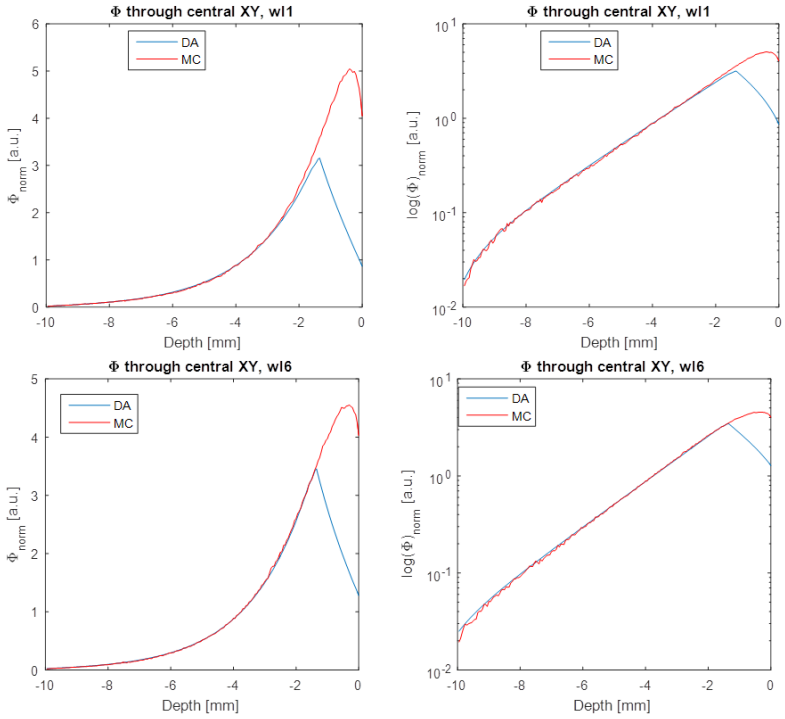

Figure 10.21: *Agreement between DA (Toast++) and MC (MCX) fluence for the cuboid ROI, with background optical properties throughout. Results are plotted as a profile depth-wise (Z=0 is the surface), from the central surface point, and normalised to a value sufficiently in depth. 750 nm (wl1) and 1060 nm (wl6) are shown, in linear and log scale.*

To investigate this further, forward Monte-Carlo simulations (MCX) were run for a medium composed solely by background, and the same was done for the DA with Toast++ (the source was placed one inverse reduced scattering depth into the domain as this ameliorates the correspondence of the DA at depth [67]). Beyond ~2.5 mm in depth agreement is satisfactory for all wavelengths imaged (Fig. 10.21 shows comparison for

profiles at 2 wavelengths). This gave indication that at least the tubes were placed in a valid region model-wise, though a large portion of the areas close to the illumination surface (upstream) were not. This discrepancy surely affected the algorithm, though not in a way that can explain specifically the observed dip in background chromophore estimations - partly because the depth to which water is erroneous is larger than the ~2.5 mm and most importantly because if anything, the DA model underestimates the superficial fluence level - an overestimation in modelled fluence would better explain the dip. Overall, it seems that the shortcomings of the DA approximation are not able to explain the effect.

Limitations in the acoustic reconstruction Another hypothesis for the mismatch is that there are some limitations in the acoustic reconstruction of the experimental data in the sub-surface region. Even though the acoustic detection procedure and reconstruction were chosen to give an image of p_0 as accurate as possible, especially where the tubes were located, some aspects can still be sub-optimal. As a first potential issue, it was observed through this work that, when using iTR reconstruction, points in the domain further from the sensors converge slower than those right next to the sensor(s), a phenomenon that was not known previously to occur in iTR. Namely, the intensity from the bottom tube will converge in fewer iterations than from the top tube, which in turn will converge quicker than the central area near the surface. It could therefore be that reconstruction in the sub-surface region (furthest from sensors) did not properly converge in the 20 iterations. More iterations could be run, but this could also promote over-fitting of noise and therefore worsening of the accurate reconstruction. As a second potential issue, the PA time-series used for reconstruction had been reduced in length to avoid mapping reflections of the water surface into the domain, which may have however compromised actual signals from points furthest away from any sensing points. These two hypotheses were tested in simulation in terms of their impact on quantification. New MBI were run where the input measured data had been reconstructed with longer time-series (10400 instead of 8000 ns) and also where 50 iterations of time-reversal were applied instead of 20. Using a longer-times series seemed to lead to improvement in the ratiometric parameter, but overall results were not conclusive (Table 10.4) (more studies needed to show significance).

A more prominent contributing factor to the mismatch may be the *de facto* still incomplete aperture. Though all tubes fell within the *visible region* as defined in Section 3.1.2, the water surface area actually did not in the strict sense since a wider scan in the upward direction of each sensor (up to the water surface level) was not possible due to instrumentation constraints. Despite this, the nature of the generated signal in that region means it is unlikely that the generated pressure will travel perpendicular to the surface and go fully undetected, meaning that in practice limited-view effects should be scarce. Related to this latter observation though, a second more believable factor contributing

Change to acoustic reconstruction routine	$RE(c^{norm}_{NiSO_4})$	$RE(c^{norm}_{CuSO_4})$	$RE(Q)$	$MAE(Q)$
None (*Main Coarse Inversion*)	6.5%	14.7%	7.1%	3.7 p.p.
Longer time-series	7.6 %	14.7%	6.0%	3.2 p.p.
Longer time-series, it=50	7.1%	14.6%	6.6%	3.5 p.p.

Table 10.4: *Error in normalised $NiSO_4$ and $CuSO_4$ concentration and in the ratiometric parameter Q is compared between the default case and cases computed with different acoustic reconstruction settings. All results computed on 200µm mesh, even the default case.*

to limited view and therefore sub-surface mismatch could be the gap between the two mapped sensor surfaces, since some wavefronts will travel directly towards this region (in a similar manner that the beam imprint at the water peak 1450 nm was affected). In future, system improvements could be implemented both to increase the scanning range and to reduce both physical and interrogation gaps between sensors.

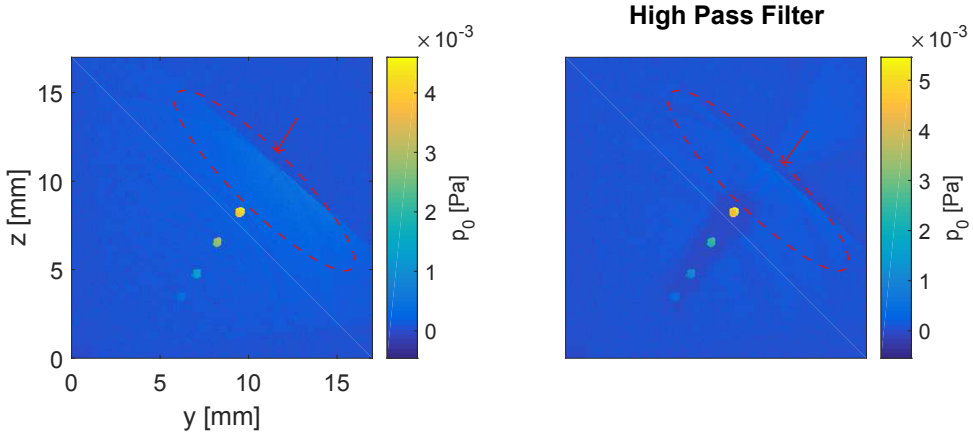

Figure 10.22: *Assessing the effect, in simulation, of the high-pass filter (300 kHz cut-off). A slice through initial pressure maps is shown. These maps were obtained by forward propagating the virtual data and then acoustically reconstructing the image. In the case with the filter, the simulated PA time-series were filtered before reconstruction. Simulations courtesy of Felix Lucka.*

The high pass filter Another factor possibly causing the mismatch is related to the 300 kHz high-pass filter incorporated in the measurement system to deal with baseline oscillations, as mentioned in Section 9.1. This filter has as negative side that some of the low-frequency content of the PA signals will also inevitably be filtered out. Given the smooth decay of the absorbed energy in the background, this area would be more likely to generate lower frequency acoustic waves and could therefore explain the issues seen in the MBI close to the source. Simulation studies seemed to confirm that filtering, more than light model or acoustic model reconstructions, probably caused the most prominent portion of the mismatch (e.g. Fig. 10.22).

Some ways to tackle this problem include designing systems that are more robust to low-frequency noise so the filter is no longer needed, or finding a compromise on the cut-off frequency by better assessing the level of high-pass filtering that is likely to only marginally affect PA signals based on their expected frequency content. An *a posteriori* approach is to incorporate the effect of high-pass filter (supposing its frequency and phase response is known) in the model. Namely, if a single-stage MBI is used this can be done efficiently through convolution of the sensor response with the modelled pressure time-series signals. Alternatively, if, like in this work, a two-stage approach is used where only the optical problem is modelled in the MBI, an analogous filter that operates on the spatial domain can be applied to the modelled mapping of the absorbed energy density. This will avoid the model mismatch that could otherwise throw the algorithm in unwanted directions to try to accommodate the discrepancy. As a potential downside, *a posteriori* model filtering may reduce the posedness of the problem, as some PA data will be missing.

10.7 Comparison with linear unmixing

Previous results focussed solely on model-based inversion approaches for quantification and compared them directly to the ground-truth. Here, we assess what would have been the outcome if simple linear unmixing had been applied instead since this is an approach recurrently and increasingly used in practical applications. Some concessions and adaptations are made due to the different nature of linear unmixing. First, linear unmixing was applied directly on the k-Wave grid (no interpolations). Also, the Grüneisen parameter was assumed known and compensated for *a priori*, since LU would have no way to estimate this in any case. Finally, since obtaining absolute concentration is not possible with linear unmixing, only comparisons of normalised concentration and ratiometric quantities were made.

The comparative performance is shown in Figure 10.23, both in terms of normalised concentration and of concentration ratio Q. LU performs especially poorly for chromophore estimation, which is expected given that no compensation is done for the fluence. In this case, the unaccounted decay of the fluence with depth, leading to spatial distortion, is no doubt the main cause of error (this is also clearly visible in the trend of extracted values with depth). LU performs more satisfatorily for the ratiometric quantity Q, given that some of the first order effects of the fluence on the two individual chromophore estimations will be similar and will therefore be partially cancelled out when the ratio is taken (e.g. some of the spatial decay). There is still error, both due to the linearisation of a non-linear problem and due to unaccounted spectral colouring. Figure 10.24 further shows the outcome of Q estimation, now for an inset of the central z-y slice in the ROI and the last row of Table 10.3 gives the computed global error metrics.

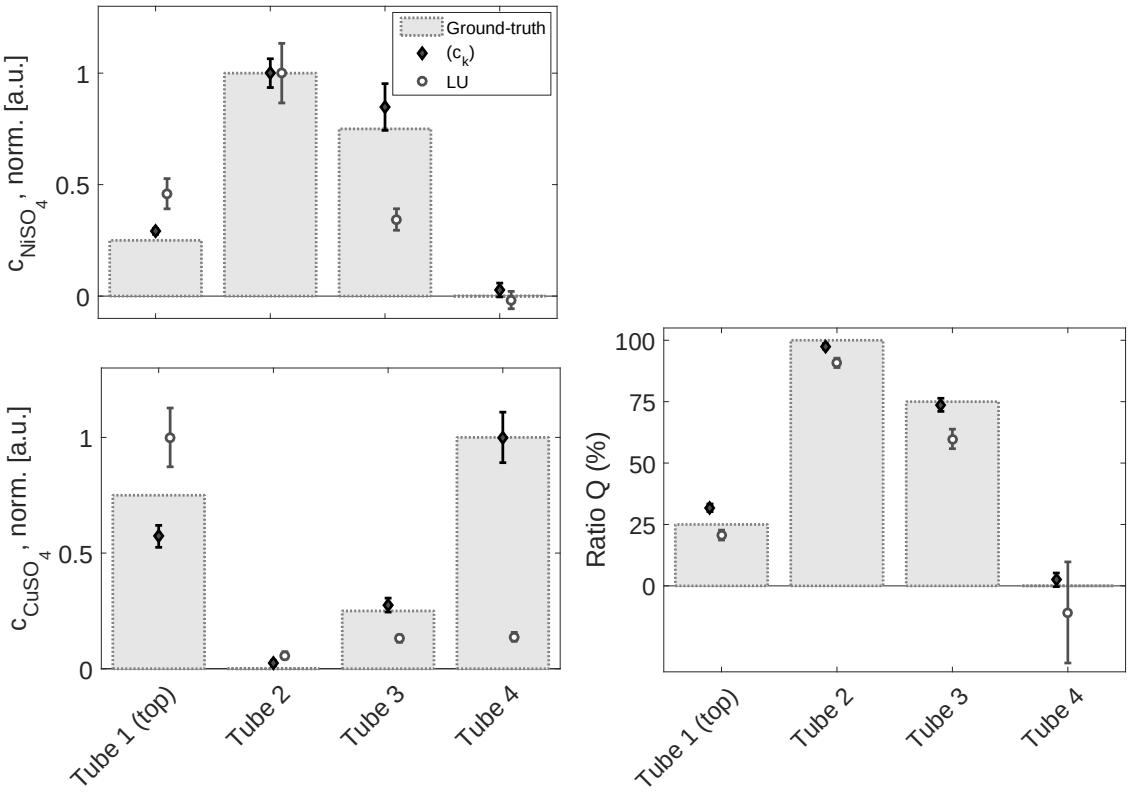

Figure 10.23: *Comparison between (c_k)-inversion and simple linear unmixing outcomes for (a) Normalised c_k estimations (normalisation to average of brightest tube); (b) Q estimation. Results are computed for the selection mask, with error bars showing standard deviation for voxel-wise estimations within.*

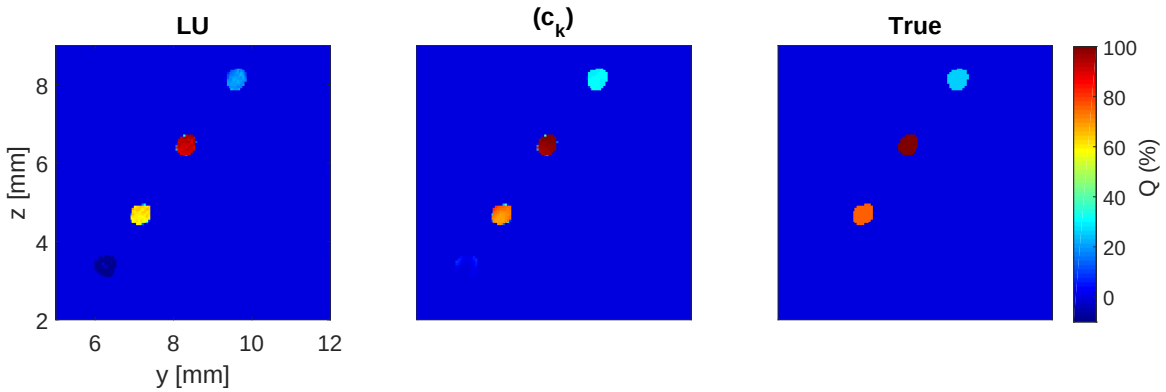

Figure 10.24: *Comparison between (c_k)-inversion and simple linear unmixing outcomes for Q estimation, as a visual representation. A detail from the central z-y slice (k-Wave ROI) is shown. Background is masked and set to zero. Colourbar has its range between -10% and 100% to show the presence of negative values in LU. Lower values were obtained, but are capped to -10% for better interpretation.*

10.8 Summary

The aim of the work was to obtain highly-resolved, volumetric mappings of chromophore distributions from PAT data, through the use of a model-based inversion scheme and the reduction and/or characterisation of all controllable uncertainty. A secondary aim was to inform on the main limiting steps, necessary improvements and future directions of research or re-engineering, both from a theoretical and experimental perspective that are necessary to improve accuracy, robustness and applicability.

• *Good estimates of normalised tube concentration and excellent agreement of the ratiometric parameter equivalent to oxygen saturation were attained.*

For the ratiometric quantity $Q(\%)$, which is analogous to the way the metric oxygen saturation is constructed, mean absolute error was 3.4 p.p. (3.7 p.p. for the coarse inversion). Considering datapoints up to one standard deviation of the mean estimate of each tube, absolute error in Q did not exceed 8.5 p.p. As for the individual chromophore distributions, promising estimates of normalised concentration of either $NiSO_4$ or $CuSO_4$ were attained. For many applications, retrieving the correct relative spatial distribution of individual chromophores will suffice rather than quantification in absolute units (e.g. in Molar or % v/v). For instance, in PAT images where a certain reporter gene is present and where one might want to know if certain regions of the domain have up-regulated expression compared to others and by what factor, or in PAT images where an exogenous biomarker has been introduced and where one might want to know if certain regions had a higher uptake or affinity to the marker.

• *Absolute quantification of chromophore concentration was overestimated by about 50% but can be improved by introducing a scaling factor in the inversion.*

In some cases, absolute quantification will be desired, e.g. when assessing both oxygen saturation SO_2 and total hemoglobin concentration c_{HbT} in a vascularised tumour region, or in any longitudinal or inter-subject studies that require a consistent concentration or absorption metric throughout the whole experiment. To improve the chances of absolute quantification, the experimental data had been calibrated both in terms of incident fluence and in terms of transduction, so that initial pressure distribution images could be expressed in known units of energy and pressure. Even so, in the inversion with these data, absolute estimates of both chromophores were overestimated by about 50%. This meant that further adjustments and improvements were still needed. On one hand, in future the calibration procedures can be improved. On the other, some MBI adaptations could be implemented to attempt to mitigate the errors. It was shown that including a scalar parameter in the inversion improved estimates to some extent. This is believed to have occurred mainly because having a scaling parameter in the model can explain errors in calibration of the experimental data. It could also potentially be that it absorbs some mean error in other inputs, as shown in Chapter 8. Equally, including Tikhonov regu-

larisation in the MBI improved absolute estimates considerably, showing great promise. More investigation would be needed to understand whether the improvement was legitimately due to the smooth nature of the data or if it was a side-effect of the dampening nature of these priors when imposed too strongly. Interestingly, normalising the data based on the ratio between the maximum of the experimental p_0 data and the maximum of the modelled ground-truth $p_{0,model}(c_{k,true})$, where $c_{k,true}$ is the ground-truth, worsened the calibration and subsequent inversion. Other compounded/entangled errors in the data or model description may have caused the lack of success. In any case, though this strategy should work perfectly in simulation and could in principle be successful in other phantom experiment attempts, the fact that it requires the use of prior knowledge of $c_{k,true}$, which is precisely what we want to invert for, means it is not suitable for use in most *in vivo* scenarios.

• *Problem formulations that improve accuracy or convergence in simulation by reducing the search space with* a priori *information may not necessarily bring improvements with experimental data.*

Some of the examples that we ran would, in purely simulated scenarios, improve speed of convergence and accuracy by reducing the parameter space: e.g. setting the distributions of some chromophores as fixed and known as the correct ground-truth, or imposing piecewise constancy on chromophore distributions based on features known to respect that condition. With the experimental data though, we saw that these inversions with legitimate *a priori* knowledge did not necessarily improve on the estimates. It seems that though on one hand the adaptations to the model add true information that should facilitate the search for the true solution, on the other the reduction in parameter space also means that the MBI has fewer degrees of freedom to cope with unexpected phenomena or sources of error. Since the experimental and modelled data are not perfectly matched (namely due to errors in calibration or in errors manifested in the sub-surface background disagreement), it may be that the negative impact of the mismatches on the inversion estimates is exacerbated in MBI with more restrictions. In future strategies, it may be interesting to still incorporate relevant prior knowledge in the MBI but to try to maintain degrees of freedom to cope with mismatches by introducing other variables specifically designed for this.

• *It is important to deal adequately with upstream stages (acoustic reconstruction, thermoelastic normalisation) of the full inverse problem.*

We have seen that incorporating a model of the fluence in the inversion has given promising estimates and evident improvements compared to naïve linear unmixing where spectral colouring and spatial distortion are disregarded (Section 10.7). We have also seen that having a good knowledge of the parameters in the optical inversion is important for accuracy (Section 10.5, 10.4). Above all though, MBI with experimental data have shown that commonly occurring or imposed limitations in upstream stages of the inverse problem (e.g. limited view, sub-optimal reconstruction method, incorrect thermoelastic efficiency description, incorrect calibration) have an especially prominent impact, more

than initially hypothesised and more than the uncertainty in optical model inputs (Section 10.4). This is relevant to note since most theoretical qPAT studies have focussed on the optical inverse problem due to it being inherently more challenging, assuming that the reconstructed pressure fields are perfect and that thermoelastic efficiency is fully known. Given that these assumptions are not that trivial to satisfy and that the effect of inaccuracies in these stages can be quite compromising, it is important that future strategies undergoing experimental translation focus more intently on obtaining better PA data, better reconstructions and better estimates of relevant acoustic and thermoelastic parameters or alternatively that they find more effective ways to mitigate the effect of these *a posteriori* or that they properly validate the scenario under study.

10.9 Future work

In terms of future work, first considerations will be given on the current experimental design, setup and phantom. One of the main priorities would be to, as discussed in the previous section, improve the agreement between model and data, namely to deal with the sub-surface background mismatch between model and data. In previous iterations of the experimental design, introducing the high-pass filters was necessary to ensure enough SNR without compromising dynamic range due to baseline oscillations. Since the high-pass filtering has a noticeable effect on the measured background data, the need and specifications of this filter could be revisited (possibly with a more optimised system the filters can be removed or its cut-off frequency lowered). It should be noted though that even without a filter module, the photodiode board will still have 50 kHz high pass filters in place.

Another aspect to tackle to reduce some of the mismatch may be to ensure that the phantom, including all the relevant background, is closer to the sensors and not so much at the edge of the visible region, so that iTR converges more quickly. This may be achieved through some minor system re-design since the current system did not allow wider scanning in the y direction due to a dichroic mirror in the interrogation path that could however be removed since backward-mode excitation is not being done. Some minor phantom re-design could instead be attempted to achieve further compaction, e.g. by using smaller tubes, by using a different relative arrangement of tubes or by employing a light model that does not preclude putting objects of interest in sub-surface regions. The current tube geometry was set in the most compact way possible but was limited by the ability to physically accommodate the four tubes in line and by the necessity to ensure enough depth from the surface for the DA to be valid.

From the perspective of the forward model employed, though it did not seem that using the DA as light model was a main source of concern for our experimental configuration, future versions could relatively easily upgrade to a delta-Eddington formulation if deemed necessary for other scenarios (e.g. where there is interest in sub-diffusive

regions). Uncertainties in reduced scattering or beam location were also not found to be prohibitive or the main limiting factors for proper quantification. The main forward model aspect that may be worth optimising in the model formulation is the size and extent of the domain. Currently a cuboid 8x8x10 mm^3 volume is considered which includes the surface and all tube structures and is contained in the physical phantom ROI. This brings improvements in speed and memory but one of the negative consequences is that the fluence is not modelled as well as desired close to the mesh boundaries [166], since the 1/e beam diameter, $6\times\sqrt{2}$ mm, is comparable to the lateral dimensions of the mesh, 8 mm. In the future, meshing the whole imaged physical domain may be of interest. A larger domain at equal resolution (100 or 200 μm) would require more efficient MBI implementations (possible through parallelisation, the use of more efficient system matrix inversion solvers, etc), though creating a mesh that is more coarsely defined for the background and more finely defined for the tubes can be designed to avoid excessive increases in dimensionality. An important additional advantage of such a fit-for-purpose mesh would be that the grid points of the acoustic reconstruction (k-Wave grid) could be set to match the node positions of the FEM mesh, bypassing interpolation. The current strategy uses a mesh that is a translated, rotated and more coarsely defined than the acoustic grid, so interpolation errors arise. A rough illustrative schematic of the current and suggested approaches is shown in Fig. 10.25.

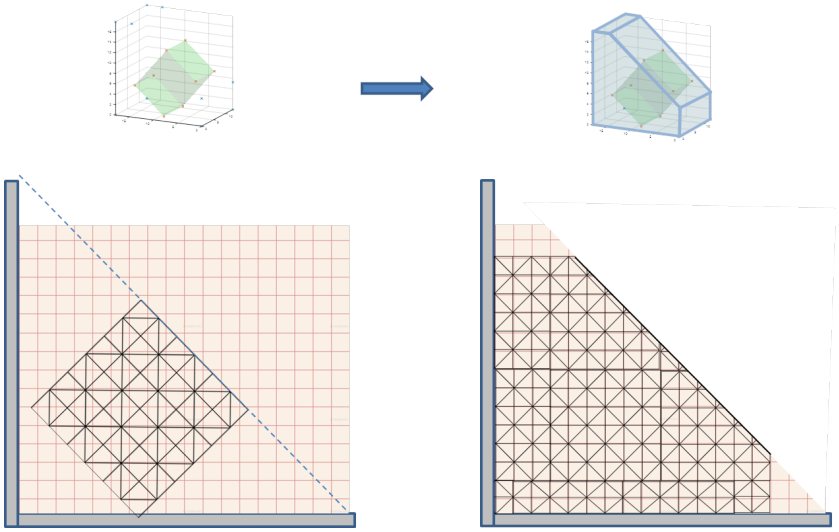

Figure 10.25: *Left - rough schematic of current mesh cross-section. Right - rough schematic of suggested mesh cross-section. Schematics are for illustrative purposes only. Pink - k-Wave grid; Black - suggested FEM mesh. Blue dashed line - water surface. Top shows current mesh ROI (green) vs full phantom ROI (blue).*

Some aspects could also be tackled to improve the overall qPAT strategy and posedness of the problem. One area of improvement is the posedness in the presence of unknown Grüneisen parameter - better but still realistic model formulations for the Grüneisen behaviour or additional regularisation terms could be investigated that reduce ill-posedness, or in alternative different minimisation strategies that can deal with local minima (e.g. genetic algorithms) could be implemented. Another avenue to investigate would be to

use more than one illumination position when acquiring and analysing the data. The current setup allows for illumination through the two FP sensors - backward illumination. Acquiring data from two consecutive illuminations (or three if the current forward illumination is used too) could help reduce ill-posedness introduced by the unknown Grüneisen parameter, or alternatively by the scattering behaviour if set as unknown [154]. This illumination arrangement was actually employed for *ex vivo* studies with this system [20] (though in tandem rather than consecutively). Some preliminary phantom acquisitions were also made during this qPAT project with these two backward illumination configurations in alternation, but more extensive research and optimisation would be needed for the procedure and data to be deemed satisfactory, namely more carefully dealing with the added complications exposed ahead. First of all, data acquisition time and data load doubles (triples), though the former could be sped up with newly developed OPO systems operating at up to 200 Hz PRF (compared to the current 10 Hz used) [274], which would increase speed by 20-fold. SNR of these systems may be a concern due to lower pulse energies, but more averaging could be employed in a way that would still be faster than the current total acquisition. Another issue to tackle is that excitation through the sensors required calibrating for transmittance through the sensors and also for total reflectance of the dichroic mirrors that redirect the light-path onto the sensors. Different illuminations also increased the number of sources of input uncertainty, though this may not be too compromising since we have shown that small variations in beam profile/position are not too damaging to quantification and also because obtaining a faithful profile of the beam on the sensor (with an appropriate absorber film) is easier than probing the beam at the water surface in its current arrangement. A more substantial system redevelopment that could promote the use of multiple illuminations and also an easier retrieval of the full acoustic field, would be to use a multi-view system (as opposed to the current two views), where e.g. a single FP sensor is mechanically rotated around the subject of interest and scans are done at N positions (N views) [275]. Illumination could be fixed at one or more locations during acquisition, or eventually made to move in tandem with the FP sensor, in which case single-step qPAT algorithms could be explored (Section 4.4).

Finally, having optimised the overall acquisition and inversion pipeline, it is important in terms of future work to assess quantification reproducibility by performing more phantom studies under different conditions - e.g. placing different solutions in the tubes, varying the background absorption, varying the general tube phantom geometry. Once this has successfully been achieved, more complex and tissue-realistic approaches can be attempted, namely by using solid phantoms such as PVCP that allow for more versatile architectures and higher levels of acoustic attenuation. Due to their long-term stability, these solid phantoms could then also be important for repeatability studies, inter-system comparisons and quality control of PA systems offering full quantification that are to be commercialised and used in the clinic.

It should be noted that the system we used was highly optimised - which for our

purposes, and the current level of intricacies and open questions in experimental qPAT, was intended and desired - but there is a clear acknowledgement that at some stage more flexible setup/prototype options would be necessary in experimental qPAT studies, in order to turn translation processes more agile, flexible and fast-changing.

Part IV

Conclusions

Chapter 11

Conclusions

The aim of this thesis was to achieve experimental quantification of chromophore concentrations and related quantities from photoacoustic tomography images, at high resolution and in 3D. Besides showing the feasibility of experimental qPAT in a well-controlled and optimised scenario, the aim was also to shed light on experimental hurdles that need to be dealt with, and implement or suggest strategies to overcome these, whether through adaptations to the sample/subject of interest, the setup, the acquisition settings or the algorithm employed. After giving an overview of the principles and applications of PAT , previously suggested quantification strategies were introduced and reviewed (Chapter 4). Afterwards, the need for tissue-realistic, stable and well-characterised experimental validation studies was highlighted, especially the need to develop appropriate phantoms and chromophores (Chapter 5). PVCP was studied as a prime phantom candidate for qPAT (Chapter 6) and aqueous solutions of $NiSO_4$ and $CuSO_4$ were assessed as adequate candidates for chromophores and blood surrogates (Chapter 7). This was followed by simulation studies assessing the effect that uncertainties in experimental inputs had on the accuracy of model-based inversions (Chapter 8). Performance comparisons were also made with slightly adapted model-based inversions and with conventional spectroscopic linear unmixing both with and without a 1D fluence correction. A full qPAT experiment was then devised that could rely on well-defined and stable ground-truth information from both the phantom, experimental settings and system characterisations, and progressively improved on (Chapter 9). All foreseeable sources of uncertainty were reduced as much as possible. Acoustic reconstruction and system geometry were chosen in order to give the best possible mapping of the initial pressure distribution. An efficient model-based inversion accounting for the fluence was then considered in order to be able to extract high-resolution, 3D and ideally absolute estimates of chromophore concentration. Results of the qPAT framework were shown and discussed, as well as various adapted versions of interest (Chapter 10).

11.1 Summary of outcomes on phantoms

PVCP, previously proposed for general purpose PA studies, was characterised extensively with qPAT applications in mind. Intrinsic optical absorption was found to be low and comparable to typical considerations for tissue background. Reduced scattering was negligible, but was successfully tuned to tissue-realistic ranges with titanium dioxide. Density was found to be comparable to water, whilst speed of sound was ~ 10% lower than most soft tissues (~ 5% for fatty tissues such as the breast), meaning that acoustic impedance relative to water was also mismatched by only ~ 10%. Acoustic attenuation at low frequencies was found to be comparable to soft tissue, but too high at increasing frequencies. Optical absorption was varied with three types of pigments. Though unique and interesting spectra were obtained that respect absorption linearity with species concentration, various results indicated there was lack of transient photostability when ns-pulsed high-peak power excitation (typical PA source) was employed. In terms of imaging, successful PAT images were obtained with scattering-rich PVCP samples with absorbing solid inclusions and also with wall-less hollow channels filled with stable absorbing solutions. Overall, PVCP was considered a good candidate. For future studies in PVCP, performing studies with other types of pigments would be useful as well as studying the use of increasing percentages of softener (plasticiser) to analyse to which point acoustic absorption could be tuned down into the upper soft tissue range.

The studies with PVCP and surveys of the wider literature on contrast agents and phantoms showed that finding suitable chromophores is more involved than expected - due to a range of issues such as transient and permanent photostability, relevancy of the spectral shapes, absorption linearity with concentration and behaviour when in mixtures with other chromophores and matrices. Having suitable chromophores is definitely the most important factor for qPAT studies, not only because they are the source of contrast but crucially because they are what we are trying to quantify, so the absence of suitable candidates is a considerable limiting step for qPAT validation. The focus was therefore reoriented from looking more broadly into matrix materials into looking first and foremost for compounds whose optical and thermoelastic properties behaved in a stable, reliable and interesting manner. A study of aqueous solutions of sulphate salts $NiSO_4$ and $CuSO_4$ showed that these compounds were good candidates as chromophores for qPAT studies, both in terms of their spectral shapes, achievable absorption levels, Grüneisen parameter behaviour and permanent and transient photostability. Preparing mixtures of these aqueous solutions with Intralipid, in order to achieve tissue-realistic scattering, also proved to be stable as long as an appropriate emulsifier was used. Their spectral shapes in the NIR window and the Grüneisen behaviour both in absolute value and in its dependence with concentration also indicated that $NiSO_4$ and $CuSO_4$ could be good candidates as oxy- and deoxyhemoglobin surrogates.

11.2 Summary of outcomes on model-based inversions in experiment

With the aim of obtaining resolved and volumetric estimations of chromophore distributions from experimental PAT data, a first priority was to assess the effect of expected uncertainties in typical model based inversion (MBI) input parameters - reduced scattering coefficient, beam position and diameter, and overall calibration (Chapter 8). Two 2D virtual phantoms were used. Despite reasonable levels of uncertainty, MBI strategies overall outperformed conventional spectroscopic linear unmixing (both with and without 1D fluence correction) when estimating oxygen saturation or analogous ratiometric parameters. The MBI also showed potential to be adapted to better cope with uncertainties - namely, including scatterer concentration as an unknown helped inversions with erroneous reduced scattering (though only partially, due to posedness). The inclusion of a scalar in the inversion also helped to avoid errors in concentration introduced by erroneous data calibration and, more unexpectedly, also reduced errors when uncertainties in other parameters (scattering, beam position and beam diameter) were introduced. Overall, it was concluded that MBI strategies would give more accurate estimates than simpler and quicker strategies such as conventional linear unmixing, even when considering the likely scenario that some model inputs will not be completely known in actual experiments.

Chapters 9 and 10 deal with the experimental framework adopted. An experimental system favouring PA signal acquisition with good bandwidth, sensitivity and omnidirectionality was adopted and the acquisition geometry was such that, together with an adequate iterative acoustic reconstruction, it could yield faithful maps of initial pressure distribution not affected significantly by limited-view. An efficient model-based minimisation accounting for fluence through the DA was employed to aim to retrieve chromophore concentrations and ratios from the initial pressure data. The phantoms - tubes filled with $NiSO_4$ and $CuSO_4$ solutions placed in an Intralipid-rich background - were chosen based on previous considerations, especially giving priority to the stability and tissue-realistic behaviour of optical properties, the access to thermoelastic behaviour and speed of sound, and a low acoustic attenuation for sufficient SNR.

The main qPAT inversion framework led to a mean absolute error in intra-tube Q estimation of 3.4-3.7 percentage points. Normalised individual chromophore concentrations were also promising, with relative errors of 6.5% and 14.7% for $NiSO_4$ and $CuSO_4$ distributions respectively. These results far outperformed linear inversion. Achieving absolute quantification of chromophore concentrations was not directly successful, with estimates being roughly 50% overestimated. It was however shown that adding a scalar factor or Tikhonov regularisation in the MBI helped towards better absolute outcomes. Some variations of the main inversion strategy were employed to further study behaviour - namely fixing certain individual chromophores as fixed and known or imposing piece-

wise constancy based on segmented regions. These did not improve on results as would have been the case in simulation - this was thought to be related to the unaccounted errors in the data or limitations of the model, whose impact worsened with the reduction in degrees of freedom in the MBI. Finally, the effect of various adaptations to the experimental pipeline, which might have been chosen by someone versed in PA but with no access to the ideal-scenario controlled ground-truth, were investigated. With experimental data, setting thermoelastic efficiency to reasonable background values, normalising all data or having acoustic reconstructions with limited-view led to errors that were significant, and more prominent than those caused by reasonable perturbations in direct optical inputs.

Overall, the study was successful in illustrating that full quantification is within reach in a well-controlled and designed experimental scenario. It also gave insights on experimental aspects that should be preferentially accommodated in qPAT frameworks and in informing future directions of improvement for the instrumentation, the acquisition settings and algorithm formulation of PAT technologies to be eventually used reliably in pre-clinical or clinical settings that aim to offer tools such as contrast agent quantification or oxygen saturation estimation

11.3 Outlook

In this work we aimed to perform an illustrative and controlled qPAT experiment in the best conditions possible and also to review, identify, characterise and/or tackle some of the challenges that have slowed down the experimental implementation of quantitative PAT strategies. Many areas would be worth tackling to further bridge the gap between theory and experiment and to ultimately enable pre-clinical and clinical widespread use. Opportunities for improvement are available from a wide range of perspectives: developing new and innovative quantification algorithms, using simulations in more versatile ways, creating and characterising new phantoms, acquiring more knowledge on systems and acquisition pipelines and changing the overall product/tool development cycle.

The product/tool development cycle Many of the efforts relevant to qPAT have been made in an isolated manner. On one hand, significant and varied advances have been made in multiwavelength PAT systems (from instrumentation to contrast agent development to data reconstruction and processing strategies). On the other, a large body of literature has tackled and optimised the quantification problem strictly in simulation. This has meant that main experimental qPAT efforts, like the ones in this thesis, are largely focussed on *bridging* the gap between successful qPAT theoretical strategies and already developed PAT systems. This involves performing assessments and adaptations to explain or accommodate unforeseen issues on both ends. From a product development and translation perspective, in the future, it would be beneficial and more efficient for

qPAT algorithms to be designed and adapted in tandem with system and acquisition developments since the initial stages of the product development, and to have both iteratively optimised during the process. Additionally, instead of developing qPAT strategies aiming for a one-size-fits-all holistic quantification approach, it seems that it would be more realistic to have qPAT equipments/tools be optimised for the application (subject, clinical intervention area and quantification metric) of interest, whilst guaranteeing the necessary robustness.

Creating and characterising new phantoms In the future, further solid materials besides PVCP that are considered for general-purpose PA should also be characterised and evaluated more extensively having qPAT applications in mind - i.e. according to the crucial conditions and criteria we have systematised in Section 5.3. This is essential for proof-of-concept, validation and re-engineering of qPAT strategies. Furthermore, once clinical translation of PAT systems starts being achieved, it will be important to have standardised and regulated quality and performance tests not only of traditional metrics such as uniformity, SNR, resolution, but also of parameters relevant to the multiwavelength nature of the data, since estimations of SO_2 and distributions of contrast agents will no doubt be of high interest to scientists and clinicians. Main areas of focus for multiwavelength qPAT solid phantoms seem to be the ability to find chromophores that are spectrally interesting and photostable as well as having access to the thermoelastic efficiency characteristics of the matrix and inclusions. The way the chromophores of interest interact with different solvents or matrices in which they are dispersed or dissolved into should also be considered carefully, not only in terms of feasibility of preparation, chemical stability and reproducibility, but also in terms of expected alterations in behaviour in terms of optical and thermoelastic properties. Given the interest of imaging complex structures at fine resolutions, considering materials that can be manipulated through manufacturing techniques that allow for detailed architectures should also be explored further (3D printing, laser cutting, milling and so on).

Having a better understanding of compounds, tissues and acquisition systems used for pre-clinical and clinical studies There are various areas worth exploring and characterising from the experimental perspective. For instance, pursuing better characterisation of typical thermoelastic efficiency characteristics of biological tissues and contrast agents (including their behaviour in mixtures, at different dilutions and with temperature). This is clearly challenging, which explains why the literature remains scarce [112, 140, 255], but necessary. Further characterisation studies should also be done on the kinetics and dynamic behaviour of photoswitching chromophores and on the transient stability of other chromophores, namely through pump-probe PA spectroscopy assessment [219], since these characteristics may be useful to be accounted for or exploited, either directly during PA acquisition or within MBI strategies. Finally, another area of focus would be to, for potential commercial systems, obtain co-variance matrices describing the uncertainty

characteristics of relevant system features. This information could be of use for weighing the relative severity of various sources of error or for propagating uncertainty.

Using theoretical and simulation studies in more versatile ways Simulations can play a crucial role in qPAT translation beyond its typical focus, which has been to deal first and foremost with the fundamental issues of non-linearity, posedness and spectral colouring in the optical inverse problem. Namely, computational studies are essential to:

1. Develop and optimise algorithms themselves.
2. Test sensitivity to expected experimental uncertainties [111].
3. Inform on better experimental design, e.g. assessing conditioning/convergence of MBI with realistic options of beam and detector positioning, *a priori* settings etc [155].
4. Re-design strategies, since what works in theory and simulation will not necessarily work in practice.

Developing and exploring new algorithms The following research areas are some that have been recently introduced in the field and that provide prospects for improving quantification in PAT that should be studied further:

- The inclusion of tools from machine-learning or statistics in the model-based inversions to improve the robustness and range of validity of MBI strategies. Examples attempted include having fluence explained as a linear combination of a reduced set of basis functions retrieved through PCA on large simulated datasets [178] or incorporating k-means clustering in the MBI to have optical properties classified as one out of an initially unknown set of tissues [170] but there is potential for various other approaches.
- The use of Bayesian strategies to ameliorate and account for uncertainty in various parameters [157]. Obtaining quantitative estimates that can cope with these uncertainties and deliver sound and reliable confidence intervals would be extremely beneficial for pre-clinical and clinical applications. Main foreseeable complications are the computational complexity (currently prohibitive for 3D, highly-resolved estimations) and the access to the relevant and trustworthy co-variance matrices to describe uncertainty from relevant sources.
- The use of MBI that also explore photoswitchable probe behaviour - the latter has been a growing trend in pre-clinical PAT with large advantages in suppressing background signal and isolating contrast from the probe of interest. Using these images within MBI strategies could ameliorate posedness of the inversion.
- The use of single-step MBI algorithms as opposed to two-step. This will bring

greater flexibility in the acquisition of data (namely dealing better with rotating sources and detectors), simplify regularisation and constraint imposition (namely total variation) and allow setting acoustic parameters as unknowns [41, 155, 172].

Bibliography

[1]J. Weber, P. C. Beard, and S. E. Bohndiek, "Contrast agents for molecular photoacoustic imaging", Nature Methods **13**, 639–650 (2016) (cit. on pp. 30, 42, 108).

[2]A. G. Bell, "On the production and reproduction of sound by light", Am. J. Sci. **20**, 305–324 (1880) (cit. on p. 30).

[3]D. Graham-Rowe, "Sounding out photons", Nature Photonics **3**, 123–125 (2009) (cit. on pp. 30, 34).

[4]P. Beard, "Biomedical Photoacoustic Imaging", Interface Focus **1**, 602–31 (2011) (cit. on pp. 30, 33, 34, 42, 43, 54, 55, 58–60, 111, 155).

[5]L. V. Wang and S. Hu, "Photoacoustic tomography: in vivo imaging from organelles to organs", Science (New York, N.Y.) **335**, 1458–1462 (2012) (cit. on pp. 30, 32, 34, 42–44, 54).

[6]V. Ntziachristos and D. Razansky, "Molecular imaging by means of multispectral optoacoustic tomography (MSOT).", Chemical Reviews **110**, 2783–94 (2010) (cit. on pp. 30, 31).

[7]S. Zackrisson, S. M. W. Y. van de Ven, and S. S. Gambhir, "Light In and Sound Out: Emerging Translational Strategies for Photoacoustic Imaging.", Cancer Research **74**, 979–1004 (2014) (cit. on pp. 30, 42).

[8]S. Mallidi, G. P. Luke, and S. Emelianov, "Photoacoustic imaging in cancer detection, diagnosis, and treatment guidance.", Trends in Biotechnology **29**, 213–221 (2011) (cit. on pp. 30, 45).

[9]M. Heijblom, D. Piras, M. Brinkhuis, J. C. G. van Hespen, F. M. van den Engh, M. van der Schaaf, J. M. Klaase, T. G. van Leeuwen, W. Steenbergen, and S. Manohar, "Photoacoustic image patterns of breast carcinoma and comparisons with Magnetic Resonance Imaging and vascular stained histopathology.", Scientific Reports **5**, 11778 (2015) (cit. on p. 30).

[10]Y. Zhou, W. Xing, K. I. Maslov, L. a. Cornelius, and L. V. Wang, "Handheld photoacoustic microscopy to detect melanoma depth in vivo.", Optics Letters **39**, 4731–4 (2014) (cit. on pp. 30, 41, 43).

[11]C. Lutzweiler, R. Meier, E. Rummeny, V. Ntziachristos, and D. Razansky, "Real-time optoacoustic tomography of indocyanine green perfusion and oxygenation parameters in human finger vasculature.", Optics Letters **39**, 4061–4 (2014) (cit. on pp. 30, 42).

[12]Y. Sun, E. Sobel, and H. Jiang, "Quantitative three-dimensional photoacoustic tomography of the finger joints: an in vivo study.", Journal of Biomedical Optics **14**, 064002 (2009) (cit. on pp. 30, 89, 90).

[13]A. Garcia-Uribe, T. N. Erpelding, A. Krumholz, H. Ke, K. Maslov, C. Appleton, J. a. Margenthaler, and L. V. Wang, "Dual-Modality Photoacoustic and Ultrasound Imaging System for Noninvasive Sentinel Lymph Node Detection in Patients with Breast Cancer.", Scientific Reports **5**, 15748 (2015) (cit. on pp. 30, 44).

[14]J. Yao, J. Xia, K. I. Maslov, M. Nasiriavanaki, V. Tsytsarev, A. V. Demchenko, and L. V. Wang, "Noninvasive photoacoustic computed tomography of mouse brain metabolism in vivo.", NeuroImage **64**, 257–66 (2013) (cit. on pp. 30, 41).

[15]S. Gottschalk, T. F. Fehm, X. L. Deán-Ben, and D. Razansky, "Noninvasive real-time visualization of multiple cerebral hemodynamic parameters in whole mouse brains using five-dimensional optoacoustic tomography.", Journal of Cerebral Blood Flow and Metabolism **35**, 531–5 (2015) (cit. on pp. 30, 71, 101).

[16]X. Wang, X. Xie, G. Ku, L. V. Wang, and G. Stoica, "Noninvasive imaging of hemoglobin concentration and oxygenation in the rat brain using high-resolution photoacoustic tomography.", Journal of Biomedical Optics **11**, 024015 (2006) (cit. on pp. 30, 71, 74, 104).

[17]C. Zhang, K. Maslov, and L. V. Wang, "Subwavelength-resolution label-free photoacoustic microscopy of optical absorption in vivo.", Optics Letters **35**, 3195–7 (2010) (cit. on p. 30).

[18]W. Liu and H. F. Zhang, "Photoacoustic imaging of the eye: A mini review", Photoacoustics **4**, 112–23 (2016) (cit. on p. 30).

[19]H.-P. Brecht, R. Su, M. Fronheiser, S. A. Ermilov, A. Conjusteau, and A. A. Oraevsky, "Whole-body three-dimensional optoacoustic tomography system for small animals", Journal of Biomedical Optics **14**, 064007-064007-8 (2009) (cit. on p. 30).

[20]R. Ellwood, O. Ogunlade, E. Zhang, P. Beard, and B. Cox, "Photoacoustic tomography using orthogonal Fabry – Pérot sensors", Journal of Biomedical Optics **22**, 041009–1–10 (2017) (cit. on pp. 30, 178, 179, 189, 190, 234).

[21]K. H. Song, E. W. Stein, J. Margenthaler, and L. V. Wang, "Noninvasive photoacoustic identification of sentinel lymph nodes containing methylene blue in vivo in a rat model", Journal of Biomedical Optics **13**, 054033 (2008) (cit. on p. 30).

[22]R. Li, E. Phillips, P. Wang, C. J. Goergen, and J.-X. Cheng, "Label-free in vivo imaging of peripheral nerve by multispectral photoacoustic tomography", Journal of Biophotonics **9**, 124–8 (2015) (cit. on pp. 30, 101).

[23]L. V. Wang and J. Yao, "A practical guide to photoacoustic tomography in the life sciences", Nature Methods **13**, 627–638 (2016) (cit. on p. 30).

[24]C. Kim, E. C. Cho, J. Chen, K. H. Song, L. Au, C. Favazza, Q. Zhang, C. M. Cobley, F. Gao, Y. Xia, and L. V. Wang, "In Vivo Molecular Photoacoustic Tomography of Melanomas Targeted by Bioconjugated Gold Nanocages", ACS Nano **4**, 4559–4564 (2010) (cit. on pp. 30, 42, 44).

[25]M. Nasiriavanaki, J. Xia, H. Wan, a. Q. Bauer, J. P. Culver, and L. V. Wang, "High-resolution photoacoustic tomography of resting-state functional connectivity in the mouse brain", Proceedings of the National Academy of Sciences **111**, 21–26 (2014) (cit. on pp. 30, 41).

[26]X. L. Deán-Ben, S. J. Ford, and D. Razansky, "High-frame rate four dimensional optoacoustic tomography enables visualization of cardiovascular dynamics and mouse heart perfusion.", Scientific Reports **5**, 13240 (2015) (cit. on pp. 30, 101).

[27]B. Wang, J. L. Su, J. Amirian, S. H. Litovsky, R. Smalling, and S. Emelianov, "Detection of lipid in atherosclerotic vessels using ultrasound-guided spectroscopic intravascular photoacoustic imaging.", Optics Express **18**, 4889–97 (2010) (cit. on pp. 30, 41).

[28]J. Laufer, P. Johnson, E. Zhang, B. Treeby, B. Cox, B. Pedley, and P. Beard, "In vivo preclinical photoacoustic imaging of tumor vasculature development and therapy", Journal of Biomedical Optics **17**, 056016–1 – 056016–8 (2012) (cit. on pp. 31, 41, 137, 139).

[29]L. V. Wang, "Tutorial on Photoacoustic Microscopy and Computed Tomography", IEEE Journal of Selected Topics in Quantum Electronics **14**, 171–179 (2008) (cit. on pp. 32, 51).

[30]J. Brunker and P. Beard, "Prospects for in vivo blood velocimetry using acoustic resolution photoacoustic Doppler", in Proceedings of spie, Vol. 9708, edited by A. A. Oraevsky and L. V. Wang (Mar. 2016), 97080R (cit. on p. 32).

[31]A. Sheinfeld, S. Gilead, and A. Eyal, "Simultaneous spatial and spectral mapping of flow using photoacoustic Doppler measurement", Journal of Biomedical Optics **15**, 066010 (2010) (cit. on p. 32).

[32]H. Ke, S. Tai, and L. V. Wang, "Photoacoustic thermography of tissue.", Journal of Biomedical Optics **19**, 026003 (2014) (cit. on p. 32).

[33]Y. Zhou, J. Yao, and L. V. Wang, "Tutorial on photoacoustic tomography", Journal of Biomedical Optics **21**, 061007 (2016) (cit. on pp. 33, 59).

[34]B. Cox, J. G. Laufer, S. R. Arridge, and P. C. Beard, "Quantitative spectroscopic photoacoustic imaging: a review", Journal of Biomedical Optics **17**, 061202 (2012) (cit. on pp. 35, 36, 39, 111, 159, 162).

[35]J. Laufer, D. Delpy, C. Elwell, and P. Beard, "Quantitative spatially resolved measurement of tissue chromophore concentrations using photoacoustic spectroscopy : application to the measurement of blood oxygenation and haemoglobin concentration", Physics in Medicine and Biology **52**, 141–168 (2007) (cit. on pp. 35, 71, 85, 86, 90, 91, 104).

[36]J. Laufer, B. Cox, E. Zhang, and P. Beard, "Quantitative determination of chromophore concentrations from 2D photoacoustic images using a nonlinear model-based inversion scheme.", Applied Optics **49**, 1219–33 (2010) (cit. on pp. 35, 67, 85, 86, 90, 92, 104, 211).

[37]F. M. Brochu, J. Brunker, J. Joseph, M. R. Tomaszewski, S. Morscher, and S. E. Bohndiek, "Towards Quantitative Evaluation of Tissue Absorption Coefficients Using Light Flu-

ence Correction in Optoacoustic Tomography", IEEE Transactions on Medical Imaging **36**, 322–331 (2017) (cit. on pp. 35, 67, 93).

[38]B. T. Cox, S. R. Arridge, and P. C. Beard, "Estimating chromophore distributions from multiwavelength photoacoustic images.", Journal of the Optical Society of America A **26**, 443–455 (2009) (cit. on pp. 36, 65, 84, 85, 87).

[39]T. Saratoon, T. Tarvainen, B. T. Cox, and S. R. Arridge, "A gradient-based method for quantitative photoacoustic tomography using the radiative transfer equation", Inverse Problems **29**, 075006 (2013) (cit. on pp. 36, 86, 159, 224).

[40]T. Tarvainen, B. T. Cox, J. P. Kaipio, and S. R. Arridge, "Reconstructing absorption and scattering distributions in quantitative photoacoustic tomography", Inverse Problems **28**, 084009 (2012) (cit. on pp. 36, 66, 86, 87).

[41]H. Gao, J. Feng, and L. Song, "Limited-view multi-source quantitative photoacoustic tomography", Inverse Problems **31**, 065004 (2015) (cit. on pp. 36, 89, 101, 245).

[42]X. Zhang, W. Zhou, and X. Zhang, "Forward – backward splitting method for quantitative photoacoustic tomography", Inverse Problems **30**, 125012 (2014) (cit. on p. 36).

[43]E. Z. Zhang, B. Povazay, J. Laufer, A. Alex, B. Hofer, B. Pedley, C. Glittenberg, B. Treeby, B. Cox, P. Beard, and W. Drexler, "Multimodal photoacoustic and optical coherence tomography scanner using an all optical detection scheme for 3D morphological skin imaging.", Biomedical Optics Express **2**, 2202–2215 (2011) (cit. on p. 41).

[44]H. F. Zhang, K. Maslov, G. Stoica, and L. V. Wang, "Functional photoacoustic microscopy for high-resolution and noninvasive in vivo imaging.", Nature Biotechnology **24**, 848–51 (2006) (cit. on pp. 41, 43, 75, 104).

[45]K. E. Wilson, S. V. Bachawal, L. Tian, and J. K. Willmann, "Multiparametric spectroscopic photoacoustic imaging of breast cancer development in a transgenic mouse model", Theranostics **4**, 1062–71 (2014) (cit. on pp. 41, 43, 71, 101).

[46]Z. Xu, C. Li, and L. V. Wang, "Photoacoustic tomography of water in phantoms and tissue.", Journal of Biomedical Optics **15**, 036019 (2010) (cit. on pp. 41–43).

[47]D.-K. Yao, K. Maslov, K. K. Shung, Q. Zhou, and L. V. Wang, "In vivo label-free photoacoustic microscopy of cell nuclei by excitation of DNA and RNA.", Optics Letters **35**, 4139–41 (2010) (cit. on pp. 41, 43).

[48]H. F. Zhang, K. Maslov, and L. V. Wang, "In vivo imaging of subcutaneous structures using functional photoacoustic microscopy", Nature Protocols **2**, 797–804 (2007) (cit. on pp. 41, 75).

[49]E. Z. Zhang, J. G. Laufer, R. B. Pedley, and P. C. Beard, "In vivo high-resolution 3D photoacoustic imaging of superficial vascular anatomy", Physics in Medicine and Biology **54**, 1035–46 (2009) (cit. on pp. 41, 43).

[50]K. Jansen, M. Wu, A. F. W. van der Steen, and G. van Soest, "Lipid detection in atherosclerotic human coronaries by spectroscopic intravascular photoacoustic imaging", Optics Express **21**, 21472 (2013) (cit. on p. 41).

[51]Y.-S. Chen, W. Frey, S. Kim, P. Kruizinga, K. Homan, and S. Emelianov, "Silica-coated gold nanorods as photoacoustic signal nanoamplifiers.", Nano Letters **11**, 348–54 (2011) (cit. on pp. 42, 108).

[52]G. A. Pang, J. Laufer, R. Niessner, and C. Haisch, "Photoacoustic Signal Generation in Gold Nanospheres in Aqueous Solution: Signal Generation Enhancement and Particle Diameter Effects", The Journal of Physical Chemistry C **120**, 27646–27656 (2016) (cit. on pp. 42, 44, 108).

[53]A. de la Zerda, Z. Liu, S. Bodapati, R. Teed, S. Vaithilingam, B. T. Khuri-Yakub, X. Chen, H. Dai, and S. S. Gambhir, "Ultrahigh sensitivity carbon nanotube agents for photoacoustic molecular imaging in living mice", Nano Letters **10**, 2168–72 (2010) (cit. on p. 42).

[54]J. Laufer, A. Jathoul, M. Pule, and P. Beard, "In vitro characterization of genetically expressed absorbing proteins using photoacoustic spectroscopy", Biomedical Optics Express **4**, 2477 (2013) (cit. on pp. 42, 44, 108, 109, 113, 114).

[55]A. P. Jathoul, J. Laufer, O. Ogunlade, B. Treeby, B. Cox, E. Zhang, P. Johnson, A. R. Pizzey, B. Philip, T. Marafioti, M. F. Lythgoe, R. B. Pedley, M. a. Pule, and P. Beard, "Deep in vivo photoacoustic imaging of mammalian tissues using a tyrosinase-based genetic reporter", Nature Photonics **9**, 239–246 (2015) (cit. on pp. 42, 44, 73).

[56]J. Laufer, E. Zhang, and P. Beard, "Evaluation of Absorbing Chromophores Used in Tissue Phantoms for Quantitative Photoacoustic Spectroscopy and Imaging", IEEE Journal of Selected Topics in Quantum Electronics **16**, 600–607 (2010) (cit. on pp. 42, 44, 92, 102, 105, 108–111, 115, 131, 136, 153, 160, 190).

[57]G. P. Luke, D. Yeager, and S. Y. Emelianov, "Biomedical applications of photoacoustic imaging with exogenous contrast agents.", Annals of Biomedical Engineering **40**, 422–37 (2012) (cit. on p. 42).

[58]V. Gujrati, A. Mishra, and V. Ntziachristos, "Molecular Imaging Probes for Multi-Spectral Optoacoustic Tomography", Chemical Communications **53**, 4653–72 (2017) (cit. on p. 42).

[59]X. Cai, B. Paratala, S. Hu, B. Sitharaman, and L. Wang, "Multiscale photoacoustic microscopy of single-walled carbon nanotube-incorporated tissue engineering scaffolds", Tissue Engineering Part C: Methods **18**, 310–7 (2012) (cit. on p. 44).

[60]D. Razansky, M. Distel, C. Vinegoni, R. Ma, N. Perrimon, R. W. Köster, and V. Ntziachristos, "Multispectral opto-acoustic tomography of deep-seated fluorescent proteins in vivo", Nature Photonics **3**, 412–417 (2009) (cit. on pp. 44, 74).

[61]J. Yao, A. A. Kaberniuk, L. Li, D. M. Shcherbakova, R. Zhang, L. Wang, G. Li, V. V. Verkhusha, and L. V. Wang, "Multiscale photoacoustic tomography using reversibly switchable bacterial phytochrome as a near-infrared photochromic probe", Nature Methods **13**, 67–73 (2016) (cit. on pp. 44, 76).

[62]L. Li, H. Zhang, R. Zemp, and L. V. Wang, "Simultaneous imaging of a lacZ-marked tumor and microvasculature morphology in vivo by dual-wavelength photoacoustic

microscopy", Journal of Innovative Optical Health Sciences **1**, 207–215 (2008) (cit. on p. 44).

[63]S. L. Jacques, "Optical properties of biological tissues: a review", Physics in Medicine and Biology **58**, 5007–5008 (2013) (cit. on pp. 45, 46, 128, 129, 147, 162).

[64]G. Alexandrakis, F. R. Rannou, and A. Chatziioannou, "Tomographic bioluminescence imaging by use of a combined optical-PET (OPET) system: a computer simulation feasibility study", Physics in Medicine & Biology **50**, 4225–4241 (2005) (cit. on pp. 46, 162).

[65]J. Viator, S. Jacques, and S. Prahl, "Depth profiling of absorbing soft materials using photoacoustic methods", IEEE Journal of Selected Topics in Quantum Electronics **5**, 989–996 (1999) (cit. on p. 47).

[66]S. Arridge, M. Schweiger, M. Hiraoka, and D. Delpy, "A finite element approach for modeling photon transport in tissue", Medical Physics **20**, 299–309 (1993) (cit. on pp. 48, 49).

[67]S. L. Jacques and B. W. Pogue, "Tutorial on diffuse light transport.", Journal of Biomedical Optics **13**, 041302 (2008) (cit. on pp. 48, 116, 225).

[68]M. Schweiger and S. Arridge, "The Toast++ software suite for forward and inverse modeling in optical tomography.", Journal of Biomedical Optics **19**, 040801 (2014) (cit. on pp. 48, 49, 162, 192, 195).

[69]C. Lutzweiler and D. Razansky, "Optoacoustic Imaging and Tomography: Reconstruction Approaches and Outstanding Challenges in Image Performance and Quantification", Sensors **13**, 7345–7384 (2013) (cit. on pp. 48, 51).

[70]B. Cox, S. Arridge, K. Köstli, and P. Beard, "Two-dimensional quantitative photoacoustic image reconstruction of absorption distributions in scattering media by use of a simple iterative method", Applied Optics **45**, 4–6 (2006) (cit. on pp. 49, 82).

[71]C. Zhu and Q. Liu, "Review of Monte Carlo modeling of light transport in tissues", Journal of Biomedical Optics **18**, 50902 (2013) (cit. on p. 49).

[72]R. Hochuli, S. Powell, S. Arridge, and B. Cox, "Forward and adjoint radiance Monte Carlo models for quantitative photoacoustic imaging", in Proc. of spie, photons plus ultrasound: imaging and sensing, Vol. 9323, edited by A. A. Oraevsky and L. V. Wang (Mar. 2015), 93231P–10 (cit. on p. 50).

[73]T. S. Leung and S. Powell, "Fast Monte Carlo simulations of ultrasound-modulated light using a graphics processing unit", Journal of Biomedical Optics **15**, 055007 (2010) (cit. on p. 50).

[74]Q. Fang and D. A. Boas, "Monte Carlo simulation of photon migration in 3D turbid media accelerated by graphics processing units", Optics Express **17**, 20178–90 (2009) (cit. on p. 50).

[75]B. T. Cox and P. C. Beard, "Fast calculation of pulsed photoacoustic fields in fluids using k-space methods", The Journal of the Acoustical Society of America **117**, 3616 (2005) (cit. on p. 52).

[76]B. E. Treeby and B. T. Cox, "k-Wave: MATLAB toolbox for the simulation and reconstruction of photoacoustic wave fields", Journal of Biomedical Optics **15**, 021314 (2010) (cit. on pp. 53, 59, 92, 141, 189).

[77]J. Yao and L. V. Wang, "Photoacoustic tomography: fundamentals, advances and prospects.", Contrast Media & Molecular Imaging **6**, 332–45 (2011) (cit. on p. 54).

[78]E. Zhang, J. Laufer, and P. Beard, "Backward-mode multiwavelength photoacoustic scanner using a planar Fabry-Perot polymer film ultrasound sensor for high-resolution three-dimensional imaging of biological tissues.", Applied Optics **47**, 561–577 (2008) (cit. on pp. 55, 73, 137, 138, 178).

[79]M. Xu and L. V. Wang, "Photoacoustic imaging in biomedicine", Review of Scientific Instruments **77**, 041101 (2006) (cit. on p. 58).

[80]M. Xu and L. V. Wang, "Universal back-projection algorithm for photoacoustic computed tomography", Physical Review E **71**, 1–7 (2005) (cit. on p. 59).

[81]X. Pan and M. A. Anastasio, "Minimal-scan filtered backpropagation algorithms for diffraction tomography", Journal of the Optical Society of America A **16**, 2896 (1999) (cit. on p. 59).

[82]D. Finch, S. K. Patch, and Rakesh, "Determining a Function from Its Mean Values Over a Family of Spheres", SIAM Journal on Mathematical Analysis **35**, 1213–1240 (2004) (cit. on p. 59).

[83]L. A. Kunyansky, "Explicit inversion formulae for the spherical mean Radon transform", Inverse Problems **23**, 373–383 (2007) (cit. on p. 59).

[84]S. J. Norton and M. Linzer, "Ultrasonic reflectivity imaging in three dimensions: exact inverse scattering solutions for plane, cylindrical, and spherical apertures.", IEEE Transactions on Biomedical Engineering **28**, 202–220 (1981) (cit. on p. 59).

[85]K. P. Köstli, M. Frenz, H. Bebie, and H. P. Weber, "Temporal backward projection of optoacoustic pressure transients using fourier transform methods", Physics in Medicine and Biology **46**, 1863–72 (2001) (cit. on pp. 59, 92).

[86]Y. Xu, D. Feng, and L. V. Wang, "Exact frequency-domain reconstruction for thermoacoustic tomography–I: Planar geometry.", IEEE Transactions on Medical Imaging **21**, 823–8 (2002) (cit. on p. 59).

[87]Y. Xu, M. Xu, and L. V. Wang, "Exact frequency-domain reconstruction for thermoacoustic tomography–II: Cylindrical geometry.", IEEE Transactions on Medical Imaging **21**, 829–33 (2002) (cit. on p. 59).

[88]M. A. Anastasio, J. Zhang, D. Modgil, and P. J. L. Riviére, "Application of inverse source concepts to photoacoustic tomography", Inverse Problems **23**, S21–S35 (2007) (cit. on p. 59).

[89]M. Xu and L. V. Wang, "Time-domain reconstruction for thermoacoustic tomography in a spherical geometry.", IEEE Transactions on Medical Imaging **21**, 814–22 (2002) (cit. on p. 59).

[90]L. A. Kunyansky, "A series solution and a fast algorithm for the inversion of the spherical mean Radon transform", Inverse Problems **23**, S11–S20 (2007) (cit. on p. 59).

[91]B. E. Treeby, J. Jaros, and B. T. Cox, "Advanced photoacoustic image reconstruction using the k-Wave toolbox", in Proceedings of spie, Vol. 9708, edited by A. A. Oraevsky and L. V. Wang (Mar. 2016), 97082P (cit. on p. 59).

[92]Y. Xu and L. Wang, "Time Reversal and Its Application to Tomography with Diffracting Sources", Physical Review Letters **92**, 3–6 (2004) (cit. on p. 59).

[93]B. E. Treeby, E. Z. Zhang, and B. T. Cox, "Photoacoustic tomography in absorbing acoustic media using time reversal", Inverse Problems **26**, 115003 (2010) (cit. on p. 59).

[94]Z. Belhachmi, T. Glatz, and O. Scherzer, "A direct method for photoacoustic tomography with inhomogeneous sound speed", Inverse Problems **32**, 045005 (2016) (cit. on p. 60).

[95]S. R. Arridge, M. M. Betcke, B. T. Cox, F. Lucka, and B. E. Treeby, "On the adjoint operator in photoacoustic tomography", Inverse Problems **32**, 115012 (2016) (cit. on p. 60).

[96]C. Huang, K. Wang, L. Nie, L. V. Wang, and M. A. Anastasio, "Full-wave iterative image reconstruction in photoacoustic tomography with acoustically inhomogeneous media.", IEEE Transactions on Medical Imaging **32**, 1097–110 (2013) (cit. on p. 60).

[97]K. Wang, R. Su, A. A. Oraevsky, and M. A. Anastasio, "Investigation of iterative image reconstruction in three-dimensional optoacoustic tomography", arXiv (2012) (cit. on p. 60).

[98]H. Azhari, "Appendix A - Typical acoustic properties of tissues", in *Basics of biomedical ultrasound for engineers* (John Wiley & Sons, Inc., Hoboken, NJ, USA, Feb. 2010), pp. 313–314 (cit. on pp. 60, 111, 126, 142).

[99]B. E. Treeby, T. K. Varslot, E. Z. Zhang, J. G. Laufer, and P. C. Beard, "Automatic sound speed selection in photoacoustic image reconstruction using an autofocus approach", Journal of Biomedical Optics **16**, 090501 (2011) (cit. on p. 60).

[100]T. Ding, K. Ren, and S. Vallélian, "A one-step reconstruction algorithm for quantitative photoacoustic imaging", Inverse Problems **31**, 095005 (2015) (cit. on pp. 60, 88).

[101]R. Ellwood, E. Zhang, P. Beard, and B. Cox, "Photoacoustic imaging using acoustic reflectors to enhance planar arrays", Journal of Biomedical Optics **19**, 126012 (2014) (cit. on p. 61).

[102]L. Yao and H. Jiang, "Photoacoustic image reconstruction from few-detector and limited-angle data.", Biomedical Optics Express **2**, 2649–54 (2011) (cit. on p. 61).

[103]S. Morscher, J. Glatz, N. C. Deliolanis, A. Buehler, A. Sarantopoulos, D. Razansky, and V. Ntziachristos, "Spectral unmixing using component analysis in multispectral optoacoustic tomography", Proc SPIE **8089**, edited by C. P. Lin and V. Ntziachristos, 0R–1–80890R–4 (2011) (cit. on pp. 63, 79).

[104]J. Laufer, C. Elwell, D. Delpy, and P. Beard, "In vitro measurements of absolute blood oxygen saturation using pulsed near-infrared photoacoustic spectroscopy: accuracy and resolution.", Physics in Medicine and Biology **50**, 4409–28 (2005) (cit. on pp. 63, 71, 85, 90, 104).

[105]R. J. Zemp, X. Chen, H. Lu, and K. Mathewson, "A new photoacoustic method for measuring optical transport Green's functions in turbid media", 2008 IEEE Ultrasonics Symposium, 1246–1249 (2008) (cit. on p. 63).

[106]J. C. Ranasinghesagara, Y. Jian, X. Chen, K. Mathewson, and R. J. Zemp, "Photoacoustic technique for assessing optical scattering properties of turbid media.", Journal of Biomedical Optics **14**, 040504 (2009) (cit. on p. 63).

[107]J. Glatz, N. C. Deliolanis, A. Buehler, D. Razansky, and V. Ntziachristos, "Blind source unmixing in multi-spectral optoacoustic tomography.", Optics Express **19**, 3175–84 (2011) (cit. on pp. 63, 70, 79).

[108]K. Maslov, H. F. Zhang, and L. V. Wang, "Effects of wavelength-dependent fluence attenuation on the noninvasive photoacoustic imaging of hemoglobin oxygen saturation in subcutaneous vasculature in vivo", Inverse Problems **23**, S113–S122 (2007) (cit. on pp. 63, 71, 72, 75).

[109]R. J. Zemp, "Quantitative photoacoustic tomography with multiple optical sources.", Applied Optics **49**, 3566–72 (2010) (cit. on pp. 65, 67, 111).

[110]T. Jetzfellner, D. Razansky, A. Rosenthal, R. Schulz, K.-H. Englmeier, and V. Ntziachristos, "Performance of iterative optoacoustic tomography with experimental data", Applied Physics Letters **95**, 013703 (2009) (cit. on pp. 66, 82).

[111]T. Soonthornsaratoon, "Gradient-based methods for quantitative photoacoustic tomography", PhD thesis (University College London, London, UK, 2014) (cit. on pp. 66, 67, 82, 164, 195, 244).

[112]D.-k. Yao, C. Zhang, K. Maslov, and L. V. Wang, "Photoacoustic measurement of the Grüneisen parameter of tissue.", Journal of Biomedical Optics **19**, 017007 (2014) (cit. on pp. 67, 111, 117, 118, 136, 142, 153, 155, 222, 243).

[113]W. Haynes, *Crc handbook of chemistry and physics, 93rd edition* (Taylor & Francis, 2012) (cit. on pp. 67, 117, 135, 136, 145, 153, 187).

[114]G. Bal and K. Ren, "On multi-spectral quantitative photoacoustic tomography in diffusive regime", Inverse Problems **28**, 025010 (2012) (cit. on pp. 67, 84–86, 159, 175).

[115]R. Hochuli, P. C. Beard, and B. Cox, "Accuracy of approximate inversion schemes in quantitative photacoustic imaging", in Proceedings of spie, Vol. 8943, edited by A. A. Oraevsky and L. V. Wang (Mar. 2014), pp. 89435V–1 – 89435V–10 (cit. on pp. 70–74, 165).

[116]C. L. Bayer, B. J. Wlodarczyk, R. H. Finnell, and S. Y. Emelianov, "Ultrasound-guided spectral photoacoustic imaging of hemoglobin oxygenation during development", Biomedical Optics Express **8**, 757 (2017) (cit. on p. 71).

[117]K. S. Valluru and J. K. Willmann, "Clinical photoacoustic imaging of cancer.", Ultrasonography **35**, 267–80 (2016) (cit. on p. 71).

[118]H. F. Zhang, K. Maslov, M. Sivaramakrishnan, G. Stoica, and L. V. Wang, "Imaging of hemoglobin oxygen saturation variations in single vessels in vivo using photoacoustic microscopy", Applied Physics Letters **90**, 053901 (2007) (cit. on pp. 71, 75, 104).

[119]M. R. Tomaszewski, I. Quiros-Gonzalez, J. Joseph, and S. E. Bohndiek, "Quantitative imaging of tumor vasculature using multispectral optoacoustic tomography (MSOT)", Proceedings of SPIE **10064**, edited by A. A. Oraevsky and L. V. Wang, 100640N (2017) (cit. on p. 73).

[120]G. P. Luke and S. Y. Emelianov, "Optimization of in vivo spectroscopic photoacoustic imaging by smart optical wavelength selection.", Optics Letters **39**, 2214–7 (2014) (cit. on p. 73).

[121]R. Hochuli, P. C. Beard, and B. Cox, "Effect of wavelength selection on the accuracy of blood oxygen saturation estimates obtained from photoacoustic images", Proceedings of SPIE **9323**, 93231V–8 (2015) (cit. on p. 73).

[122]D. Razansky and V. Ntziachristos, "Hybrid photoacoustic fluorescence molecular tomography using finite-element-based inversion", Medical Physics **34**, 4293 (2007) (cit. on p. 74).

[123]L. Meng-Lin, O. Jung-Taek, X. Xueyi, K. Geng, W. W., G. Lungu, G. Stoica, and L. Wang, "Simultaneous Molecular and Hypoxia Imaging of Brain Tumors Using In Vivo Spectroscopic Photoacoustic Tomography", Proceedings of the IEEE **96**, 481–489 (2008) (cit. on p. 74).

[124]K. Maslov, M. Sivaramakrishnan, H. F. Zhang, G. Stoica, and L. V. Wang, "Technical considerations in quantitative blood oxygenation measurement using photoacoustic microscopy in vivo", Proc. of SPIE, Photons Plus Ultrasound: Imaging and Sensing **6086**, edited by A. A. Oraevsky and L. V. Wang, 60860R–60860R–11 (2006) (cit. on p. 75).

[125]J. R. Rajian, P. L. Carson, and X. Wang, "Quantitative photoacoustic measurement of tissue optical absorption spectrum aided by an optical contrast agent.", Optics Express **17**, 4879–89 (2009) (cit. on p. 75).

[126]B. Cox, J. Laufer, and P. Beard, "Quantitative Photoacoustic Image Reconstruction using Fluence Dependent Chromophores", Biomedical Optics Express **1**, 5830–5835 (2010) (cit. on p. 76).

[127]X. L. Dean-Ben, A. C. Stiel, Y. Jiang, V. Ntziachristos, G. G. Westmeyer, and D. Razansky, "Light fluence normalization in turbid tissues via temporally unmixed multispectral optoacoustic tomography", Optics Letters **40**, 4691 (2015) (cit. on p. 76).

[128]Z. Yuan and H. Jiang, "Three-dimensional finite-element-based photoacoustic tomography: Reconstruction algorithm and simulations", Medical Physics **34**, 538 (2007) (cit. on pp. 77, 86, 89).

[129]L. Yin, Q. Wang, Q. Zhang, and H. Jiang, "Tomographic imaging of absolute optical absorption coefficient in turbid media using combined photoacoustic and diffusing light measurements", Optics Letters **32**, 2556 (2007) (cit. on pp. 77, 86, 89).

[130]J. C. Ranasinghesagara and R. J. Zemp, "Combined photoacoustic and oblique-incidence diffuse reflectance system for quantitative photoacoustic imaging in turbid media.", Journal of Biomedical Optics **15**, 046016 (2010) (cit. on p. 77).

[131] A. Q. Bauer, R. E. Nothdurft, T. N. Erpelding, L. V. Wang, and J. P. Culver, "Quantitative photoacoustic imaging: correcting for heterogeneous light fluence distributions using diffuse optical tomography", Journal of Biomedical Optics **16**, 096016 (2011) (cit. on p. 77).

[132] X. Li, L. Xi, R. Jiang, L. Yao, and H. Jiang, "Integrated diffuse optical tomography and photoacoustic tomography: phantom validations.", Biomedical Optics Express **2**, 2348–53 (2011) (cit. on p. 77).

[133] K. Daoudi, A. Hussain, E. Hondebrink, and W. Steenbergen, "Correcting photoacoustic signals for fluence variations using acousto-optic modulation", Optics Express **20**, 14117 (2012) (cit. on p. 77).

[134] K. Daoudi and W. Steenbergen, "Towards quantitative tissue absorption imaging by combining photoacoustics and acousto-optics", arXiv, 14 (2012) (cit. on p. 77).

[135] L. An and B. Cox, "Independent component analysis for unmixing multi-wavelength photoacoustic images", in Proceedings of spie, Vol. 9708, edited by A. A. Oraevsky and L. V. Wang, 1 (Mar. 2016), p. 970851 (cit. on p. 79).

[136] X. Luis Deán-Ben, N. C. Deliolanis, V. Ntziachristos, and D. Razansky, "Fast unmixing of multispectral optoacoustic data with vertex component analysis", Optics and Lasers in Engineering **58**, 119–125 (2014) (cit. on p. 79).

[137] X. L. Deán-Ben, A. Buehler, D. Razansky, and V. Ntziachristos, "Estimation of optoacoustic contrast agent concentration with self-calibration blind logarithmic unmixing.", Physics in Medicine and Biology **59**, 4785–4797 (2014) (cit. on p. 79).

[138] S. Tzoumas, N. Deliolanis, S. Morscher, and V. Ntziachristos, "Un-mixing Molecular Agents from Absorbing Tissue in Multispectral Optoacoustic Tomography.", IEEE Transactions on Medical Imaging **33**, 48–60 (2013) (cit. on p. 79).

[139] A. Rosenthal, D. Razansky, and V. Ntziachristos, "Quantitative optoacoustic signal extraction using sparse signal representation.", IEEE Transactions on Medical Imaging **28**, 1997–2006 (2009) (cit. on pp. 79, 104).

[140] T. Stahl, T. Allen, and P. Beard, "Characterization of the thermalisation efficiency and photostability of photoacoustic contrast agents", in Proceedings of spie, Vol. 8943, edited by A. A. Oraevsky and L. V. Wang (Mar. 2014), 89435H–1 – 89435H–8 (cit. on pp. 81, 108, 112, 115, 117, 243).

[141] A. A. Karabutov, N. B. Podymova, and V. S. Letokhov, "Time-resolved optoacoustic measurement of absorption of light by inhomogeneous media", Applied Optics **34**, 1484–7 (1995) (cit. on p. 81).

[142] A. A. A. Oraevsky, S. L. S. Jacques, R. O. Esenaliev, F. K. Tittel, FK, and SL, "Direct measurement of laser fluence distribution and optoacoustic imaging in heterogeneous tissues", Proceedings of SPIE **2323**, 37–46 (1995) (cit. on p. 81).

[143] Y. Petrov, D. Prough, D. Deyo, I. Petrova, M. Motamedi, and R. Esenaliev, "In vivo noninvasive monitoring of cerebral blood with optoacoustic technique.", Conference proceedings : Annual International Conference of the IEEE Engineering in Medicine and Biology Society. **3**, 2052–4 (2004) (cit. on p. 81).

[144]Y. Y. Petrov, I. Y. Petrova, I. A. Patrikeev, R. O. Esenaliev, and D. S. Prough, "Multiwavelength optoacoustic system for noninvasive monitoring of cerebral venous oxygenation: a pilot clinical test in the internal jugular vein.", Optics Letters **31**, 1827–9 (2006) (cit. on p. 82).

[145]Y. Y. Petrov, D. S. Prough, I. Petrova, I. A. Patrikeev, I. Cicenaite, and R. O. Esenaliev, "Noninvasive cerebral blood oxygenation monitoring: clinical test of multiwavelength optoacoustic system", Proceedings of SPIE **6437**, 643705–643705–7 (2007) (cit. on p. 82).

[146]Z. Yuan and H. Jiang, "Quantitative photoacoustic tomography: Recovery of optical absorption coefficient maps of heterogeneous media", Applied Physics Letters **88**, 231101 (2006) (cit. on pp. 82, 104).

[147]H. Jiang, Z. Yuan, L. Yin, Q. Wang, and Q. Zhang, "Quantitative photoacoustic tomography: recovery of optical absorption coefficient maps of heterogeneous media", Proceedings of SPIE **6437**, edited by A. A. Oraevsky and L. V. Wang, 64371S–64371S–4 (2007) (cit. on p. 82).

[148]L. Yao, Y. Sun, and H. Jiang, "Quantitative photoacoustic tomography based on the radiative transfer equation.", Optics Letters **34**, 1765–7 (2009) (cit. on p. 82).

[149]B. T. Cox, S. R. Arridge, and P. C. Beard, "Gradient-based quantitative photoacoustic image reconstruction for molecular imaging", Proceedings of SPIE **6437**, 64371T–64371T–10 (2007) (cit. on pp. 83–86, 164, 195).

[150]P. Shao, B. Cox, and R. J. Zemp, "Estimating optical absorption, scattering, and Grueneisen distributions with multiple-illumination photoacoustic tomography", Applied Optics **50**, 3145–3154 (2011) (cit. on pp. 84, 159).

[151]A. Pulkkinen, B. T. Cox, S. R. Arridge, J. P. Kaipio, and T. Tarvainen, "Quantitative photoacoustic tomography using illuminations from a single direction", Journal of Biomedical Optics **20**, 036015 (2015) (cit. on p. 84).

[152]G. Bal and K. Ren, "Multi-source quantitative photoacoustic tomography in a diffusive regime", Inverse Problems **27**, 075003 (2011) (cit. on pp. 84, 86, 175).

[153]W. Naetar and O. Scherzer, "Quantitative Photoacoustic Tomography with Piecewise Constant Material Parameters", SIAM Journal on Imaging Sciences **7**, 1755–1774 (2014) (cit. on p. 84).

[154]G. Bal and G. Uhlmann, "Inverse diffusion theory of photoacoustics", Inverse Problems **26**, 085010 (2010) (cit. on pp. 84, 234).

[155]N. Song, C. Deumié, and A. D. Silva, "Considering sources and detectors distributions for quantitative photoacoustic tomography", Biomedical Optics Express **5**, 3960–3974 (2014) (cit. on pp. 84, 89, 244, 245).

[156]A. V. Mamonov and K. Ren, "Quantitative photoacoustic imaging in the radiative transport regime", Communications in Mathematical Sciences **12**, 201–234 (2014) (cit. on pp. 85, 86, 111).

[157]A. Pulkkinen, B. T. Cox, S. R. Arridge, J. P. Kaipio, and T. Tarvainen, "A Bayesian approach to spectral quantitative photoacoustic tomography", Inverse Problems **30**, 065012 (2014) (cit. on pp. 85, 101, 244).

[158]J. Nocedal and S. J. Wright, *Numerical optimization*, 2nd (Springer, New York, 2006) (cit. on pp. 86, 164).

[159]B. T. Cox, J. G. Laufer, and P. C. Beard, "The challenges for quantitative photoacoustic imaging", in Proceedings of spie, Vol. 7177 (2009), pp. 717713–717713–9 (cit. on p. 86).

[160]B. Cox, T. Tarvainen, and S. Arridge, "Multiple Illumination Quantitative Photoacoustic Tomography using Transport and Diffusion Models", Contemporary Mathematics **559**, 1–12 (2011) (cit. on pp. 86, 87).

[161]H. Gao, H. Zhao, and S. Osher, "Bregman methods in quantitative photoacoustic tomography", UCLA CAM report **10-42** (2010) (cit. on pp. 86, 87).

[162]H. Gao, H. Zhao, and S. Osher, "Quantitative photoacoustic tomography", UCLA CAM report **11-28** (2011) (cit. on pp. 86, 101).

[163]T. Saratoon, T. Tarvainen, S. R. Arridge, and B. T. Cox, "3D quantitative photoacoustic tomography using the δ-Eddington approximation", Proceedings of SPIE **8581**, edited by A. A. Oraevsky and L. V. Wang, 85810V–85810V–12 (2013) (cit. on pp. 86, 87, 101, 224).

[164]R. Hochuli, S. Powell, S. Arridge, and B. Cox, "Quantitative photoacoustic tomography using forward and adjoint monte carlo models of radiance", Journal of Biomedical Optics **21**, 126004 (2016) (cit. on pp. 86, 87, 95).

[165]J. Buchmann, B. A. Kaplan, S. Prohaska, and J. Laufer, "Experimental validation of a Monte-Carlo-based inversion scheme for 3D quantitative photoacoustic tomography", in Proceedings of spie, Vol. 10064, edited by A. A. Oraevsky and L. V. Wang (Mar. 2017), p. 1006416 (cit. on pp. 86, 94).

[166]B. A. Kaplan, J. Buchmann, S. Prohaska, and J. Laufer, "Monte-Carlo-based inversion scheme for 3D quantitative photoacoustic tomography", Proceedings of SPIE **10064**, 1006416 (2017) (cit. on pp. 87, 94, 233).

[167]O. Nykänen, A. Pulkkinen, and T. Tarvainen, "Quantitative photoacoustic tomography augmented with surface light measurements", Biomed. Opt. Express **8**, 4380–4395 (2017) (cit. on p. 87).

[168]Z. Yuan, Q. Wang, and H. Jiang, "Reconstruction of optical absorption coefficient maps of heterogeneous media by photoacoustic tomography coupled with diffusion equation based regularized Newton method.", Optics Express **15**, 18076–81 (2007) (cit. on pp. 87–89).

[169]L. An, T. Saratoon, M. Fonseca, R. Ellwood, and B. Cox, "Exploiting statistical independence for quantitative photoacoustic tomography", Proceedings of SPIE, Photons Plus Ultrasound **10064**, 1006419 (2017) (cit. on p. 88).

[170]E. Malone, B. T. Cox, S. Arridge, E. Malone, S. Powell, B. T. Cox, and S. Arridge, "Reconstruction-classification method for quantitative photoacoustic tomography", Journal of Biomedical Opics **20**, 126004–1 (2015) (cit. on pp. 88, 193, 244).

[171]E. Malone, B. Cox, and S. Arridge, "Multispectral reconstruction methods for quantitative photoacoustic tomography", in Proceedings of spie, Vol. 9708, edited by A. A. Oraevsky and L. V. Wang, 0 (Mar. 2016), p. 970827 (cit. on p. 88).

[172]M. Haltmeier, L. Neumann, and S. Rabanser, "Single-stage reconstruction algorithm for quantitative photoacoustic tomography", Inverse Problems **31**, 065005 (2015) (cit. on pp. 88, 89, 245).

[173]Y. Sun, E. S. Sobel, and H. Jiang, "First assessment of three-dimensional quantitative photoacoustic tomography for in vivo detection of osteoarthritis in the finger joints", Medical Physics **38**, 4009 (2011) (cit. on p. 89).

[174]Y. Sun and H. Jiang, "Quantitative three-dimensional photoacoustic tomography of the finger joints: phantom studies in a spherical scanning geometry.", Physics in Medicine and Biology **54**, 5457–67 (2009) (cit. on pp. 89, 104).

[175]Y. Sun, E. Sobel, and H. Jiang, "Noninvasive imaging of hemoglobin concentration and oxygen saturation for detection of osteoarthritis in the finger joints using multispectral three-dimensional quantitative photoacoustic tomography", Journal of Optics **15**, 055302 (2013) (cit. on p. 90).

[176]K. G. Held, M. Jaeger, J. Ricka, M. Frenz, and H. G. Akarcay, "Multiple irradiation sensing of the optical effective attenuation coefficient for spectral correction in handheld OA imaging", Photoacoustics **4**, 70–80 (2016) (cit. on p. 90).

[177]T. Kirchner, J. Gröhl, and L. Maier-Hein, "Local context encoding enables machine learning-based quantitative photoacoustics", arXiv (2017) (cit. on p. 95).

[178]S. Tzoumas, A. Nunes, I. Olefir, S. Stangl, P. Symvoulidis, S. Glasl, C. Bayer, G. Multhoff, and V. Ntziachristos, "Eigenspectra optoacoustic tomography achieves quantitative blood oxygenation imaging deep in tissues", Nature Communications **7**, 12121 (2016) (cit. on pp. 96, 244).

[179]P. Shao, T. J. Harrison, and R. J. Zemp, "Consecutively reconstructing absorption and scattering distributions in turbid media with multiple-illumination photoacoustic tomography", Journal of Biomedical Optics **19**, 126009 (2014) (cit. on p. 101).

[180]N. Huynh, E. Z. Zhang, M. Betcke, S. Arrridge, P. C. Beard, and B. Cox, "Single-pixel optical camera for video rate ultrasonic imaging", Optica **3**, 26–29 (2016) (cit. on p. 101).

[181]T. Tarvainen, S. R. Arridge, B. T. Cox, J. P. Kaipio, V. Kolehmainen, and A. Pulkkinen, "Approximate marginalization of unknown scattering in quantitative photoacoustic tomography", Inverse Problems and Imaging **8**, 811–829 (2014) (cit. on p. 101).

[182]M. Fonseca, B. Zeqiri, P. C. Beard, and B. T. Cox, "Characterisation of a phantom for multiwavelength quantitative photoacoustic imaging", Physics in Medicine and Biology **61**, 4950–4973 (2016) (cit. on pp. 102, 106, 119, 126, 127, 129, 130, 132, 134–136, 139, 140).

[183]B. W. Pogue and M. S. Patterson, "Review of tissue simulating phantoms for optical spectroscopy, imaging and dosimetry.", Journal of Biomedical Optics **11**, 041102 (2006) (cit. on pp. 102, 106–108, 115, 128, 150).

[184]M. Firbank, D. T. Delpy, and M. Oda, "A design for a stable and reproducible phantom for use in near infra-red imaging and spectroscopy", Physics in Medicine and Biology **38**, 955–61 (1993) (cit. on pp. 102, 116).

[185]M. Firbank, M. Oda, and D. T. Delpy, "An improved design for a stable and reproducible phantom material for use in near-infrared spectroscopy and imaging.", Physics in Medicine and Biology **40**, 955–61 (1995) (cit. on pp. 102, 107).

[186]M. O. Culjat, D. Goldenberg, P. Tewari, and R. S. Singh, "A review of tissue substitutes for ultrasound imaging.", Ultrasound in Medicine and Biology **36**, 861–73 (2010) (cit. on pp. 102, 105–107).

[187]E. Madsen, J. Zagzebski, R. Banjavie, and R. Jutila, "Tissue mimicking materials for ultrasound phantoms", Medical Physics **5**, 391–4 (1978) (cit. on p. 102).

[188]G. M. Spirou, A. A. Oraevsky, I. A. Vitkin, and W. M. Whelan, "Optical and acoustic properties at 1064 nm of polyvinyl chloride-plastisol for use as a tissue phantom in biomedical optoacoustics", Physics in Medicine and Biology **50**, N141–53 (2005) (cit. on pp. 102, 106, 108, 121, 126–129).

[189]C. Avigo, N. D. Lascio, P. Armanetti, C. Kusmic, L. Cavigli, F. Ratto, S. Meucci, C. Masciullo, M. Cecchini, R. Pini, F. Faita, and L. Menichetti, "Organosilicon phantom for photoacoustic imaging", Journal of Biomedical Opics **20**, 046008 (2015) (cit. on pp. 102, 106, 108, 109).

[190]J. R. Cook, R. R. Bouchard, and S. Y. Emelianov, "Tissue-mimicking phantoms for photoacoustic and ultrasonic imaging.", Biomedical Optics Express **2**, 3193–206 (2011) (cit. on pp. 102, 105, 108–110, 181).

[191]S. E. Bohndiek, S. Bodapati, D. Van De Sompel, S.-R. Kothapalli, and S. S. Gambhir, "Development and application of stable phantoms for the evaluation of photoacoustic imaging instruments.", PloS One **8**, e75533 (2013) (cit. on pp. 102, 105, 106, 109, 121, 122).

[192]B. C. Gross, J. L. Erkal, S. Y. Lockwood, C. Chen, and D. M. Spence, "Evaluation of 3D printing and its potential impact on biotechnology and the chemical sciences", Analytical Chemistry **86**, 3240–3253 (2014) (cit. on p. 104).

[193]B. Z. Bentz, A. V. Chavan, D. Lin, E. H. R. Tsai, and K. J. Webb, "Fabrication and application of heterogeneous printed mouse phantoms for whole animal optical imaging", Applied Optics **55**, 280 (2016) (cit. on p. 104).

[194]L. A. Dempsey, M. Persad, S. Powell, D. Chitnis, and J. C. Hebden, "Geometrically complex 3d-printed phantoms for diffuse optical imaging", Biomedical Optics Express **8**, 1754–1762 (2017) (cit. on p. 104).

[195]A. Selfridge, "Approximate material properties in isotropic materials", IEEE Transactions on Sonics and Ultrasonics **SU-32**, 381–394 (1985) (cit. on pp. 104, 182).

[196]N. G. Parker, M. L. Mather, S. P. Morgan, and M. J. W. Povey, "Longitudinal acoustic properties of poly(lactic acid) and poly(lactic-co-glycolic acid).", Biomedical Materials **5**, 055004 (2010) (cit. on p. 104).

[197]J.-S. Lee, J. M. Hong, J. W. Jung, J.-H. Shim, J.-H. Oh, and D.-W. Cho, "3D printing of composite tissue with complex shape applied to ear regeneration", Biofabrication **6**, 024103 (2014) (cit. on p. 104).

[198]M. Wang, S. Shen, J. Yang, E. Dong, and R. Xu, "3D printing method for freeform fabrication of optical phantoms simulating heterogeneous biological tissue", in, Vol. 8945, edited by R. J. Nordstrom, J.-P. Bouchard, and D. W. Allen (Mar. 2014), p. 894509 (cit. on p. 104).

[199]A. Kharine, S. Manohar, R. Seeton, R. G. M. Kolkman, R. A. Bolt, W. Steenbergen, and F. F. M. de Mul, "Poly(vinyl alcohol) gels for use as tissue phantoms in photoacoustic mammography.", Physics in Medicine and Biology **48**, 357–70 (2003) (cit. on p. 105).

[200]W. Xia, D. Piras, M. Heijblom, W. Steenbergen, T. G. van Leeuwen, and S. Manohar, "Poly(vinyl alcohol) gels as photoacoustic breast phantoms revisited.", Journal of Biomedical Optics **16**, 075002 (2011) (cit. on p. 105).

[201]N. Hungr, J.-A. Long, V. Beix, and J. Troccaz, "A realistic deformable prostate phantom for multimodal imaging and needle-insertion procedures.", Medical Physics **39**, 2031–41 (2012) (cit. on pp. 106, 121, 127, 128).

[202]J. Hwang, H.-J. Kim, P. Lemaillet, H. Wabnitz, D. Grosenick, L. Yang, T. Gladytz, D. McClatchy, D. Allen, K. Briggman, and B. Pogue, "Polydimethylsiloxane tissue-mimicking phantoms for quantitative optical medical imaging standards", Proceedings of SPIE **10056**, 1005603 (2017) (cit. on pp. 106, 115, 117).

[203]J. Tsou, L. J, B. AI, and I. MF, "Role of ultrasonic shear rate estimation errors in assessing inflammatory response and vascular risk", Ultrasound in Medicine and Biology **34**, 2522–2535 (2008) (cit. on p. 106).

[204]S. M. Srinivasan R, "Development of biological tissue-equivalent phantoms for optical imaging", Indian Journal of Experimental Biology **40**, 531–535 (202) (cit. on p. 106).

[205]T. Arun Kumar, M. Singh, and M. Kumaravel, "Laser Reflectance Imaging of Curved Tissue-equivalent Phantoms", Engineering in Medicine and Biology Society, 2005. IEEE-EMBS 2005. 27th Annual International Conference of the, 1468–1471 (2005) (cit. on p. 106).

[206]S. L. Vieira, T. Z. Pavan, J. E. Junior, and A. a. O. Carneiro, "Paraffin-gel tissue-mimicking material for ultrasound-guided needle biopsy phantom.", Ultrasound in Medicine and Biology **39**, 2477–84 (2013) (cit. on p. 106).

[207]S. Andersson Engels, R. Berg, S. Svanberg, and O. Jarlman, "Time-resolved transillumination for medical diagnostics.", Optics Letters **15**, 1179–81 (1990) (cit. on p. 106).

[208]H. J. van Staveren, C. J. M. Moes, J. van Marie, S. A. Prahl, M. J. van Gemert, H. J. van Staveren, J. van Marie, and M. J. C. van Gemert, "Light scattering in Intralipid-10% in the wavelength range of 400-1100 nm.", Applied Optics **30**, 4507–14 (1991) (cit. on pp. 108, 151, 160).

[209]W. C. Vogt, C. Jia, K. A. Wear, B. S. Garra, and T. J. Pfefer, "Development and validation of a biologically realistic tissue-mimicking material for photoacoustics and other bimodal optical-acoustic modalities", in Proceedings of spie, Vol. 10056, edited by R. Raghavachari, R. Liang, and T. J. Pfefer (Mar. 2017), p. 100560C (cit. on p. 108).

[210]H. G. Akarçay, S. Preisser, M. Frenz, and J. Rička, "Determining the optical properties of a gelatin-TiO2 phantom at 780 nm.", Biomedical Optics Express **3**, 418–34 (2012) (cit. on p. 108).

[211]A. V. Bykov, A. P. Popov, M. Kinnunen, T. Prykäri, A. V. Priezzhev, and R. Myllylä, "Skin phantoms with realistic vessel structure for OCT measurements", Proceedings of SPIE **7376**, edited by M. Kinnunen and R. Myllylä, 73760F–73760F–7 (2010) (cit. on pp. 108, 115, 116, 128, 129, 141).

[212]W. U. Malik and Muzaffar.M, "Biuret Reaction of Transfusion Gelation .II. Influence of Some Bivalent Metal Ions on Absorption Spectrum of Nickel-Transfusion Gelation Complex", Journal Fur Praktische Chemie **30**, 145–148 (1965) (cit. on pp. 109, 110).

[213]A.-K. Kirchherr, A. Briel, and K. Mäder, "Stabilization of indocyanine green by encapsulation within micellar systems.", Molecular Pharmaceutics **6**, 480–91 (2009) (cit. on p. 109).

[214]A. Marcano O., N. Melikechi, and G. Verde, "Shift of the absorption spectrum of organic dyes due to saturation", The Journal of Chemical Physics **113**, 5830 (2000) (cit. on pp. 109, 115, 131).

[215]F. Duck, *Physical properties of tissue: a comprehensive reference book* (Academic Press, Inc., San Diego, 1990) (cit. on p. 111).

[216]R. Alfano, *Biological events probed by ultrafast laser spectroscopy* (Elsevier, 2012) (cit. on p. 114).

[217]R. F. Khairutdinov and N. Serpone, "Laser-induced light attenuation in solutions of porphyrin aggregates", The Journal of Physical Chemistry **99**, 11952–11958 (1995) (cit. on pp. 114, 131).

[218]I. R. Piletic, T. E. Matthews, and W. S. Warren, "Probing near-infrared photorelaxation pathways in eumelanins and pheomelanins", The Journal of Physical Chemistry A **114**, PMID: 20882951, 11483–11491 (2010) (cit. on pp. 114, 143).

[219]J. Märk, F.-J. Schmitt, C. Theiss, H. Dortay, T. Friedrich, and J. Laufer, "Photoacoustic imaging of fluorophores using pump-probe excitation", Biomedical Optics Express **6**, 2522–2535 (2015) (cit. on pp. 114, 243).

[220]C. F. Bohren and D. Huffman, *Absorption and scattering of light by small particles*, Wiley science paperback series (Wiley, 1983) (cit. on p. 115).

[221]A. V. Bykov, A. P. Popov, A. V. Priezzhev, and R. Myllyla, "Multilayer tissue phantoms with embedded capillary system for OCT and DOCT imaging", Proceedings of SPIE-OSA Biomedical Optics **8091**, edited by R. A. Leitgeb and B. E. Bouma, 80911R–80911R–6 (2011) (cit. on pp. 115, 116, 121).

[222]S. A. Prahl, M. J. C. van Gemert, and A. J. Welch, "Determining the optical properties of turbid media by using the adding-doubling method", Applied Optics **32**, 559 (1993) (cit. on pp. 116, 203).

[223]J. Pickering, S. Prahl, N. Van Wieringen, J. Beek, H. Sterenborg, and M. Van Gemert, "Double-integrating-sphere system for measuring the optical properties of tissue", Applied Optics **32**, 399–410 (1993) (cit. on p. 116).

[224]P. Kubelka, "New Contributions to the Optics of Intensely Light-Scattering Materials. Part I", Journal of the Optical Society of America **38**, 448–457 (1948) (cit. on p. 116).

[225]P. Kubelka, "New Contributions to the Optics of Intensely Light-Scattering Materials. Part II: Nonhomogeneous Layers", Journal of the Optical Society of America **44**, 330–335 (1953) (cit. on p. 116).

[226]J. Bouchard, I. Veilleux, and I. Noiseux, "Accurately characterized optical tissue phantoms: how, why and when?", Proceedings of SPIE **7906**, 79060K–79060K–7 (2011) (cit. on p. 117).

[227]J. M. M. Pinkerton, "The absorption of ultrasonic waves in liquids and its relation to molecular constitution", Proceedings of the Physical Society. Section B **62**, 129 (1949) (cit. on pp. 117, 118).

[228]K. Zimmermann and J. Smith, "Ultrasound velocity in fixed human liver: empirical anova and regression modelling on histologically assessed abnormalities", Ultrasonic Imaging **5**, 280–294 (1983) (cit. on p. 118).

[229]B. Zeqiri, W. Scholl, and S. P. Robinson, "Measurement and testing of the acoustic properties of materials: a review", Metrologia **47**, S156–S171 (2010) (cit. on pp. 118, 119, 125).

[230]N. Bilaniuk and G. S. K. Wong, "Speed of sound in pure water as a function of temperature", The Journal of the Acoustical Society of America **93**, 1609–1612 (1993) (cit. on pp. 118, 136, 187, 190).

[231]W. C. Vogt, C. Jia, K. A. Wear, B. S. Garra, and J. Pfefer, "Biologically relevant photoacoustic imaging phantoms with tunable optical and acoustic properties.", Journal of Biomedical Optics **21**, 101405 (2016) (cit. on pp. 121, 126).

[232]W. C. Vogt, C. Jia, K. A. Wear, B. S. Garra, and J. Pfefer, "Design and phantom-based validation of a bimodal ultrasound-photoacoustic imaging system for spectral detection of optical biomarkers", Proceedings of SPIE **9315**, edited by R. Raghavachari, R. Liang, and T. J. Pfefer, 931502 (2015) (cit. on pp. 121, 141).

[233]M. S. Wróbel, A. P. Popov, A. V. Bykov, M. Kinnunen, M. Jędrzejewska-Szczerska, and V. V. Tuchin, "Measurements of fundamental properties of homogeneous tissue phantoms", Journal of Biomedical Optics **20**, 045004 (2015) (cit. on p. 121).

[234]W. C. Vogt, C. Jia, K. a. Wear, B. S. Garra, and J. Pfefer, "Quantitative assessment of photoacoustic tomography systems integrating clinical ultrasound transducers using novel tissue-simulating phantoms", Proceedings of SPIE **9323**, edited by A. A. Oraevsky and L. V. Wang, 932333 (2015) (cit. on pp. 121, 126, 129).

[235]E. L. Madsen, G. R. Frank, T. A. Krouskop, T. Varghese, F. Kallel, and J. Ophir, "Tissue-Mimicking Oil-in-Gelatin Dispersions for Use in Heterogeneous Elastography Phantoms", Ultrasonic Imaging **25**, 17–38 (2003) (cit. on p. 126).

[236]UKAS, *M3003 - The Expression of Uncertainty and Confidence in Measurement*, tech. rep. November (UKAS, 2012), pp. 21–47 (cit. on pp. 126, 127).

[237]W. Phillips and D. Griffen, *Optical mineralogy: the nonopaque minerals* (W.H. Freeman & Co, 1981) (cit. on p. 129).

[238]R. F. Goddu and D. A. Delker, "Spectra-structure correlations for near-infrared region", Analytical Chemistry **32**, 140–141 (1960) (cit. on p. 129).

[239]J. D. Van de Ven and A. G. Erdman, "Near-infrared laser absorption of poly(vinyl chloride) at elevated temperatures", Journal of Vinyl and Additive Technology **12**, 166–173 (2006) (cit. on p. 129).

[240]Pigments and Additives Division: Clariant International Ltd, *The Coloration of Plastics and Rubber*, tech. rep. (2007) (cit. on pp. 131, 143).

[241]M. Berins, *Plastics engineering handbook of the society of the plastics industry* (Springer Science and Business Media, 1991) (cit. on pp. 131, 143).

[242]R. Berera, R. van Grondelle, and J. Kennis, "Ultrafast transient absorption spectroscopy: principles and application to photosynthetic systems", Photosynthesis Research **101**, 105–118 (2009) (cit. on pp. 131, 133).

[243]I. M. Kislyakov and C. S. Yelleswarapu, "Nonlinear scattering studies of carbon black suspensions using photoacoustic Z-scan technique", Applied Physics Letters **103**, 151104 (2013) (cit. on p. 131).

[244]K. F. Palmer and D. Williams, "Optical properties of water in the near infrared", Journal of the Optical Society of America **64**, 1107–1110 (1974) (cit. on pp. 132, 135, 161, 183, 185, 203).

[245]M. Fonseca, B. Zeqiri, P. Beard, and B. Cox, "Characterisation of a pvcp based tissue-mimicking phantom for quantitative photoacoustic imaging", in Opto-acoustic methods and applications in biophotonics ii (2015), p. 953911 (cit. on p. 137).

[246]P. C. Beard, "Two-dimensional ultrasound receive array using an angle-tuned Fabry-Perot polymer film sensor for transducer field characterization and transmission ultrasound imaging", IEEE Transactions on Ultrasonics, Ferroelectrics and Frequency Control **52**, 1002–12 (2005) (cit. on p. 137).

[247]E. Zhang and P. Beard, "Broadband ultrasound field mapping system using a wavelength tuned, optically scanned focused laser beam to address a Fabry Perot polymer film sensor.", IEEE Transactions on Ultrasonics, Ferroelectrics, and Frequency control **53**, 1330–8 (2006) (cit. on p. 137).

[248]*Tables of physical and chemical constants*, Kaye and Laby Online Version 1.0 (National Physical Laboratory, 2005) (cit. on p. 142).

[249]R. Su, H. Brecht, S. A. Ermilov, V. Nadvoretsky, A. Conjusteau, A. A. Oraevsky, F. M. Technologies, and N. P. O. Rd, "Towards Functional Imaging Using the Optoacoustic 3D Whole-Body Tomography System", Proc SPIE **7564**, 1–6 (2010) (cit. on p. 145).

[250]K. Wang, R. Su, A. A. Oraevsky, and M. A. Anastasio, "Investigation of iterative image reconstruction in three-dimensional optoacoustic tomography", Physics in Medicine and Biology **57**, 5399–5423 (2012) (cit. on p. 145).

[251]J. Balderas-Lopez, J A; Diaz-Reyes, "Photoacoustic technique in the transmission configuration for quantitative analysis of liquids", Revista Mexicana de Fisica **57**, 452–459 (2011) (cit. on p. 145).

[252]A. Arnold, E. Bascetta, and F. Gunstone, "Effect of sodium chloride on pro-oxidant activity of copper (ii) in peroxidation of phospholipid liposomes", Journal of Food Science **56**, 571–573 (1991) (cit. on p. 150).

[253]P. Walstra, CRC Food Science and Technology (CRC, 2002) Chap. Bonds and interaction forces, pp. 46–58 (cit. on p. 150).

[254]L. Cui, H. T. Cho, D. J. McClements, E. A. Decker, and Y. Park, "Effects of salts on oxidative stability of lipids in tween-20 stabilized oil-in-water emulsions", Food Chemistry **197, Part B**, 1130–1135 (2016) (cit. on p. 151).

[255]E. Petrova, S. Ermilov, R. Su, V. Nadvoretskiy, A. Conjusteau, and A. Oraevsky, "Using optoacoustic imaging for measuring the temperature dependence of Grüneisen parameter in optically absorbing solutions", Optics Express **21**, 25077–090 (2013) (cit. on pp. 153, 243).

[256]E. V. Petrova, S. A. Ermilov, R. Su, V. Nadvoretskiy, A. Conjusteau, and A. A. Oraevsky, "Temperature dependence of Grüneisen parameter in optically absorbing solutions measured by 2D optoacoustic imaging", Proceedings of SPIE **8943**, 1–6 (2014) (cit. on p. 153).

[257]E. V. Savateeva, A. Karabutov, V. Solomatin, and A. Oraevsky, "Optical properties of blood at various levels of oxygenation studied by time resolved detection of laser-induced pressure profiles", Proceedings of SPIE **4618**, 63–75 (2002) (cit. on p. 153).

[258]M. Fonseca, T. Saratoon, B. Zeqiri, P. Beard, and B. Cox, "Sensitivity of quantitative photoacoustic tomography inversion schemes to experimental uncertainty", in Proceedings of spie, Vol. 9708, edited by A. A. Oraevsky and L. V. Wang, 0 (Mar. 2016), p. 97084X (cit. on pp. 161, 163, 167, 169–172).

[259]S. Prahl, *Omlc tabulated molar extinction coefficient for hemoglobin in water*, `http://omlc.org/spectra/hemoglobin/summary.html`, Accessed: 2015-08-05 (cit. on p. 161).

[260]S. Prahl, *Omlc optical absorption of fat*, `http://omlc.org/spectra/hemoglobin/summary.html`, Accessed: 2016-01-19 (cit. on pp. 161, 184).

[261]R. L. van Veen, H. Sterenborg, A. Pifferi, A. Torricelli, and R. Cubeddu, "Determination of vis- nir absorption coefficients of mammalian fat, with time- and spatially resolved diffuse reflectance and transmission spectroscopy", in Biomedical topical meeting (2004), SF4 (cit. on pp. 161, 184).

[262]J. Hall, *Guyton and hall textbook of medical physiology*, Guyton Physiology (Elsevier Health Sciences, 2010) (cit. on p. 162).

[263]D. B. Jakubowski, A. E. Cerussi, F. Bevilacqua, N. Shah, D. Hsiang, J. Butler, and B. J. Tromberg, "Monitoring neoadjuvant chemotherapy in breast cancer using quantitative diffuse optical spectroscopy: a case study", Journal of Biomedical Optics **9**, 230–238 (2004) (cit. on p. 162).

[264]A. N. Bashkatov, E. A. Genina, and V. V. Tuchin, "Optical properties of skin, subcutaneous, and muscle tissues: a review", Journal of Innovative Optical Health Sciences **04**, 9–38 (2011) (cit. on p. 162).

[265]G. Paltauf, R. Nuster, M. Haltmeier, and P. Burgholzer, "Experimental evaluation of reconstruction algorithms for limited view photoacoustic tomography with line detectors", Inverse Problems **23**, S81–S94 (2007) (cit. on p. 178).

[266]Y. Xu, L. V. Wang, G. Ambartsoumian, and P. Kuchment, "Reconstructions in limited-view thermoacoustic tomography", Medical Physics **31**, 724 (2004) (cit. on p. 178).

[267]S. J. Arconada-Alvarez, J. E. Lemaster, J. Wang, and J. V. Jokerst, "The development and characterization of a novel yet simple 3D printed tool to facilitate phantom imaging of photoacoustic contrast agents", Photoacoustics **5**, 17–24 (2017) (cit. on pp. 180, 182).

[268]L. Díez, H. Calás, A. Ramos, and T. G. Álvarez-Arenas, "Ultrasonic properties of biocompatible silicone rubbers for matching transit-time piezoelectric transducers for blood flow estimation in coronary vessels", in 2011 ieee international ultrasonics symposium (Oct. 2011), pp. 852–855 (cit. on p. 182).

[269]A. Myronenko, A. Myronenko, X. Song, X. Song, M. Á. Carreira-Perpiñán, and M. Á. Carreira-Perpiñán, "Non-rigid point set registration: Coherent Point Drift", Advances in Neural Information Processing Systems 19, 1009–1016 (2007) (cit. on p. 189).

[270]P. Stefanov and G. Uhlmann, "Thermoacoustic tomography with variable sound speed", Inverse Problems **25**, 075011 (2009) (cit. on pp. 189, 190).

[271]G. Paltauf, J. A. Viator, S. A. Prahl, and S. L. Jacques, "Iterative reconstruction algorithm for optoacoustic imaging", The Journal of the Acoustical Society of America **112**, 1536 (2002) (cit. on pp. 189, 190).

[272]C. Geuzaine and J.-F. Remacle, "Gmsh: a 3-d finite element mesh generator with built-in pre- and post-processing facilities", International Journal for Numerical Methods in Engineering **79**, 1309–1331 (2009) (cit. on p. 193).

[273]M. Fonseca, E. Malone, F. Lucka, R. Ellwood, L. An, S. Arridge, P. Beard, and B. Cox, "Three-dimensional photoacoustic imaging and inversion for accurate quantification of chromophore distributions", in Proceedings of spie, Vol. 10064, edited by A. A. Oraevsky and L. V. Wang (2017), p. 1006415 (cit. on pp. 202, 204, 205, 209, 212).

[274]N. Huynh, F. Lucka, E. Zhang, M. Betcke, S. Arridge, P. Beard, and B. Cox, "Sub-sampled fabry-perot photoacoustic scanner for fast 3d imaging", in, Vol. 10064 (2017), 100641Y–100641Y5 (cit. on p. 234).

[275]R. Ellwood, F. Lucka, E. Z. Zhang, P. C. Beard, and B. T. Cox, "Photoacoustic imaging with a multi-view Fabry-Pérot scanner", Proceedings of SPIE **10064**, 1–7 (2017) (cit. on p. 234).